2015

Molecular dynamics simulation of fracture behaviour in nanocrystalline fcc structures

Linqing Pei
University of Wollongong

Molecular dynamics simulation of fracture behaviour in nanocrystalline fcc structures

A dissertation submitted for the award of the degree of

DOCTOR OF PHILOSOPHY

From

University of Wollongong

By

Linqing Pei

School of Mechanical, Materials and Mechatronics Engineering

Faculty of Engineering

2015

DECLARATION

I, Linqing Pei, declare that this thesis, submitted in fulfilment of the requirements for the award of Doctor of Philosophy, in the School of Mechanical, Materials and Mechatronics Engineering, University of Wollongong, Australia, is wholly my own work unless otherwise referenced or acknowledged, and has not been submitted for qualifications at any other university or academic institution.

Linqing Pei

October 2015

ACKNOWLEDGEMENTS

I would like to thank to my PhD advisors, Professor Kiet Tieu and Associated Professor Cheng Lu for their scientific advice and knowledge and many insightful discussions and suggestions that contributed to the completion of this thesis. I also have to thank the members of my research group, Mr. Xing Zhao, Dr. Kuiyu Cheng, Mr. Liang Zhang, Dr. Hongtao Zhu, Dr. Guillaume Michal and Dr. Ajit Godbole for their helpful advice and suggestions on my PhD subject.

I wish to gratefully acknowledge the help of Associated Professor Xiaoyan Li, Dr. Haofei Zhou and Mr Fuqi Qin in the pre-processing and the post-processing of my simulation work.

I would like to thank the China Scholarship Council and University of Wollongong for providing the scholarships.

Thanks also go to the University of Wollongong and the National Facility of the National Computational Infrastructure of Australia for providing the access to the supercomputer.

My time was also made enjoyable in large part due to the many friends who became a part of my life. I am grateful for time spent with my housemate (Dr. Wenxu Li) and friends (Dr. Binjing Lin and Mr. Peitang Wei). They gave me many supports in my life and a lot of suggestions on my research.

At last, I would like to thank my family for all their love and encouragement. For my parents who raised me with their unwavering love, for my brothers and uncle whose faithful supports during the final stages of this PhD, they are appreciated. I love all of them forever.

PUBLICATIONS

1. Linqing Pei, Cheng Lu, Xing Zhao, Zhang Liang, Kuiyu Cheng, Guillaume Michal, Kiet Tieu, 2015. Brittle versus ductile behaviour of nanotwinned copper: A molecular dynamics study. *Acta Materialia*, 89, 1-13.

2. Linqing Pei, Cheng Lu, Kiet Tieu, Xing Zhao, Kuiyu Cheng, Liang Zhang, 2015. Ductile-to-brittle fracture transition in polycrystalline nickel under tensile hydrostatic stress. *Computational Materials Science*, 109, 147-156.

3. Linqing Pei, Cheng Lu, Kiet Tieu, Xing Zhao, Liang Zhang, Kuiyu Cheng, 2015. Brittle versus ductile fracture behaviour in nanotwinned FCC crystals. *Materials Letters*, 152, 65-67.

4. Liang Zhang, Cheng Lu, Kiet Tieu, **Linqing Pei**, Xing Zhao. 2015. Molecular dynamics study on the grain boundary dislocation source in nanocrystalline copper under tensile loading. *Materials Research Express,* 2, 035009.

5. Liang Zhang, Cheng Lu, Kiet Tieu, Xing Zhao, **Linqing Pei**, Guillaume Michal, 2015. Molecular dynamics simulation on generalized stacking fault energies of FCC metals under preloading stress. *Chinese Physics B*, 24, 088106.

6. Liang Zhang, Cheng Lu, Kiet Tieu, Xing Zhao, **Linqing Pei**, 2015. Shear response of copper bicrystal with $\sum 11$ symmetric and asymmetric tilt grain boundaries by molecular dynamics simulation. *Nanoscale*, 7, 7224-7233.

7. Linqing Pei, Cheng Lu, Kiet Tieu, Xing Zhao, Kuiyu Cheng, Zhang Liang, 2014. Influence factors for brittle-to-ductile transition in twinned copper. *TMS 2014 Annual Meeting Supplemental Proceedings*, 487-494.

8. Liang Zhang, Cheng Lu, Kiet Tieu, **Linqing Pei**, Xing Zhao, 2014. Effect of stress state on deformation and fracture of nanocrystalline copper: molecular dynamics simulation. *Chinese Physics B*, 9 (23), 098102.

9. Kuiyu Cheng, Kiet Tieu, Cheng Lu, Hongtao Zhu, **Linqing Pei**, 2014, Effect of pre-heating on the microstructural evolution and super-plasticity of Al deformed by accumulative roll bonding. *Steel Research International*, 84, 1209-1215.

10. Liang Zhang, Cheng Lu, Kiet Tieu, Xing Zhao, **Linqing Pei**, 2014. Atomistic simulation on the structure and mechanical response of Σ3, Σ5 tilt grain boundaries under tension. *TMS 2014 Supplemental Proceedings*, 817-823.

11. Linqing Pei, Cheng Lu, Kiet Tieu, Hongtao Zhu, Xing Zhao, Kuiyu Cheng, Zhang Liang, 2013. A molecular dynamics simulation of fracture in nanocrystalline copper. *Journal of Nano Research*, 25, 188-194.

ABSTRACT

The study of material failure has always been very important for human beings. Previous studies were mostly conducted at the macroscopic and microscopic scale based on continuum mechanics. However, the effect of nanostructural features on fracture has not been fully understood. Therefore, it is necessary to investigate the fracture mechanics at the atomic scale. Computational modelling, particularly atomistic (or molecular) simulation is becoming an increasingly important technology with which to analyse fracture. In this thesis, molecular dynamics (MD) simulations were carried out to investigate the fracture behaviours in Face Centred Cubic (fcc) nanocrystals.

Nanotwinned Copper (Cu) has an unusual combination of ultra-high yield strength and high ductility, and in fact a brittle-to-ductile transition was previously observed in nanotwinned Cu despite Cu being an intrinsically ductile metal. However, the atomic mechanisms responsible for brittle fracture and ductile fracture in nanotwinned Cu are still not clear, so in this thesis, MD simulations at different temperatures were carried out to investigate the fracture of a specimen of nanotwinned Cu with a single-edge-notched crack whose surface coincides with a twin boundary. Three temperature ranges were identified as being indicative of the distinct fracture regimes under tensile straining that are perpendicular to the twin boundary. Below 1.1 K, the crack propagated in a brittle fashion, but between 2 K and 30 K a dynamic brittle-to-ductile transition occurred, and above 40 K the crack propagated in a ductile mode. A detailed analysis has been carried out to understand the atomic fracture mechanism in each fracture regime.

The specific type of fracture depends on competition between the atomic bonds breaking and the dislocation nucleation/emission associated with the energy barriers of materials, including the free surface energy, and stable or unstable stacking fault energy, etc. These barriers differ markedly between fcc metals. The search for brittle versus ductile fracture in nanotwinned nickel (Ni) crystal was carried out using MD calculations. These simulations revealed an obvious brittle-to-ductile fracture transition that involves the formation of a dynamic atomic ledge and the occurrence

of a local phase transition around the crack tip that is identical to nanotwinned Cu, but with different temperature regimes and crack propagation speeds for crack proliferation.

The molecular dynamic simulations using the embedded-atom-method potentials (EAM) to study the fracture in other fcc twinned crystals subjected to tensile deformation was also presented. A fundamental brittle-to-ductile transition observed in fcc nanotwinned crystals could be understood in terms of the ratio between the surface energy and unstable stacking fault energy, or the ratio of ideal tensile strength to the ideal shear strength in a confined range of twinning spacing distance.

The fracture of materials where brittle/ductile cracks begin and propagate along the cleavage plane depends not only on the orientations of the lattice, but also on details of the crack configurations. Exactly how and to what extent brittle fracture is influenced by the local atomic configuration around the crack tip has not been explored in detail in fcc single crystals. The study of brittle versus ductile fracture in single Ni with different crack orientations and with a pre-existing centred-notched crack using MD simulations was carried out and revealed that fracture in single Ni depends entirely on the specific crack cleavage plane, the direction of crack propagation and the direction and front of the crack. Furthermore, the atomic mechanism for the brittle-to-ductile fracture transition in single Ni crystal was also explained.

Finally, an MD simulation was used to study the tension deformation and failure in a polycrystalline Ni under tensile hydrostatic stress. The simulations revealed the mechanism of void nucleation and growth, and under external tensile hydrostatic stress the failed samples underwent ductile-to-brittle fracture transition. It was proposed that this fracture transition can be attributed to the more active activities of void/crack propagations, the more suppressed grain boundary (GB) and dislocation activates due to the additional tensile hydrostatic stress applied. Moreover, the effect of temperature on the brittle versus ductile fracture at a given tensile hydrostatic stress was investigated and showed that the incremental temperature helped to increase the brittleness of the material.

The work in this thesis covered the main aspects of fracture mechanics at the atomistic scale in fcc metals. It gave an insight into the fracture mechanism that is currently missing from theoretical analyses of dynamic fracture mechanics, some of which could help us understand the in situ experimental observations.

TABLE OF CONTENTS

LIST OF FIGURES

LIST OF TABLES

INTRODUCTION

Human beings are often faced with catastrophic phenomena, such as earthquakes, buildings collapse, the breakdown of planes, ships and cars, and the failures of bones due to injuries, etc. All have one common character: the breakdown of the basic constituents of any material ultimately leads to the failure of its overall structure and intended function. To understand how materials fail has always been of great importance in saving human lives and properties.

As is well known, material failure can be mainly divided into two categories: brittle failure and ductile failure. For the brittle failure mode, atomic bonds are broken as the material separates along a direction normal to the cleavage plane (see Figure 0.1(a)). This type of failure usually happens quickly, in which the fracture propagation velocity can be close to, or even larger than, the speed of sound in the material. In case of the ductile failure mode, the above-mentioned rapid fracture propagation is prevented by the motion of dislocations inside the material (Figure 0.1(b)). Which failure mode prevails in any particular situation depends on a number of factors such as the intrinsic atomic microstructure, temperature, grain size, the magnitude and direction of the applied force, misorientation, inserted twinning, impurities, sample size, etc.

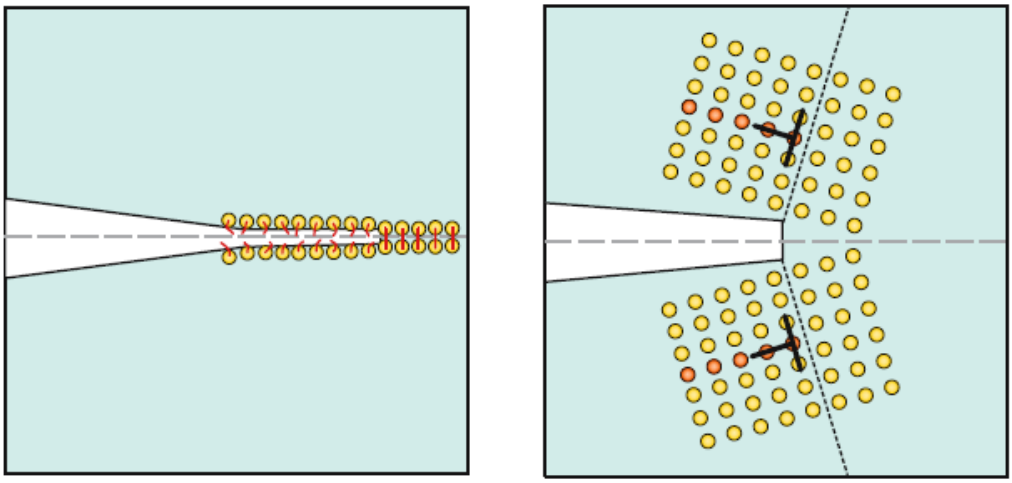

(a) (b)

Figure 0.1 Schematic of brittle (a) versus ductile (b) materials behaviour [1].

Figure 0.2 shows schematically the dependence of the failure mode on the temperature during an impact test. The material exhibits higher impact energy at higher temperature. As the temperature decreases, the impact energy decreases rapidly. Simultaneously, the fracture mode changes from ductile to brittle.

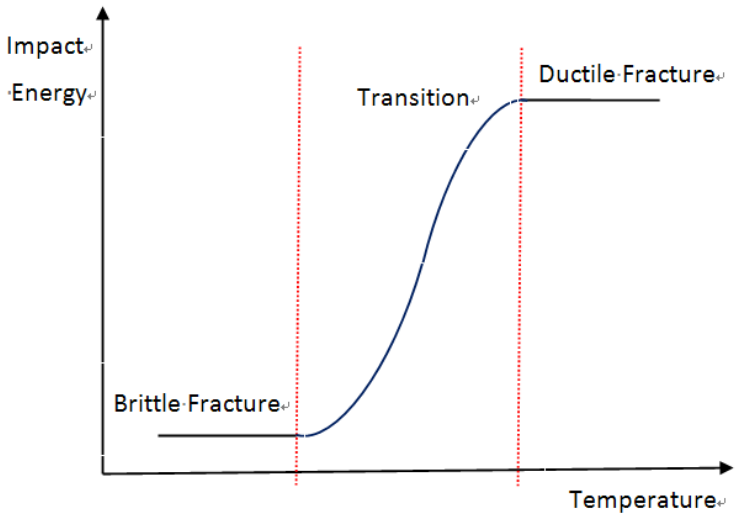

Figure 0.2 Schematic of brittle-ductile transition.

Nanocrystalline (NC) materials have attracted significant research interest particularly during the last two decades. Compared with conventional coarse-grained materials with grain size of the order of microns, NC materials show some excellent properties without the need to change the chemical composition, such as ultrahigh strength, high electrical conductivity and preserving ductility [2, 3]. For coarse grained materials, the yield stress, flow stress and hardness usually increase when the grain size of the material is reduced [4]. It has been found that the yield stress is inversely proportional to the square root of the grain size for a range of the coarse grained materials, as shown by the Hall-Petch relation, and the deformation mechanism is dominated by dislocation motion. However, the material exhibits decreasing flow stress as the grain size decreases to a critical value, for example smaller than 12 nm for Cu and Ni [5-7]. This indicates that the deformation mechanism no longer obeys the Hall-Petch rule. Instead, plastic deformation occurs due to grain boundary migration, sliding and diffusion in the nanostructured materials. This also makes the fracture propagation behaviour different from that in coarse-grained materials.

It has long been of great interest to investigate the fracture mechanism of materials. From the engineering point of view, in many cases a macroscopic approach may be sufficient. However, the microscopic and nanoscale aspects have gradually attracted increasing attention in recent years. Conventionally, the fracture mechanism of materials has been studied in the framework of continuum models, ranging from elastic theory to plastic theory. In recent times, the rapid development of computer technology has pushed researchers to investigate mechanical phenomena on the nano scale. These technical tools range from quantum mechanics-based methods and molecular dynamics (MD) methods, mesoscopic methods, to numerical continuum mechanics methods. The MD simulation technique has become an accurate and effective way to study deformation and fracture on the nano scale. Some MD simulations [8-12] have been carried out on the scale of micrometers and several nanoseconds, compared to the limited range for quantum-mechanical-based treatments (of the order of a few nanometers and picoseconds). The MD simulation technique also has the advantage of better description at small scales compared to continuum mechanics-based methods and less detailed failure processes for mesoscopic methods.

In this thesis, MD simulations are carried out for twinned single crystals, single crystals, polycrystals to reveal the fracture behaviour with consideration of several influencing factors such as temperature, model size, applied strain rate, crack system, and hydrostatic stress. These studies yield detailed information about the deformation and failure mechanisms on the atomic scale.

The work begins with a literature review of fracture as studied using continuum mechanics, MD simulation and in situ experimental/ analytical methods (Chapter 1).

In Chapter 2, the fundamental features of MD are described. The details of MD model construction and other particular related techniques are explained.

In Chapters 3 and 4, MD simulations are used to study the fracture behaviour in a twinned single Cu crystal and Ni crystal respectively. The effects of twinning space distance, temperature, model size and applied strain rate are discussed.

Chapter 5 discusses the competition between brittle fracture and ductile fracture in a single twinned fcc crystal. These competitive mechanisms were generalised from the point of energy, ideal shear stress and ideal tensile stress.

Chapter 6 focuses on the fracture behaviour of a single Ni crystal with various crack features (crack plane, crack propagation direction, crack front direction) at low temperature.

In Chapter 7, the effect of tensile hydrostatic stress on the transition from brittle failure to ductile failure in a Ni polycrystal is studied. In addition, the effect of temperature for a given constant tensile hydrostatic stress is investigated.

Finally, Chapter 8 presents the major conclusions drawn from all MD simulations and proposes a direction for future work.

CHAPTER 1 LITERATURE REVIEW

This chapter reviews the published research on topics considered essential for the best understanding of the mechanism of fracture at the atomic scale.

1.1 Basic continuum fracture mechanics

Continuum theory is the foundation on which structural failure at the macroscopic level can be understood. One of the most important developments in this field was a criterion proposed by Griffith [13], which was based on the criterion of simple energetic and thermodynamic considerations. The Griffith criterion assumed that brittle materials failed when the mechanical elastic energy released by crack extension (referred to as G_{clea}) equalled the energy required to create two new surfaces (referred to as $2r_{sur}$), its equation is written in Eq. 1.1.

$$G_{clea} = 2r_{sur} \tag{1.1}$$

Irwin [14] and his co-workers modified the Griffith criterion and found that plasticity played a significant role in the fracture of ductile materials. The plastic zone increases until the cracks grow and the material behind the crack tip unloads with the increasing load. Because of the plastic loading and unloading cycle near the crack tip that leads to the dissipation of energy as heat, a dissipative term has to be added to the energy balance relationship for ductile materials:

$$G_{clea} = 2r_{sur} + G_P \tag{1.2}$$

where G_{clea} is the mechanical energy release rate, r_{sur} is the surface energy, and G_P is the plastic dissipation per unit area of crack growth.

In addition, Irwin [14] found a method of calculating the amount of energy available for fracture in terms of the asymptotic stress and displacement fields near the crack tip in a linear elastic solid with various fracture modes. For a homogeneous linear elastic material, linear elastic deformation theory predicts the stresses by

$$\sigma_{ij}(r,\theta) = \frac{K}{\sqrt{2\pi r}} f_{ij}(\theta) \tag{1.3}$$

where σ_{ij} is a stress component. K is denoted as stress intensity factor. f_{ij} is a dimensionless function of θ, r and θ are the cylindrical polar coordinates defining the position of the stress element with origin at the crack tip. As shown in Figure 1.1(a), there are three ways of applying a force to enable a crack to propagate. K is a function of the cracking mode, the applied load, the sample geometry, the size and the location of the crack.

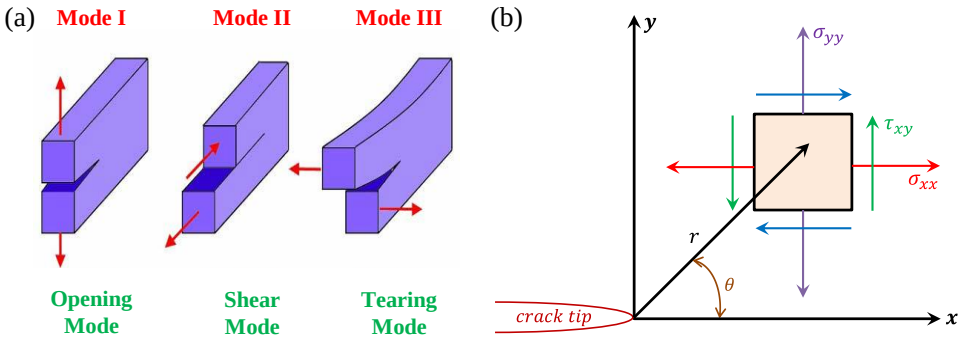

Figure 1.1 (a) Three modes of fracture in a 2D dimension. (b) Various stress components around the crack tip.

Consider an infinite plate containing a through-the-thickness mode I crack of length *2a* under a tensile stress σ at infinity. An element near the crack tip is subjected to normal stresses σ_{xx} (or σ_x), σ_{yy} (or σ_y) and a shear stress τ_{xy} in the x-y plane (Figure 1.1(b)). The stresses can be expressed by

$$\sigma_{xx} = \frac{K_I}{\sqrt{2\pi r}} cos\left(\frac{\theta}{2}\right)\left(1 - sin\left(\frac{\theta}{2}\right) sin\left(\frac{3\theta}{2}\right)\right) \tag{1.4}$$

$$\sigma_{yy} = \frac{K_I}{\sqrt{2\pi r}} cos\left(\frac{\theta}{2}\right)\left(1 + sin\left(\frac{\theta}{2}\right) sin\left(\frac{3\theta}{2}\right)\right) \tag{1.5}$$

$$\tau_{xy} = \frac{K_I}{\sqrt{2\pi r}} cos\left(\frac{\theta}{2}\right) sin\left(\frac{\theta}{2}\right) cos\left(\frac{3\theta}{2}\right) \tag{1.6}$$

$$K_I = \sigma\sqrt{\pi a} \tag{1.7}$$

where the subscript I indicates mode I, K_I is the stress intensity factor for mode I loading and a is the crack length.

It can be seen that the stress intensity factor (K) is a parameter that amplifies the magnitude of the stresses near the crack tip in a linear elastic material. If one assumes that the material fails at some critical combination of stresses, then it follows that fracture must occur at a critical stress intensity K_c. This critical value is a measure for the crack resistance of a material. It is also called the fracture toughness of the material. K_c is a material property and can be determined by experiment.

Dugdale and Barenblatt [15, 16] believed that a region of non-linear behaviour existed at the crack tip, and designed cohesive zone models to account for the non-linear behaviour to replace the singularity of the crack tip. They used a non-linear surface traction-displacement law to specify the evolution of material damage and separation. This model is widely used for fractured inelastic materials. However, the non-linear response of the cohesive zone changes the interactions between the cracks and dislocations such that it is still restricted to the cohesive surface.

Rice and Thomson [17] introduced a concept for the origin of brittle versus ductile behaviour of materials. Their studies indicated there was a competition between brittle (cleavage) and ductile (dislocation emission) mechanisms at the tip of a crack. Furthermore, they extended their study to the material parameters which characterise this behaviour [18, 19]. Their results showed that once the brittle and ductile parameters (free surface energy and unstable stacking fault) are known, the results can predict whether the material is intrinsically brittle or ductile. Zhou and Thomson [20] proposed that the ledges on cracks could be efficient sources for dislocation emission at loads well below the critical load, and that dislocations could easily be emitted, unlike homogenous dislocations, because of the finite lengths of dislocations at the

ledge. Freund and Hutchinson [21] found that the brittle-to-ductile transition could be determined by the ability of the crack to overrun the active plastic zones. As Argon [22] pointed out, it is possible to nucleate dislocations from the tip of a propagating cleavage crack at finite temperatures in many intrinsically brittle solids. While the cleavage at the crack tip is mainly independent of temperature, the initiation of dislocation loops from the crack tip can be greatly assisted by thermal activation. At a given temperature, and at a crack velocity below a critical value, more dislocation emissions from the crack tip lower the stress at the crack tip below the level needed for continued cleavage, resulting in a brittle-to-ductile transition.

A proper theoretical description of fracture should not only comprise the linearity/nonlinearity in the vicinity of near the crack, it should also consist of the bond breaking between atoms near the crack tip, as well as the formation of extended defects such as dislocations that are slightly beyond the crack tip. Once the dimensions of the material reach ultra-small scales, a continuum description of the materials is often questionable, and its method cannot give very much information on the dynamic evolution of the fracture. For these reasons, an MD simulation provides a good tool to study the behaviour of fracture at the atomic scale.

1.2 MD simulations of fracture

The earliest MD simulation of fracture was conducted by Ashurst and Hoover [23]. Although their model was extremely small, with just 64×16 atoms, they successfully described many fracture dynamic features. Abraham et al. [24, 25] used the Lennard-Jones potential to carry out an MD simulation of fracture of up to 500,000 atoms; the results of the so-called mirror-mist-hackle transition were striking because the MD simulation reproduced phenomena that had been discovered in experiments a few years earlier [26]. In the recent decade, researchers used MD simulation to investigate the plastic deformation and the failure mode that includes brittle, brittle versus ductile transition, ductile, in single crystal or polycrystal. Those materials include fcc, bcc,

hcp, diamond cubic structures. Most studies on fcc or hcp structured metals have shown the ductile fracture failure modes, but only a few of them show the brittle modes, while more studies about bcc and diamond cubic structures have shown the brittle fracture failure modes under the same or similar working conditions with fcc structural metals. The deformation with brittle fracture behaviour shows a sharp difference compared with ductile fracture behaviour. As mentioned previously, for the brittle failure mode, atomic bonds are broken as the material separates at a higher crack propagation speed along the direction normal to the cleavage plane. But for the ductile failure mode, the above-mentioned rapid fracture propagation is prevented by the motion of dislocations inside the material. However, the brittle failure could be closely relevant to the ductile failure from the atomic point of view. The impact factors such as model size, impurity, pre-existing twin, applied force, etc., could present very similar laws to influence the deformation/failure of brittle and ductile materials. The understanding of brittle fracture failure mode in fcc metals is still superficial, less than in bcc and diamond cubic structures. In fcc, bcc, hcp, diamond cubic structural metals, they may share the same fracture transition mechanisms that the occurrence of phase transformation and the ledge ahead of the crack tip induces a final brittle-to-ductile fracture transition. So with the literature review in this thesis, the MD simulation work on the deformation/failure in bcc, hcp, diamond cubic, fcc structural metals were all mentioned. The MD simulation works on bcc and diamond cubic structures were firstly reviewed, and then followed by that on fcc structure. In other words, some literatures are on bcc metals and Si, which are relevant to my work.

1.2.1 Crack wave speed

Crack propagation within brittle materials normally runs faster than within ductile materials. This led to an interesting question: what is the limiting speed of cracks. Broberg [27] reported that it is impossible for a mode I crack to propagate at a velocity greater than the Rayleigh wave speed (mode I: $v < c_r$). Similarly, there is also a forbidden velocity zone for a mode II crack between the Rayleigh and shear

wave speed. Many researchers wondered whether shear cracks could jump from sub-Rayleigh to super-shear velocity. In 1976, Andrews [28] used a slip weakening model to find that a shear crack approaching the Rayleigh wave speed induced a microcrack or a daughter crack that triggered speeds exceeding the shear wave speed. Huang and Gao [29] studied the intersonic propagation of shear cracks along a weak interface using MD simulations and continuum elastodynamics methods. Their results showed that the initial crack started to grow at a critical time and then quickly reached the Rayleigh wave speed, but afterwards when an intersonic daughter crack was nucleated in front of the mother crack, the crack propagation speed immediately jumped to the longitudinal wave speed. These results also indicated that continuum mechanics could not provide qualitatively useful insights into the mechanisms of intersonic shear crack propagation. Geubelle and Kubair [30] found that without a daughter crack, intersonic speeds began to form for a crack propagating in a pre-stressed specimen under large mixed mode loading. Rosakis [31] first reported an experimental method to validate whether mode II loaded cracks could move at intersonic velocities through mother-daughter mechanisms. Buehler et al. [32] investigated a crack under mode I and mode II loading conditions that suddenly stopped, and also discussed the possibility of cracks stopping from super-Rayleigh and supersonic speeds.

Because metals can become weaken or softer, and polymers may stiffen as the strain approaches the material failure state, linear elasticity theories are no longer applicable. Abraham et al. [33, 34] proposed that the hyper-elastic effects at the crack tip may play an important role in the dynamics of fracture. Indeed their findings showed that limiting velocities can be arrived at higher speeds-supersonic crack propagation, which can be in excess of the conventional sound speeds of a solid. Buehler et al. [35, 36] demonstrated this theory by using a 2D large-scale molecular-dynamics simulations combined with continuum mechanics concepts. The simulated interatomic potential chosen was the biharmonic potential, and to avoid crack

branching, the author set a weak fracture layer in the centre of the model by assuming atomic bonds across the path expected by the crack path snap. They found that if a local stiffening zone existed near the crack tip, a mode I crack could move faster at intersonic speed than the Rayleigh wave speed (see Figure 1.2(a)), and for mode II, supersonic cracks were observed in Figure 1.2(b), whereas conventional linear theory accepts that mode I and mode II cracks are limited by the Rayleigh wave speed and longitudinal wave speed, respectively. In addition, Buehler et al. [35] revealed that the hyperelastic region and crack speed were inversely proportional to the onset strain for the hyperelastic effect.

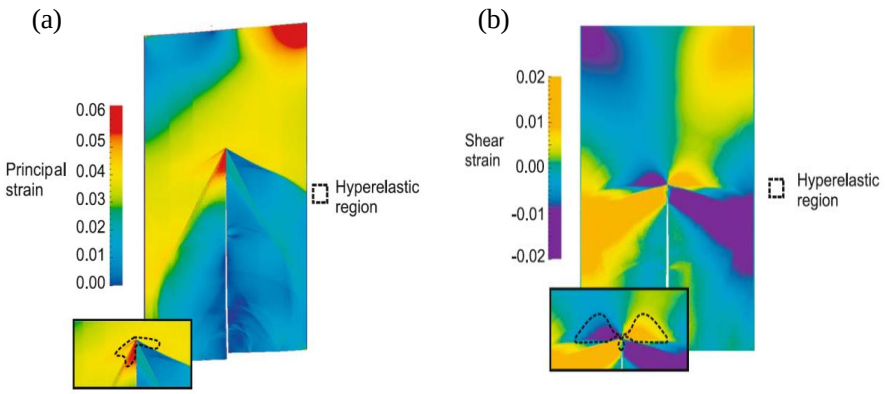

Figure 1.2 (a) Intersonic mode I crack, the Mach cone is associated with the shear wave speed. (b) Supersonic mode II crack, the two Mach cones associated with shear wave and longitudinal wave can clearly be recognised if a local stiffening zone exists near the crack tip. Data from Buehler et al. [35].

1.2.2 Preferred crack plane and orientation

deCelis et al. [37] studied the brittle cleavage in alpha iron and found the preferred plan (010) of instability for cracks at 0 K by utilising the Johnson and Morse potential, even in some instances the initial propagation on the $(\bar{1}10)$ plane. Kohlhoff et al. [38] used the Finnis-Sinclair and Johnson potential and found that both crack planes {110} and {100} were prone to cleavage without dislocation emission.

Comparatively speaking, the {100} plane was more prone to cleavage than the {110} plane. Shastry and Farkas [39] focused on studying MD crack propagation under mode I loading with Simonelli potential, using a crack plane with a different front direction ⟨100⟩, ⟨110⟩, and ⟨111⟩. They discovered that both crack orientations {011}⟨011⟩ and {011}⟨111⟩ showed a dislocation emission at 0 K, whereas the [100]{01$\bar{1}$} showed crack cleavage. Borodin and Vladimirov [40] limited the relevant crack orientation systems on (001)[100], (001)[110], (011)[100], and found that crack with crack orientation of (001)[100] was more likely to propagate than (011)[100]. However, in a slip band emission it was normal for cracks to propagate in both directions ⟨100⟩ and ⟨110⟩. A formation of multilayer stacking faults on {112} was observed for ⟨110⟩ propagation direction. Nishimura and Miyazaki [41] studied the influence of (112)[110] and (111)[110] GB on the propagation of cracks and found the first kind of GB prevented the propagation of brittle cracks because it had a low GB energy, and its structure was symmetrical and stable. Conversely, the high GB energy of (111)[110] cannot prevent brittle cracks from propagating. Takahashi et al. [42] carried out experimental investigations of microscopic patterns in Fe-3% Si and showed that cracks could have propagated on (011) planes if hydrogen was around the fatigue crack.

1.2.3 Phase transformation

Latapie and Farkas [43] discovered that in polycrystalline Fe, the stress can induce a Body Centred Cubic (bcc) to fcc phase transformation and new grain nucleated at the crack tip without dislocation emissions at temperatures of 100 K, 300 K, and 600 K. As the intensity of stress increased the stress-induced region grew and the new bcc structure rotated about 45° around a ⟨110⟩ axis from the original grain within the {110} GB plane (see Figure 1.3). A simulation was conducted to study crack propagation on (001)[100] plane [40], and it has been found that in some loading conditions, bcc-to-fcc transformation took place in front of the crack tip. Cheung et al. [44] proposed a phase transformation mechanism for Fe under mode I loading method

using an MD simulation, and then pointed out that the bcc to Hexagonal Close Packed (hcp) phase transformation resulted from homogeneous shear and atomic shuffling, and the reverse transformation (by uniaxial compression) only resulted from homogeneous shear without atomic shuffling. An increasing temperature has a positive role in deforming structures because of the critical stress required for the transformation decreasing with increasing temperature. Guo and Zhao [45] investigated five types of mode I cracks in bcc-iron crystal, including types of $\{011\}\langle 011\rangle$, $\{100\}\langle 110\rangle$, $\{110\}\langle 110\rangle$, $\{111\}\langle 110\rangle$, $\{100\}\langle 010\rangle$, $\{110\}\langle 010\rangle$, and found that for cracks with a $\langle 110\rangle$ front, the stress-induced transformation (from original bcc structure to hcp structure) was accompanied with new grain nucleation at the crack tip. They explained that the concentration of stress at the crack tip was relaxed by twinning and the formation of new grain and deformation energy, because the energy of the hcp structure was greater than the original bcc structure. They determined that the possibility of transformation happening from bcc-to-hcp must be at a much higher loading level. Guo et al. [46] further discovered that in bcc metals and alloys, for cracks with $\langle 100\rangle$ crack fronts, the bcc-to-fcc phase transformation occurred, and for $\langle 110\rangle$ crack fronts, the bcc-to-fcc and bcc-to-hcp transformation occurred. Nishimura and Miyazaki [41] achieved a similar structural transition from bcc to hcp structures induced by hydrostatic stress that was concentrated around the crack tip for a $\{101\}\langle 010\rangle$ plane system.

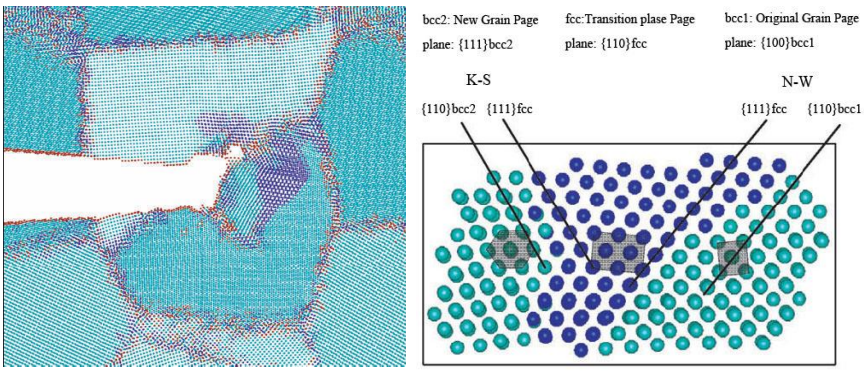

Figure 1.3 Phase transformation from bcc structure to fcc structure in polycrystalline Fe [43].

1.2.4 Grain size and impurity

Unlike a single crystal, individual grains of a polycrystal are not subjected to a single uniaxial tensile stress because the neighbouring grains are compatible. This means that the GB effects and grain size effects should be considered when discussing crack propagation in the polycrystalline model. An early polycrystal study was performed in 1995 with a model containing about 8000 atoms of pure iron. The model showed that the fracture process was dominated by the growth of subcracks from the GB (intergranular fracture), while at higher temperatures, GB diffusion and slip led to a fracture transition from brittle to ductile. Plastic deformation of nanocrystalline molybdenum with a grain size of 11.8 nm at high strain rates was studied by Frederiksen et al. [47]. It was found that during the plastic deformation process, different deformation mechanisms were involved, including GB sliding, dislocation migration, and twin formation. One of the most striking phenomena was that an intergranular fracture appeared when deformation was beyond 6%, which meant that breaking bonds on the grain boundaries (GBs) became more feasible. One possible reason was that the applied interatomic potential (EAM potential) had low surface energies which tended to make the bonds break easier. The results also showed that low temperatures and high strain rates favoured the occurrence of intergranular fracture. Latapie and Farkas [43, 48] examined the effect of temperature (from 100 to 600 K), the average grain size (from 6 to 12 nm) and crystallographic/GB orientation on the fracture mechanisms and properties in nanocrystalline α-Fe crack propagation. The simulation results showed that for all grain sizes, there was intragranular fracture combined with an intergranular fracture. Intragranular fracture was mainly decided by crystallographic orientation, so if the crystal were oriented favourably, crack propagation would occur in a brittle manner, and vice versa. However, intergranular fracture depended mainly on the orientation of the GBs. When the angle between the GB and crack plane was below 44°, a crack propagated along the GB. When the angle

was more than 75° the crack stoped propagating. With crack arrest, increasing the intensity of stress tended to induce intergranular fracture followed by the coalescence of formed nanovoids in front of the crack tip. Zhang et al. [49, 50] used a columnar grain model to observe an obvious intergranular failure. It was explained that a local concentration of stress was generated by the incompatible plastic deformation of two neighbouring grains when a twin reached a GB. These findings were related to the grain size effect, where the decreasing grain size improved ductility with less intergranular fracture.

It was interesting to observe that impurities can strengthen the GBs and significantly improve the ductility of relatively larger size grains, whereas impurities decrease the ductility of the smallest grain sizes [43, 48, 51, 52]. Figure 1.4 shows that under the same conditions, the sample without C impurities supported the development of crack propagation more than the sample with C impurities. The author attributed this to the impurities hindering grain-boundary sliding because the existing C impurities decreased the free volume available in the GBs.

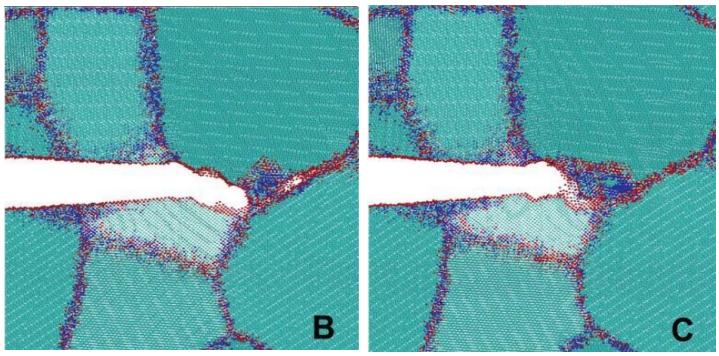

Figure 1.4 The crack-tip configuration at a loading of three times the Griffith value for the sample without C impurities, showing the formation of a nano-crack ahead of the main crack. (C) The crack-tip configuration at a loading of three times the Griffith value for the sample with C impurities, showing that the formation of a nano-crack ahead of the main crack is suppressed [52].

1.2.5 Dislocation activity and twinning around the crack tip

Ductile materials are characterised by their capacity to withstand large deformation and deform permanently. Two basic concepts must be grasped to understand the crack-tip processes, one being dislocation nucleation-emission at the crack tip and the other being dislocation mobility. Rice [19] observed that a leading partial dislocation was emitted from the crack tip leaving an intrinsic stacking fault ribbon, and then the trailing partial dislocation was emitted on the same slip plane, which completed the dissociated dislocation. It was believed that competition between the dislocation emission and crack propagation determines how failure occurs. Hirsch and Roberts [53] proposed that dislocations were emitted by sources activated by the high stresses near the crack tip and the rate at which they moved away from the crack-tip (dislocation mobility) determined the toughness of the material, and the dislocation shield emitted at the crack tip and the source, inhibited crack cleavage.

The development of atomic computation enabled researchers to study dislocation and twinning ahead of the crack tip and see how the crack propagates and becomes blunt. Farkas [54] studied the multiple-dislocation emissions from the crack tip in Al using EAM potential. Crack cleavage can still advance after crack blunting if the number of dislocations emitted remains small. Another important result was that perfect dislocations never emerged from the crack-tip, which is why the higher-energy barrier for the emission of a trailing partial dislocation or a microtwin was energetically favourable. Tadmor and Hai [55, 56] found that twins were generated by a layer-by-layer emission of Shockley partial dislocations from the crack tip by competing with the trailing partial emitted on the same plane with leading partial dislocation, and further found that the criterion for a twin beginning at the crack tip was affected by the system crystallography and loading mode.

Noronha and Farkas [57] used a multiscale approach combining MD and discrete dislocation dynamics (DD) simulation to study the effects of dislocation blocking on the fracture of Al, and found that fracture resistance increased as the dislocation blocking distance increased. Zhu et al. [58] did the first atomistic study of the saddle-point configuration and activation energy for the nucleation of a 3D dislocation loop from a stressed crack-tip in single crystal Cu using many-body interatomic potential, and found that the homogeneous nucleation of a dislocation loop at an atomically smooth crack tip in a Cu was unlikely to be the dominant process; it was more likely that local structural heterogeneities such as a crack-tip ledge would dominate the brittle-ductile response of fcc metals. Warner et al. [59] used the extensive multiscale simulations technique coupling MD and FEM to capture the transition from crack-tip twinning at short times to the formation of full dislocation at long times about Al at temperature 300 K. Furthermore, they extended their twinning predictions to the twinning of other fcc metals; the results are shown in Table 1.1. These striking results differed from earlier atomistic simulations and experimental observations because any significant deformation event can be allowed to occur on those time- and length-scales by applying unrealistically high loads or deformation rates compared with the values used in experiment. Yamakov and Glaessgen [60] also commented on the controversy between modelling and experiment being reconciled by multiscale simulation through time and length scales. Warner and Curtin [61] used a similar multiscale simulation model to evaluate the temperature-dependent activation energy barriers for dislocation nucleation in Al and Ni. It was revealed that for Al, a transition from twinning to full dislocation emission ahead the crack-tip would return to twinning as the temperature increased to 500 K, but Ni behaved in a more traditional manner, with its twinning tendency monotonically increasing with lower temperatures and higher rates without the transition from twinning to full dislocation emission.

Table 1.1 Material parameters at 300 K used to examine the transition from twinning to full dislocation emission in various fcc metals [59].

Material	b_p (Å)	μ (GPa)	ν	γ_{usf} (J m^{-2})	γ_{ssf} (J m^{-2})	γ_{utf} (J m^{-2})	γ_{stf} (J m^{-2})	ΔU_{trans} (eV Å^{-1})	$\Delta U_{trans}^{approx}$ (eV Å^{-1})	Transition time
Al	1.65	29.2	0.319	0.128	0.079	0.168	0.087	0.034	0.031	micro-seconds
Pt	1.60	65.2	0.393	0.388	0.240	0.522	0.240	0.058	0.049	micro-seconds
Au	1.66	30.9	0.416	0.110	0.040	0.135	0.040	0.066	0.058	micro-seconds
Ni	1.44	93.2	0.285	0.173	0.104	0.236	0.104	0.089	0.075	seconds
Ag	1.67	56.7	0.354	0.093	0.018	0.106	0.014	0.113	0.101	hours
Cu	1.48	54.8	0.325	0.200	0.053	0.236	0.053	0.127	0.115	hours
Ir	1.57	221.6	0.242	0.679	0.280	0.872	0.280	0.442	0.436	$\gg$ giga-years

Fakas et al. [62] found that crack propagation proceeds at a small grain size from 5 to 12 nm in an intergranular fracture, not an intrangranular dislocation based process in an Ni MD simulation. When a crack tip has pre-existed in the grain, the crack initially blunted by emitting a limited partial dislocation along the crack, but this was soon taken over by the creation of nanovoids in the surrounding GBs. The consequent result was that the cracks propagated in an intergranular pathway. Kadau et al. [63] achieved similar intergranular fracture results in Al with grain sizes smaller than 10 nm. Farkas et al. [64] studied the dislocation activity around the crack tip and found that the plasticity near the crack tip was mediated by partial dislocations, unlike the previous observation of nc-Ni. Full dislocations and twinning were both observed (see Figure 1.5) in nanocrystalline Ni MD simulation with an average grain size 10 nm and a temperature 300 K. Further study in Ni with a mean grain size of 5 and 8 nm was conducted by Farkas [65], who summarised that by comparing two grain sizes, the smaller grain sizes were more ductile and therefore needed higher intensity stresses for cracks to propagate. This summary agreed with the inverse Hall-Petch relationship. The influence of grain size on crack blunting in nanocrystalline materials was also studied by Ovid'ko and Sheinerman [66], who found that with a decreasing grain size, less of the possible generated dislocations were emitted from the crack tip due to the effective suppression of GB. However the crack can easily grow rather than experience blunting, although in some nanocrystalline fcc metals it exhibited a brittle-to-ductile transition as the grains decrease in size. Cao et al. [67, 68] drew attention to

the study of fully dense nanoscale metals with EAM potential for Ni, and also observed intergranular fracture by coalescing nanovoids at GBs and triple junctions.

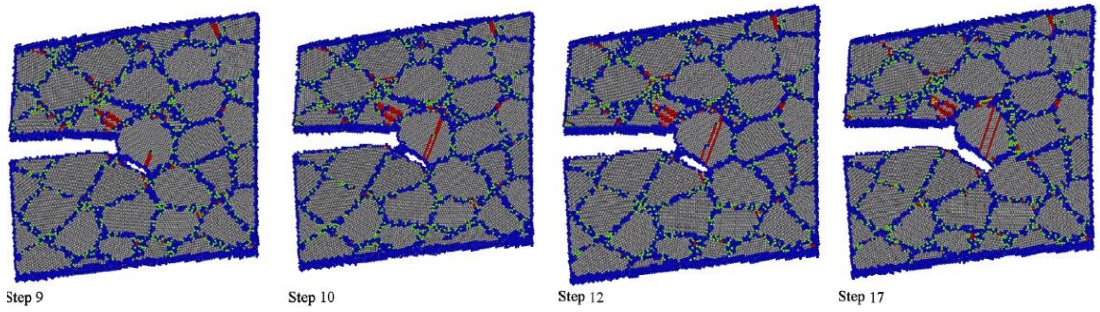

Figure 1.5 Sequence of events detailing the formation of a twinned area [64].

The classic model by Rice that can predict brittle cleavage along a given GB is favoured for crack propagation in one direction, whereas dislocation emissions from the crack-tip are preferred in the opposite direction. However, Cheng et al. [69] found that for some incoherent GBs such as $\Sigma 9\ (2\bar{2}1)$ etc., such directional anisotropy in intrinsic ductility was not observed; instead, dislocation emissions were forwarding in both crack propagation directions, because in copper, the dislocation emission was nucleating at a distance ahead of the crack tip rather than directly from the crack tip. Homogeneous dislocation also formed on the TB around the crack tip due to the high concentration of stress in nano twinned Cu [9]. Dislocation gradually piled up and evolved into virtually impenetrable dislocation walls ahead of the TB that eventually confined the crack nucleation and resisted propagation [70]. Zhang and Ghosh [71] captured the transition behaviour from softening to hardening effect due to the loss of dislocation mobility around the crack tip; their results showed that the local hardening effects at the crack tip stemmed from the high density stair-rod dislocations. In hierarchically nanotwinned metals with the same primary twin spacing, Yuan and Wu [72] observed that the smaller secondary twin spacing led to crack-tip blunting and crack propagation at GB followed by void coalescence at the sites of TB. Partial dislocations were nucleated from GB and no dislocations were nucleated from TB

ahead of the crack tip. For the larger of the secondary twin spacing, the crack mainly showed ductility dominated by blunting and extensive dislocation ahead of the crack tip. Bitzek and Gumbsch [73] found many dislocations at the crack tips that led to the emission of blunting dislocations on slip planes that initially were not available by local reorientation of the crack front due to its interaction between a pre-existing dislocation and crack tip. In Ni, the pre-existing crack cannot propagate or blunt further because the pre-existing nanocracks healed completely due to disinclination by GB migration [74].

Li et al. [75] used the experimental and MD simulation methods and found that in Al, there was twinning and reversible twinning at the crack tip at temperatures of 300 K. They showed that detwinning included two stages: (1) thinning of the twins, and (2) shortening of the TBs, while the high propensity for detwinning originated from the high stacking fault energy and low frictional forces pitted against the motion of partial dislocations at the twinning boundaries in Al.

1.3 Brittle-to-ductile fracture transition

1.3.1 Experiment observations

Experiments on silicon were investigated to observe the brittle-to-ductile transition [76-80]. This transition was found as a result of the emission configuration of dislocation where the process can be fulfilled by varying the temperature. Gumbsch et al. [81] found that brittle-to-ductile transition is controlled by dislocation mobility [82] rather than by dislocation nucleation [17] with decreasing temperature in single crystal Tungsten. The brittle-to-ductile transition temperature was related to the strain rate [83-86], such that the brittle-to-ductile transition temperature increased with an increasing strain rate in pure single-crystal Fe [85].

With assistance from impurities in the materials, brittle-to-ductile transition became easier, for example, the brittle-to-ductile transition (BDT) temperature in arsenic/antimony doped silicon was lower than in non-doped silicon [87, 88]. However, high-interstitial Fe-Cr-Mn alloys had a lower brittle BDT temperature when combined with N and C elements. Li [89] compared electrodeposited pure Ni (grain sizes of 44 nm) with Ni-15%Fe (grain sizes of 9 nm), and found there was brittle-to-ductile transition with changing grain sizes. For pure Ni, the coalescence of microvoids at GB or triple junctions occurred by breaking the last atomic bond. This resulted in the formation of actual cavities that appeared on fracture surfaces as a 'cup-cup' characteristic. This fracture performed a typical ductile behaviour whereby as the grain size was reduced to the regime where dislocations were generated and motions were improbable, and grain-boundary-related activities dominated the deformation. Tensile samples fractured with a limited reduction in area, which made fracture into a typical brittle behaviour (see Figure 1.6).

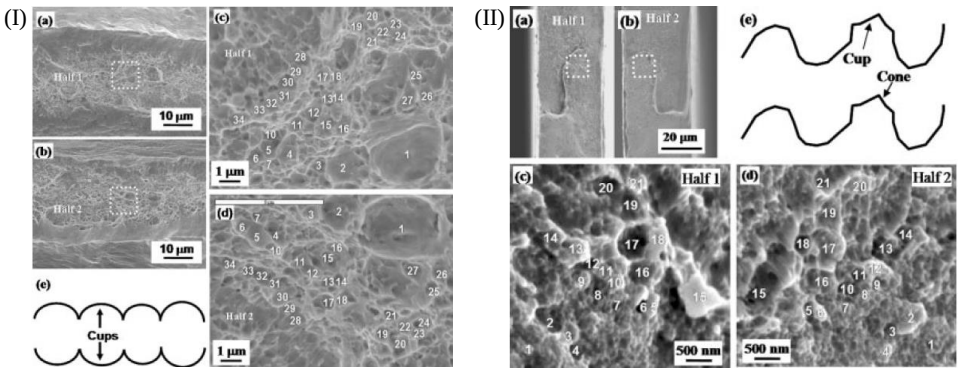

Figure 1.6 (I) Cup-cup fracture of pure Ni. (II) Cup-cone fracture of Ni-15% Fe alloy [89].

Other experimental observations of brittle-to-ductile transition demonstrated that the transition was influenced by the effect of sample size. Li and Ebrahimi [90] found that material showed a very high strain-hardening rate and failed by microcracking without any noticeable reduction in area as the grain size decreased to a critical regime. Copper nanowires exhibited both ductile and brittle-like fracture depending

on the diameters of the nanowires [91, 92]. The competitive mechanism of plastic deformation and fracture was controlled by density of the initial defects and the probability of dislocation interactions. A relative work was conducted in Ni nanowire to study the size dependence of brittle-to-ductile transition [93]. However, the unexpected brittle-like fracture in a single Au of sub-20 nm nanowires was associated with twin structures at the fracture zone [93]. This differs from the classic surface dislocation nucleation/propagation mediated mechanism in ductile fracture. Jang et al. [94] investigated the influence of sample size and the twin-boundary spacing and twin-boundary orientation on the mechanical responses of nanopillar Cu. A brittle-to-ductile transition was observed. Wang et al. [95] showed that ultrahigh-density twins triggered a ductile-to-ductile transition at a critical size that was caused by homogeneous nucleation of dislocations inside the nanowires (see Figure 1.7).

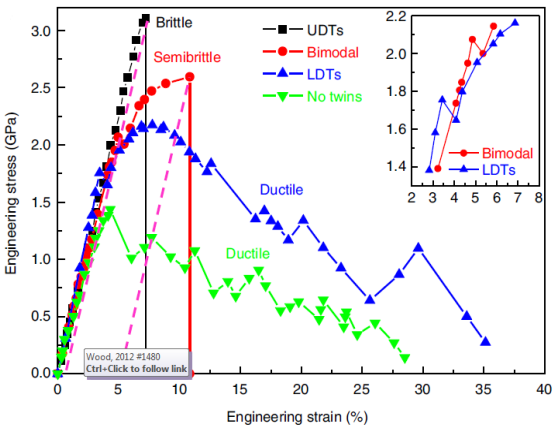

Figure 1.7 Representative stress-strain curves for Au nanowires with different twin structures. Dash lines in pink colour indicate the permanent inelastic deformation after fracture [95]. Samples are with ultra-high density of twins (UDTs), low desity of twins (LDTs) or medium density of twins (bimodal structures). The inset shows a close-up view of the yield points in the specimens with bimodal and LDTs.

1.3.2 MD simulations

Cheung [96] used the EAM potential to simulate the brittle-to-ductile transition in α-iron at temperatures between 200 K and 300 K. The results showed that temperature played an important role in brittle-to-ductile transition at temperatures of 200 K and below. The associated three crack orientations exhibited brittle behaviour and cleavage crack on the {110} and {100} planes. As the temperature increased, a dislocation emission accompanied by crack tip blunting occurred. An atomistic simulation of the formation of stacking faults in bcc iron under mode I loading was performed by Machová et al. [97], who stated that the growth of smaller cracks was associated with the emission of partial dislocations from the crack tip, and further transformation of the stacking faults behind the dislocations to multilayer twins. Guo et al. [98] simulated crack cleavage and blunting in bcc-Fe using the Finnis-Sinclair potential, and showed that at low temperatures (5 K, 100 K, 200 K), the cleavage fracture and twin formation were cooperative processes in brittle fracture. They further explained that the formation of twinning played an active role in brittle cleavage because the formation of twins at the crack tip was favourable for bond breakage. At a high temperature, the twinning process at the crack tip was weakened and disappeared and the fracture showed ductile behaviour due to an increasing dislocation movement. Hora et al. [99] obtained similar results by investigating the 3D molecular dynamics simulation of bcc iron single crystals using N-Body potential at a temperature of 0 K (brittle fracture) and 300 K (ductile fracture).

Apart from the influence of temperature on brittle-to-ductile transition, Uhnáková et al. [100-102] found the brittle-to-ductile behaviour at the crack front was affected by the T-stress (a nonsingular contribution to the stress field--a term that remains finite as the crack tip is approached) because increasing the T-stress can increase the critical load for dislocation nucleation and reduce the energy and peak stress required for the formation of twin; this could make cracks behave in a brittle manner. Song and Curtin

[103] studied the embrittlement of hydrogen in Fe and revealed that a ductile-to-brittle transition was caused by the suppression of dislocation emissions at the crack tip due to the aggregation of H.

The brittle-to-ductile transition was also observed in single silicon crystal [104]. The simulation used the first principles based on the reactive force field to test the transition from crack tip cleavage to dislocation emission. It was found that with a 10 K temperature interval, an abrupt change from brittle cracking to dislocation emission occurred because the intrinsically formed ledge laid down a local mode II shear component ahead of the crack tip which led to a dislocation nucleation on the (111) plane. As Figure 1.8 shows, there was a sharp change in the small interval temperature between 880-890 K, where the crack stopped in the middle of the sample and propagated no more.

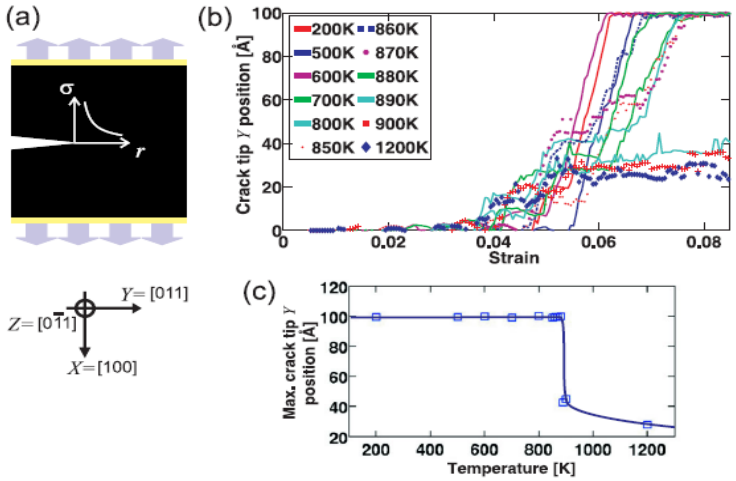

Figure 1.8 System geometry and crack dynamics analysis [104]. (a) Silicon single crystal. (b) Relation between strain and crack-tip position for a range of temperature from 200 to 1200 K. (c) Analysis of the maximum Y position of the crack at the end of simulation.

Experiments have shown that the fcc metals tend to have either ductile or brittle fracture under different working conditions, but there are only a few atomic

simulations that observed the same phenomenon in in situ fcc metals. Wu et al. [10] found the brittle-to-ductile transition in Cu single crystal using MD simulation: long sample length--brittle and short sample length--ductile (see Figure 1.9). Short nanowires can fail via dislocation plasticity along multiple slip planes within ductile necking, while long nanowires fail by an unstable localised shear along a single slip plane. By changing the length of the nanowires, ductile-to-brittle transition was also observed in single Au [105]. Interestingly, Jang and Wang [94, 95] recently showed that the brittle-to-ductile or ductile-to-brittle fracture when the distance of the twinning spacing decreases below a critical value; this distinct behaviour was probably attributed to the effect of size, facet features, and stacking fault energy curves of metal.

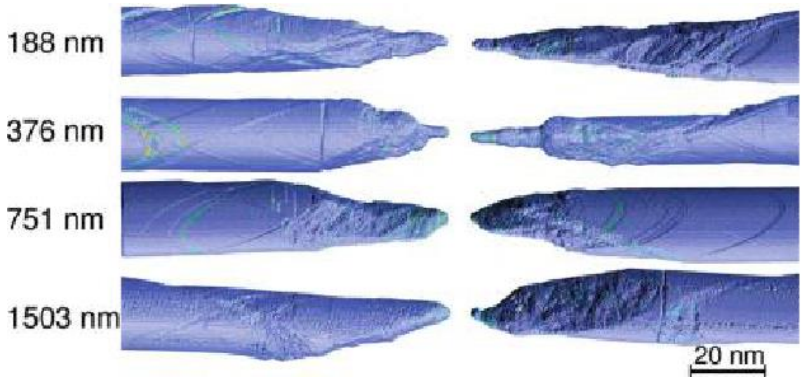

Figure 1.9 Fracture surfaces of nanowires with diameter d = 20 nm and different lengths in single Cu [10].

For polycrystal, the size-dependent deformation of nanocrystalline Ni for a range of diameters was identified [68] (see Figure 1.10). Small diameter nanowires fail by GB sliding, but GB sliding for thicker nanowires is inhibited due to the kinetic geometric constraints imposed by the neighbouring grains. Therefore, the sample failed by ductile necking, and by void nucleation and coalescence along the GBs. The inserted twins made the crack propagate from intergranular to intragranular in the sample of

thin polycrystalline Ni, while the fracture was concurrent with the nucleation of nanovoids at the intersections of TBs and GBs [106].

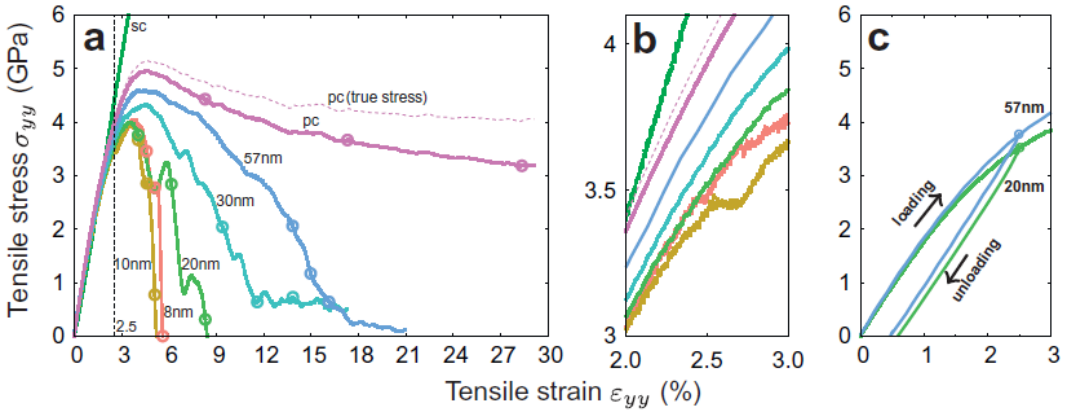

Figure 1.10 The engineering stress-engineering strain curves for the tensile deformation of nanocrystalline Ni samples of six diameters [68].

1.4 MD studies on deformation mechanism

Nucleation and propagation of dislocation and/or twinning are not only the major mechanisms of ductile fracture, but also the major mechanisms of plastic deformation. In order to better understand the activities of dislocation and twinning, this section reviews the previous MD studies on deformation mechanism at the atomic scale.

1.4.1 Generalised stacking fault curves

Stacking fault energy is considered to be the primary intrinsic material property that affects the propensity for dislocation and twinning. It is well known that a lower stacking fault energy promotes deformation twinning in coarse-grained/nanocrystalline fcc metals. But recent MD simulations and experimental observations have revealed that the fault energy alone is not enough to explain the dislocation/twin behaviour. A correct interpretation should include the generalised stacking fault energy curve, involving both stable and unstable stacking fault energies [107]. As mentioned before, Rice [19] used the unstable stacking fault energy (r_{usf})

to evaluate the brittle versus ductile response in fcc and bcc metals in terms of a competition between dislocation nucleation and Griffith cleavage at the crack tip. The unstable stacking fault energy was taken as the barrier that a partial dislocation must overcome in order to nucleate. As the partial dislocation began to emit, it left behind a stacking fault defect. Tadmor and Hai [55, 56] concluded that the tendency towards twinning depended on $(r_{utf}/r_{usf})^{-1/2}$, where r_{utf} is the unstable twin fault energy. Van Swygenhoven et al. [107] simulated 3D samples containing 15 grains using different model potentials (as seen in Table 1.2), and found that the deformation mechanism could not be explained by means of the absolute value of stable stacking fault energy (r_{sf}). They concluded that the formation of full dislocation and partial dislocation must be understood in terms of the ratio r_{sf}/r_{usf}, which is 0.97 for Al, 0.55 for Ni, and 0.13 for Cu respectively. When this ratio is almost unity, the energy barrier for creating a trailing partial is very low, so full dislocation in Al and partial dislocation in Ni and Cu can be seen. Table 1.2 shows the energy barrier for twin formation, where the value $r_{utf} - r_{sf}$ was twice as high as the barrier for a full dislocation $r_{usf} - r_{sf}$ in Al and Ni, except for Cu. This means that a twin was not normally seen in Al and Ni nanocrystalline samples with grains that were free of defects, although the sample was subjected to special conditions such as the high local stress intensity in GB, sample geometry [108, 109] and high shear stresses during ball milling and high-pressure torsion [110]. Froseth et al. [108, 111, 112] used three dimensional MD simulation to investigate the presence of in-grown twin boundaries (TBs) in nanocrystalline Al, while Ni and Cu promoted slip activity in the form of twin boundary (TB) migration by different ratios of the extrema of the generalised planar fault curves. Compared to different ratios r_{usf}/r_{utf} for Al, Ni, Cu, the value was about 3, 1, and 1.3 respectively, so TB migration was preferable to single partial dislocation nucleation in Al. Both TB migration and extended partial dislocations occurred simultaneously on high Schmid factor slip planes in Ni and Cu.

Table 1.2 Relaxed values for stacking fault energy (r_{sf}), unstable stacking fault energy (r_{usf}) and unstable twin fault energy (r_{utf}) for various potentials. The ratios r_{sf}/r_{usf} and r_{utf}/r_{usf} characterising the GPF curves are also listed below [107].

Potential	r_{sf} (mJ m^{-2})	r_{usf} (mJ m^{-2})	r_{utf} (mJ m^{-2})	r_{sf}/γ_{usf}	r_{utf}/r_{usf}
Al MF	146.0	151.3	200.0	0.97	1.32
Al EA	95.4	123.9	149.7	0.77	1.21
Ni CR	304.4	550.9	704.4	0.55	1.28
Ni MF	120.3	172.2	234.2	0.70	1.36
Cu CR	20.6	154.1	163.3	0.13	1.06
Cu SJ	33.5	173.1	190.0	0.19	1.10

MF, Mishin–Farkas; EA, Ercolessi–Adams; CR, Cleri–Rosato; SJ, Schiøtz–Jacobsen.

The Generalized Stacking Fault Curves could also be used to explain the effect of grain size on twinning and stacking faults [113]. A stacking fault was first formed by a leading partial dislocation and then a twinning partial converted the stacking fault into a twin nucleus. Leading partials were first activated in grains with a wide range of grain sizes to generate stacking faults. Twinning partials found it more difficult to nucleate and slip as the grain size decreases, if the inverse grain-size effect was operating. Finally, a higher applied stress was needed to emit a twinning partial than a leading partial. A similar validation was carried out by Kumar et al. [110, 114], who found that higher stresses were needed to emit partial dislocations in smaller grains.

1.4.2 Dislocation and twinning formation mechanism in fcc materials

Plastic deformation in an fcc single crystal depends on the dislocation nucleation and emission. It is largely accepted that the intrinsic deformation of fcc polycrystal stems from the dynamic interplay between dislocation and GB processes; the dislocation pile-up mainly occurs in coarse grained materials, while plastic deformation involves the continuous nucleation of dislocations from the Frank-Read source and their glide

motion through the crystal [115]. When the grains are less than 100 nm, GB provides the necessary dislocation sources of nanocrystalline materials. This means that if the grains reach their "strongest size", transition from a dislocation-based to a grain-boundary-based deformation will occur in nanocrystalline fcc metals [116]. It is known that slip in fcc crystals is almost exclusively limited to $\{111\}$ slip planes and $\langle 110\rangle$ slip directions (see Figure 1.11), so a common dislocation with Burgers vector $1/2\,\langle 110\rangle$ usually splits into two Shockley partial dislocations:

$$\frac{1}{2}<110>\rightarrow\frac{1}{6}<211>+\frac{1}{6}<12\bar{1}> \tag{1.8}$$

The crack tips can serve as nucleation sites for dislocation and twinning nucleation [19]. It was discovered that a leading partial dislocation was emitted from the crack tip that leaves an intrinsic stacking fault ribbon, and then a trailing partial dislocation was emitted on the same slip plane to complete the dissociated dislocation. Based on Rice's theory, Tadmor and Hai [55, 56] thought that instead of emitting a trailing partial, the second leading partial was nucleated on the neighbouring slip plane, but a two-layer thick microtwin was nucleated instead of a dissociated dislocation. The microtwin formed by increasing the load would finally become the true twin.

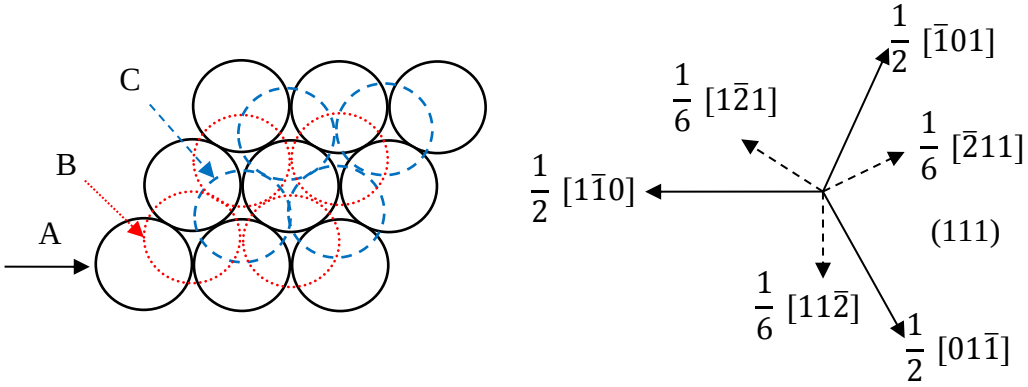

Figure 1.11 Three types of stacking positions A, B, C and vector notations on (111) plane in fcc crystal

Yamakov et al. [117] established a columnar Al atomic model with four angles oriented to the tensile direction (X direction) by rotating about [110] by 0°, 30°, 60°

and 90° angles using EAM potential. It was found that when the splitting distance was bigger than the grain diameter, the leading partials nucleated from the boundaries gliding across the grains and became incorporated into the boundaries on the opposite GB, while leaving behind a grain transected by a stacking fault. On the other hand, when the diameter of a grain was big enough (bigger than the splitting distance), a trailing partial dislocation connecting the previous formed leading partial dislocation was emitted, which means a fully developed and extended $1/2\,[011]$ dislocation dissociated into two partials occurred, as seen in Figure 1.12).

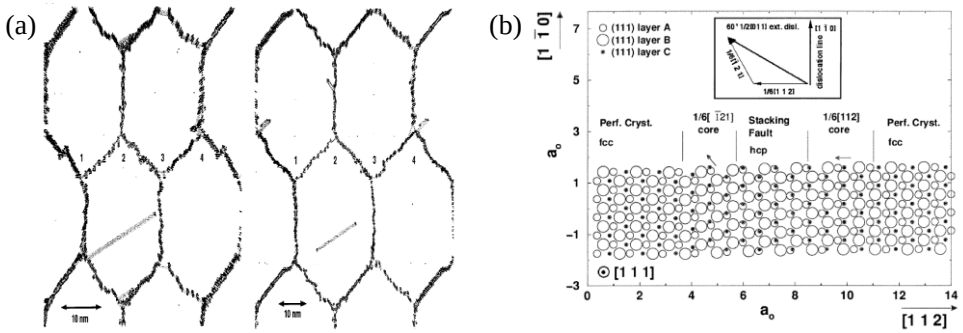

Figure 1.12 (a) A leading partial dislocation and a second trailing dislocation formation from a fully developed extended dislocation. (b) A complete dislocation 60^o--1/2[110] split into 30^o--1/6[-121] partial and 90^o--1/6[112] pure-edge partial on a (111) plane. Data from Yamakov et al. [117].

Yamakov et al. [8, 109] complemented their study on the twinning mechanism by proposing two different twinning forming mechanisms: (1) heterogeneous nucleation of a twin lamella from the GBs; and (2) homogeneous nucleation of twin lamellae from the grain interior. In the first case, twinning occurred by emitting successive $1/6\,[112]$ partial dislocation on adjacent $(11\bar{1})$ planes for the GB that involved the five regions defined in Figure 1.13(a), that are labelled 1, 2, 3, 4, 5. Another twinning formation involved the splitting and subsequent migration of a GB segment. In the second case it was explained that when the Shockley partials of two extended

dislocations on neighbouring planes glided past each another the intrinsic stacking fault of two dislocations in the overlap region combined to form an extrinsic stacking fault (see labelled 7a in Figure 1.13). This process can proceed further when a third extended dislocation joined the overlapped pair to form an extrinsic stacking fault configuration that leaded to a two-layer microtwin like labelled 7b in Figure 1.13(a-b). Another possibility was that when two extrinsically dissociated dislocations such as extended dislocations were terminated by two double-Shockley partials and then connected by an extrinsic stacking fault; a three-layer microtwin labelled 7c was then formed.

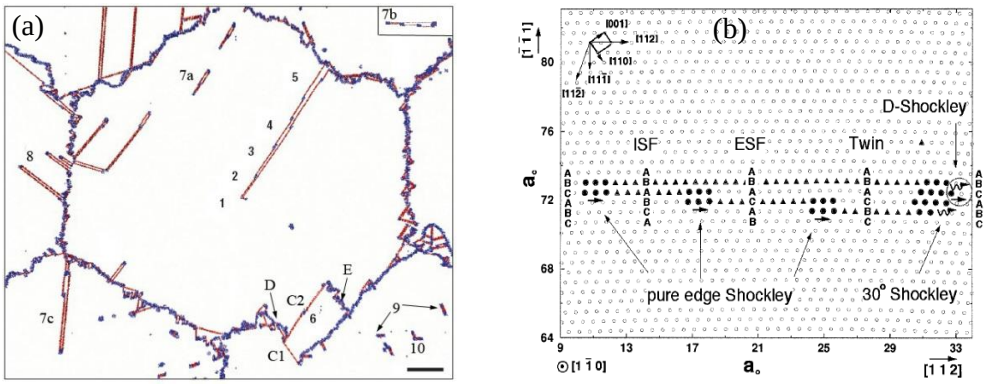

Figure 1.13 (a) 1--Perfect fcc crystal, 2--Intrinsic stacking fault, 3--Extrinsic stacking fault, 4--Twin separated by two (111) plane, 5--More widely separated twins. (b) View down the [1-10] texture axis of the atomic structure of three overlapping ISFs producing the two-layer twin configuration 7b in (a). Common-neighbour analysis distinguishes atoms in fcc (o), hcp (▲) and defected (●) surroundings. Data from Yamakov et al. [8].

1.4.3 Grain size

With coarse grained metals, the yield stress, flow stress, and hardness usually increase when the grain size is reduced [4], and the increasing yield stress is inversely proportional to the square root of the grain size. The other quantities follow a similar relationship that is called the Hall-Petch relationship, where deformation is dominated

by a dislocation piling up motion. However, the detailed mechanisms behind this relationship are not fully resolved because the grain size decreases into some critical nanometres [118]; for example, when the grains for copper and nickel are smaller than 12 nm [5-7], there is a decreasing flow stress and the deformation mechanism no longer obeys the Hall-Petch rules, instead, plastic deformation is carried out by atomic sliding in GBs (reverse Hall-Petch) or the dislocation-nucleation controlled mechanism.

A hexagonal grain structure in nanocrystalline Al was investigated by Shimokawa et al. [119], and they discovered a transition from grain-size hardening to grain-size softening when the grains decreased in size to a critical value of 30 nm. For the grain-size hardening case, plastic deformation occurred due to the intragranular deformation by twin-boundary migration and deformation twinning. For the softening case, the dominant deformation mechanism became intergranular defamation through GB sliding due to a relative high volume of the grain boundary in the whole model. Li et al. [9] established a large scale atomic model of copper to show that dislocation governs the strength of materials. The results indicated that the deformation mechanism changed from traditional dislocation piling up and cutting through the twin plane to a dislocation-nucleation-controlled softening mechanism with twin-boundary migration. The relationship between the critical twinning spacing for the onset of softening and the maximum strength was revealed: the smaller the grain size, the smaller the critical twinning spacing and the correspondingly higher maximum strength of materials (see Figure 1.14).

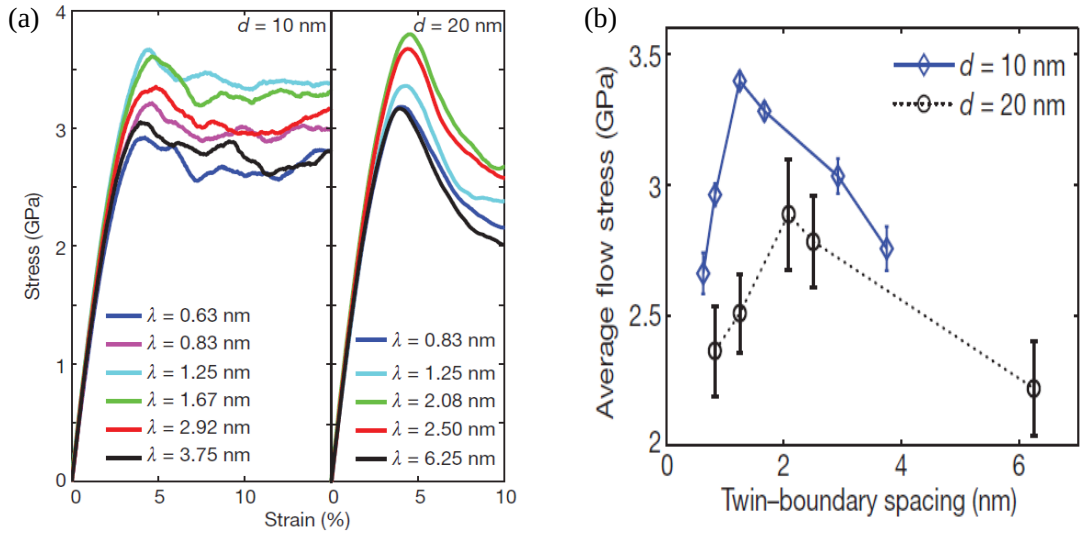

Figure 1.14 (a), (b) Stress-strain relations and flow stress in nano-twinned Cu. λ and d is the twin-boundary spacing and the average grain size [9].

1.4.4 Pre-existing twin

Twinned materials have good mechanical properties with ultrahigh strength without a loss of ductility. The increasing density of the twinning boundaries can accommodate a considerable amount of plastic strain that improves the ductility [3, 9, 94, 120] and the strength. The relatively high ductility of nano-twinned cooper was found to be caused by the twinning boundaries gradually losing coherency during plastic deformation [121-123]. The twins are considered to be effective barriers to prevent dislocation slipping, and they can also be effective sites for dislocation nucleation during deformation which contributes to plasticity [11, 124-131]. Stukowski et al. [126] studied the nanocrystalline Cu and Pd using MD simulations and found opposite results by comparing the twinned and nanotwinned samples where the twinned Cu had a hardening effect and Pd did not.

Sun et al. [132] found that the fivefold TBs caused significant strain hardening under indentation in Ag nanowire, and a similar work referred to fivefold twinned structure in Cu [133]. This showed that the microstructure-hardening mechanism due to the

TBs acted like a barrier for dislocation emissions and propagations, while ductility was lower because of the scarcity and low mobility of dislocations. An anisotropic response of nanotwinned, including parallel, inclined, and perpendicular twins to its applied force direction, using a molecular dynamic simulation was investigated by Wei et al. [123, 134-136]. Deformation was dominated by three dislocation modes: dislocation gliding in between the twins, dislocation transferring across the TBs, and dislocation-mediated boundary migration (for polycrystal). A new nanotwinned atomic model with hierarchically twinned structures was developed [137], where the smaller primary twin spacing (λ_1) corresponded a smaller critical secondary twin spacing (λ_2) to transition the deformation mechanisms (seen Figure 1.15). Above a critical value of λ_2, deformation was dominated by the Hall-Petch type strengthening mechanism and the partial dislocation was emitted from GBs or TBs and later travelled across other GBs or TBs. Below the critical value of λ_2, deformatin was governed by two softening mechanisms: (a) partial dislocation emitted from the primary TB forward parallel to the secondary TB that led to a detwinning of the secondary twin, and; (b) the boundary of the primary twin changed entirely, with one thickening in one part of the primary twins and thinning in the other part. Imperfections such as incoherent segments and partial dislocations of defective TBs in nanotwinned metal were reported [138].

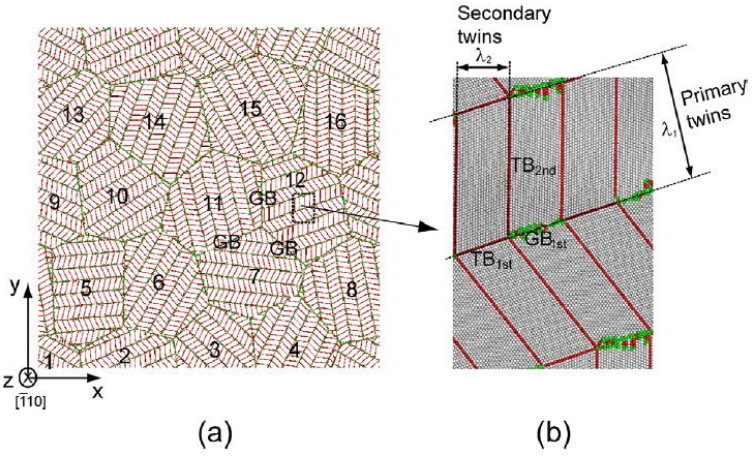

Figure 1.15 The relaxed nanotwinned (NT) Cu with hierarchically twinned structures [137].

Further studies to investigate the effect of the inserted twin in nano-structure on plastic deformation [139-146] showed the change of mechanical properties.

Twin was also regarded as one kind of intrinsic brittle crystal GB [69]. Lu, et al. [147, 148] found that the fracture criterion is associated with the competition between the micro-twin formation and surface dislocation nucleation/propagation. Li and Wang [94, 95] have recently shown opposite results where the brittle-to-ductile fracture occurred when the twinning spacing decreased below a specific limited value.

1.4.5 Model size and shape

Many experimental results showed that deformation depends on the size of a specimen [149-153]. Recent MD results obtained similar observations in the nano scale [154]. Wu et al. [10, 68] studied a single Cu and a polycrystal Ni. In a single crystal, the increasing length of the sample reduced the ductility because the longer sample could store more elastic energy that in turn increased the unstable localised shear along a single slip plane without any appreciable surface necking. In polycrystal, the small diameter of the models failed by GB sliding and the large diameters by necking as the void coalesced. The effect of sample size may not be limited in one direction, the whole sample size may also be affected, or be coupled with twin spacing and grain size effects [134]. Deng et al. [124] found that plasticity depended on the diameter of the sample and the density of the twins, while site-specific surface dislocation emissions and cross slip also contributed to the size-dependent yield stress. They discovered a transition in the mechanical behaviour (strain softening and strain hardening) when the ratio between the diameter and twin spacing was more than 2.14 angstrom in twinned Au [155]. In nanocrystalline Pt, the trend “the smaller the ratio of diameter to grain size, the weaker the strength” was observed in an MD simulation [156]. The coupled effect of sample size and grain size revealed that the “smaller was stronger”, “not significant effect”, “the smaller the weaker” for diameters of samples with different size grains and strength [157].

The MD simulation model shape may affect dislocation propagation or arresting, and in turn influence the mechanical properties. Zhang et al. [125, 129] summed up that plasticity increased from strain-softening to strain-hardening in twinned metal because a lower stress nucleated dislocation and a higher stress was needed for dislocation to penetrate the TBs with a square cylindrical shape rather than circular cylindrical. This led to strain-hardening in square cylindrical nanowires. A transition from surface dislocation nucleation to homogeneous dislocation occurred in surface faceting (zigzag shape) of Au nanowires when the TB spacing and diameters were below a critical value [158]. The Au nanowires approached an almost ideal strength. A similar work was seen with MD simulations of Au [159], Ag [132] and other fcc structures [160], and also in in situ experiments about semiconductor nanowires [144].

1.4.6 Applied force

In reality, a sample may be subjected to complex work conditions where a local region may be subjected to biaxial or triaxial forces. A uniaxial compression experiment under hydrostatic pressure was conducted by Chen et al. [161-163]. It has been found that the dislocation activity can be extended down to 3 nm in Ni under high external pressures [161].

An MD simulation showed that the shock-induced void collapsing in Cu occurs by shear loops' emission [164]. Bringa et al. [165] studied the pressure effect in nanocrystal Cu by MD simulation under shock loading. An ultrahigh strength behind the shock front occurred because of the high pressure and suppression of the GB sliding effect. A similar observation was found in nanotwinned Cu due to the suppression of GB sliding and increasing dislocation activities [166]. The maximum average flow stress was associated with the critical TBs spacing, which then decreased as the TBs spacing became smaller. This process was mainly determined by two competitive dislocation activities with dislocation-twin intersection and

detwinning through the migration of TBs. Another biscrystal [167] and polycrystal [168, 169] simulation is for Cu were performed, where, under compression from a shock wave, the model deformed with spallation along the coherent and symmetric incoherent TBs or GBs, or even local and bulk melting. An MD simulation to investigate the effect of hydrostatic pressure on the deformation in Al [170] and Cu [171, 172] was carried out. Hydrostatic pressure contributed to the different behaviours of dynamic GB de-cohesion in bicrystal [170]. Above and below the critical hydrostatic pressure, dislocation either increased or decreased with increasing hydrostatic pressure. GB sliding was suppressed by the increasing hydrostatic pressure [172]

1.4.7 Other effects

The different interatomic potentials for the same materials were detected as important factors in plastic deformation [125]. Their simulations revealed that a fundamental transition from strain-softening to strain-hardening was caused by the varied stacking fault energy. Other studies focused on the temperature or strain-rate dependence of the deformation mechanism [173-177]. Moreover, the microstructure was studied [69, 175, 178, 179], and Cheng et al. [69] found the intrinsic brittleness and ductility along the specific symmetrical tilt GB in Cu.

These factors that influenced dislocation and twinning formation or its interaction with GB did not act independently after nucleation. A number of researchers [9, 111, 113, 127, 180-186] investigated the dislocation-twin interactions, including dislocation-dislocation, dislocation-twin and dislocation/twin-GB reactions in fcc metals. They found that dislocation would occur in the way of cross-slip, and then leave the stair-rod and transmit across the TB when it reacted with twin. The more results were gotten that the dislocation/twin reacted with GB via absorption, trapping, emission, transmission, and reflection under favourable conditions, such as temperature, the constraint slip orientation of sample geometries, pre-existing twin,

high stress/strain rate, applied stress mode, and the average grain size, etc. These complicated dislocation-twin-GB interactions dominated the deformation mechanism, which resulted in a change of ductility and strength of the materials.

1.5 Summary

A number of researchers made an effort to study brittle and ductile fracture and the transition between them via experiments and MD simulations. They considered the effects of temperature, grain size (from coarse grain to nano-grain size), applied force, strain rate, crystal orientation, and potential function, etc., on the dynamic behaviour of fractures at the atomic scale. These studies provided insights into the mechanics of fracture. However, there were still many limitations about the former works: (1) most researchers observed the brittle versus ductile fracture transition in bcc and diamond cubic structures using MD simulation. Very few people could capture the brittle versus ductile fracture transition in fcc structural metals, including models of single, nanotwinned single crystal and polycrystal fcc metals; (2) the current understanding of the underlying mechanisms that happen the brittle versus ductile fracture transition from the atomic point of view are severely lacking or superficial; (3) there are still a lot of issues related to the influence factors, such as temperature, crystal orientations and tensile hydrostatic stress, etc., on the fracture behaviour (including the fracture transition) in nanotwinned single/single crystal and polycrystal fcc metals, which still remain unclear and unquantified.

So, in this thesis, the significance and contribution of my research work are to fill in this knowledge gap to explore the brittle versus ductile fracture and the transition between them in fcc structural metals. I systematically investigated the brittle versus ductile fracture behaviour (including the fracture transition from brittle to ductile fracture) in single, nanotwinned single crystal, and polycrystal fcc structural metals with different influence factors (such as temperature in nanotwinned single Cu and Ni crystals, crystal orientations in single Ni crystal and the tensile hydrostatic stress in Ni

polycrystal, etc.), and revealed their underlying mechanisms of the brittle versus ductile fracture/fracture transition by applying MD simulations. These are original contributions that have not been covered by others.

CHAPTER 2 MOLECULAR DYNAMICS FUNDAMENTALS

2.1 Introduction

The MD simulation can instantaneously determine the position and velocity of each atom, as well as providing valuable information on the behaviour of materials that is not accessible by experiments. In experiments, because of its limitation of instruments or visualization techniques, it is not easy and sometimes unable to capture the microstructural evolution inside of materials. MD simulation provides the tool to detect the process and structures which are difficult to access from experiments.

MD simulation is only capable of conducting the qualitative comparison with experiments. However, there is still a big gap in the quantitative comparison between MD simulation and experiments. Due to the intrinsically limitations of MD simulation in time and length scale, it requires unrealistically high deformation rates to be applied in MD simulation, which is many orders of magnitude higher than the commonly used value in experiment. And the current MD simulations can only deal with nanoscale model size. The rapid increase in computational power and simulation techniques provide a possible support in improving the length-scale and time-scale of MD simulations, which will cause the shrinkage of gap between MD simulation and the real experiments. This chapter introduces the fundamental knowledge of molecular dynamics simulation and its related pre or post-processing issues.

2.2 MD simulations

Molecular dynamics simulations are based on classic many-particle physics that captures the motion of each atom. Assuming a given multi-atom energy:

$$V(\tilde{r}_1, \dots, \tilde{r}_N) \tag{2.1}$$

where $\tilde{r}_1, \dots, \tilde{r}_N$ consists of 3N spatial coordinates of the atomic configuration, the basic thought for an MD solution is to solve Newton's equation:

$$m_i \ddot{\tilde{r}}_i(t) = F(\tilde{r}_1, \ldots, \tilde{r}_N) = -\tilde{\nabla}_i V(\tilde{r}_1, \ldots, \tilde{r}_N) \quad (2.2)$$

While solving these 3N equations of motion, it needs to define the initial boundary condition at first, including defining the initial spatial position and initial velocity of each atom. Initial velocities are usually determined by [187]:

$$\frac{3N}{2} k_b T = \frac{1}{2} \sum_i m_i \dot{\tilde{r}}_i \cdot \dot{\tilde{r}}_i \quad (2.3)$$

where k_b is the Boltzmann constant and *T* is temperature. After defining the starting configuration, the MD equations of motions are repeatedly solved under the applied conditions.

2.3 Ensemble

There are three major statistical ensembles: the microcanonical ensemble (NVE); the isothermal ensemble (NVT); and the isothermal-isostress ensemble (NPT) where N is the number of atoms, V the volume, E the energy, T the temperature, and P the pressure.

A microcanonical ensemble is regarded as an exchange of potential and kinetic energy without any temperature or pressure control, but the total energy is conserved. This method is not suited to the given desired temperature or pressure used in an experiment.

An improved Nose-Hoover algorithm can set the system to the expected temperature (NVT) because it connects a system to a heat bath where the heat will flow back and forth between the system and heat bath to maintain a constant system temperature. If it is expected to control the constant pressure as well, the isothermal-isostress ensemble (NPT) is a useful ensemble that is connected to a heat bath and to an external stress. The NPT ensemble is mainly used in studies for different atomic models.

2.4 Periodic boundary conditions

One essential approach in an MD simulation is to reduce the cost of calculating a number of atoms and decrease the surface effects on the atomic model by applying the periodic boundary condition (PBC). In a PBC, the simulation box is repeated by copies of itself (In a 2 dimensional system--8 copies; 3D--26 copies), so an atom (a1--green circle) that leaves one side of the box boundary will come back into the system on the opposite side (a2--purple circle) of the simulation box with the same dynamic properties (In Figure 2.1(a)). Figure 2.1(b) shows a cross section of the structure in 3D polycrystal, where the grey and green atoms represent the grain boundary and perfect fcc atoms, respectively.

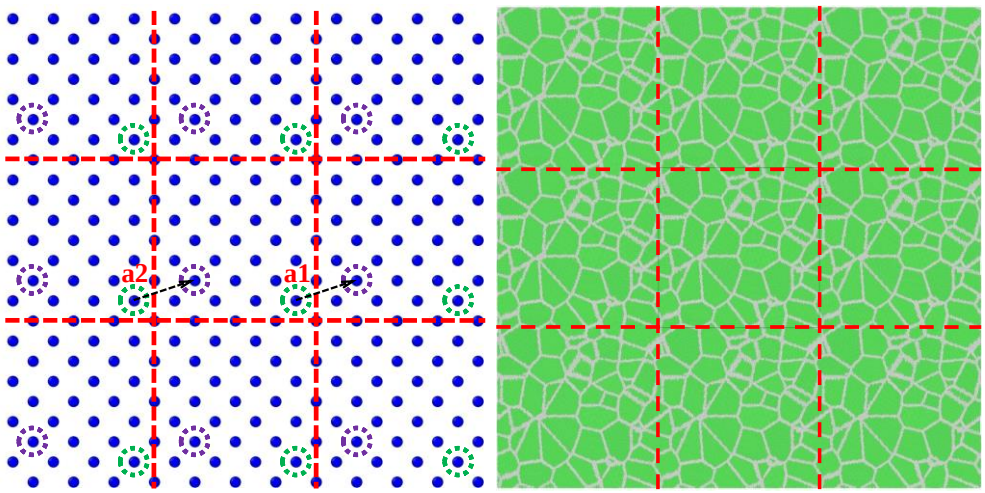

Figure 2.1 (a) Two-dimensional periodic boundary condition where the central configuration is surrounded by 8 exact copies of itself. (b) A cross section of polycrystal with periodic boundary condition.

2.5 Potential selection

The inter-atomic potential function directly determines the accuracy of MD results. The popular potentials for metals includes the EAM potential, the Lennard-Jones potential (LJ), the Stillinger-Weber potential, the Tersoff potential, and the reactive bond-order potentials (REBO), etc. The most widely used potentials are the pair

potential (e.g. Lennard-Jones potential and Morse potential) and the multi-body potential (EAM potential) in MD simulations of pure metals. Compared to other potentials, EAM has many advantages in representing the atomic interplay (see Figure 2.2). For example, the atomic bonds of atoms at the surface of a crystal may have different properties than those inside the body when the EAM potential is used, whereas pair potentials cannot capture this effect. In order to accurately exhibit the change in bond properties at a surface, the bond strength and local environment of an atom must be considered. In other words, the bond energy between two atoms is no longer taken as a function of its distance; it is a function of the positions of all the other atoms nearby. This behaviour can be determined by multi-body potentials, such as the EAM potential. The use of EAM has largely been demonstrated in MD simulations of bcc (e.g. Fe) and fcc crystals (e.g. Ni, Cu, Al et al.) [9, 48, 69, 108, 181, 188-190]. In this study, the EAM potential will be used.

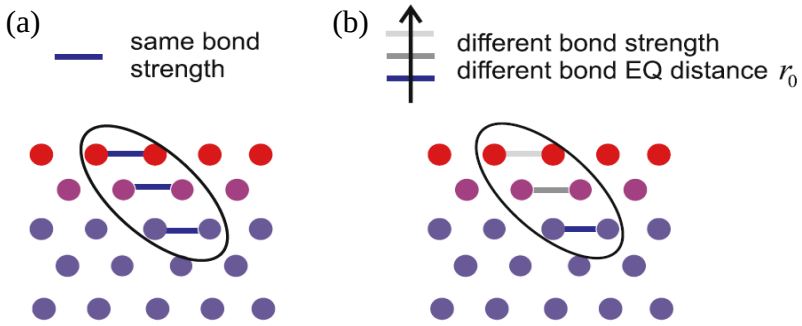

Figure 2.2 Different descriptions of the properties of atomic bonds between a Pair potential and a Multi-body at a surface [4].

An EAM potential is given by:

$$U_i = \sum_{j=1}^{N_i} \emptyset(r_{ij}) + f(\rho_i) \tag{2.4}$$

where ρ_i represents the local electron density, f is the embedding function, and ρ_i is calculated based on a simple pair potential that features a contribution from a two-

body term ∅ to capture the basic repulsion and attraction of atoms, combined with a multi-body term that describes the local electronic environment of an atom.

2.6 Polycrystal model setup

There are two methods used to establish the atomic polycrystal. One is the quasi-3D idealised columnar, uniform hexagonal bcc/fcc grains with different misorientations [8, 109, 116, 117]. The advantage of this model is that it can simulate relatively large grains because only a few lattice planes must be considered in the periodically repeated texture direction, but the disadvantage is having no description of all three dimensional information of dislocation and GBs. Another method that is regarded as a closer treatment of the underlying physics is using the voronoi method [9, 48, 112, 191]. This method mainly includes two parts. Part one is to establish a perfect single atomic model with same lattice length as the expected polycrystalline model. If a twin must be embedded into the polycrystal (nanotwinned polycrystal), then a suitable crystal orientation of $\langle 11\bar{1}\rangle$, $\langle \bar{1}1\bar{1}\rangle$ and $\langle 110\rangle$ must be established first. This is followed by a successive displacement of fixed groups atoms along the slip direction with partial Shockley dislocations vector of $1/6\langle 112\rangle$ to create the twinned single crystal. The second part, based on the voronoi method, is to input the previously established perfect sample atomic data into polycrystalline codes to create polycrystalline models. This stage involves controlling the distribution of seed points (to control the distribution of grain volumes or the mean grain size) and then controlling the misorientations of the two neighbouring grains (to control the distribution of high angle GB and low angle GB).

A voronoi diagram for setting the S of N planar points is a partition of the plane into N polygonal regions, where each of them is associated with some point p_i, and S_1 is the locus of points closer to that point than any other points S_i in the whole 3D spacing coordinates). The 2D voronoi diagram of this can be seen in Figure 2.3. Figure 2.4 shows a 3D atomic model generated after using the voronoi algorithm.

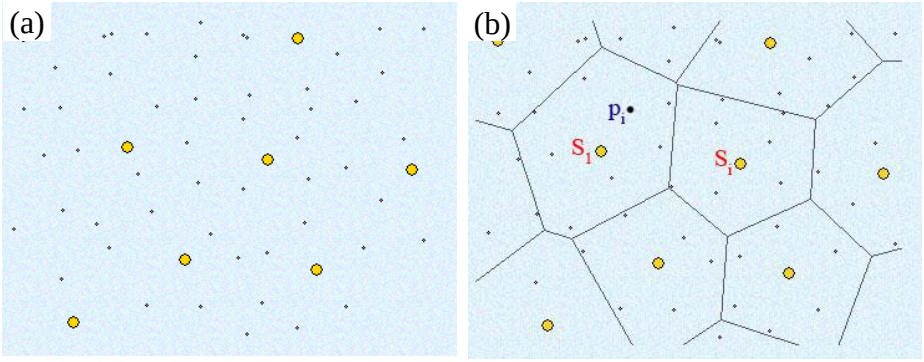

Figure 2.3 (a) Environmental sampling stations scattered throughout a region. (b) Assigning each sampling point to the nearest collection centre (seed point) (images from website).

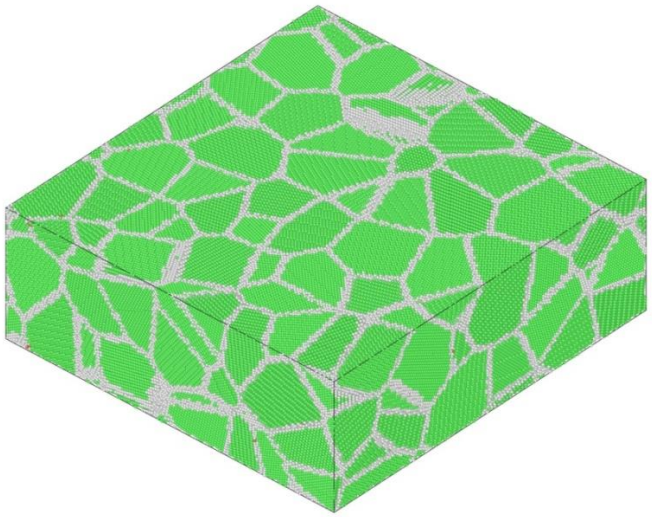

Figure 2.4 The polycrystalline model generated using a 3D voronoi algorithm.

2.7 Loading applied methods

To explore the brittle versus ductile fracture behaviour under the tensile deformation, it needs to apply the external load to all of atoms along the required loading direction. In MD simulations, there are usually four loading methods are used to apply the strain or stress on the atomic model: (1) the first method is to change the dimension of simulation box via a "given displacement" for each atom along the required loading direction every certain time steps; (2) the second one is to change the volume of the

simulation box at a constant strain via rescaling the coordinates of atoms every certain time steps; (3) the third one is to change a dimension of the box at a "constant velocity" on atoms at the ends along the required loading direction in each time step; and (4) the fourth one is to set each component of constant force on each atom along the required loading direction. In this study, the second loading method was chosen.

2.8 Visualisation

After running atomic models, MD calculations usually produce huge amounts of data. In order to analyse the MD results, appropriate methods of visualisation are needed.

2.8.1 Centro-symmetric symmetry

The centro-symmetry parameter is computed using the formula:

$$P = \sum_{i=1}^{N/2} \left| \vec{R}_i + \vec{R}_{i+N/2} \right| \tag{2.5}$$

where N is the number of the nearest neighbours for fcc or bcc, N is set to 12 and 8 respectively. R_i and $R_{i+N/2}$ are vectors from the central atom to a particular pair of nearest neighbours. The different values of P allow atoms to be identified within the perfect lattice, dislocation core, stacking fault, and free surface.

2.8.2 Common neighbour analysis

The common neighbour analysis (CNA) can be used to determine the local crystal structure around each atom. It was carried out by selecting the common neighbours of a pair of atoms separated by no more than the distance to the second nearest neighbour, and by introducing a classification scheme for the nearest-neighbour bond pathways between the two atoms [187].

Currently, there are five kinds of CNA patterns: (1) fcc = 1; (2) hcp = 2; (3) bcc = 3; (4) icosahedral = 4; (5) unknown = 5 and 0 for atoms not in the specified computed

group. This visualisation method can identify the twinning, intrinsic stacking fault and extrinsic stacking fault and GB [9, 107].

2.8.3 Local stress and strain

In MD simulation, the stress field is regularly calculated when the simulation is carried out. The stress tensor is the derivative of the free energy of the atomic system with respect to the imposed strain [6]. It means that the effective medium theory permits us to define the energy for each atom, and then it enables us to define an "atomic" stress for each atom. The stress is a derivative of the energy with respect to the interatomic distances. The atomic stress using the Virial stress theorem is computed as following [6]:

$$\sigma_{i,kl} = \frac{1}{V_i}\left(-\frac{p_{i,k}p_{i,l}}{m_i} + \frac{1}{2}\sum_{j\neq i}\frac{\partial U}{\partial r_{ij}}\frac{r_{ij,k}r_{ij,l}}{r_{ij}}\right) \quad (2.6)$$

where $\sigma_{i,kl}$ is the *kl* component of stress tensor for atom i, V_i is the volume assigned to atom i, $p_{i,k}$ is the *k* component of its momentum of atom i, m_i is the mass of atom i, $r_{ij,k}$ is the *k* component of interatomic distance $\mathrm{r_{ij}} = \mathrm{r_i} - \mathrm{r_j}$ between atom i and j. The atomic stress tensor cannot be uniquely defined. The Virial stress needs to be averaged over space and time that the various definitions quickly converge to a macroscopic stress field (like Cauchy stress tensor). During the MD simulation, the stress-strain curves were obtained by averaging the atomic stresses over the entire atomic system.

2.8.4 Dislocation extraction algorithm

The Crystal Analysis (CA) tool [192] and Dislocation Extraction Algorithm (DXA) code [193] developed by Stukowski and his co-workers were used to identify dislocations and stacking faults. This method can yield a geometric description of the dislocation network contained in an arbitrary crystal. The dislocation results were viewed using the ParaView software.

2.9 High performance computing and supercomputers

High-performance computing (HPC) uses supercomputers and computer clusters to solve the large-scale computing problems [194]. HPC unites systems administration and massively parallel systems into a multidisciplinary field that includes hardware, digital electronics, software, algorithms, programming tools, visualization and computational techniques by multi-core processors [195].

Supercomputers play an important role in the field of computational science, particularly at high speed and large-scale of calculation [194]. Supercomputers are used for a wide range of highly calculation-intensive tasks in various fields, such as quantum mechanics, weather forecasting, climate research, oil and gas exploration, molecular modelling (computation of the structures and properties of chemical compounds, biological macromolecules, polymers, and crystals), and physical simulations (such as simulations of the early moments of the universe, airplanes in wind tunnels and spacecraft aerodynamics, simulation of the detonation of nuclear weapons, and research into nuclear fusion) [194]. In this study, access to the supercomputer facilities was provided by the University of Wollongong and the National Facility of the National Computational Infrastructure of Australia.

2.10 Summary

In this chapter, the basic concept of molecular dynamic simulation was introduced. The MD simulation process generally includes the model construction, relaxation of system, objective running, and post processing.

CHAPTER 3 BRITTLE-TO-DUCTILE TRANSITION IN NANOTWINNED COPPER

3.1 Introduction

Nanotwinned Cu is a relatively new material with a special microstructure. It has been the subject of intensive research due to its unusual combination of ultrahigh yield strength and high ductility [3, 94, 120]. The high ductility of nanotwinned Cu has been attributed to the gradual loss of coherency of the Twinning Boundaries (TB) during plastic deformation [121-123]. A brittle-to-ductile transition was experimentally observed in nanotwinned Cu despite it being an intrinsically ductile metal. Jang et al. [94] conducted *in situ* Scanning Electron Microscope (SEM) uniaxial tension tests on nanotwinned Cu nanopillars with different twin boundary orientations and twin boundary spacings. The nanopillars with twin boundary spacings of up to 2.8 nm exhibited the characteristics of ductile fracture clearly, while those with the larger twin boundary spacing of 4.3 nm failed in a brittle fashion. Jang et al. [94] also performed MD simulations of crack propagation along a twin boundary in nanotwinned Cu to understand the distinct fracture modes observed in their experiments. It was found that when the twin boundaries were spaced sufficiently closely, the high stresses at the crack tip could induce twinning dislocation nucleation and propagation on the twin boundaries in close proximity to the crack tip, leading to a cascade of dislocation activities and eventually ductile failure.

The intriguing findings of the TB-spacing-induced brittle-to-ductile transition in nanotwinned Cu from Jang et al.'s work raises some fundamental questions: 1) can the brittle-to-ductile transition be observed in this material when the temperature varies, and 2) what is the atomic mechanism responsible for nucleation and mobility of dislocations emitted from the crack tip? In this chapter, I explored these questions

for nanotwinned Cu with a pre-existing edge-notched crack using MD simulations at various temperatures.

3.2 Model set-up

Molecular Dynamics (MD) simulations were performed with the open-source code Large-scale Atomic/Molecular Massively Parallel Simulator (LAMMPS) [196]. The MD domain of this study is illustrated in Figure 3.1. The domain is 496 Å × 501 Å × 25.16 Å in the X, Y and Z directions respectively. It was filled with Cu atoms arranged in an fcc structure. The original crystal, referred to as the matrix crystal in the following, was aligned along the $[1\bar{1}\bar{2}]$, $[\bar{1}1\bar{1}]$ and $[110]$ crystallographic directions in the X, Y and Z directions respectively. A set of the twinned crystals, labelled T1-T6 in Fig. 1, was then introduced by rotating the matrix crystal along its X axis by 180^{o}. This resulted in a set of separated matrix crystals, labelled M1-M6. The twinned crystals had crystallographic directions $[1\bar{1}\bar{2}]$, $[1\bar{1}1]$ and $[\bar{1}\bar{1}0]$ in the X, Y and Z directions respectively. All the crystals (T1-T6 and M1-M6) had the same height of 4.17 nm along the Y direction. In Figure 3.1, the grey spheres are atoms with perfect fcc structures and green spheres are atoms with free surface or disordered structures. The coherent TBs between the matrix crystals and the adjacent twinned crystals are marked by red colour. A through-thickness crack was created by removing a number of atoms in the middle of the left-hand edge of the simulation cell, as shown in Figure 3.1. The crack surface was parallel to the TB plane between the T3 crystal and the M4 crystal and the front of the crack was along the Z direction. The initial length of the crack was about 65 Å. A detail of the crack tip region is given in the top-right corner of Figure 3.1. The atoms surrounding the crack are coloured green. The simulation cell encapsulates over half a million atoms.

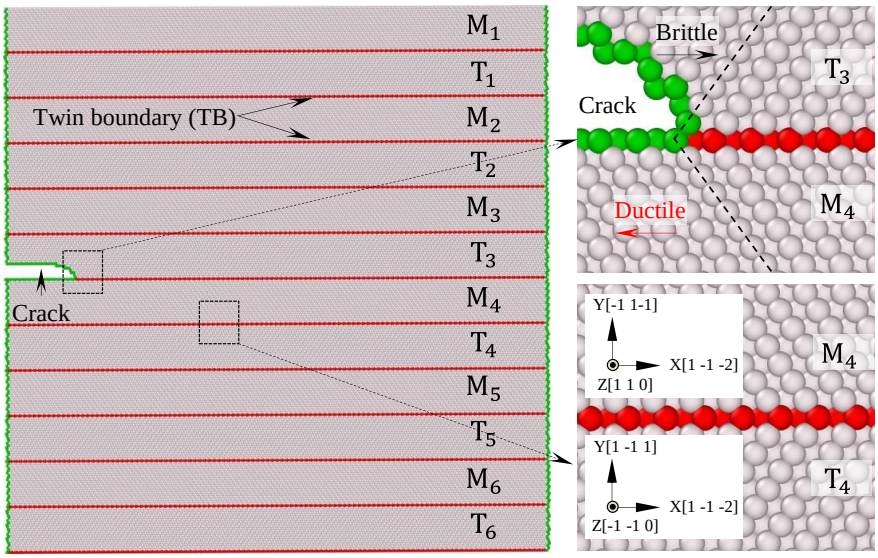

Figure 3.1 Simulation cell of nanotwinned Cu with a single-edge-notched crack.

The EAM interatomic potential developed by Mishin et al. [190] was employed in all the simulations. This potential was calibrated using experimental and ab initio data for Cu. It has been shown to precisely predict the lattice properties, point and extended defects, various structural energies and transformation paths. The simulations were conducted in a constant NPT ensemble (fixed number of atoms (N), constant pressure (P) and constant temperature (T)). Periodic boundary conditions were applied in the Y and Z directions and free boundary conditions were used in the X direction. In each simulation, random velocities were initially assigned to atoms, followed by a relaxation process for 10^5 time steps. The simulation cell was subsequently stretched at a constant strain rate of 1×10^8 s^{-1} along the Y direction while the normal stress along the Z direction was fixed to zero using the Parinello-Rahman barostat [197]. The equations of the atomic motion were integrated using the velocity Verlet algorithm. The total simulation time was 702 ps with a time step of 0.003 ps, leading to a total strain of 7.02% along the Y direction. 10 simulation cases at temperatures (0.5 K, 1.1 K, 2 K, 5 K, 10 K, 20 K, 30 K, 40 K, 50 K and 60 K) were conducted. In each simulation the temperature was maintained using the Nose-Hoover thermostat. Ovito software [198] was used to visualise the atomic configuration. The Crystal

Analysis (CA) tool [192] and Dislocation Extraction Algorithm (DXA) code [193] developed by Stukowski and his co-workers were used to identify dislocations and stacking faults respectively. The results were viewed using the ParaView software.

The deformation behaviour is determined by the instant stress response. The atomistic stress tensor is defined in component from the Virial stress formulation [199]. In order to clearly judge the plastic deformation, more stress indications were introduced in this thesis. The hydrostatic pressure (mean stress) and the von Mises effective average atomic stress are defined as follows [200]:

$$\sigma_m = \frac{1}{3}(\sigma_x + \sigma_y + \sigma_z) \tag{3.1}$$

$$\sigma_{von} = \sqrt{\frac{1}{2}\left[(\sigma_x - \sigma_y)^2 + (\sigma_y - \sigma_z)^2 + (\sigma_x - \sigma_z)^2\right] + 6(\sigma_{xy}^2 + \sigma_{yz}^2 + \sigma_{zx}^2)} \tag{3.2}$$

Then the Stress triaxiality at an atom was defined as the ratio of the mean stress and the von Mises stress at atom, it can get,

$$\sigma_{tri} = \sigma_m / \sigma_{von} \tag{3.3}$$

3.3 Results and discussion

3.3.1 Effect of temperature

3.3.1.1 Stress-strain relation

Figure 3.2 shows the normal stress along the Y direction ($\bar{\sigma}_y$) (tensile stress) as a function of the imposed strain (ε) for 7 simulation cases. The results of the other three cases (5 K, 20 K and 50 K) were not included because they were very similar to the presented cases. The stress components were calculated using the expression taken from the Virial theorem, and the average atom volume was used in the stress calculations [196]. The strain (ε) was calculated from the applied strain rate multiplied by the deformation time. It can be seen from Figure 3.2 that all the simulation cases

have a nearly-linear stress-strain relationship up to a strain of 2.52% with a tangent modulus of about 181 GPa, close to the elastic modulus of 191 GPa for pure copper along the [111] direction [201]. The difference between these two values was due to existence of the edge crack.

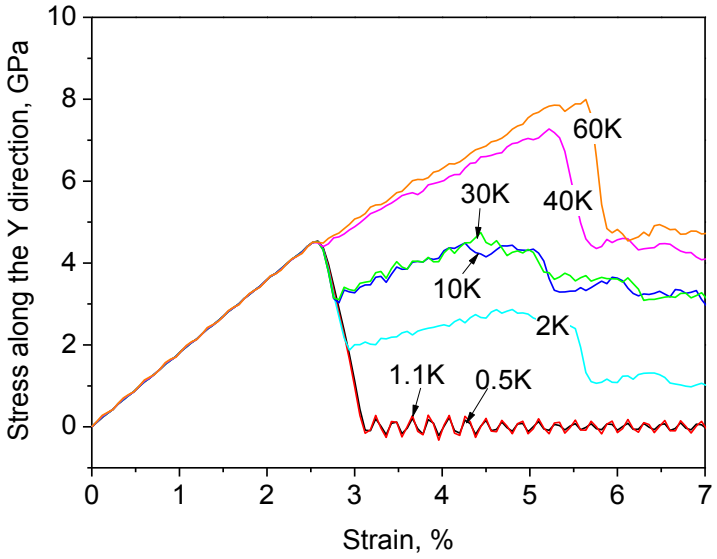

Figure 3.2 Average normal stress along the Y direction as a function of the imposed strain for different simulation cases.

After the strain exceeded 2.52%, all the curves dropped in Figure 3.2. The simulation results at 0.5 K and 1.1 K are almost identical. They dropped to almost zero stress at about ε = 3.12% and then oscillated as the strain increased further. At 2 K, 10 K, and 30 K, the stress did not reduce to zero. Instead, the drop in stress stopped at strains of 2.92%, 2.82% and 2.82% respectively. Subsequently, $\bar{\sigma}_y$ increased slightly with increasing strain. In comparison, the cases at 40 K and 60 K indicated a slight decrease in stress at ε = 2.52%, followed immediately by a significant stress increase with increasing strain. The tangent modulus at 60 K was larger than at 40 K for strains greater than 2.52%.

Three stages of the crack propagation process at 1.1 K are shown in Figure 3.3. The onset of crack propagation occurred at ε = 2.52%, which corresponded to the peak of the stress-strain curve in Figure 3.2. Crack propagation took place at the TB between the T_3 crystal and the M_4 crystal, as shown in Figure 3.3(a). In Figure 3.3(b) the crack continued to propagate along the TB in a straight line as the imposed strain increased to 2.733%. The crack left a smooth cleavage surface in its wake. The atomic bonds broke continuously during the propagation of the crack. This will release the stress on all the atoms located on the left-hand side of the crack and in turn reduce the average stress of the system, leading to the lower $\bar{\sigma}_y$ observed in Figure 3.3. No dislocation was observed in this case, implying that the crack was brittle. The crack travelled through the whole simulation cell along the X direction at ε = 3.12% (Figure 3.3(c)), resulting in near-zero stress observed in Figure 3.3.

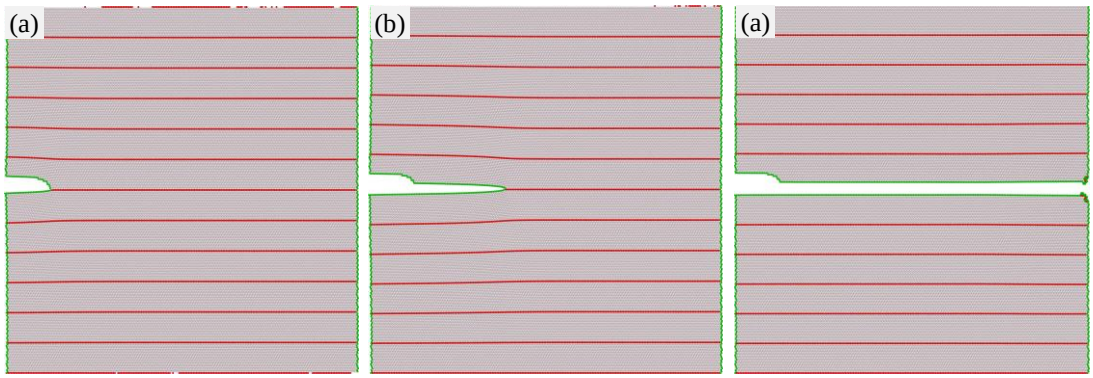

Figure 3.3 Snapshots of the simulation cell subjected to different strains at 1.1 K: (a) ε = 2.52%; (b) ε = 2.733%; (c) ε = 3.12%.

3.3.1.2 Crack length

Figure 3.4 shows a sequence of atomic configurations around the crack tip for a small strain range from 2.741% to 2.744% at 1.1 K. It can be seen in Figure 3.3 that during the crack propagation, two adjacent planes perpendicular to the Y direction separated to move the crack tip forward. This means that the normal stress along the Y direction

(σ_y) played an important role. The colour assigned to each atom in Figure 3.4 represents the magnitude of σ_y. Eight atoms near the crack tip were selected for analysis. Group-A atoms, marked A_1, A_2, and A_3, and A_4, are located on a plane above the TB, while the other four atoms (Group-B), labelled B_1, B_2, B_3, and B_4, are exactly at the TB. Figure 3.4(a) corresponds to the imposed strain of 2.741%. It can be seen that a high stress region exists near the crack tip and the highest value of σ_y is associated with the atom in front of the crack tip. Atom B_1 has the highest σ_y in Figure 3.4(a).

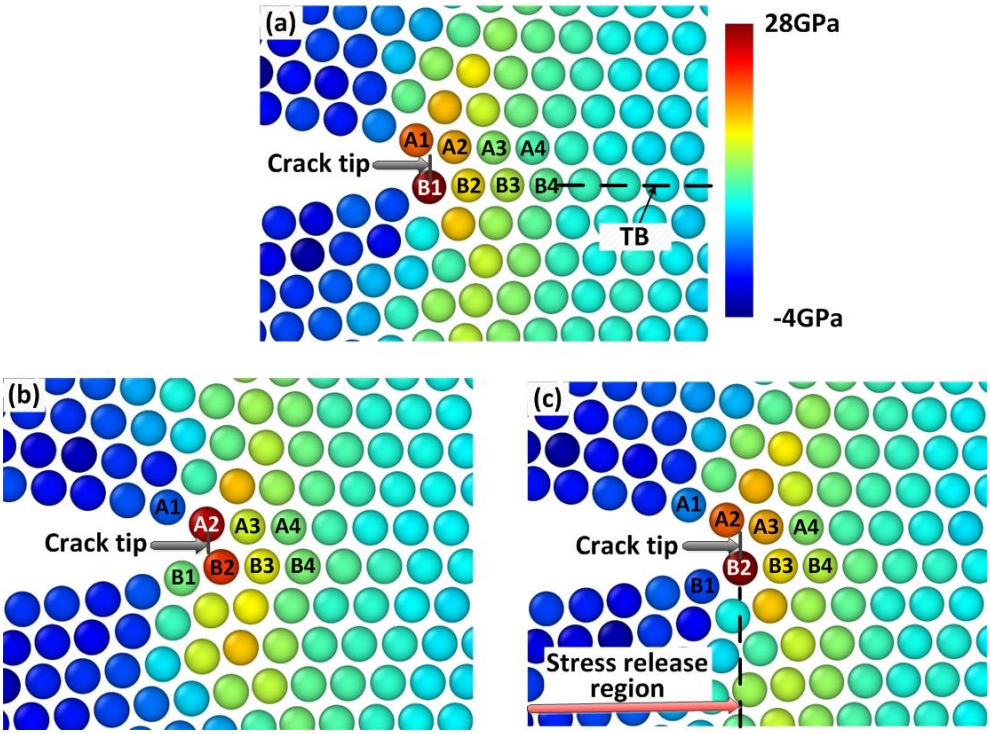

Figure 3.4 Sequence of atomic configurations around the crack tip at 1.1 K: (a) ε = 2.741%; (b) ε = 2.743%; (c) ε = 2.744%.

As the imposed strain increased to ε = 2.743%, Atom A_1 moved up and Atom B_1 moved down, as shown in Figure 3.4(b). The distance between A_1 and B_1 and the distance between B_1 and A_2 increased significantly and the position of the maximum σ_y transferred to Atom A_2. This indicates that the crack tip has moved. As the

imposed strain increased to ε = 2.744%, as shown in Figure 3.4(c), Atom B_2 has the largest σ_y.

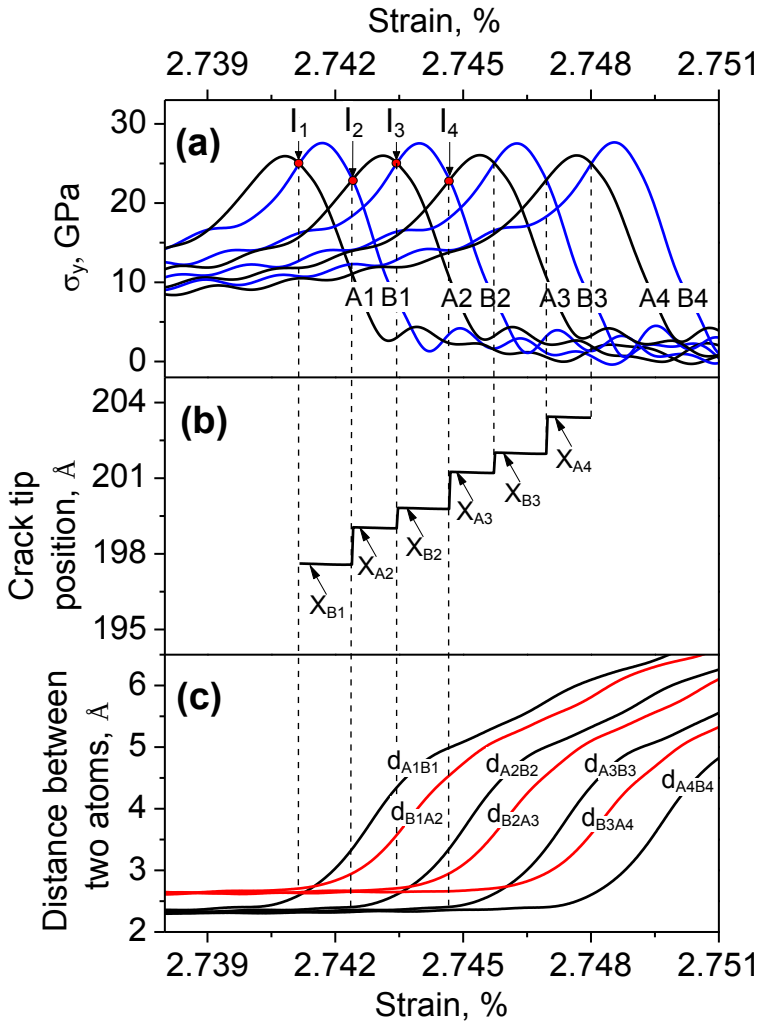

Figure 3.5 Simulation results of selected atoms at 1.1 K: (a) σ_y; (b) Crack tip position; (c) Distance between a Group-A atom and a Group-B atom.

Figure 3.5(a) plots σ_y as a function of the imposed strain for the eight selected atoms. All the curves exhibit a similar pattern: σ_y increases initially with increasing strain and then decreases after it reaches a peak value. It is obvious that the peak stresses of Group-B atoms were higher than those of the Group-A atoms, and the curves corresponding to two neighbouring atoms intersect at a certain point. For instance, Atom A_1 and Atom B_1 have an intersection point (Point I_1) at a strain of 2.7412%, as

shown in Figure 3.5(a). To the left of Point I_1, Atom A_1 has a higher σ_y value than Atom B_1, while the stress for Atom B_1 exceeds that for Atom A_1 after Point I_1. Atom B_1 has its maximum stress at $\varepsilon = 2.7417\%$ and soon afterwards its σ_y decreases with the strain. Atom A_2, another neighbour of Atom B_1, is subjected to a continuously increased σ_y during this period. Curves of Atom B_1 and Atom A_2 interact at Point I_2. It is clear in Figure 3.5(a) that Atom B_1 has the highest σ_y over all the atoms between Point I_1 and Point I_2. As observed in Figure 3.4 the atom with the highest σ_y is always located in front of the crack tip, and therefore such an atom defines the location of the crack tip in this study.

Figure 3.5(b) plots the crack position, which is equal to the crack length, as a function of the imposed strain based on the results of Figure 3.5(a). Between Point I_1 and Point I_2, Atom B_1 has the highest σ_y. Therefore, the crack tip is located at X_{B1}, the X coordinate of Atom B_1. Similarly the crack tip is located at Atom A_2 (X_{A2}) during the strain range between Point I_2 and Point I_3. Using this approach the position of the crack tip was automatically determined by post-processing the simulation data. It is noted that this approach is only suitable for the brittle fracture propagation. Once a dislocation nucleates around the crack tip, the highest σ_y is not associated with the atom at the crack tip.

Figure 3.5(c) shows the distances between Group-A atoms and Group-B atoms. The symbol "d" in the figure means the distance between two atoms and its subscript consists of the names of two linked atoms. For instance, d_{A1B1} stands for the distance between Atom A_1 and Atom B_1. It is known from Figure 3.5(a) that from Point I_1 to Point I_2, Atom B_1 has the highest σ_y, implying that the crack tip has moved to this atom. It is interesting to see that the distance between Atom B_1 and Atom A_2 starts to increase at Point I_1. This may indicate that the stretching of the B_1-A_2 bond is driven by Atom B_1. This conclusion also applies to the other atomic bonds (such as A_2-B_2,

B_2-A_3 and A_3-B_3 as shown in Figure 3.5(c)). The first-mentioned atoms in the bond names are always the 'driving' atoms.

3.3.1.3 Brittle-to-ductile transition

Figure 3.6 shows the crack length as a function of the imposed strain for four different cases (1.1 K, 2 K, 10 K and 40 K). The solid lines and the dashed lines represent the results of brittle fracture and ductile fracture, respectively. The data in Figure 3.6 was recorded for every 20 simulation steps. Only within a very small strain range simulation data was saved for every single simulation step to give the detailed analysis as shown in Figure 3.5. The 1.1 K case exhibited brittle fracture behaviour for the entire simulation. The cases of 2 K and 10 K showed a dynamic brittle-to-ductile transition the fracture first propagated in a brittle mode and then transferred to a ductile mode at a critical strain. The critical strains in the 2 K and 10 K cases were different, whereas in the 40 K case the fracture only moved by a very short distance in a brittle fashion and then stopped moving due to the emission of a dislocation.

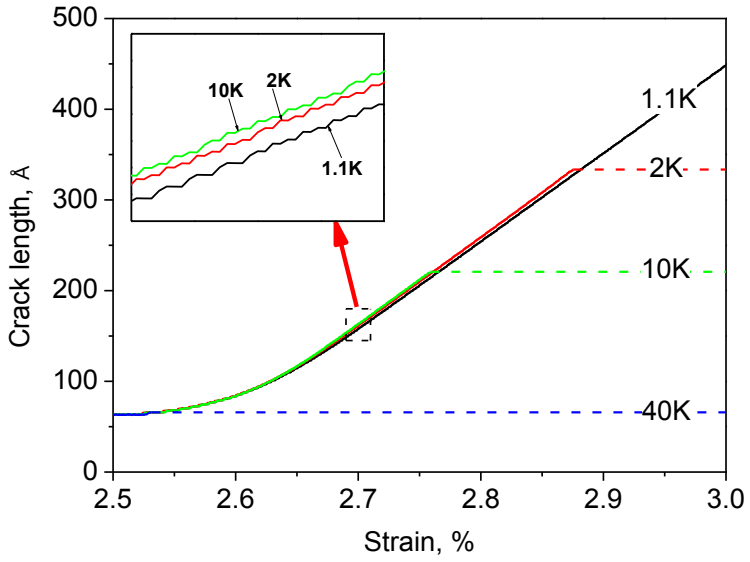

Figure 3.6 Crack length as a function of the imposed strain.

All the 1.1 K, 2 K and 10 K cases exhibited a certain period of brittle crack propagation. As shown in Figure 3.6 the solid curves corresponding to these cases almost overlapped. The crack length increased slowly initially until the slope of the curves gradually increased with the imposed strain. The slope of the solid lines remained nearly constant after a strain of about 2.66%. Since the slope of the curve represents the crack propagation speed, Figure 3.6 indicates that the speed of brittle crack propagation increased from zero with the strain and reached a saturation value at $\varepsilon = 2.66\%$. When a brittle crack underwent transition to a ductile fracture, the crack speed suddenly dropped.

The change in crack length at 1.1 K, 2 K and 10 K was not significant but the inset in Figure 3.6 shows that the brittle crack travelled faster at higher temperature. The average crack propagation speed (v) (average slope of the solid curves) for the strain range of 2.69%~2.75% was 957.1 m/s, 969.2 m/s and 978.6 m/s for the 1.1 K, 2 K and 10 K cases, respectively. Continuum fracture theory typically assumes that cracks can accelerate to a limiting speed equal to the Rayleigh sound speed of the material [202]. The Rayleigh speed (c_r) can be calculated by $c_r = 0.93\sqrt{\mu/\rho}$ [203], where μ is the shear modulus and ρ is the material density. If I choose μ = 45.2 GPa and ρ = 8931 kg/m^3 for copper [204], it yields c_r = 2092 m/s. Therefore, the propagation speed of the brittle crack observed in this study is about 45.7%~46.7% of the Rayleigh speed. This is consistent with findings in experiments [26, 205] and MD simulations [206, 207], which indicated that brittle cracks have limiting velocities well below predictions by continuum fracture theory.

It appears from the above analysis that the propagation speed of the brittle crack increased with temperature which implies that brittle crack propagation is a thermally activated process. According to transition state theory [208], the activation energy barrier (Q) for brittle crack propagation can be expressed by the equation v =

$v_0 \exp(-Q/(k_B T))$, where v is the brittle crack propagation speed, v_0 is a reference speed, k_B is the Boltzmann constant and T is the temperature. Q can be determined by a regression of this equation using the speeds of the three temperatures obtained before. The calculated activation energy was 0.11 eV. Zhu et al. [122] conducted atomistic modelling to investigate the dislocation/TB interaction in a twinned Cu bicrystal. In their simulations a perfect screw dislocation was driven toward the TB by a shear stress. Two competing pathways were identified. The first path was a two-step process involving the absorption of the incoming screw dislocation into the TB, followed by desorption. The second pathway involved direct transmission of the incoming screw dislocation by cross slip. The activation energies calculated from the Zhu et al.'s simulations were 0.49 eV for the absorption process and 0.67 eV for the direct transmission process, respectively. The activation energy for the desorption process was much higher, approximately 5 eV. A comparison of our prediction with these results indicated that brittle crack propagation requires a lower energy barrier than the dislocation/TB reaction in nanotwinned Cu.

The crack lengths at a strain of 3% were plotted against the temperatures in Figure 3.7. The cases at 0.5 K and 1.1 K have longer cracks. The crack length decreased significantly as the temperature increases from 1.1 K to 2 K, and a further increase in temperature led to a near plateau from 10 K to 30 K. A second reduction in the crack length occurred between 30 K and 40 K, followed by a slight reduction as the temperature increased further. The studied simulation cases can be categorised into three groups according to their fracture behaviour shown in Figure 3.7. In Group 1 the fracture propagated in a brittle mode during the entire simulation period. In Group 2 the fracture exhibited a dynamic brittle-to-ductile transition, while in Group 3 ductile fracture dominated even though a short brittle fracture period appeared soon after the fracture began. Figure 3.4 clearly indicates that brittle fracture is controlled by a

sequential bond breaking process. The cases at 10 K and 40 K were chosen to further understand the fracture mechanisms in Group 2 and Group 3 respectively.

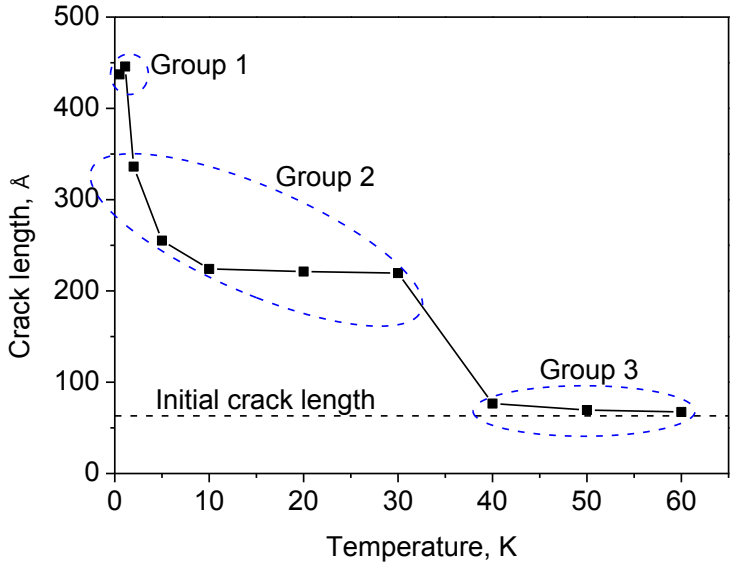

Figure 3.7 Crack length at ε = 3% for different temperatures.

3.3.1.4 Dislocation activity

Figure 3.8 shows the activities of dislocations radiating from the crack tip at 10 K. In Figure 3.8(a), the envelope of the crack is represented by a grey-coloured surface. The simulation cell is observed from the top-right-front direction. The TBs are highlighted in red. At the imposed strain of 2.751% (Figure 3.8(a)), the crack still propagated in a brittle mode. The envelope of the crack is smooth and the crack tip is sharp. No defect is observed around the crack tip. As the imposed strain increased to 2.764% (Figure 3.8(b)), a new coherent twin boundary, parallel to the envelope surface of the crack tip, was generated below the crack tip. The crack tip became blunt in Figure 3.8(b). The newly formed TB was narrow in the X direction and spread along the Z direction, and did not extend during the subsequent deformation.

In the following, the subscript 'M' of a dislocation Burger vector, a crystallographic plane or a stacking fault normal indicates the Miller index of the matrix crystal. The

subscript T indicates the Miller index of the twinned crystal. In Figure 3.8(c), representative of ε = 2.767%, a perfect dislocation with the Burger vector of $1/2[1\bar{1}0]_M$ was seen to emit from the crack tip and travel on the $(001)_M$ plane. The perfect dislocation is represented in the figure by a green tube. Previous studies [37, 209, 210] reported that Shockley partial dislocations can be emitted from the crack tip in Cu. However, the release of a perfect dislocation on the (001) plane has not been reported to date.

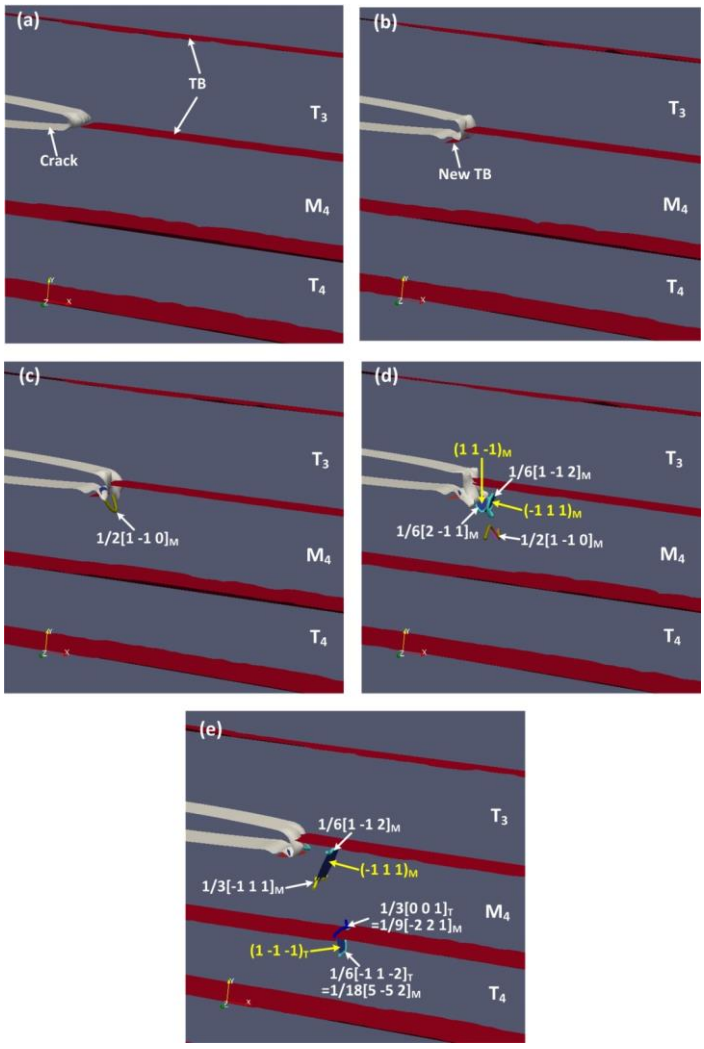

Figure 3.8 Dislocation activities around the crack tip for the 10 K case: (a) ε = 2.751%; (b) ε = 2.764%; (c) ε = 2.767%; (d) ε = 2.78%; (e) ε = 2.793%.

The $1/2[1\bar{1}0]_M$ perfect dislocation continued to travel on the (001) plane as the strain reached 2.78% (Figure 3.8(d)).The Burger vectors of dislocation and the normal vectors of the stacking faults are marked by white and yellow symbols in the figure. It can be seen that this perfect dislocation is curved, which indicates it is a combination of edge dislocation and screw dislocation. When the $1/2[1\bar{1}0]_M$ perfect dislocation moved, a $1/6[1\bar{1}2]_M$ Shockley partial dislocation loop was generated on the $(\bar{1}11)_M$ plane above the travelling $1/2[1\bar{1}0]_M$ perfect dislocation, as shown in Figure 3.8(d). It should be noted that the $1/6[1\bar{1}2]_M$ Shockley partial dislocation loop was not emitted from the crack tip but inside the M_4 crystal. In addition, a leading$1/6[2\bar{1}1]_M$ Shockley partial dislocation, followed by a trailing $1/6[1\bar{2}\bar{1}]_M$ Shockley partial dislocation (not shown in Figure 3.8(d)), was released from the crack tip.

In Figure 3.8(e) the $1/6[1\bar{1}2]_M$ Shockley partial dislocation loop expanded, enveloping an intrinsic stacking fault with the normal vector of $(\bar{1}11)_M$. As it meets the front and rear boundary surfaces of the simulation cell the dislocation loop separated into two dislocation lines with the same Burger vector connected by the $(\bar{1}11)_M$ stacking fault. The top $1/6[1\bar{1}2]_M$ dislocation line propagated towards the TB between the T_3 crystal and the M_4 crystal. The bottom $1/6[1\bar{1}2]_M$ dislocation line soon reacted with the $1/6[2\bar{1}1]_M$ leading and $1/6[1\bar{2}\bar{1}]_M$ trailing partial dislocations emitted from the crack tip. The reaction resulted in a $1/3[1\bar{1}\bar{1}]_M$ Frank partial dislocation, as marked in Figure 3.8(e). The $1/3[1\bar{1}\bar{1}]_M$ Frank partial dislocation and the top $1/6[1\bar{1}2]_M$ dislocation are connected by the $(\bar{1}11)_M$ stacking fault. Since the Frank partial dislocation is sessile, it pinned the $(\bar{1}11)_M$ stacking fault to prevent the stacking fault from shrinkage.

Figure 3.8(e) also shows that the first released $1/2[1\bar{1}0]_M$ perfect dislocation cut through the TB between the M_4 crystal and the T_4 crystal. The reaction between the dislocation and the TB resulted in a step at the twin boundary. $1/2[1\bar{1}0]_M$ dissolved

into two dislocations in the Miller index of the M_4 crystal: $1/9[\bar{2}21]_M$ and $1/18[5\bar{5}2]_M$. In the Miller index of the twinned crystal these two dislocations were $1/3[001]_T$ and $1/6[\bar{1}1\bar{2}]_T$, respectively. $1/9[\bar{2}21]_M = 1/3[001]_T$ was sessile in both crystals. Therefore, it will stay at the TB. $1/6[\bar{1}1\bar{2}]_T$ was glissile in the twinned crystal (T_4), and then it moved on the $(1\bar{1}\bar{1})_T$ plane in the T_4 crystal, dragging an intrinsic stacking fault.

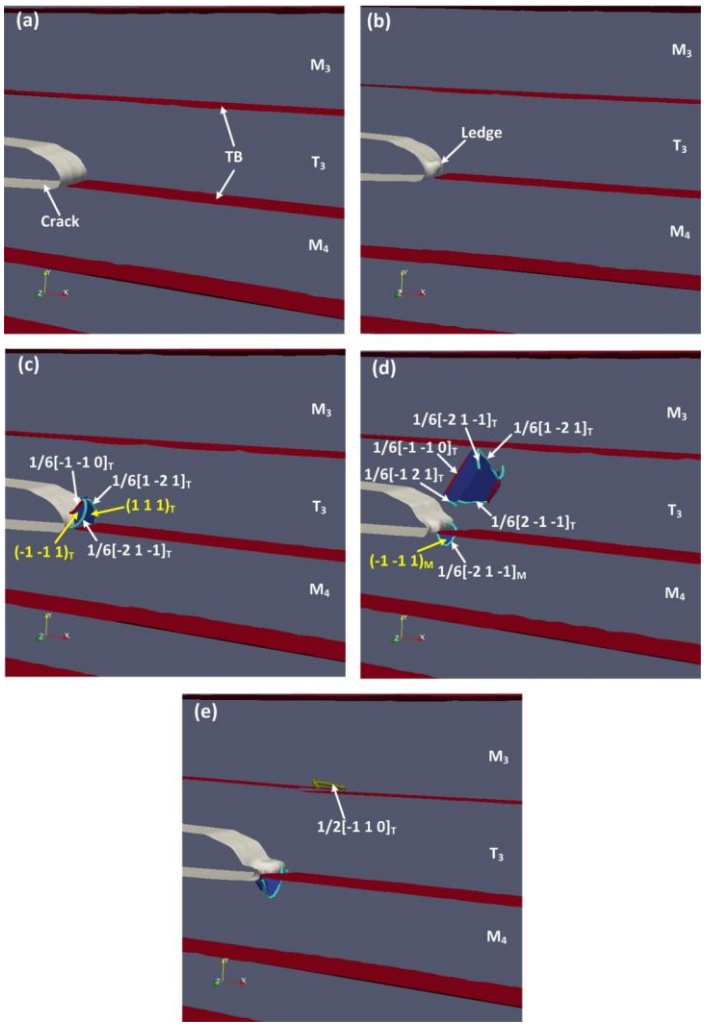

Figure 3.9 Dislocation activities around the crack tip for the 40 K case: (a) ε = 2.52%; (b) ε = 2.537%; (c) ε = 2.559%; (d) ε = 2.59%; (e) ε = 2.604%.

Figure 3.9 shows the dislocation activities around the crack tip at 40 K. The simulation cell is observed from the top-right-front direction. In Figure 3.9(a) the

imposed strain was 2.52%, a condition at which the crack just began to propagate in a brittle mode along the TB. The crack envelope is quite smooth. Soon afterwards ledges appear on the crack tip as shown in Figure 3.9(b). When the strain increased to 2.559% (Figure 3.9(c)) a V-shape defect structure was emitted around the ledges into the twinned crystal (T_3), which was constructed with two intrinsic stacking faults with normals of $(\bar{1}\bar{1}1)_T$ and $(111)_T$, respectively. These two intrinsic stacking faults were bounded by leading $1/6[\bar{2}1\bar{1}]_T$ and $1/6[1\bar{2}1]_T$ Shockley partial dislocations that intersected at a $1/6[\bar{1}\bar{1}0]_T$ stair-rod dislocation. It has been reported that such a V-shape defect structure can nucleate from a grain boundary in nanocrystalline palladium [126].

In Figure 3.9(d), representative of ε = 2.59%, the V-shape defect structure evolved into a Z-shape defect structure due to the periodic boundary condition imposed in the Z direction. The leading partial dislocations headed towards the TB between the M_3 crystal and the T_3 crystal. The corresponding trailing partial dislocations ($1/6[\bar{1}21]_T$ and $1/6[2\bar{1}\bar{1}]_T$) were released from the crack tip and a new Shockley partial dislocation ($1/6[\bar{2}1\bar{1}]_M$), bounding an intrinsic stacking fault, was emitted from the crack tip into the matrix lattice (M_4). The partial dislocation then evolved into another V-shape defect structure in Figure 3.9(e). As observed in Figure 3.9(e), the leading partials and trailing partials in the T_3 crystal merged into a $1/2[\bar{1}10]_T$ perfect dislocation at the TB between the M_3 crystal and the T_3 crystal.

3.3.1.5 Phase transformation

The MD simulation results indicated that different types of dislocations can be emitted from the crack tip at different temperatures in nanotwinned Cu, leading to a brittle-to-ductile transition. In the following paragraphs the atomic mechanism responsible for the dislocation nucleation will be discussed.

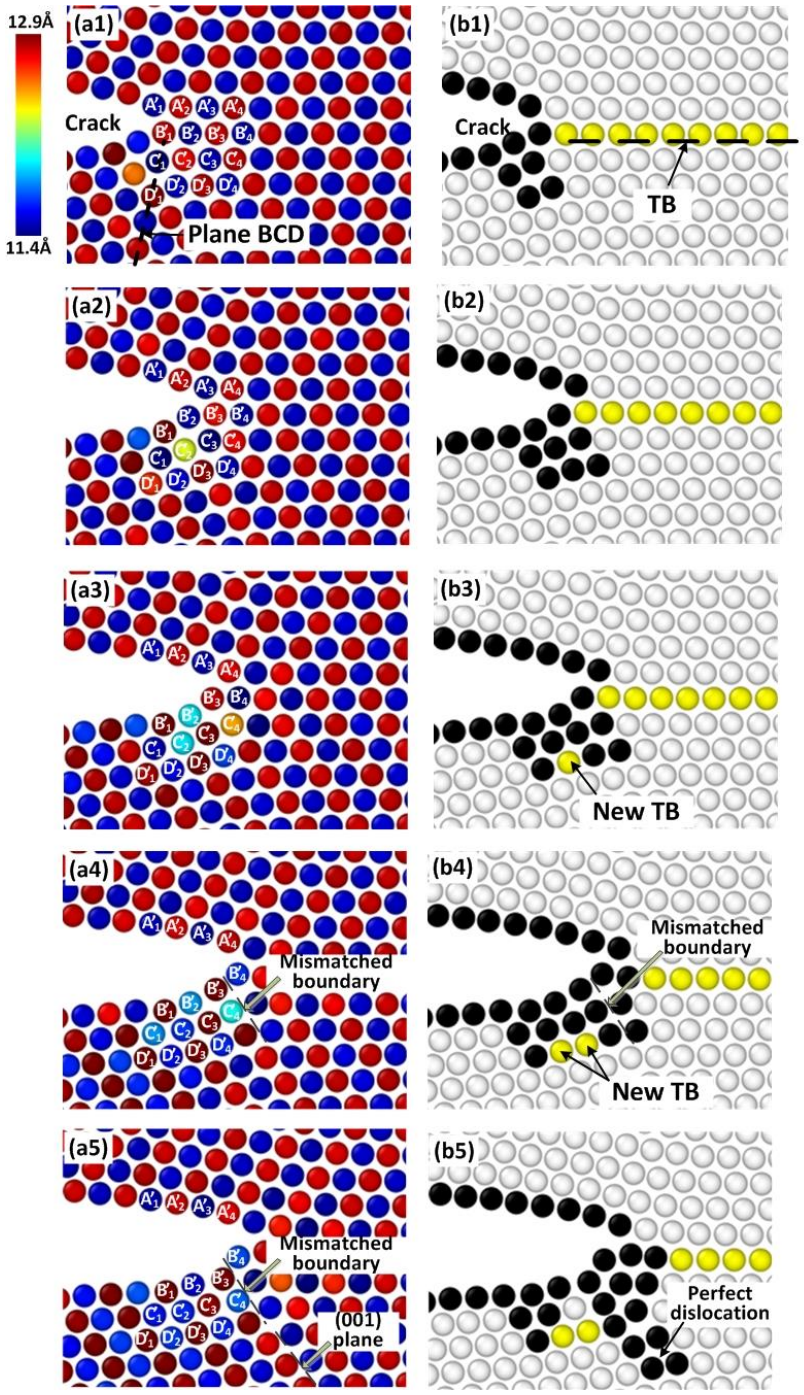

Figure 3.10 Atomic configuration (a1-a5) and local crystal structure (b1-b5) around the crack tip for two successive (110) planes at different strains: (a1-b1) ε = 2.751%; (a2-b2) ε = 2.755%; (a3-b3) ε = 2.758%; (a4-b4) ε = 2.761%; (a5-b5) ε = 2.763%; in (b1-b5) the perfect fcc and hcp atoms are shown in grey and yellow, respectively, and the free surface atoms are shown in black.

The simulation cell in this study had a two-layer (110) stacking sequence along the Z direction. Figure 3.10(a1-a5) shows atomic configurations around the crack tip for two successive (110) planes. These planes were initially located at Z = 11.505 Å and Z = 12.786 Å. In the following, they will be referred to as the first (110) plane and the second (110) plane respectively. The Z coordinates of the atoms are colour-coded according to the colour bar in Figure 3.10(a1). The first (110) plane and the second (110) plane are coloured near-blue and near-red, respectively, in Figure 3.10(a1). Figure 3.10(b1-b5) shows the same atomic configurations as in Figure 3.10(a1-a5) but they use different colouring to distinguish the local crystal structure around each atom, as determined by the CNA method. In the CNA method the nearest neighbours of an atom are first obtained within the cut-off distance for the presumed crystal structure. Different crystal structures have different cut-off distances. By comparing the nearest neighbours for each atom with the nearest neighbours for perfect structure crystals, the following crystal structures can be determined: fcc lattice, hcp lattice, bcc lattice, icosahedral lattice, and unknown lattice. The atoms coloured grey and yellow in Figure 3.10(b1-b5) are in the perfect fcc structure and hcp structure, respectively. Both the TB and the intrinsic stacking fault have an hcp structure. The atoms not associated with either the fcc structure or the hcp structure are coloured black in Figure 3.10(b1-b5).

Four groups of atoms have been marked in Figure 3.10(a1). They are A_1'~A_4', B_1'~B_4', C_1'~C_4' and D_1'~D_4', respectively. It can be seen in Figure 3.10(a1), corresponding to ε = 2.751%, that all the atoms maintained their original (110) planes. Atoms C_1', $D_{1,}'$ and D_2' are disordered due to the disturbance of the bond breaking process as shown in Figure 3.10(b1).

As shown in Fig. 10(a1), Atoms C_1', B_2', D_2' and C_3' were initially located at the same (110) plane while Atom C_2' was located at the neighbouring (110) plane. It is

interesting to note that Atom C_2' changed from near-red in Figure 3.10(a1) to near-green in Figure 3.10(a2), indicating that it moved from the second (110) plane towards the first (110) plane along the plane normal. That is, C_2' attempted to squeeze into the space between Atom B_2' and Atom D_2'. This resulted in the fact that five atoms C_1', B_2', C_2', D_2' and C_3' being located at roughly the same plane. A careful inspection indicates that a base-centred orthorhombic structure has been locally formed with lattice constants a = 2.326 Å, b = 4.270 Å and c = 2.556 Å. Once the $A_2' - B_2'$ bond breaks, the stretching between B_2' and D_2' stopped and Atom B_2' springsback towards Atom D_2'. This destabilised the new phase structure and one of its constitutive atoms C_3' jumped from the first (110) plane to the (110) plane above it, which is equivalent to the second (110) plane, along the positive Z direction. A C_3'-type atom then moved into the space between Atom B_3' and Atom D_3' as shown in Figure 3.10(a3). The consequence of these activities is that a twin boundary (TB) was generated at Atom D_3', as shown in Figure 3.10(b3). Following the same mechanism, as the imposed strain increases to 2.761%, the newly formed TB was extended by an atomic distance, as observed in Figure 3.10(b4). However, the newly formed TB shielded the atom at the crack tip and impeded the increase of its stresses, which arrested the bond breaking process. In turn, the expansion of the newly formed TB no longer continued. It can be seen in Figure 3.10(b4) that Atoms B_2', C_2', B_3', C_3' and C_4' make up a new twinned region relative to the M_4 crystal. This newly twinned region has a mismatched boundary with the M_4 crystal, as marked in Figure 3.10(a4) and Figure 3.10(b4). The mismatched boundary is a weak link where sliding can easily occur under straining. It can be seen in Figure 3.10(a5) and Figure 3.10(b5) that the mismatched boundary coincides with the (001) plane of the M_4 crystal. Therefore, as the imposed strain increases, the relative movement at the mismatched boundary can trigger the nucleation of a $1/2[1\bar{1}0]$ perfect dislocation on the (001) plane, which leads to the observation in Figure 3.8(c).

Hai and Tadmor [56] observed deformation twinning at the crack tip of aluminium using a mixed continuum and atomistic approach. In their simulation, the first partial dislocation was emitted from the crack tip and travelled on the plane intersecting the crack tip, leaving an intrinsic stacking fault in its wake. Subsequently, a second partial dislocation was emitted on the plane adjacent and behind the previous emission plane, laying down an extrinsic stacking fault and resulting in the formation of a microtwin. The twin boundary observed in Hai and Tadmor's simulation was inclined towards the crack propagation surface. They suggested that twinning occurs when the direction of the maximum resolved shear stress coincides with the Burgers vector of a partial dislocation. The twinning mechanism observed in our study differed from that reported by Hai and Tadmor [56]. Here twinning was triggered by phase transformation and its formation can nucleate a $1/2[1\bar{1}0]$ perfect dislocation onto the (001) plane.

To accurately examine the out-of-plane movements, the probability distribution of U_z displacement is shown in Figure 3.11. For the case of full brittle fracture (Figure 3.11(b) for temperature of 1.1 K spans the whole process of crack propagation), there was no movement along Z direction, the atoms only moved in the XY plane. In contrast, the transition region tended to break first, which was identical to the fully brittle fracture case (in Figure 3.11(a) and in Figure 3.11(c), covering snapshots before the first dislocation nucleation). At a critical value of deformation, atoms occurred on the out-of-plane movement, by identifying their displacement in Z direction. In Figure 3.10 and Figure 3.11, it indicates that the out-of-plane motion is the underlying reason for local phase transformation. After the initiation of the atomic jump motion began, the crack showed different propagation behaviour.

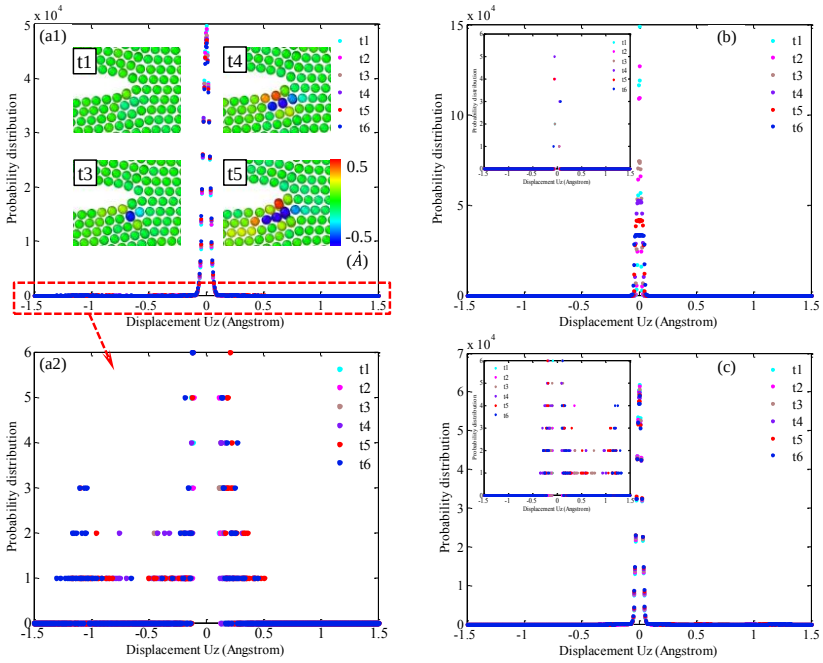

Figure 3.11 Probability distribution of Uz displacement ((a1-a2) 10 K; (b) 1.1 K; (c) 5 K.). t1~t6 are different time instants. (a1) Atomistic details of t1, t3~t5 are displacements in Z direction around the crack tip. (a2) shows the enlarged probability distribution of Uz displacement between 0 and 6.

3.3.1.6 Atomic mechanism for dynamic brittle-to-ductile transition

At 10 K, phase transformation occurred around the crack tip and induced the formation of a twinned region that nucleated a perfect dislocation. To understand the reason for phase transformation, two groups of atoms were considered. Group-B consisted of all the atoms initially located at the TB between T_3 and M_4, including Atoms B_1', B_2', B_3' and B_4' marked in Figure 3.10(a1).Group-D consisted of all the atoms initially located at the second plane below the TB between T_3 and M_4 including Atoms D_1', D_2', D_3' and D_4'. The maximum distance (d_{BD}^{max}) between the Group-B atoms and Group-D atoms always occurred near the crack tip. Figure 3.12 shows d_{BD}^{max} as a function of the imposed strain for three temperatures (1.1 K, 2 K and 10 K). It can be seen that the temperature affected d_{BD}^{max} after the strain exceeded 2.6%. At 1.1 K, d_{BD}^{max} slowly increased with the strain, whereas the increase in d_{BD}^{max} where the

strain was faster at 2 K. d_{BD}^{max} became higher when the temperature increased to 10 K. Phase transformation occurred when d_{BD}^{max} reached about 5.4 Å at both 2 K and 10 K. However, d_{BD}^{max} never reached this critical value in the present simulation of 1.1 K. It is concluded that there was critical distance between the Group-B atoms and Group-D atoms for phase transformation to occur. When the distance between the Group-B and Group-D atoms increased, the space between the two groups widened. These results in a large attractive force formed between the atoms at the periphery of the enlarged region. When the space between the Group-B atoms (such as B_2' in Figure 3.10(a2)) and Group-D atoms (such as D_2' in Figure 3.10(a2)) is large enough, the attractive force will assist atoms (such as C_2' in Figure 3.10(a2)) located between Group-B atoms and Group-D atoms to overcome the energy barrier to fill in the space, resulting in a phase transformation from the fcc structure to the base-centred orthorhombic structure.

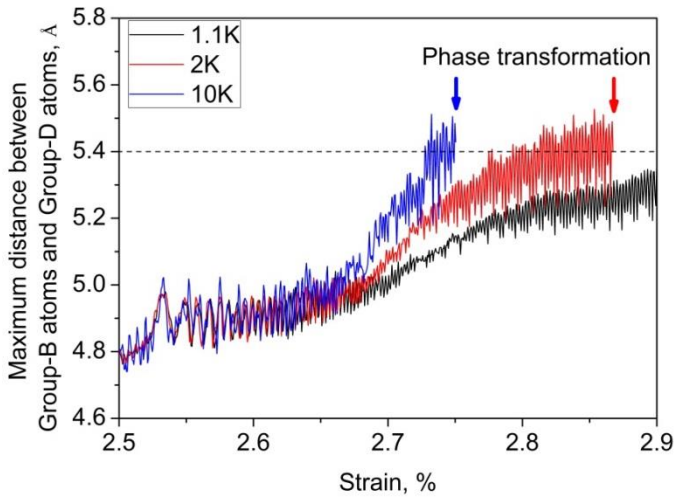

Figure 3.12 Maximum distance (d_{BD}^{max}) between Group-B atoms and Group-Datoms as a function of the imposed strain.

A plane passing through a Group-B atom and its corresponding Group-D atom and parallel to the Z axis was called Plane BCD, as shown in Figure 3.10(a1). The angle (θ_{BCD}) between Plane BCD and the X axis was plotted against the imposed strain in Figure 3.13, and θ_{BCD} generally increases with the imposed strain. As the crack

propagated the stress of most of the atoms located on the left hand side of the crack tip was released. The stress release region is shown schematically in Figure 3.4(c). The stress release in this region will cause the lattice to expand along the X direction, but the lattice on the right-hand side of the crack is still subjected to shrinking along the X direction due to the strain imposed along the Y direction. This strain rotated Plane BCD slightly to a higher θ_{BCD} value as the crack propagated.

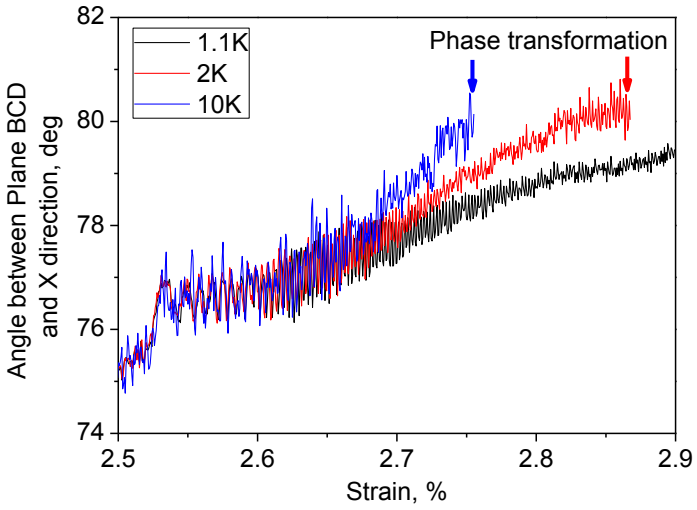

Figure 3.13 Angle (θ_{BCD}) between Plane BCD and the X direction as a function of the imposed strain.

When the temperature increased, thermal expansion also promoted the rotation of Plane BCD. It can be seen in Figure 3.13 that θ_{BCD} increased with an increasing temperature once the strain became larger than about 2.6%. This increased θ_{BCD} at a higher temperature helped the Group-B atoms at the crack tip (such as B_2' in Figure 3.10(a2)) to move towards the crack opening (left hand side of the simulation cell). This atomic flow provided more stretching space between the Group-B atoms and Group-D atoms (B_2' and D_2' in Figure 3.10(a2)). This was accompanied by an increase in d_{BD}^{max}, and therefore d_{BD}^{max} reached the critical value earlier at higher temperatures and caused a phase transformation at a lower strain. Hence, the dynamic brittle-to-

ductile transition occurred earlier at 10 K than at 2 K, as observed in Figure 3.6. At 1.1 K, θ_{BCD} increased slowly with increasing strain, but it did not reach the critical maximum distance at the end of the simulation, so no dynamic brittle-to-ductile transition was observed in this case.

Abraham and Broughton [207] also observed dynamic brittle-to-ductile transition in their MD simulation of notched fcc solids using simple interatomic potentials. They attributed this phenomenon to a dynamic instability of brittle fracture. In this study I found that the local atomic space around the crack tip can increase during the brittle crack propagation in nanotwinned Cu at temperatures between 2 K and 30 K, but when the space exceeded a certain level, a phase transformation occurred that formed a new twinned region and nucleated a perfect dislocation on the (001) plane. The formation of the twinned region and the emission of a dislocation shield at the crack tip and lowered the stress at the crack tip, which resulted in the transition of the crack propagation from a brittle mode to a ductile mode.

3.3.1.7 Atomic mechanism for ductile fracture

In Figure 3.9, the case at 40 K indicated that ledges were first formed on the crack tip first, followed by nucleation of dislocation around the ledges. It is interesting to know why ledge was generated. Figure 3.14(a) shows two successive $(\bar{1}\bar{1}0)$ planes within the Z range of 11.3 Å $\leqslant$ Z $\leqslant$ 13 Å at a strain of 2.529%. Figure 3.14(b) displays two successive $(\bar{1}\bar{1}0)$ planes within the Z range of 17.7 Å $\leqslant$ Z $\leqslant$ 19.3 Å at the same strain. The atoms in Figure 3.14 are coloured according to their stress along the Y direction (σ_y). Six atoms were marked in the figures. Atoms $B_1^{"}$ and $B_2^{"}$ are initially located at the TB between the T_3 crystal and the M_4 crystal. Atoms $A_1^{"}$ and $A_2^{"}$ are initially located at the first $(1\bar{1}1)$ plane above the TB. Atoms $E_1^{"}$ and $E_2^{"}$ are at the second $(1\bar{1}1)$ plane above the TB. It can be seen in Figure 3.14(a) that the bond ruptured between Atom $B_1^{"}$ and Atom $A_1^{"}$ for 11.3 Å $\leqslant$ Z $\leqslant$ 13 Å, but when the

observation domain moved to 17.7 Å ⩽ Z ⩽ 19.3 Å, as shown in Figure 3.14(b), the atomic bond between Atom $E_1^{''}$ and Atom $A_1^{''}$ broke. The thermal fluctuation of Atom $A_1^{''}$ could cause variations in the $E_1^{''}$ - $A_1^{''}$ and $B_1^{''}$ - $A_1^{''}$ distances because at a lower temperature the $B_1^{''}$-$A_1^{''}$ distance is always greater than the $E_1^{''}$-$A_1^{''}$ distance, and therefore atomic bond breaking always occurs between the $A_1^{''}$-$A_2^{''}$ plane and the $B_1^{''}$-$B_2^{''}$ plane at lower temperatures. However, higher temperatures may significantly increase the $E_1^{''}$-$A_1^{''}$ distance because when the $E_1^{''}$-$A_1^{''}$ distance exceeded a critical value, atomic bond breaking will occur between the $E_1^{''}$-$E_2^{''}$ plane and the $A_1^{''}$-$A_2^{''}$ plane. This means that due to thermal influence, the crack may propagate along two adjacent crystallographic planes at different Z locations. In other words, the crack tip front is no longer straight in the Z direction. This results in ledges perpendicular to the crack propagation plane. Zhu and Thomson [20] proposed that a ledge might be formed by passing a number of screw dislocations through the crack tip on a slip plane normal to the crack line. I found an alternative mechanism to explain the formation of a ledge on; thermal fluctuation at a higher temperature caused the crack to propagate simultaneously along different crystallographic planes, and this resulted in ledges on the crack tip.

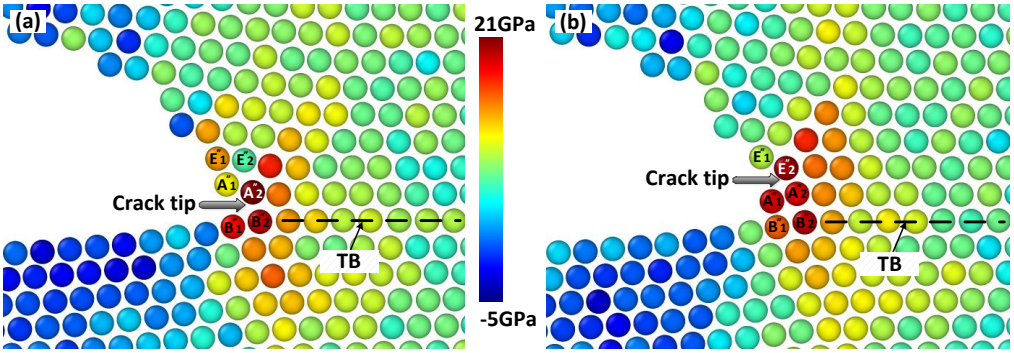

Figure 3.14 Stress along the Y direction (σ_y) for the 40 K case at ε = 2.529%: (a) 11.3 Å ⩽ Z ⩽ 13 Å; (b) 17.7 Å ⩽ Z ⩽ 19.3 Å.

3.3.1.8 Criteria for void nucleation and crack propagation

The atomic cleavage process is the response of local and large interatomic stresses near the crack tip. As shown in Figure 3.15(c-f) (also in Figure 3.16(c-f)), the stress distribution is symmetrical to the central twin plane. Stress components--stress triaxiality (σ_{tri}) (or mean stress--σ_m) or tensile stress (σ_y) are good indicators with which to judge the atomic de-bonding behaviour. These high localised stress concentrations make the atom bonds break in a specific cleavage plane, which agrees with the classic criterion that void nucleation and crack growth must satisfy three requisites [211]: (1) $\sigma_{tri} \geq \sigma_{tri\_crit}$; (2) $\sigma_y \geq \sigma_{y\_crit}$ and (3) $\varepsilon_p \geq \varepsilon_{p\_crit}$, where σ_{tri_crit}, σ_{y_crit}, ε_{p_crit} is the critical value of stress triaxiality, tensile stress, and localised regional deformation, respectively. These three conditions are crucial in three fields for crack propagation, including preventing the crack tip from blunting ($\sigma_{tri} \geq \sigma_{tri\_crit}$), propagating the crack ($\sigma_y \geq \sigma_{y\_crit}$), and initiating a crack nucleus ($\varepsilon_p \geq \varepsilon_{p\_crit}$). In Figure 3.15(c-f), it is very interesting to see that the crack cleavage associated with the process of elastic wave dispersion. When each atom de-bonds at the crack tip the elastic wave disperses from the crack tip and there is an instantaneous dispersion of energy from the crack tip. In Figure 3.15(c1-f1), the elastic wave located in positions 1_1, 2_1, 3_1, turned to positions 1_2, 2_2, 3_2 in Figure 3.15(c2-f2), and moved to positions 1_3, 2_3, 3_3 in Figure 3.15(c3-f3). Figure 3.15(c-f) shows that the directions of two major elastic wave dispersions are symmetrical to the twin plane, and the elastic wave was mainly coupled with two component vectors of dispersion that had decomposed onto $\{111\}_M$ and $\{100\}_M$ planes or $\{100\}_M$ and $\{100\}_T$ planes. This was consistent with the movement of atomic cleavage that occurred in {111} plane and {100} plane. No further elastic energy accumulated at the crack tip due to dispersion by instantaneous atomic breakage that led to a relatively ordered atomic arrangement without obvious lattice rotation or atom reconstruction at the crack tip, but only with atoms shuffling in terms of in-plane movement. This therefore reduced the lattice trapping effect, which was largely

believed to contribute to the dislocation nucleation in refs. [104, 212]. Figure 3.15(b) shows that all the atoms moved only in (110) (including $(110)_T$ and $(110)_M$ or (110) and $(\bar{1}\bar{1}0)$) plane by identifying its Z axial displacement in [110] (including $[110]_T$ and $[110]_M$ or [110] and $[\bar{1}\bar{1}0]$) direction.

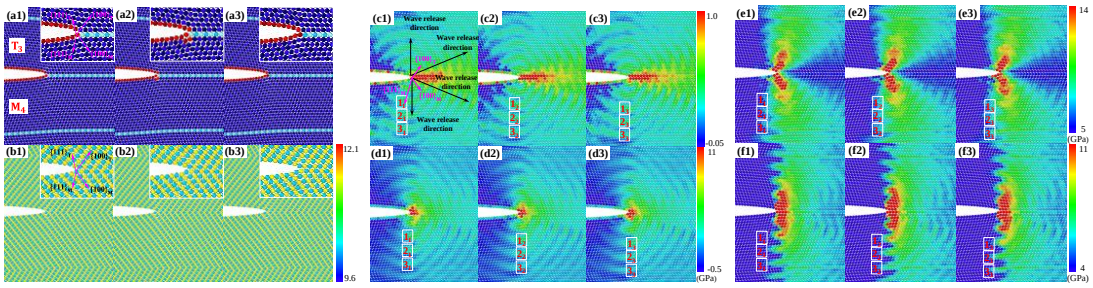

Figure 3.15 Atomic views of crack propagation coexisting with elastic wave dispersion from the crack tip of temperature 1.1 K. (a) Atoms were coloured based on CNA method with two layers in [110]/[-1-10] direction. Perfect fcc atoms are light blue and dark blue. hcp atoms are light cyan and dark cyan. Disordered atoms (e.g. free surface, dislocation core) were rendered in dark and light red. The dark and light colours indicated atoms in the neighbouring two layers along the [110]/[-1-10] direction; (b) Z axial position along [110]/[-1-10] direction. (c) Stress triaxiality--σ_{tri}; (d) Mean stress--σ_m; (e) Von Mises stress--σ_{von}; (f) Tensile stress--σ_y.

For BDT temperature, crack behaviour was different from complete atomic cleavage at extremely low temperatures (seen in Figure 3.15). Here the crack exhibited a complete atomic cleavage at an early stage and non-atomic cleavage at a later stage. In Figure 3.16(a1-f1), the way of atomic de-bonding was the same as in Figure 3.15 where high localised stresses concentrated at the crack tip and induced atomic cleavage in {111} and {100} planes. Meanwhile the elastic wave dispersed from the crack tip along these two cleavage planes. All atomic movement belongs to an in-plane way in (110), (including $(110)_T$ and $(110)_M$ or (110) and $(\bar{1}\bar{1}0)$) plane (in Figure 3.15(a1-b1)). However, the scenario of in-plane movement changed in Figure 3.16(a2-b2) where there is a small displacement in the [110] (including $[110]_T$ and

$[110]_M$ or [110] and $[\bar{1}\bar{1}0]$) (Z axis) direction out of the original (110) plane. It was called out-of-plane movement because the atoms migrated out of the initially locating (110) plane. Accordingly, dispersion of the elastic wave was less appreciable compared to that in Figure 3.15(a1-b1), but since out-of-plane movement/local phase transformation has occurred, the situation continually deteriorated with increasing tensile deformation (Figure 3.16(c2-c4)-(f2-f4)).

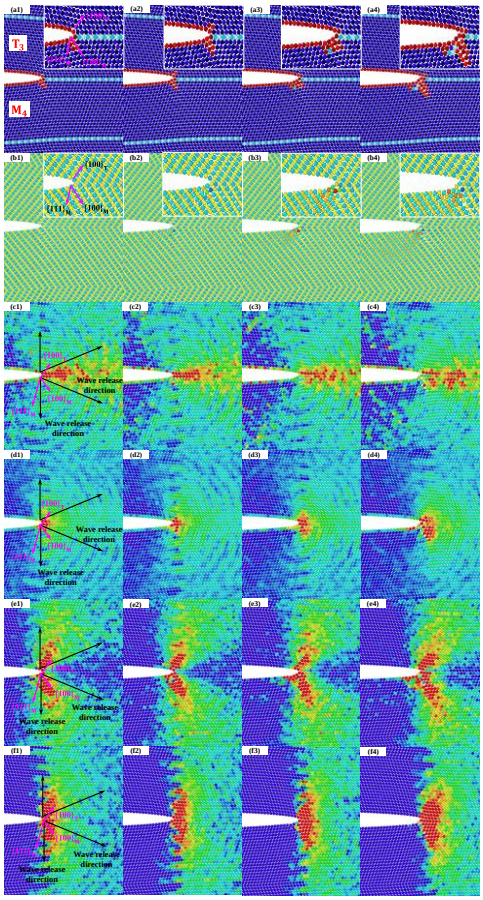

Figure 3.16 Atomic views of crack propagation coexisting with elastic wave dispersion at the earlier stage from the crack tip of temperature 10 K. (a) CNA (see Figure 3.15(a)); (b) Z axial position in [110]/[-1-10] direction; (c) σ_{tri}; (d) σ_m; (e) σ_{von}; (f) σ_y. Stress colour bar is same shown with in Figure 3.15.

The tensile stress and stress triaxiality (or mean stress) exhibited an extended area of concentration with small localised stress values at the crack tip. The atomic bonds could not break at the crack tip, so the crack was almost arrested at the right middle of the atomic model, but by then, elastic wave dispersion had almost stopped being emitted from the crack tip (Figure 3.16(c4-f4)). The crack finally changed from brittle to ductile because of the local phase transformation and its associated local twin formation near the crack tip.

3.3.1.9 Twin boundary effect on plastic deformation

A twin boundary can be regarded as an inherent boundary for crack propagation. In my MD simulations, at extremely low temperatures, the crack propagated within full atomic cleavage along the TBs, and the elastic wave was instantly dispersed from the crack tip in {111} and {100} plane. Thus no energy accumulated ahead the crack tip, which means the stress distributions at the crack tip always favours perfect crack cleavage. However, if TB is taken as a specific crystal construction, it destroys the continuity of dispersion direction for releasing an elastic wave and causes the TBs to block the elastic wave dispersion, and the stress piles up at its corresponding barrier region. As Figure 3.17 shows, the stresses pile up at the TBs near the crack tip (seen as red dashed rectangular lines), and they are symmetrical to the central TB. In Figure 3.17(d), and (f), at the upper and lower TBs, the stress distribution exhibited a localised shear effect along the TBs. When the shear effect becomes large big enough, it may lead to the movement of localised atomic shear along the TBs to destroy the perfect atomic cleavage, even at an extremely low temperature. The influence of TB spacing on the brittle versus ductile fracture will be introduced later.

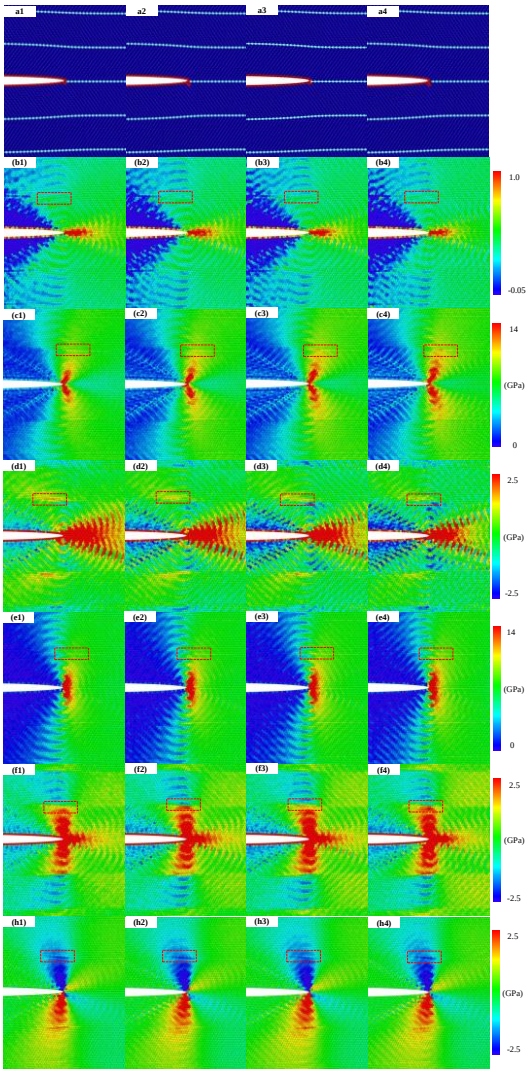

Figure 3.17 Stress components pile up on the TBs nearby the crack tip with temperature 1 K. (a) CNA (see Figure 3.15(a)), (b) σ_{tri}, (c) σ_{von}, (d) σ_x, (e) σ_y, (f) σ_z, (h) σ_{xy}.

3.3.2 Effect of twin boundary spacing

As mentioned above, the TB blocks the release of an elastic wave which leads to the concentration of a more stress on the TBs, but when the distance between the TBs is small enough, the accumulated stress can induce homogeneous nucleation and propagation of twinning partial dislocations on TBs near the crack tip, which causes ductile failure in twinned copper; according to Rice's model of dislocation emissions from a crack tip and deduction in Ref. [94].

The critical stress intensity factor at the crack tip can be written:

$$K_{IC} = \sqrt{\frac{2G\mu}{1-\nu}} = \sqrt{\frac{2\mu(2r_{sur}-r_{tb})}{1-\nu}} \tag{3.4}$$

Where r_{sur} is the fracture surface energy, r_{tb} is the TB energy, and μ is the shear modulus and Poisson ratio.

The resolved shear stress on the TB is

$$\tau_{tb} = \frac{1}{2}\sqrt{\frac{2\mu(2r_{sur}-r_{tb})}{1-\nu}}\sqrt{|\sin\theta|}\sin\theta\cos\frac{3\theta}{2} \tag{3.5}$$

So

$$|\tau_{tb}|_{max} = \alpha\sqrt{\frac{2\mu(2r_{sur}-r_{tb})}{1-\nu}} \tag{3.6}$$

Where $\alpha = \sqrt{|\sin\theta|}\sin\theta\cos\frac{3\theta}{2}$, the critical TB spacing can be deduced,

$$\lambda \le \lambda_{crit} = \frac{\alpha^2\mu(2r_{sur}-r_{tb})}{\pi\tau_{crit}^2(1-\nu)} \le |\tau_{tb}|_{max} \tag{3.7}$$

All the parameters in the above Equations are shown in Table 3.1, and some of them are shown in Chapter 5.

Table 3.1 Values of parameter for copper

μ (GPa)	ν	r_s (mJ/m^2)	r_{tb} (mJ/m^2)	τ_{crit}
48	0.34	1239	22.24	4.88

Then λ_{crit} was calculated to be of 0.464 nm, when the spaces between the TBs was more than the critical value, and when the crack propagation was supposed to exhibit perfect cleavage along the TB in the absence of homogeneous dislocation nucleated near the crack tip.

Figure 3.18(a) shows the stress versus strain curves with different TB spacing. The sharp fracture transition from brittle to ductile behaviour at a low temperature when

the TB spacing decreased below a critical value can be seen, but due to the intrinsic brittleness of the pre-existing TB, the crack in pure single copper crystal can propagate differently. The brittle-to-ductile transition was mainly determined by competition between crack cleavage and dislocation emission/mobility, but with TB spacing larger than 1.25 nm, the relatively strong tensile effect governs the shear effect and crack cleavage prior to dislocation nucleation as the tensile stress dropped sharply to a low level as an extensive strain deformation. The brittleness of the crack propagated along the TB without any dislocation activities, but as the TB spacing decreased further it triggered a brittle-to-ductile transition because the high concentration of stress at the crack tip was enough to induce a twinning dislocation nucleation on neighbouring TBs near the crack tip; this activated more dislocation motions as the crack propagated, which led to a final ductile fracture. In fact, in the latter stage where TB spacing was 1.25 nm, very few homogenous dislocations began to form on the neighbouring TB near the crack tip, and a subtle dislocation did not evolve into more dislocation activities because the model was limited in size, although the crack could still propagate with completely brittle fracture behaviour. For a TB spacing of 0.63 nm, the highest twin density made the TBs into facilitated sites for dislocation nucleation where dislocation movement almost concurred with crack cleavage and the system stress did not relax as it did with TB spacing larger than 0.63 nm. With more activated dislocations to accommodate deformation, the strength increased to its highest level and then dropped sharply. During deformation, the incipient nucleated dislocations were blocked by the TBs. The atomic model exhibited an obvious strain hardening effect which increased its strength. Moreover, the intersections between dislocation and TB caused a successive loss of coherence of the twin, which further improved the ductility. It is worth noting that in my simulation there was a critical TB spacing of 1.25~2.09 nm to induce brittle-to-ductile transition; this was smaller than the theoretical deduction and previous MD observation with a critical value of 3~4 nm [94].

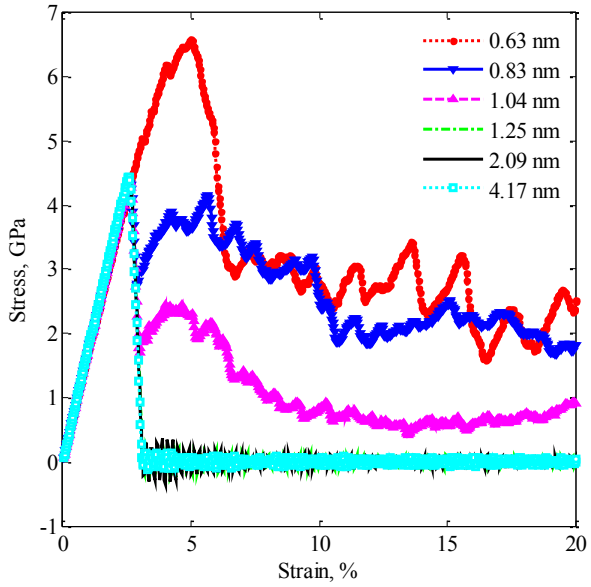

Figure 3.18 Tensile stress versus strain rate for varied twin boundary spacing.

3.3.3 Effect of model size

In nanopillars with TB spacing of 4.3 nm [94], the crack was a full brittle failure regardless of the size of the pillar, whereas my MD results presented in Figure 3.19 showed that size has an effect in twinned copper. These distinct deformation mechanisms revealed a mode size transition was induced between brittle and ductile fracture. Observations that revealed the thinner the model the more brittle the crack, can be found in the MD simulations. Below a critical thickness of model (20 lattices in orientation of [110]), the crack propagated in brittle fashion without dislocation nucleation, but as the thickness increased the crack gradually changed from brittle to ductile transition by crack cleavage in the early stage, followed by dislocation emission from the crack tip. The sample finally failed due to surface necking. The enlarged figure on the right side of Figure 3.19 covers the onset of dislocation nucleation, and shows that the tension stress did not follow the former trend with a sharp drop to almost 0 GPa after the crack began to propagate because the dislocation activity increased the tensile stress value.

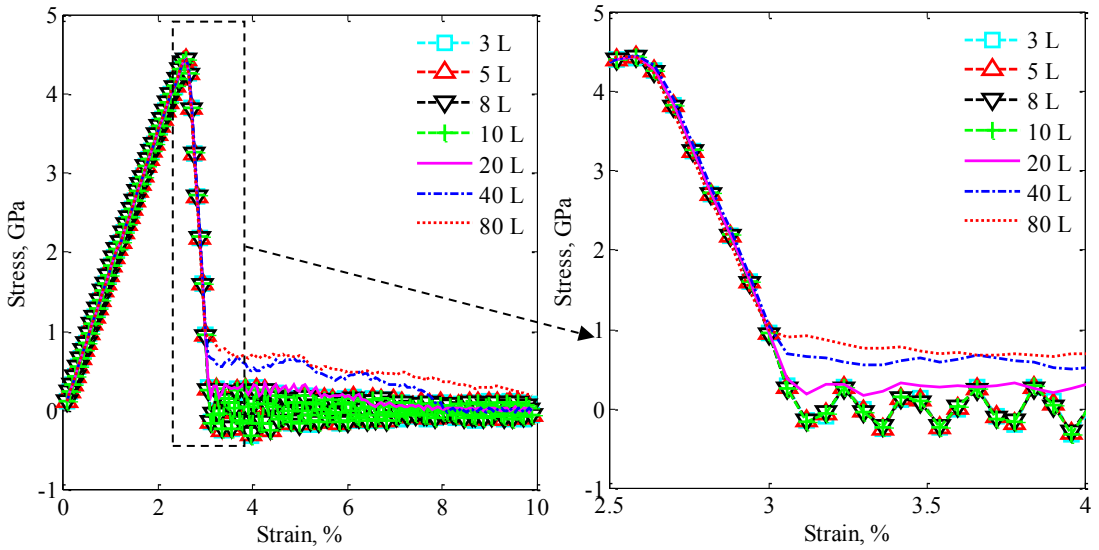

Figure 3.19 Tensile stress-strain rate curves for a model with varying thicknesses. A transition of thickness-induced brittle fracture to ductile fracture is clearly visible. The figure on the right is a close up view of the brittle-to-ductile transition point where the thickness of the model changed. "L" means the lattice constant.

3.3.4 Effect of strain rate

It was found the temperature of brittle-to-ductile transition was strongly influenced by the applied strain rate in experiments [81, 85]: such that higher strain rates always lowered the fracture toughness, and vice versa. However, in this MD simulation the opposite conclusion was reached; refer to Figure 3.20(a), which shows that at a smaller strain rate, the crack was more ductile, but when the strain rate was no larger than 1×10^{8} s^{-1}, the crack was fully brittle, without any dislocation nucleation because as the strain rate increased the crack tended to become more ductile at the latter stage (including 5×10^{8} s^{-1} and 1×10^{9} s^{-1}). It was explained that the two apparently contradictory observations between the results of the MD simulation and the experiments may have stemmed from the intrinsic limitation of strain rate for MD simulation. In an MD simulation, the applied strain rate was typically 11~12 orders of magnitude higher than in the in situ experiment.

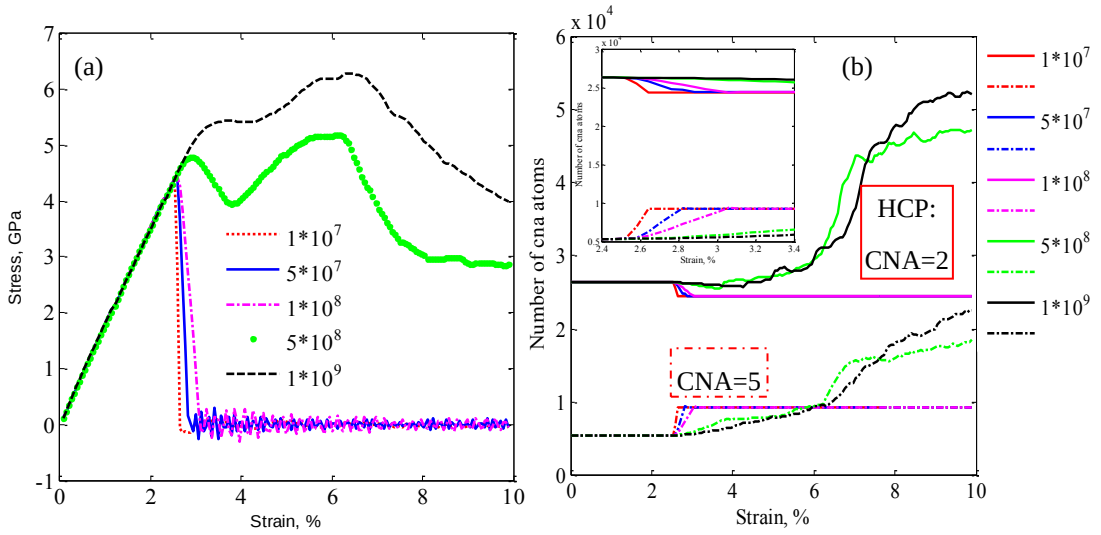

Figure 3.20 (a) Tensile stress-strain curves with various applied strain rates (unit: s^{-1}). (b) Evolution of number of CNA atoms during strain deformation.

Figure 3.20(a) shows the tensile stress-strain curves with various applied strain rates. Crack cleavage could have occurred at about 2.52% for all cases, including the early stages, until the dislocation nucleated ahead of the crack tip at 3.6%, and 3.96% deformation for cases of 5×10^8 s^{-1} and 1×10^9 s^{-1} respectively. Interestingly, unlike the smaller applied strain rate, the tension stress did not decrease immediately to a very low level (e.g. strain rates of 5×10^8 s^{-1} and 1×10^9 s^{-1}), it was continually enhanced as the deformation increased. It was difficult to use classic theory to explain this because systematic stress was supposed to have relaxed considerably by the initial crack propagation. The probable reason is that such a large applied strain rate makes changing the stress conditions possible. The relaxation of system stresses after crack cleavage cannot have just vanished due to the large imposed strain rate. This is why we just may observe an increase of tension stress rather than a sharp drop since the onset of crack cleavage had begun. Moreover, exerting a large strain rate means that the atomic model needs more time to reach the energy equilibrium configuration because of a no equilibrium system state, and the temperature tended towards large fluctuations. The activated atoms induced by the oscillating temperature could easily have been taken as an embryo site for dislocation nucleation. Finally, the dislocation

activities dominated the deformation mechanism that leads to ductile fracture. Figure 3.20(b) shows the number of CNA atoms during deformation but since the crack cleaved the number of hcp (CNA=2) atoms decreased and the number of disorder atoms (CNA=5, surface or defect atoms) increased. The higher strain rate indicated slight changes due to less brittleness, but the number of hcp or disorder atoms shifted largely due to a smaller strain rate. As deformation proceeded the emerging dislocation contributed to a continuous increase in the number of hcp atoms and disorder atoms.

3.4 Summary

In this chapter, MD simulations were carried out to investigate fracture behaviour in nanotwinned Cu. A through-thickness crack was generated on one side of the simulation cell with the crack surface coinciding with a twin boundary. Under tensile straining perpendicular to the twin boundary, the crack behaved in three different manners at different temperatures. The major observations can be summarised as follows:

1) At temperatures up to 1.1 K, the crack propagated in a brittle fashion, and atomic bond breaking caused the brittle fracture behaviour.
2) From about 2 K to about 30 K, a dynamic brittle-to-ductile transition was observed. The fracture propagated in a brittle mode before it changed to a ductile mode when the imposed strain reached a critical level. It was found that the local inter-atomic spacing around the crack tip can increase during the brittle crack propagation as the temperature increased and/or the brittle crack propagated. When the spacing exceeded a certain level, a phase transformation that can induce the formation of a newly twinned region around the crack tip and nucleate a perfect dislocation on the (001) plane. The formation of the twinned region and the emission of the dislocation shielded the crack tip and lowered the stress at the crack tip. This resulted in a transition from brittle mode to ductile mode.

3) The crack propagated in a ductile mode as the temperature was raised above 40 K. In this regime the crack can propagate along two adjacent crystallographic planes due to a thermal activation of atoms at the crack tip. This resulted in a jogged crack tip front with ledges perpendicular to the crack propagation plane, followed by an emission of dislocations around the ledges. The latter activity shielded the atoms around the crack tip and impeded the propagation of brittle cracks.
4) The occurrence of crack cleavage was associated with three conditions that: (i) $\sigma_{tri} \geq \sigma_{tri\_crit}$, (ii) $\sigma_y \geq \sigma_{y\_crit}$, (iii) $\varepsilon_p \geq \varepsilon_{p\_crit}$.

MD simulations were also used to study other factors of influence such as the TB spacing distance, model size (here, just for thickness), the applied strain rate on the brittle-to-ductile transition in nanotwinned copper at low temperature. For three different cases, some critical values related to fracture transition exist: (a) when the TB spacing increased to 1.25~2.09 nm, the fracture transitioned from brittle to ductile; (b) with a critical thickness of about 20 lattices, the crack showed two different characteristics such that the less the thickness was, the more brittleness the crack showed; (c) the MD results showed opposite observations from the in situ experiment, in that smaller strain rate (no larger than 1×10^8 s^{-1}) promoted more brittle behaviour, possibly due to the intrinsic limits of MD simulation.

In this chapter the MD results shed light on the brittle versus ductile fracture behaviour in nanotwinned Cu. I speculated whether the same mechanism of crack cleavage and phase transformation induced the brittle-to-ductile fracture in nanotwinned Cu could be applicable in other nanotwinned fcc crystals with different energetic barriers (e.g. Ni). In the next chapter (Chapter 4), I focused on studying the brittle-to-ductile fracture transition in nanotwinned Ni.

CHAPTER 4 BRITTLE-TO-DUCTILE TRANSITION IN NANOTWINNED NICKEL

4.1 Introduction

It is known that brittle-to-ductile transition fracture depends on competition between crack cleavage and dislocation nucleation ahead of the crack tip, or dislocation mobility away from the crack tip [17, 53, 81, 213, 214]. Rice et al. [19] proposed that the nucleation of leading partial dislocation must overcome the energy barrier related to the unstable stacking fault energy r_{usf}, and nucleation of the trailing partial will be a function of the difference in energy ($r_{usf} - r_{sf}$). Tadmor and Hai [55] found that the tendency towards twinning depends on the ratio of r_{utf}/r_{usf}. Van Swygenhoven et al. [107] concluded that a correct interpretation of deformation mechanism requires the generalised stacking fault energy curve, involving stable and unstable stacking fault energies: (i) the extended partials or full dislocations nucleation must be understood in terms of the ratio r_{sf}/r_{usf}; (ii) twin nucleation depends on the ratio r_{utf}/r_{usf}. However, based on Griffith's theory of fracture [13], crack cleavage is associated with the energy item r_{sur}--free surface energy. Those intrinsically different energetic factors for different materials may imply different brittle/ductile fracture behaviour. Cu and Ni exhibited different stacking fault energies and free surface energies, as seen in Chapter 5. I speculated whether brittle-to-ductile fracture transition could happen in twinned Ni the same as in twinned Cu, and whether the same mechanism that caused this transition exists. In this chapter, I focussed on exploring these problems.

4.2 Model set-up

The atomic configuration simulation cell is referred to in Chapter 3. An initially semi-infinite crack with size of 80 Å × 18 Å × 24.89 Å (in X, Y, Z directions) was inserted into the sample and a twin spacing distance of 4.06 nm was introduced into the single

nickel crystal. The geometric size was 491.49 Å × 487.75 Å × 24.89 Å in the X, Y, and Z directions (with a total of 544520 atoms). A periodic boundary condition was imposed along the direction of the crack front (Z axis) and the direction of tension (Y axis).

The EAM interatomic potential [215] based on the ab initio method was adopted. After the model was constructed, the sample was minimised by the conjugate gradient algorithm, and then the model was relaxed through a Nose-Hoover thermostat and the Parrinello-Rahman barostat (NPT) method to ensure that the temperature had the desired values and the external pressure at 0 bar in Y and Z directions for 10^5 time steps prior to tensile deformation. A multiple time algorithm was used with a time step of 3 femtoseconds. Several simulation cases at temperatures (1.1 K, 10 K, 15 K, 20 K, 30 K, 50 K, 100 K, 200 K, 300 K, 400 K and 500 K) were conducted. A constant strain rate of 1×10^8 s^{-1} was applied along the Y axis until it stretched to 9.9% of deformation. As the model stretched, the NPT method was used to control the temperature at the temperatures required and the external pressure at zero in the Z direction. The detailed information of twinned Ni was identical to twinned Cu (see Chapter 3).

4.3 Results and discussion

4.3.1 Stress-strain relationship

Figure 4.1 shows the engineering stress-strain curves for a uniaxial tension of nanotwinned nickel with temperatures ranging from 1.1 K to 500 K. The stress-strain curve exhibited an identical almost linear stress-strain relationship for a strain of less than 2.34% with a tangent modulus of about 257 GPa for every case, except those with higher temperatures (200 K, 300 K, 400 K, 500 K), that were close to the elastic modulus of 303 GPa for pure nickel along the [111] direction [216]. The difference between two values was caused by the pre-existing edge-notched crack. The

increasing temperature resulted in a smaller tangent modulus, which agreed with the MD simulation [217, 218]. As Figure 4.1 shows, the fracture behaviour had undergone a temperature-dependent transition process by identifying the three distinct temperature scopes of tensile deformation. At 1.1 K and 10 K, the tensile stress increased linearly up to a peak value of about 2.34%, and then decreased sharply to almost zero GPa with about 2.7% deformation, followed by an oscillating movement as the strain continued to increase. The temperate range was from 15 K to 100 K (15 K, 20 K, 30 K, 100 K), and showed that the trends of the stress-strain curves were almost identical to the 1.1 K and 10 K cases before the strain of ε = 2.31975%, but did not decrease to almost zero at about 2.7 % deformation. Instead, the stress ceased to drop at strains of 2.7%, 2.64%, 2.64%, and 2.52% respectively. The tensile stress increased slightly with increasing strain, but when the temperature increased to over 100 K, the stress did not drop sharply at 2.34% strain it continued to increase with the increasing strain until the stress reached its maximum value. At a lower temperature the strength was greater at temperatures above 100 K, as seen in Figure 4.1. After the strain exceeded the critical strain for maximum strength, the stress dropped with a lot of serrations as the imposed strain increased.

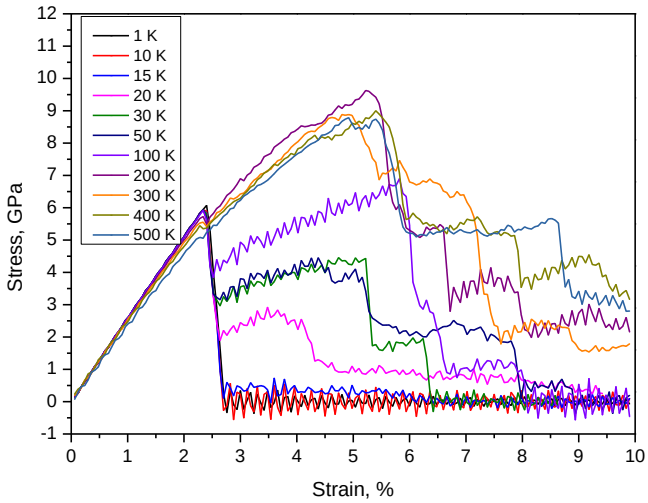

Figure 4.1 Tensile stress-strain curves for tensile deformation of twinned nickel.

To understand the stress-strain curve better, Figure 4.2 plots the relationship between toughness and temperature by integrating their areas amongst the curves between the stress and the strain. This toughness reflects the material's resistance to fracture when under stress. Three Groups exist according to their toughness under different temperatures. In the first Group (1.1 K and 10 K), the toughness is least, indicating that crack cleavage will occur in these atomic models easier than in those cases with higher temperatures. In Group 2 (15 K, 20 K, 30 K, 50 K, 100 K), the toughness increased significantly as the temperature increased, but when the temperatures was not less than 200 K (e.g. 200 K, 300 K, 400 K, and 500 K), the toughness increased to about 0.5 $N.m.m^{-3}.10^{-9}$. This observation indicated that when the temperature was equal to or higher than 200 K, the samples behaved in a similar way to impede crack propagation.

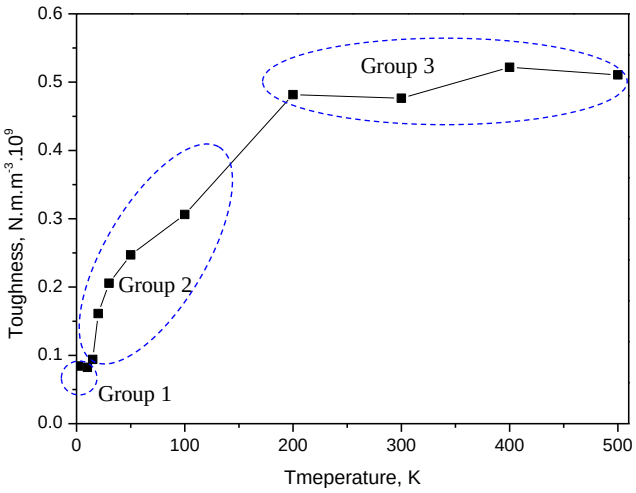

Figure 4.2 Toughness-temperature curve for tensile deformation.

The temperatures of 1.1 K, 20 K, and 500 K that correspond to temperatures in Group 1, Group 2, and Group 3 shown in Figure 4.2, respectively, were chosen to inspect facture deformation based on the atomic view. Figure 4.3 shows a series of snapshots of atomic configuration for crack propagation during tensile deformation under 1.1 K, 20 K, and 500 K. Three stages for each temperature are shown in Figure 4.3. Figure

4.3(a1) shows a strain of 2.28% before the onset of crack propagation, albeit crack remained stationary, but when the strain increased to almost 2.34%, which corresponded to the peak of the stress-strain curve (see Figure 4.1), the crack began to grow along the TB between the T_3 and M_4 crystals. As Figure 4.3(a2) shows, at ε = 2.52% the crack had propagated a long way, and with a strain of ε = 2.70%, the crack had propagated through the entire atomic model, leaving a flat cracked surface behind. There is a lot of evidence to show that the crack propagated in a perfectly brittle fashion. During crack cleavage, the stress on all the atoms located on the left-hand size of the crack was released, which led to a decrease in the average stress in the system. This explains why the tensile stress shown in Figure 4.1 dropped sharply after the strain exceeded 2.34%. At a temperature of 20 K, the crack underwent a brittle-to-ductile fracture, at a strain of ε = 2.52% it propagated the same as for 1.1 K where the crack was brittle, but as the strain increased to 2.64%, the dislocation/twin-associated activity dominated the plastic deformation.

As seen in Figure 4.3(b3), a twin below the crack tip, parallel to the TB was formed and the dislocation nucleated in front of the twin region around the crack tip travelled across the M_4 to enter the crystal of T_4 and almost stopped inside the atomic model. The sample failed by surface necking after the incremental imposed strain. At 500 K, dislocation was easily nucleated from the crack tip, so there was no obvious crack propagation during tensile deformation which implies that at this temperature, the fracture was ductile. The following parts will be used to explain the three different types of dynamic fracture modes, such as perfect crack cleavage, brittle-to-ductile transition, and ductile mode.

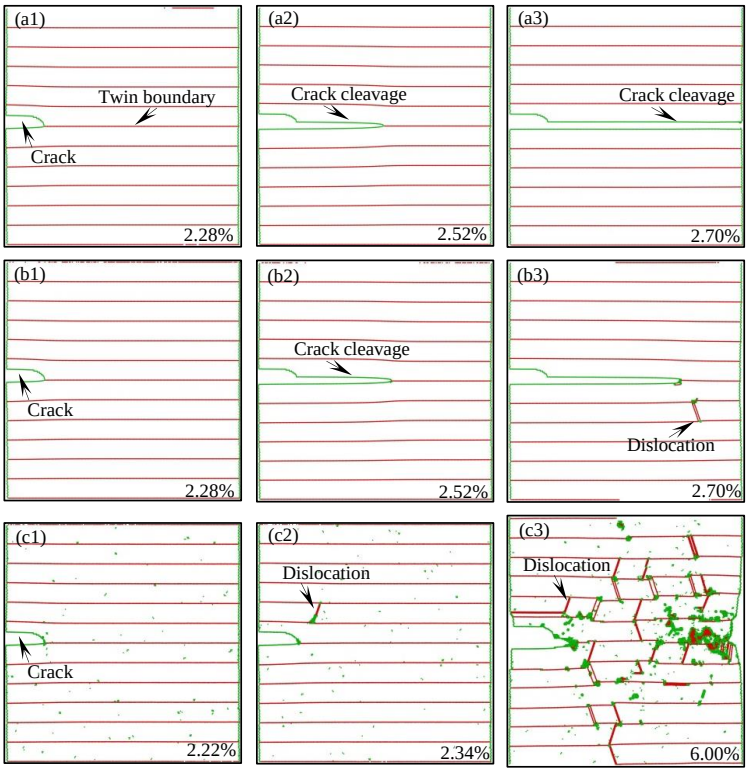

Figure 4.3 Atomistic views of a sequence of snapshots for crack propagation under varying temperatures. (a1-a3) 1 K, (b1-b3) 20 K and (c1-c3) 500 K corresponds brittle fracture (non-dislocation activity), brittle-to-ductile fracture transition (mixed non-dislocation and dislocation activity), and ductile fracture (dislocation activity), respectively. Atoms are coloured based on CNA method. Here, perfect fcc atoms are filtered.

4.3.2 Crack cleavage

A deeper understanding of crack cleavage can be seen in the sequence of snapshots of atomic configuration around the crack tip (see Figure 4.4). A slice with a regime of $10.55 \leq Z \leq 13.05$ Å in the Z direction was used to describe the crack propagation process. Figure 4.4(a1-d1) shows the atomic configurations based on the CNA method. In Figure 4.4(a2-d2), and (a3-d3), the atoms were assigned a colour according to the tensile stress and stress triaxiality, the two crucial factors involved in atomic breakage. As described in Chapter 3, crack cleavage was preceded by two adjacent planes perpendicular to the Y direction but separate from each other. Several

atoms around the crack tip were selected for analysis. They were marked Group-A atoms, and labelled A1, A2, A3, A4, located on a plane above the TB between T_3 and M_4; while the other four atoms (Group-B), labelled B1, B2, B3, B4 are located exactly on this TB. Figure 4.4 shows that the high stresses concentrating at this region covering Group-A and Group-B atoms, and the highest value of σ_y was always associated with the atom in front of the crack tip; this was exactly the same as those cases in nanotwinned copper model. Other Atoms labelled C/C′, D/D′, E/E′, F/F′ located near the crack tip were also marked.

In Figure 4.4(a2), the Atom A1 had the largest σ_y and Atoms B1 and B2 had the largest stress triaxiality. The shape of the crack was constructed by Atoms C, D, E, F, and as the plastic strain increased up to ε = 2.44575%, Atom A1 moved up and Atom B1 moved down, as shown in Figure 4.4(b). The distance between A1 and B1 and the distance between B1 and A2 increased significantly and the position of maximum σ_y transferred to Atom B1. The largest stress triaxiality on atoms then changed to the positions of Atoms A2 and B2, and the crack tip shifted its shape to the structure connected by Atoms C′, D′, E′, and F′. This indicated that the crack tip had moved forwards along the X axis, but as the strain continually increased to ε = 2.44620% and ε = 2.44755%, the largest σ_y transferred to the positions of Atom A2 and Atom B2 (see Figure 4.6(c), and (d)), respectively, while the atomic position with the largest stress triaxiality kept on moving in the direction of crack propagation. This means that when the plastic strain reached a critical value, the atomic bonds began to break in the regions of highest stress concentration. This observation is consistent with continuum theory [211]. The simulation results validated the fact that three criteria for cleavage fracture must be satisfied: (1) $\sigma_{tri} \geq \sigma_{tri\_crit}$ to prevent the crack tip from blunting; (2) $\sigma_y \geq \sigma_{y\_crit}$ for propagating the crack; and (3) $\varepsilon_p \geq \varepsilon_{p\_crit}$ for initiating a crack nucleus where σ_{tri_crit}, σ_{y_crit}, ε_{p_crit} is the critical value of stress triaxiality, tensile stress and localised deformation.

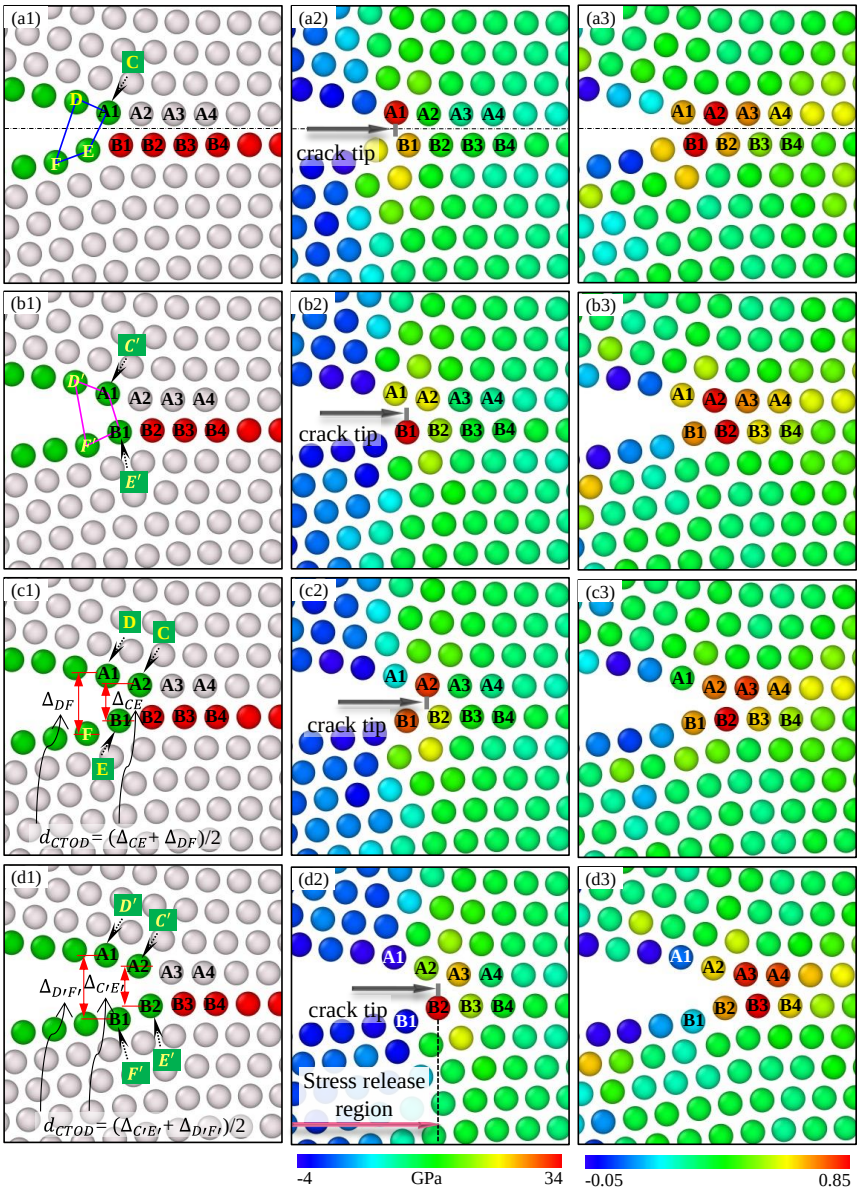

Figure 4.4 Field contours of stress indicators distribution just before the onset of dislocation nucleation nearby the crack tip at (a) ε = 2.44470%, (b) ε = 2.44575%, (c) ε = 2.44620%, (d) ε = 2.44755%. (a1-d1) CNA, (a2-d2) σ_y, (a3-d3) σ_{tri}.

The tensile stress along the Y direction provided the driving force for the crack to propagate, and it relationship with the various strains for the Group-A and Group-B atoms was plotted in Figure 4.5(a). Here, all the curves had a similar trend where σ_y gradually increased to a peak value, and then decreased to almost zero. It was noted that the peak stresses of the Group-B atoms were higher than the Group-A atoms, and

the tensile stress-strain curves for each two groups of neighbouring atoms has an intersection, such as Points I_1, I_2, I_3, I_4, I_5. Between each two Points, one group's atom was always σ_y, being equal to the maximum σ_y of the whole system, and it means that one such group atom is the main driving atom for the atomic bond breaking. For example, between Point I_1 and Point I_2, Atom A1 had the maximum tensile stress, and it was larger than Atom B1, but this was reversed when Atom B1 has larger σ_y beyond Atom A1 after the strain exceeded Point I_2 (ε = 2.44515%). As the σ_y of Atom B1 increased to a peak value it soon decreased to a lower level. To the right side of Point I_3 (ε = 2.4468%), Atom B1 gave way to Atom A2 who had the largest σ_y of all the atoms. At the same time the σ_y of Atom B2 increased continuously as the strain increased during this period, but after the curves of Atom A2 and Atom B2 interacted at Point I_4, the largest σ_y changed to Atom B2. All these atoms A1→B1→A2→B2→A3⋯, involved in the events of changing the largest σ_y were always in front of the crack.

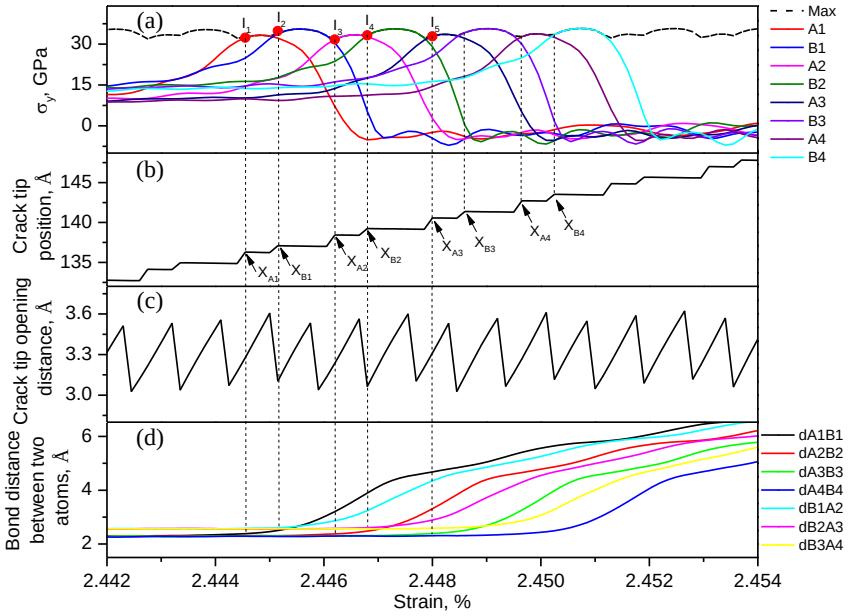

Figure 4.5 Simulation results of selected atoms at 1.1 K: (a) σ_y; (b) crack tip position; (c) crack tip opening distance (CTOD); (d) bond distance between a Group-A atom and a Group-B atom.

Figure 4.5(b) shows the crack tip position as a function of the imposed strain based on the results of Figure 4.5(a). Atom A1 had the largest σ_y between Point I_1 and Point I_2. The crack tip was located at Atom A1 (X_{A1}), as seen in Figure 4.4(a). Returning to Figure 4.4(b) and Figure 4.5 (a), Atom B1 had the largest σ_y between Point I_2 and I_3, which indicated that the crack tip had moved to the position of Atom B1 (X_{B1}). Similarly, the crack tip then moved to the positions of X_{A2}, X_{B2}, X_{A3}, X_{B3} ⋯. With this approach the position of the crack tip can be traced automatically.

The crack tip opening displacement (CTOD) can be used to estimate the fracture toughness of brittle fracture, but because the shape of the crack tip changed during the crack cleavage process, defining the opening displacement [219] of the crack tip is difficult because the crack profiles must be determined due to local disturbances from variations at the crack tip such as bond breaking, bond healing, crack path, rearrangement of local structure, and the thermal fluctuation of local atoms' position. Here, the CTOD was defined using the equation: $d_{CTOD} = (\Delta_{CE} + \Delta_{DF})/2$ (or $d_{CTOD} = ((\Delta_{C'E'} + \Delta_{D'F'}))\ /\ 2$). Figure 4.5(c) shows the relationship of CTOD against the imposed strain where the CTOD varied periodically with the strain. The up and down serration were caused as the shape of the crack tip shifted. The peaks of the CTOD--strain curve show the approximate constant values with 3.5～3.6 Å, which indicates that the CTOD tends to maintain a small and constant value after brittle fracture began at the typical brittle cleavage stage. This differed from the ductile fracture where the CTOD apparently increased with the crack cleavage [104].

Figure 4.5(d) shows the bond distance between Group-A atoms and Group-B atoms. The bond distance changed as a result of highly concentrated local stresses at the crack tip, which corresponded perfectly to Figure 4.5(a). The bond distance had an obvious increase because the atomic bonds between one Group-A atom and one Group-B atom broke. In Figure 4.5(a), at Point I_1, Atom A1 has the largest tensile

stress in the atomic system. At that moment, Atom A1 was the main driving atom, and it can see that Atom A1 moved up and Atom B1 moved down as d_{A1B1} began to increase. After Point I_2, Atom B1 had more tensile stress than Atom A1, and Atom B1 became the driving atom for the bonds between Atom B1 and Atom A2 breaking. Moreover, d_{B1A2} initially increased at Point I_2, which means the process of brittle fracture in nanotwinned Ni was exactly the same as the results seen in the nanotwinned Cu in Chapter 3.

As discussed above, if the concentrated stresses ahead of the crack tip are always big enough during tensile deformation, especially for the indicators of tensile stress and stress triaxiality, they cause the atomic bonds to break in specific cleavage planes. The schematic diagram of a perfect atomic cleavage in nanotwinned Ni could also be described from the point of geometric configuration, as shown in Figure 4.6, where this crack cleavage process can be generalised to the atomic bond breaking in both $\{111\}_M/\{111\}_T$ and $\{100\}_M/\{100\}_T$ planes. Two Group atoms (Group-A and Group-B) were marked around the crack tip (see Figure 4.4). Due to the closely packed atomic arrangement in the $\{111\}_M/\{111\}_T$ plane, the linkage between Atom A1 and Atom B1 at the crack tip normally broke first under the large local tensile stress along the $\langle 112\rangle_T$ direction with distance *d1* (see Step 1 in Figure 4.6(a)); this led to an instant relaxation of stress in the local region along $\{111\}_T$ plane. The stresses gradually accumulated to the right side of the local region covering Atom B1 and Atom A2 in $\{100\}_T$ plane, but when stresses became large enough, the linkage between Atom B1 and Atom A2 de-bonded in the $\langle 110\rangle_T$ direction in the $\{100\}_T$ plane (see Step 2 in Figure 4.6(b)). Similarly, the stresses continued to concentrate in the neighbouring region covering the bond between Atom A2 and Atom B2 in the $\{111\}_T$ plane, which in turn led to cleavage between Atom B2 and Atom A3. This cascade of atomic bond cleavages at the crack tip means that the crack propagated in a completely brittle manner, with no dislocation movement during crack propagation. It

should be noted that the atomic cleavage by way of Step 1 and Step 2 shown in Figure 4.6(a-b), may have occurred concurrently if the stress components were large enough.

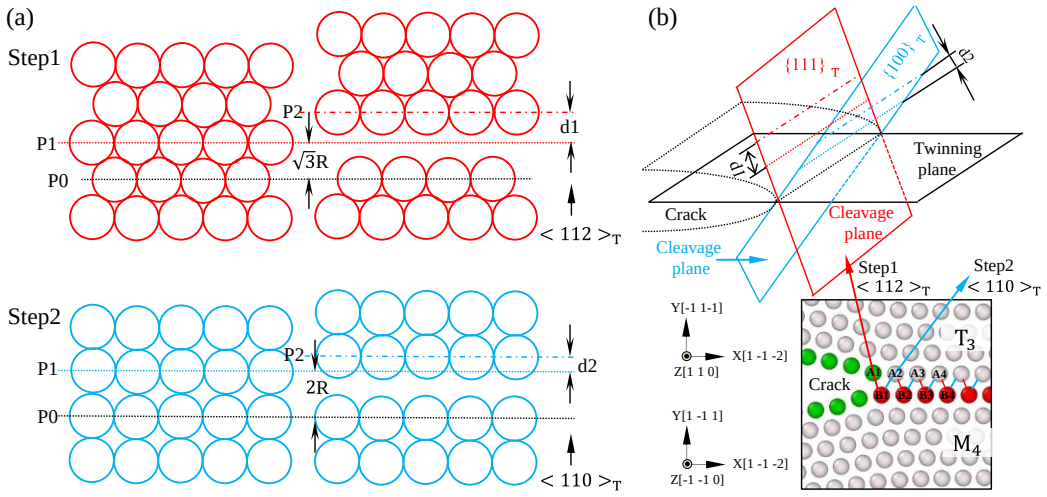

Figure 4.6 Schematic diagram of a perfect atomic cleavage in the $\{111\}_M/\{111\}_T$ and the $\{100\}_M/\{100\}_T$ planes, resulting in a brittle fracture. (a)-(b) Atomic cleavage by two ways of Step 1 and Step 2 in the $\{111\}_M/\{111\}_T$ and the $\{100\}_M/\{100\}_T$ planes. *R* is the radius of the atom. Red and cyan lines represent the tracks of crack cleavage in the $\{111\}_M/\{111\}_T$ and $\{100\}_M/\{100\}_T$ planes, and *d1*, *d2* is the corresponding bond distance in the $\{111\}_M/\{111\}_T$ and $\{100\}_M/\{100\}_T$ plane, respectively. *P0*, *P1* and *P2* are the referrence planes.

4.3.3 Brittle-to-ductile transition

Figure 4.7 shows the crack length as a function of the applied strain for cases with different temperatures. The results of the other cases were not shown because they were similar to the cases already presented. The sloping and parallel lines represent the results of brittle fracture and ductile fracture, respectively. The data in Figure 4.7 was saved for every 5 simulated steps to monitor the position of the crack tip using the approach discussed in Figure 4.5(b) where the length of the crack depended on the temperature. In the 1.1 K and 10 K cases, the crack propagated with perfect brittle fracture during plastic deformation and increased in length with the increasing strain

after the crack began to cleave, until the atomic model completely separated. For the 15 K, 20 K, and 50 K cases there was a dynamic brittle-ductile transition where the fracture propagated in a brittle fashion at the early stage and then changed to a ductile fashion at a critical strain. The critical strains for these three cases were different because the largest critical strain was at a low temperature and the case with a temperature of 500 K exhibited the ductile fracture because the dislocation was emitted easily from the crack tip, leading to almost no crack cleavage. It was noted that for the perfect brittle and brittle-to-ductile facture transition cases, the crack began to propagate earlier along the TB at a higher initial temperature. This finding can be seen in the enlarged image in Figure 4.7 and suggests that thermal fluctuation may assist the atomic bonds breaking for the incipient crack cleavage.

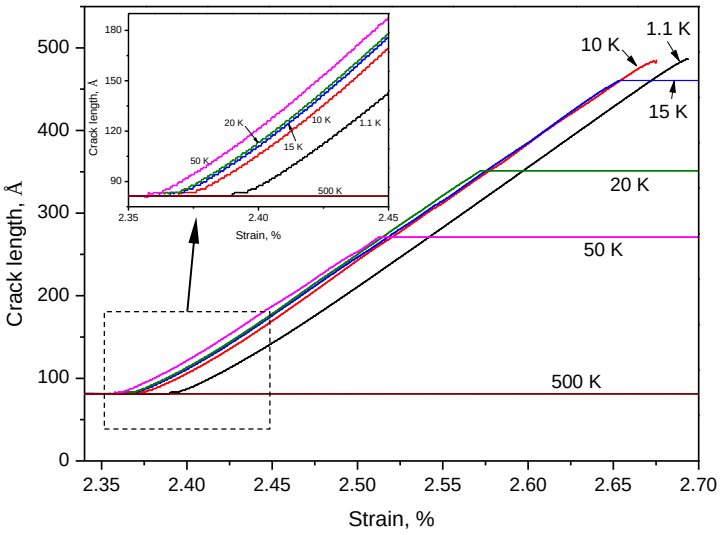

Figure 4.7 Crack length as a function of the imposed strain.

All the 1.1 K, 10 K, 15 K, 20 K, and 50 K cases had a certain period of brittle crack propagation where the slope of the crack length versus strain curve represents the crack propagation speed. Figure 4.7 shows that the crack propagation speed increased from zero with strain and quickly reached a high level. When a brittle crack undergoes transition to a ductile fracture, its speed suddenly drops, although in

comparison to the brittle fracture in nanotwined Cu where the length of the crack did not change very much as the temperatures varied, crack propagation was more sensitive to the temperature in nanotwinned Ni. For the cases where a higher temperature travelled faster than those at lower temperatures, I calculated the average crack propagation speed for strain range of 2.45%~2.475% where the crack propagation almost reached saturation. The speed at which brittle cracks propagated for the 1.1 K, 10 K, 15 K, 20 K, and 50 K cases was 959.029 m/s, 1096 m/s, 1111.327 m/s, 1141.754 m/s, 1173.461 m/s, respectively. The critical Rayleigh sound speed can be calculated by equation: $c_r = 0.93\sqrt{\mu/\rho}$ [203], where μ is the shear modulus and ρ is the density of the material. In this model μ = 77.63 GPa [220] and ρ = 8931 kg/m^3 was chosen, and so the $c_r = 2745.413$ m/s. The propagation of brittle speed in this study appeared to be about $0.35c_r$~$0.43c_r$, which agreed with the findings in MD simulations [207, 221]. The differential brittle crack propagation for cases under varying temperatures suggested that the perfectly brittle crack cleavage is a thermally activated deformation process.

Figure 4.8 plots the curve of crack length versus temperature at an instant strain of 2.7%, and the low temperatures (1.1 and 10 K) show the longest cracks. The crack length decreased significantly as the temperature increased to 15 K, but further increases temperature led to more drops in the crack length (20 K, 30 K, 50 K and 100 K). At temperatures higher than 100 K (200 K, 300 K, 400 K, 500 K), the crack length almost had a constant value equal to the initial crack length. The tendency for crack length versus temperature corresponds to the snapshots of atomic configuration shown in Figure 4.3, and shows there were three groups of fracture behaviour (see Figure 4.3 and Figure 4.8) in nanotwinned Ni crystal subjected to uniaxial tension at various temperatures. In Group 1 the fracture propagated in a perfect brittle mode during the entire simulation period, and the crack surface had a very smooth facet. In Group 2 the fracture exhibited a dynamic brittle-to-ductile transition as the crack

propagated along the TB first, followed by ductile necking failure due to the dislocation-mediated deformation mechanism. In Group 3 the crack propagated in a ductile fracture manner and dislocation was activated early due to a competition over the onset of crack propagation.

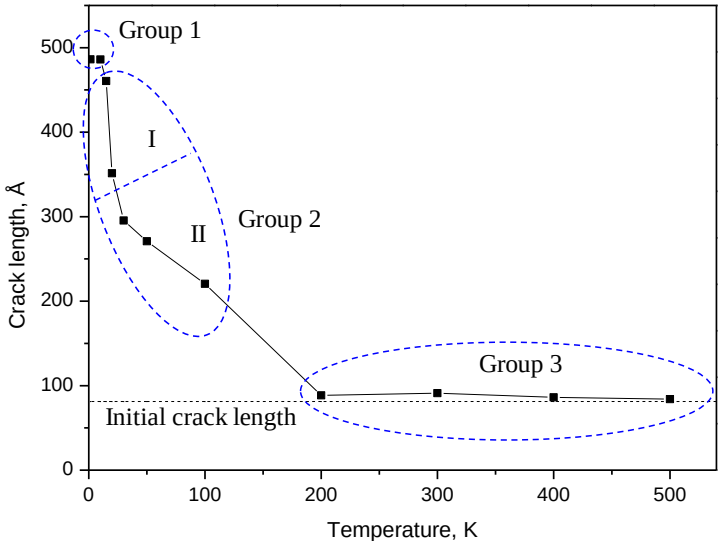

Figure 4.8 Crack length at ε = 2.7% for different temperatures.

4.3.4 Dislocation activity

Figure 4.9 shows the dislocations emitted from the crack tip at 20 K. The simulation cell was rotated to a reasonable spatial position to show more dislocation information. The envelope of the crack surface is represented by a grew-coloured surface and the stacking faults, including the twin boundaries (TBs), are highlighted in red. Different types of dislocations were identified by the various colourful solid lines. It can be seen that at an imposed strain of 2.565%, just before the initial nucleation of dislocation, the crack still propagated in a brittle mode without any dislocations. The envelope of the crack surface is relatively smooth, but as the strain increased to 2.58%, a new TB parallel to the surface envelope of the crack tip was nucleated below the crack tip. It was noted that the crack tip blunts were wider and the crack tip front became more curved. The newly formed TB spanned across the atomic configuration

in the Z direction and extended a little wider in the X direction during the subsequent deformation.

At a strain of 2.58555% shown in Figure 4.9(c), two dislocations were nucleated from the crack tip; the $1/2\,[1\bar{1}0]_{\mathrm{M}}$ perfect dislocation in $(1\bar{1}0)_{\mathrm{M}}$ plane coupled with the Shockley partial dislocation in $(\bar{1}\bar{1}1)_{\mathrm{M}}$ and $(111)_{\mathrm{M}}$ slip planes. These dislocations grew to form a more complicated structure than the single nanotwinned Cu crystal where only a single perfect dislocation of $1/2\,[1\bar{1}0]_{\mathrm{M}}$ was emitted from the crack tip first. The $1/2\,[1\bar{1}0]_{\mathrm{M}}$ perfect dislocation combined with the $1/6\,[1\bar{2}\bar{1}]_{\mathrm{M}}$ trailing partial and the $1/6\,[2\bar{1}1]_{\mathrm{M}}$ leading partial dislocations moved collectively towards the TB between the M_4 and T_4 gains, while the $1/6\,[2\bar{1}1]_{\mathrm{M}}$ partial dislocation connected to the $1/6\,[\bar{1}2\bar{1}]_{\mathrm{M}}$ partial dislocation constructed a V-shaped defect structure. At the interaction of these two slip plane stacking faults a $1/6\,[110]_{\mathrm{M}}$ stair-rod dislocation was formed. This structure has been seen before in a single nanotwinned Cu crystal at 40 K. This new finding of a perfect dislocation on the (001) plane excluded the usual way that Shockley partial dislocations are emitted from the crack tip. By analysing the MD results, it can be concluded that specific types of dislocations not only depend on the detailed initial atomic configuration, but also on the detailed local atomic configuration state at an instant strain event when the onset of dislocation core occurs.

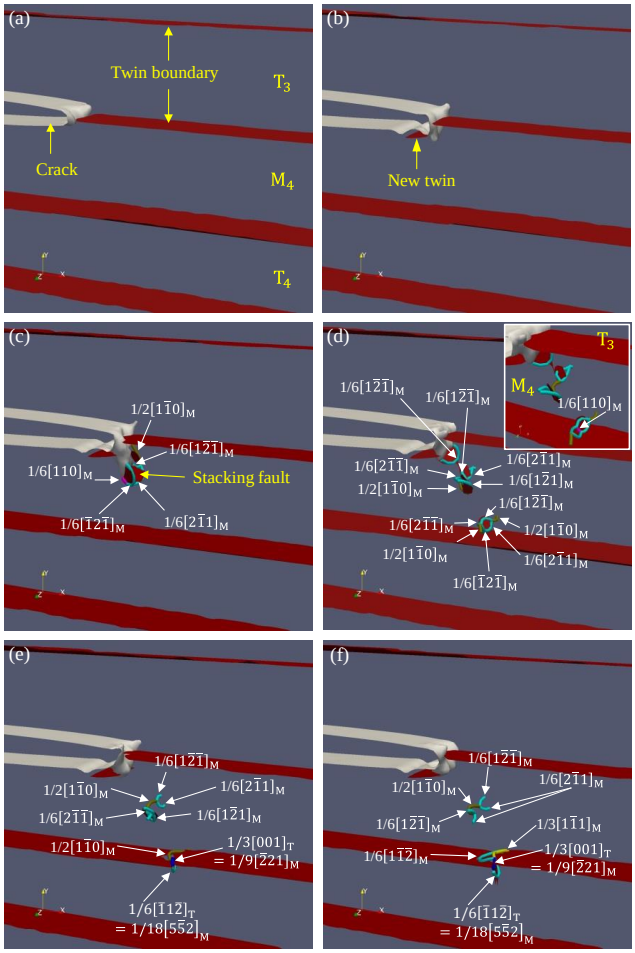

Figure 4.9 Dislocation activities around the crack tip for the 20 K case: (a) ε = 2.565%; (b) ε = 2.58%; (c) ε = 2.58555%; (d) ε = 2.6001%; (e) ε = 2.6046%; (f) ε = 2.60655%.

As Figure 4.9(d) shows, this defect structure connected by the $1/2\,[1\bar{1}0]_M$ perfect dislocation, stair-rod dislocation $1/6\,[110]_M$ and three Shockley partial dislocations shown in Figure 4.9(c) quickly propagated through the Matrix crystal, followed by the $1/6\,[2\bar{1}\bar{1}]_M$ trailing partial dislocation gliding on the $(111)_M$ plane. Another similar structure with a $1/2\,[1\bar{1}0]_M$ perfect dislocation on the $(001)_M$ plane linked by the $1/6\,[2\bar{1}1]_M$ leading partial and $1/6\,[1\bar{2}\bar{1}]_M$ trailing partial dislocations on $(\bar{1}\bar{1}1)_M$ plane, and by the $1/6\,[1\bar{2}1]_M$ leading partial and $1/6\,[2\bar{1}\bar{1}]_M$ trailing partial dislocations on $(111)_M$ plane was formed and moved down to repeat the same path as the first defect structure. From Figure 4.9(d) it can be seen that a new $1/6\,[1\bar{2}\bar{1}]_M$ partial has now nucleated on the $(111)_M$ plane. Note that the newly formed

$1/6\,[1\bar{2}\bar{1}]_{\mathrm{M}}$ dislocation did not move away from the crack tip immediately as the strain increased, it was being reabsorbed into crack tip.

The defect structure consisting of the $1/2\,[1\bar{1}0]_{\mathrm{M}}$ perfect dislocation on the $(001)_{\mathrm{M}}$ plane and other Shockley partials dislocation on $(\bar{1}\bar{1}1)_{\mathrm{M}}$ and $(111)_{\mathrm{M}}$ planes were unstable because they evolved into a single $1/2\,[1\bar{1}0]_{\mathrm{M}}$ perfect dislocation on the (001) before approaching the TB. When the $1/2\,[1\bar{1}0]_{\mathrm{M}}$ perfect dislocation interacted with the TB, one part of this dislocation split into a $1/6\,[\bar{1}1\bar{2}]_{\mathrm{M}}$ partial dislocation on the $(1\bar{1}\bar{1})_{\mathrm{T}}$ plane, and the sessile $1/3\,[001]_{\mathrm{T}}$ dislocation on the TB. These two dislocations were equal to $1/9\,[\bar{2}11]_{\mathrm{M}}$ and $1/18\,[5\bar{2}2]_{\mathrm{M}}$ and were presented by the Miller index of the M_4 crystal, respectively. The perfect dislocation transmitted across the TB into T_4 [122, 128]. Another alternative option for the dislocation-twin reaction is that part of the $1/2\,[1\bar{1}0]_{\mathrm{M}}$ perfect dislocation dissociated into the $1/3\,[1\bar{1}1]_{\mathrm{M}}$ Frank partial dislocation at a coherent TB, while a $1/6\,[1\bar{1}\bar{2}]_{\mathrm{M}}$ Shockley partial dislocation was gliding along the TB [180, 185]. This latter dislocation motion indicated that the cross-slip of dislocation occurred at the TB [155, 183], and led to either a twinning or a detwinning process. $1/3(1\bar{1}\bar{2})[1\bar{1}1]_{\mathrm{M}}$ is one kind of sessile stair-rod dislocations at the TB, but it was further dissociated into a $1/6\,[1\bar{1}\bar{2}]_{\mathrm{M}}$ Shockley partial dislocation and a $1/2\,[1\bar{1}0]_{\mathrm{M}}$ perfect dislocation (not shown in Figure 4.9).

Figure 4.10 shows the activities of dislocations emitted from the crack tip at 50 K. The stacking faults in enlarged images around the crack tip in Figure 4.10(d), and (e) were removed to gain clearer views of the dislocation details. At ε = 2.49075%, the crack propagated in a brittle fashion and its front remained straight, but as the imposed strain increased to 2.5095%, the crack front began to curve, leading to the formation of some tiny ledges on it. The crack tip blunted increasingly and the crack tip almost ceased to grow along the TB, but when the strain increased to 2.51685%,

two defective structures were distributed up and below the central TB and emitted around the ledges into the Matrix and Twin crystal. In Figure 4.10(c), a stair-rod dislocation with a Burgers vector of $1/6\,[110]_T$ was connected by a $1/6\,[2\bar{1}1]_T$ partial dislocation on $(\bar{1}\bar{1}1)_T$ plane and a $1/6\,[\bar{1}2\bar{1}]_T$ partial dislocation on $(111)_T$ plane was formed in the T_3 crystal. On the other side, another stair-rod dislocation with a Burgers vector of $1/6\,[110]_M$ was connected by a $1/6\,(\bar{1}\bar{1}1)[2\bar{1}1]_M$ partial dislocation and a $1/6\,(111)[\bar{1}2\bar{1}]_M$ partial dislocation was nucleated in the M_4 crystal. As the imposed strain increased, these two defective structures inside the twin grains continued to increase, giving rise to a rather complex V-shaped structures involving a type of dislocation-dislocation process on different slip systems. As seen in Figure 4.10(d), two trailing Shockley partial dislocations of $1/6\,(\bar{1}\bar{1}1)[\bar{1}21]_M$ and $1/6\,(111)[2\bar{1}\bar{1}]_M$ were nucleated from the crack tip.

When the trailing partial dislocations joined the overlapped pair by the stair-rod dislocation and the leading partial dislocations, a new $1/6[1\bar{1}0]_M$ perfect dislocation was formed near the TB (see Figure 4.10(e)). The dislocation structures consisted of various types of dislocation-dislocation interplays, as shown in the T_3 grain in Figure 4.10(e). Those interactions include: (a) $1/6[2\bar{1}1]_T + 1/6[\bar{1}2\bar{1}]_T \rightarrow 1/6[110]_T$; (b) $1/6[2\bar{1}\bar{1}]_T + 1/6[\bar{1}21]_T \rightarrow 1/6[110]_T$; (c) $1/6[2\bar{1}1]_T + 1/6[\bar{2}11]_T \rightarrow 1/3[001]_T$; (d) $1/6[1\bar{2}1]_T + 1/6[\bar{1}21]_T \rightarrow 1/3[001]_T$. They subsequently combined to form a $1/2[1\bar{1}0]_T$ perfect dislocation structure before interacting with the TB between M_4 and T_3 crystals. In Figure 4.10(f), the representative of ε = 2.5575%, $1/2[1\bar{1}0]_T$ perfect dislocation reacted with the pre-existing TB and resulted in a $1/6[1\bar{1}\bar{2}]_M$ (or $1/6[1\bar{1}\bar{2}]_T$) Shockley partial dislocation gliding along the TB, and a $1/3[1\bar{1}1]_M$ (or $1/3[1\bar{1}1]_T$) Frank partial dislocation being pinned on the TB. Such cross-slip dislocation motion onto the TB created a step on this TB that contributed to the TB migrating. Unlike the observation shown in Figure 4.10(e), and (f), no components of Shockley partial dislocations transmitting the TB were seen as the imposed strain

increased. It is of great interest to see that another V-shaped defect structure was proceeding through the T_3 crystal.

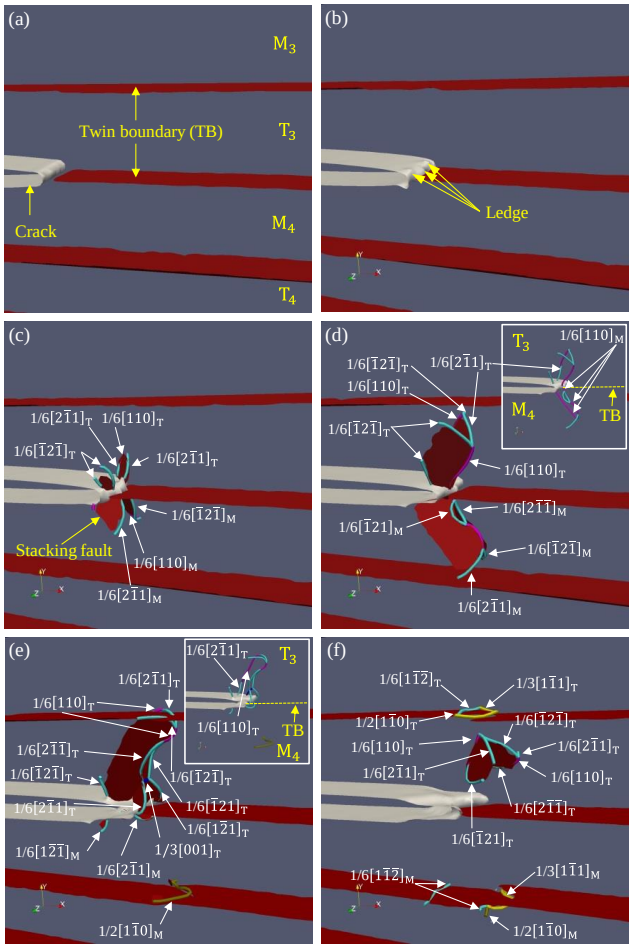

Figure 4.10 Dislocation activities around the crack tip for the 50 K case: (a) ε = 2.49075%; (b) ε = 2.5095%; (c) ε = 2.51685%; (d) ε = 2.52945%; (e) ε = 2.5395%; (f) ε = 2.5575%.

Figure 4.11 shows the activities of dislocations emitted from the crack tip at 500 K. Unlike the 20 K and 50 K cases, the case with 500 K crack had almost no propagation, but at about ε = 2.3103%, ledges were nucleated at the crack front, and a V-shaped defect structure like the structure described earlier in Figure 4.9 and Figure 4.10, was subsequently emitted at the ledge regions into the T_3 crystal (see Figure 4.11(c) of ε = 2.31975%). More successive trailing partial dislocations with Burgers vectors of $1/6[2\bar{1}\bar{1}]_T$ and $1/6[\bar{1}21]_T$ were nucleated to join the V-shaped defect structure,

forming a more complex defect structure (see Figure 4.11(d)). This defect structure passed through the T_3 grain until it met the next TB between T_3 and M_3 crystals and then annihilated as a $1/2[1\bar{1}0]_T$ perfect dislocation near the TB, as seen in Figure 4.11(e). When this perfect dislocation impinged the TB, it resulted in a cross-slip event by a Shockley partial dislocation gliding on the TB, and a Frank partial dislocation pinning on the TB (see Figure 4.11(f)).

Based on the analysis of Figure 4.9-Figure 4.11, the results showed that the plastic deformation softening mechanism was not just attributed to the TB migration that came from the results of dislocation nucleation at the TB [9], it was also attributed to the TB migration from a dislocation across the TB [127]. This was because both the cross-slip and transmission events during the dislocation-twin interaction can leave a pair of steps behind on the TB, which severs further as the sources for dislocation nucleation and emission in the TB contribute to the TB migration A comparison between Figure 4.9 and Figure 4.10, shows that the brittle-to-ductile fracture transition was associated with two types of deformation mechanism. The first type was where the occurrence of local phase transformation around the crack tip caused a twin formation which triggered the brittle-to-ductile fracture transition. Another type was the formation of ledge at the crack front which contributed to the brittle-to-ductile fracture transition. Therefore, the Group 2 region shown in Figure 4.8 can be further divided into two regions where Region I with a temperature of 15 K, and 20 K exhibited a dynamical brittle-to-ductile transition, and Region II with temperatures ranging from 30 K to 100 K exhibited a thermal fluctuation/dynamical-associated brittle-to-ductile transition. Above all, the different types of dislocations emitted from the crack tip at different temperatures in nanotwinned Ni, eventually led to a brittle-to-ductile fracture transition. In the following paragraphs, the atomic mechanism responsible for this dislocation nucleation is discussed.

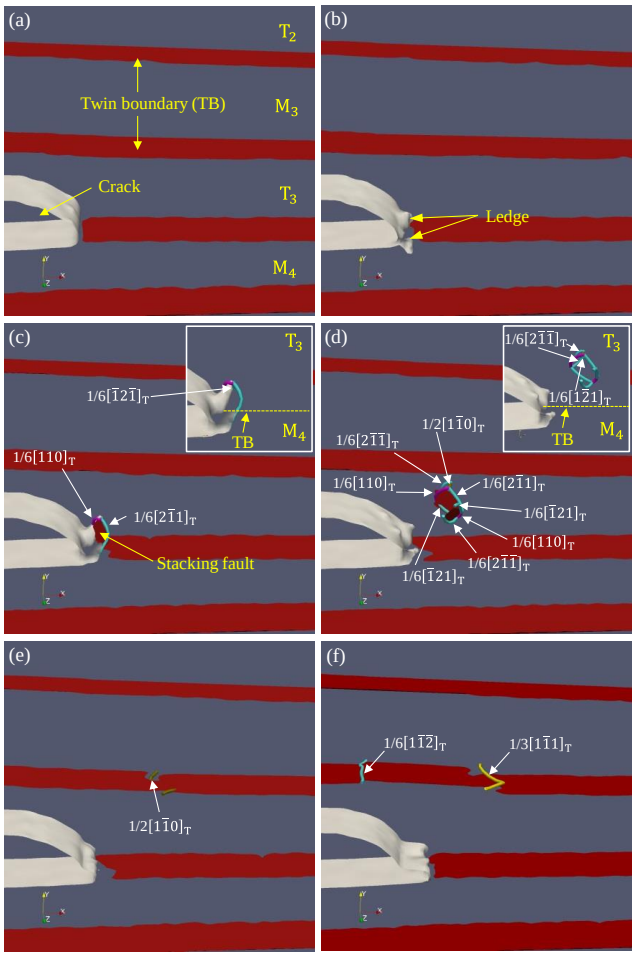

Figure 4.11 Dislocation activities around the crack tip for the 500 K case: (a) ε = 2.22%; (b) ε = 2.3103%; (c) ε = 2.31975%; (d) ε = 2.33925%; (e) ε = 2.352%; (f) ε = 2.3904%.

4.3.5 Phase transformation

In Figure 4.12, it was displayed a two-layer (110) stacking sequence of the simulation cell. Figure 4.12(a1-a5) shows the atomic configuration around the crack tip for two successive (110) planes, with their colour being set according to the Z direction coordinates of atoms. These two planes (the first (110) plane and the second (110) plane) were initially located at positions Z = 11.18 Å and Z = 12.44 Å. They are represented by near-blue and near-red colours, respectively, as shown in Figure 4.12(a1-a5). Figure 4.12(b1-b5) shows the same atomic configuration as Figure 4.12(a1-a5), but they have a different colouring method to distinguish the local crystal structure around each atom based on the CNA method. The perfect fcc and hcp atoms

are grey and yellow, respectively, and the free surface atoms or disorder atoms are green. Both the TB and intrinsic stacking fault are shown as the hcp structure. Four groups of atoms labelled A_1~A_8, B_1~B_8, C_1~C_8, and D_1~D_8, were marked in Figure 4.12(a1), respectively, where the Group-A atoms sit on the $(1\bar{1}1)_T$ plane above the TB between the T_3 and M_4 crystals, and the Group-B, Group-C, and Group-D atoms sit on the neighbouring $(\bar{1}1\bar{1})_M$ planes below the TB, and between the T_3 and M_4 crystals.

In Figure 4.12(a1) with a strain of 2.5665%, Atoms C_2, B_3, C_4, and D_4 were initially located on the same (110) plane while Atom C_3 was on the closest neighbouring (110) plane. Atoms C_2, B_3, C_4, and D_4 constructed 4 vertices for a basic fcc cell in the (110) plane; this is the square region coloured yellow. It is noteworthy that Atom C_3 was formerly located at the second (110) plane, and changed from the near-red in Figure 4.12(a1) to the near-green in Figure 4.12(a2), indicating that this atom moved from the second (110) plane towards the first (110) plane along the negative Z direction, with the result that Atom C_3 attempted to squeeze into the space surrounded by Atoms C_2, B_3, C_4, and D_4, This resulted in the fact that five atoms C_2, B_3, C_4, D_4 and C_3 were roughly located at the same (110) plane. A careful examination revealed that this occurred in nanotwinned Cu crystal (in Chapter 3). A base-centred orthorhombic structure has been locally formed with lattice constants a = 4.14 Å, b = 2.40 Å and c = 2.49 Å. This newly formed phase structure was unstable because of the stretching space between atoms (e.g. Atoms B_4 and D_4) in front of the region of Atoms B_3 and D_3 increased, and these atoms (e.g. Atom B_2 and B_3) to be left of the crack tip atoms (e.g. Atom B_4) sprang back towards the left hand side of the M_4 crystal as the imposed strain increased. As Figure 4.12(a3) shows, the space between B_4 and D_4 increased sharply, which induced the C_4 atoms to jump from the first (110) plane to the neighbouring (110) plane, which is equivalent to the second (110) plane along the negative Z direction. That means that more local phase transform occurred

due to the C_4 shuffling to a new (110) plane. Atom C_5 shuffled from the second (110) plane to the first (110) plane at ε = 2.5755%. This motion can be identified by the change of colour from the near-red to near-blue. The consequence of these activities was that a TB formed at D_4 (see Figure 4.12(a4), (b4)).

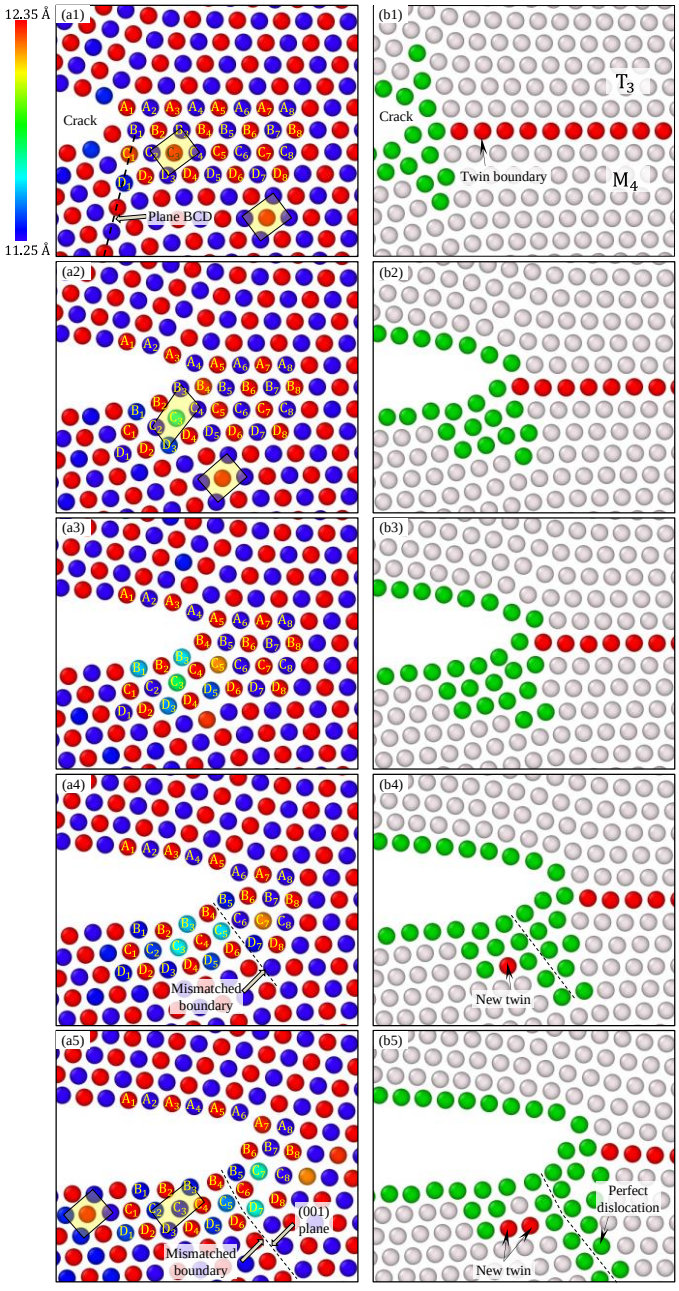

Figure 4.12 Atomic configuration (a1-a5) and local crystal structure (b1-b5) around the crack tip for two successive (110) planes at different strains at 20 K: (a1-b1) ε = 2.5665%; (a2-b2) ε = 2.57115%; (a3-b3) ε = 2.57265%; (a4-b4) ε = 2.5755%; (a5-b5) ε = 2.57895%.

Similarly, as the imposed strain increased to ε = 2.57895%, an extended width of TB structure in the X direction was formed at the crack tip (see Figure 4.12(b5)) due to the Z direction's movement of Atom C_6 and Atom C_7. The newly formed TB structure was approved to shield the atom at the crack tip and impede its stress concentrating at the crack tip, leading to an incremental crack tip blunting and almost no atomic bonds breaking around the crack tip. Figure 4.12(a5) and (b5) shows that Atoms B_2, C_3, B_3, C_4, B_4, C_5 make up a newly twinned region relative to the M_4 crystal. This newly twinned region has a mismatched boundary with M_4, as marked in Figure 4.12(a5), and (b5). This mismatched boundary is a weak link where sliding can easily occur under straining, and therefore as the imposed strain continues, the relative movement at the mismatched boundary can trigger the nucleation of a perfect dislocation on the (001) plane, which leads to the dislocation activity observed in Figure 4.9. The underlying reason for the dislocation nucleation associated with the local phase transformation and twin formation around the crack tip in nanotwinned Ni is exactly the same as the reasons discussed previously for nanotwinned Cu. For more detailed information please return to the descriptions of nanotwinned Cu given in Chapter 3. However, we should keep the discrepancy between them in mind such that in nanotwinned Cu, only the $1/2\,[1\bar{1}0]_M$ perfect was nucleated from the mismatched region (i.e. (001) plane), while in nanotwinned Ni a mixture of dislocation activities by the Shockley partial dislocation were being nucleated on the $\{111\}$ planes and the $1/2\,[1\bar{1}0]_M$ perfect was being nucleated at the mismatched boundary (i.e. (001) plane). I calculated the Schmid factors for different slip systems and found that the two best slip systems for dislocation nucleation were the $\{001\}$ planes with Schmid factors of 0.47, and the $\{111\}$ planes with Schmid factors of 0.31. This was because during the formation of twin, a series of ledges can form near the mismatched boundary or crack tip, which further activates the Shockley partial dislocations nucleation and emission on the $\{111\}$ main slip planes. In other words, the atomic lattice around the crack tip may be rearranged by the atoms shuffling and rotating

once the new local twin/phase transformation was generated. All these mean that the detailed dislocation nucleation did not depend on just the initial atomic structure, it also depended on the current atomic configuration after the complex atomic motions of shuffling and rotation under the imposed strain. These findings indicated that the twin/phase transformation-induced dislocation activity was a new kind of mechanism for the formation of twin in nanotwinned fcc metals. This differs from the previous observations [56, 59] which proposed that deformation twinning at the crack tip was formed by successive Shockley partial dislocations nucleating on the adjacent {111} slip planes. The another intriguing finding is that the dislocation with Burgers vector of $1/2\,[1\bar{1}0]$ nucleated first on the (001) plane, rather than the Shockley partial dislocation that nucleated on {111} slip planes, which was not seen in previous MD studies.

4.3.6 Atomic mechanism for dynamic brittle-to-ductile transition

As shown in Figure 4.12, at 20 K, phase transformation occurred around the crack tip accompanied by the formation of twin, which further induced dislocation nucleation in front of the newly formed twin region. Two groups of atoms were used to analyse the phase transformation. Group-B consisted of all the atoms initially located at the TB between T_3 and M_4 crystals, including Atoms B_1-B_8 marked in Figure 4.12(a1). Group-D consisted of all the atoms initially located at the second $(\bar{1}1\bar{1})_M$ plane below the TB between T_3 and M_4. Those Atoms included D_1-D_8 (see Figure 4.12(a1)). It was known that the maximum distance (d_{BD}^{max}) between Group-B atoms and Group-D atoms always occurred near the crack tip. Figure 4.13 plots d_{BD}^{max} as a function of the imposed strain at temperatures of 1.1 K, 15 K, and 20 K. These three temperatures shared a common law that the d_{BD}^{max} generally increased with the incremental imposed strain. At 1.1 K, d_{BD}^{max} slowly increased with strain, unlike the 15 K and 20 K, and at 15 K and 20 K, the d_{BD}^{max} quickly increased to a higher level at about ε = 2.57% and ε = 2.64% of strain, respectively, although there was some fluctuation in value of d_{BD}^{max}. We can see that local phase transformation occurred when d_{BD}^{max} reached about 5.6 Å

at both 15 K and 20 K, but it never reached this critical value in the case of 1.1 K, so only perfect brittle crack cleavage occurred at this temperature. Figure 4.13 reveals there was also a critical distance between Group-B atoms and Group-D atoms for phase transformation to occur; this means that as the distance between the Group-B atoms and Group-D atoms increased, the space between the two groups widened, leading to a large attractive force between the atoms at the periphery of the enlarged region. Like Atom B_3 and Atom D_3 shown in Figure 4.12(a2), when the distance between these two atoms increases enough, the attractive force will help Atom C_3 to overcome the energy barrier and fill in this space, resulting in a phase transformation from the fcc structure to the base-centred orthorhombic structure (for more descriptions, refer to Chapter 3).

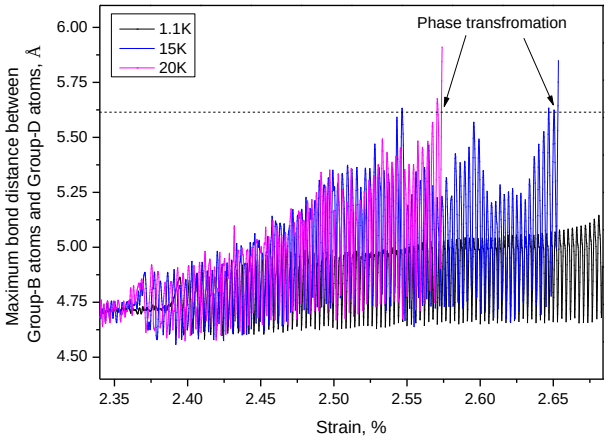

Figure 4.13 Maximum distance (d_{BD}^{max}) between Group-B atoms and Group-D atoms as a function of the strain at 20 K.

Figure 4.14 shows the angle (θ_{BCD}) between the reference plane (Plane BCD) and the X axis as a function of the imposed strain, where Plane BCD cuts through a Group-B atom and a Group-D atom and is parallel to the Z axis (as seen in Figure 4.12). Here the θ_{BCD} generally increased as the strain Increased, although the angles at 15 K and 20 K increased faster than at 1.1 K. With a strain of approximately ε = 2.57% and ε = 2.64%, these two angles reached high values, and the phase transformation that

occurred at these strains corresponded with the critical value of d_{BD}^{max} shown in Figure 4.12. The MD results revealed that the increase of θ_{BCD} was responsible for the increasing d_{BD}^{max}. As described in nanotwinned Cu, the stress of most of the atoms located on the left-hand side of the crack tip was released during crack propagation, causing the lattice to expand along the X direction, but the lattice on the right hand side of the crack kept shrinking along the X direction due to the strain imposed along the Y direction. This led to the Plane BCD rotating slightly to gain a higher θ_{BCD} value as the crack propagated. Moreover, the increasing temperature also induced the Plane BCD to rotate, which created more stretching space between the Group-B atoms and Group-D atoms due to an increasing θ_{BCD} as the crack propagated. This also led to an increasing d_{BD}^{max} as shown in Figure 4.12. The result was that at higher temperatures (e.g. 15 K and 20 K), when the d_{BD}^{max} reached a critical value that stemmed from the increasing θ_{BCD} during crack propagation, local phase transformation would occur, that leads to a final brittle-to-ductile fracture transition. However, at very low temperatures (e.g. 1.1 K), the d_{BD}^{max} never reached the critical value in the present atomic model at the end of the simulation, which meant there was no dynamic brittle-to-ductile transition under those temperatures (similar explanations are given in Chapter 3 on nanotwinned Cu). Figure 4.13 and Figure 4.14 explain the underlying reasons for the occurrence of phase transformation at 20 K.

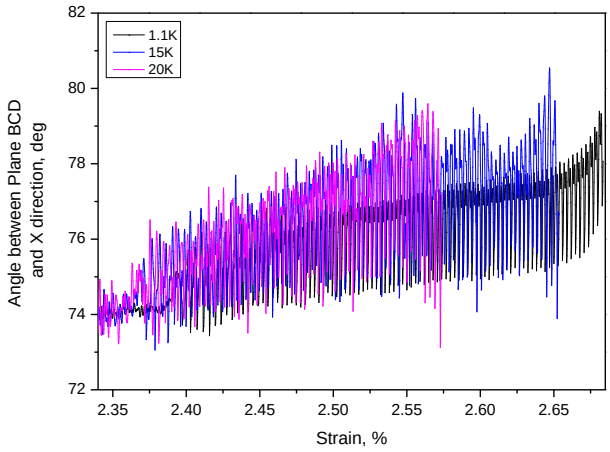

Figure 4.14 Angle (θ_{BCD}) between Plane BCD and the X direction as a function of the strain at 20 K.

At a temperature of 50 K, as shown in Figure 4.10, after an early stage of a perfect crack cleavage process, dislocation activities dominated the deformation mechanism when the strain exceeded 2.515%; this led to the final brittle-to-ductile fracture transition. Unlike at 20 K, local phase transformation accompanied by the formation of twin was not involved in the transition process at 50 K. The dislocation activities were related to the formation of a ledge that formed on the crack tip, and then dislocation nucleated around the ledge (see Figure 4.10(b), and (c)). Figure 4.15 was used to understand the formation of a ledge, and shows two discrete across sections of (110) plane for atomic configurations around the crack tip within the Z ranges of 1.45 Å $\leqslant$ Z $\leqslant$ 3.95 Å (Figure 4.15(a)) and 17.15 Å $\leqslant$ Z $\leqslant$ 19.65 Å (Figure 4.15(b)) at ε = 2.51055%. Figure 4.15(a1-b1) coloured the atoms based on the CNA method, and Figure 4.15(a2-b2) coloured the atoms based on the tensile stress. Two groups of atoms were marked in Figure 4.15(a), A_1'~A_4' and B_1'~B_4'. In Figure 4.15(a), the crack tip is located at Atom A_2', while the crack tip is located at Atom A_3' in Figure 4.15(b). This indicated that the crack front became non-synchronous in the Z direction, i.e., the crack front was not straight, and a series of tiny ledges formed at the crack front, as seen the Figure 4.10(b). A lot of studies have agreed that the ledge could be an effective source for the nucleation of the dislocation core [104, 212] because the formed ledge triggers the dislocations nucleating on it, and are emitted across the T_3 and M_4 crystals (see Figure 4.10(c)). This reason for the formation of a ledge may be attributed to three factors: (i) the large thermal fluctuation at higher temperatures (e.g. 50 K) activates the atomic bonds to break into different crystallographic $[1\bar{1}1]_T$ planes along the Y direction (see the mechanism of ledge formation in Figure 4.15) easier, or break at different positions along the Z direction in the same $[1\bar{1}1]_T$ plane, unlike at 15 K and 20 K; (ii) the wave at the crack front induced the variations in roughness along the crack front due to the wave speeding up and slowing down to distort the crack front and serve as an effective source for dislocation nucleation from the crack tip [212, 222]; (iii) the dynamical instability increased the roughness of the

crack surface as the crack speed increased [36, 223]. By referring back to Figure 4.7, a higher temperature (e.g. 50 K) led to a faster crack propagation speed than the lower temperature (e.g. 1.1 K, 10 K, 15 K and 20 K), which means that the ledge was able to form faster at the crack front at 50 K with the highest crack speed, compared to the lower temperatures (1.1 K, 10 K, 15 K and 20 K) with lower crack speeds. This leads to two distinct mechanisms inducing the brittle-to-ductile fracture transition, as shown in Figure 4.9 and Figure 4.10.

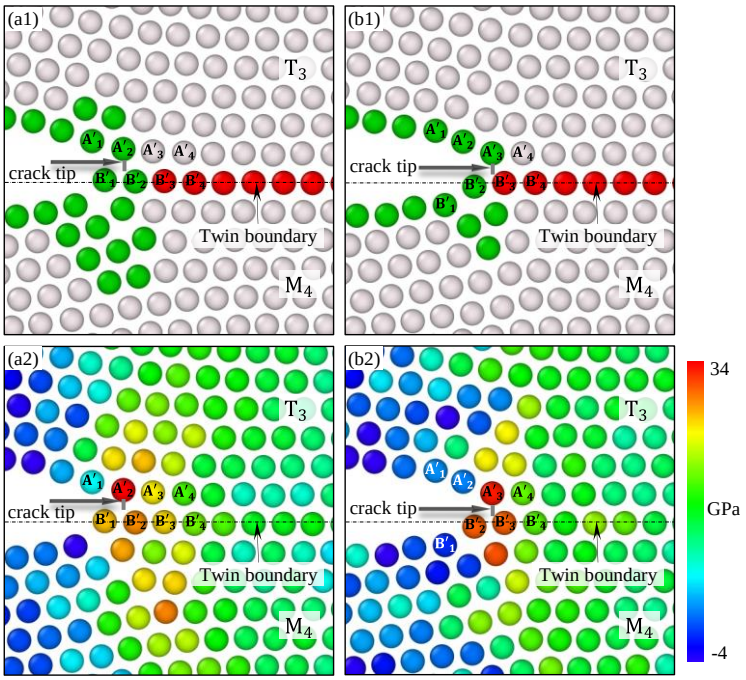

Figure 4.15 Atomic configurations for case of 50 K at ε = 2.51055%: (a) 1.45 Å ⩽ Z ⩽ 3.95 Å; (b) 17.15 Å ⩽ Z ⩽ 19.65 Å.

4.3.7 Atomic mechanism for ductile fracture

As the temperature continued to increase, the thermal fluctuation gradually became the main driving force for the formation of a ledge. At temperatures higher than 100 K (200 K, 300 K, 400 K, 500 K), the ledge formed easily at the early strain stage, further inducing dislocation nucleation around it without any apparent crack cleavage (see the dislocation activities in case of 500 K in Figure 4.11). Figure 4.16 shows the atomic

configurations for the case of 500 K at ε = 2.295% to understand the role of thermal fluctuation in the formation of a ledge. Two successive $(\bar{1}\bar{1}1)$ planes (Slice 1 and Slice 2) within the Z ranges of 4.45 Å $\leqslant$ Z $\leqslant$ 6.95 Å (Figure 4.16(a)) and 10.55 Å $\leqslant$ Z $\leqslant$ 13.05 Å (Figure 4.16(b)) were selected. The atoms in Figure 4.16 (a1-b1) and Figure 4.16(a2-b2) were coloured according to their local crystal structure using the CNA method and their tensile stress, respectively. Three groups of atoms were marked in the figures; Group-A′ Atoms were labelled A'_1, A'_2, A'_3, and the Group-E′ Atoms were labelled E'_1, E'_2, E'_3 and are located at the first $(1\bar{1}1)$ plane and the second $(1\bar{1}1)$ plane above the TB between T_3 and M_4 crystals. The Group-B′ Atoms were labelled B'_1, B'_2, B'_3, and are located on the TB between T_3 and M_4 crystals. Figure 4.16(a1-b1) shows that atomic bond broke between Atom A'_2 and Atom B'_2 in slice 1, and the crack tip was located at Atom B'_2. However, in slice 2, as shown in Figure 4.16(a2-b2), the atomic bond broke between Atom A'_2 and Atom E'_3, and the crack tip was located at Atom E'_3. The thermal fluctuation of Group-A′ Atoms could have caused variations of distance between Group-A′ and Group-B′ Atoms (e.g. A'_1-B'_1, A'_2-B'_2, A'_1-B'_2, A'_2-B'_3), Group-A′ and Group-E′ Atoms (e.g. A'_1-E'_1, A'_2-E'_2, A'_1-E'_2, A'_2-E'_3). At lower temperatures, the distance between one Group-A′ Atom and one corresponding Group-B′ Atom was always supposed to be greater than the distance between one Group-A′ Atom and one corresponding Group-E′ Atom, because of the highly concentrated stresses at the crack tip (see Figure 4.4). This means that atomic bonds always break between the A'_1-A'_3 plane and the B'_1-B'_3 plane at a lower temperature, but at higher temperatures, the distance between the Group-A′ and Group-E′ Atoms' might change due to thermal fluctuation, as seen by the concentration of tensile stress shown in Figure 4.16(a2-b2). When the distance between one Group-A′ Atom and one corresponding Group-E′ Atom exceeds a critical value the atomic bond will break between the A'_1-A'_3 plane and the E'_1-E'_3 plane, which means that the crack may propagate along two adjacent crystallographic planes at different Z locations due to the thermal influence. This would cause ledges to form

around the crack tip. These findings provide a new and alternative mechanism for the formation of a ledge around the crack tip where thermal fluctuations at a higher temperature causing the crack to propagate simultaneously along different crystallographic planes (similar observations are referred to in the case of nanotwinned Cu in Chapter 3), leading to ledges forming around the crack tip. The result is that at higher temperatures, dislocations are easily nucleated from the ledge within only a very few crack cleavages, or without any crack cleavage, at the initial position of crack tip during crack propagation. As a consequence, the fracture behaves exactly as if it were in a ductile fracture mode.

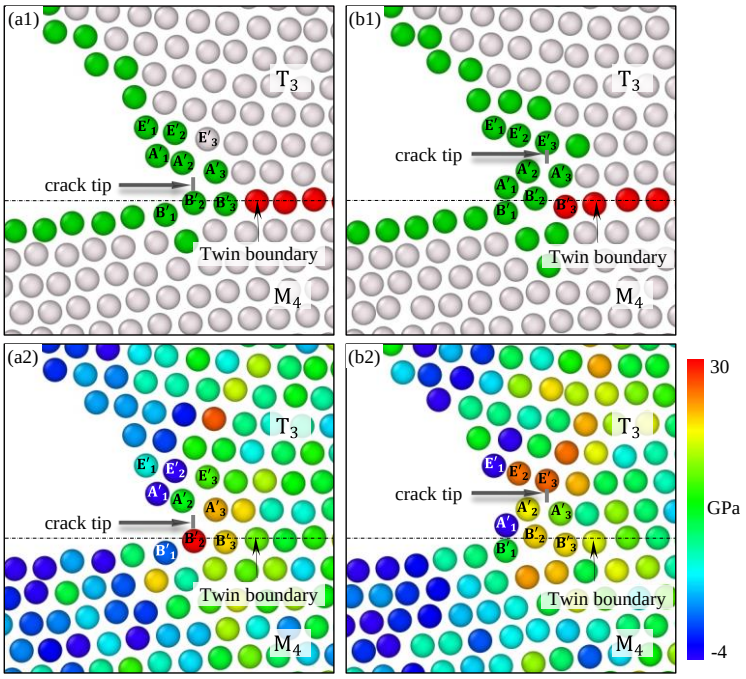

Figure 4.16 Atomic configuration for case of 500 K at ε = 2.295%: (a) 4.45 Å ⩽ Z ⩽ 6.95 Å; (b) 10.55 Å ⩽ Z ⩽ 13.05 Å.

To compare the dynamic fracture in nanotwinned Cu (in Chapter 3) and Ni crystal, both atomic models exhibited a brittle-to-ductile fracture transition under various temperatures. With the three types of fracture behaviour: brittle, brittle-to-ductile, ductile, their mechanisms in both metals were similar. Brittle fracture was correlated

with the perfect atomic bonding breaking process as the crack propagated; ductile fracture was attributed to the dislocation activity induced by the formation of a ledge due to thermal fluctuation, and the transition from brittle-to-ductile fracture stemmed from the nucleation/emission of dislocations due to local phase transformation accompanied by the formation of a twin and a ledge around the crack tip. This formation of a ledge may be caused by the thermal fluctuation or the dynamic crack speed, but the difference for two metals is that they exhibit different critical brittle-to-ductile transition temperatures. Ni metal had a higher brittle-to-ductile transition temperature compared to the Cu metal; in nanotwinned Ni, the transition temperature range was about 15~100 K in the MD cases presented, whereas in nanotwinned Cu, its temperature range was about 2~30 K. The crack speed of Ni was more sensitively dependent on the varying temperature than Cu for the propagation of brittle cracks. These differences were caused by the intrinsic properties of the different metals. In continuum theory there are two equations used to determine crack cleavage [13] and dislocation nucleation [19]:

$$G_{clea} = 2\mathrm{r}_{\mathrm{sur}} \tag{4.1}$$

$$G_{disl} = 8\mathrm{r}_{\mathrm{usf}}[1+(1-\mathrm{v})\tan^2\emptyset]/[(1+\cos\theta)\sin^2\theta] \tag{4.2}$$

Where G_{clea} and G_{disl} is the energy release rate for cleavage and for dislocation nucleation, respectively; r_{sur} is the surface energy, r_{usf} is the unstable stacking fault energy, v is Poisson's ratio, and $\emptyset$ and θ is the angle between the crack front and Burges vector and the angle between the crack plane and slip planes, respectively. It is known that crack propagation is a competitive process between the crack cleavage and nucleation/mobility of dislocation. The detailed parameters are given in Chapter 5. The Ni favoured brittle fracture more than the Cu with a high transition temperature, and with the given EAM potentials. The simulations revealed a new mechanism for the transition from brittle-to-ductile fracture and provide an atomistic-level

understanding of the events at the crack tip during crack propagation in nanotwinned Ni and Cu.

4.4 Summary

In this Chapter, MD simulations were used to investigate the fracture of nanotwinned Ni crystal with a pre-existing edge-notched crack under uniaxial tensile deformation in the Y direction. Three different temperature-dependent fracture modes were found for the tensile samples. The major observations can be summarised as follows:

1) At temperatures up to 10 K, the crack propagated in a brittle manner without any dislocation activities, and pure atomic bond breaking caused the brittle fracture behaviour.

2) For temperature regimes from 15 K to 100 K, a dynamic brittle-to-ductile fracture transition occurred, and in every case the crack propagated a brittle fashion first before it changed to ductile fashion. When the spacing of the local atomic bonds around the crack tip exceeded a critical value during crack propagation, a local phase transformation accompanied by the formation of new twin around the crack tip occurred, followed by dislocation nucleation in front of the twin region. This formation of a twin and the emission of dislocation impeded any brittle fracture, although at temperatures of 30 K, 50 K, and 100 K, ledges were nucleated ahead of the crack tip due to the increasing fluctuation in temperature and/or the increasing dynamic speed of the crack, resulting in dislocation nucleating around these regions. The occurrence of dislocation motion resulted in a final fracture transition from brittle mode to a ductile mode.

3) At temperatures higher than 100 K, such as 200 K, 300 K, 400 K, 500 K, the crack propagated in a ductile manner. The active thermal fluctuation can activate crack propagation along two different crystallographic planes around the crack tip. This

resulted in ledges forming near the crack tip, followed by the nucleation/emission of dislocation from the ledges. The dislocation activity shielded the atoms around the crack tip and impeded any brittle crack propagation.

In previous studies fcc structured metals were often considered to be intrinsically ductile materials, but in Chapters 3 and 4, fracture in nanotwinned Cu and Ni under very low temperatures can exhibit three different types, including brittle, brittle-to-ductile transition, and ductile. It is very interesting to speculate whether the same observations on brittle fracture could happen in other ductile fcc metals and what the factors are in determining the brittle versus ductile fracture in different fcc metals. In Chapter 5, the brittle versus ductile fracture in fcc twinned single crystals was predicted.

CHAPTER 5 PREDICTION OF BRITTLE VERSUS DUCTILE FRACTURE IN NANOTWINNED FCC CRYSTALS

5.1 Introduction

The issue with regards to the brittle versus ductile response of a solid has attracted enormous attention for many years. Griffith [13] proposed a criterion stating that a crack grows because the rate of energy released must be more than the energy required to create two new surfaces. Armstrong and Kelly [224, 225] went further with the perspective of brittle versus ductile response and pointed out that a solid would be either inherently ductile or inherently brittle depending mainly on the ratio between the theoretical shear strength and theoretical tensile strength. Rice and Thomson [17] believed that a correct description of brittle versus ductile behaviour should include the competition between the cleavage and dislocation emitted from the crack tip. Furthermore, Rice [19] concluded that the brittle versus ductile transition can be simply characterised by the ratio between the unstable stacking fault (r_{usf}) and surface energy (r_{sur}). Zhou et al. [226] argued that the brittle-to-ductile crossover of a crack did not depend on the surface energy, it only related to the unstable stacking fault.

More researchers were devoted to improving Rice's model by considering those factors that included tension-coupling, the creation of extra surfaces (such as the formation of a ledge), the specific crack tip configuration and corresponding stress, stress softening, thermal softening, and elastic anisotropy, but their results often deviated from Rice's prediction. Zhou et al. [20, 104, 212, 227] proposed that ledges on cracks can be efficient sources of dislocation emission at loadings well below the critical loading where the tension-shear coupling effect facilitates dislocation nucleation or incipient on inclined planes under mode I loading within a higher than unstable stable energy to surface energy ratios [227-229], but such a small ratio only

supports ductile facture while a large value favours brittle fracture. Cleri et al. [230-232] investigated the characteristics of crack tip nonlinearity and specific crack tip configuration to fracture behaviour, while Zhu et al. [233-237] found that the lattice trapping effect can change the fracture behaviour based on the atomistic point.

As mentioned above, many in situ experiments and simulations had similar or even contradictory results compared to classic continuum theory, which poses an interesting question: can the continuum concept where free surface energy versus unstable stacking fault energy or the ideal shear strength versus ideal tensile strength still be used to predict brittle/ductile fracture, and to what extent would it be applicable to twinned fcc metals? In this chapter, MD simulations were performed to investigate the question regarding pre-inserted twinning fcc metals.

5.2 Model set-up

Geometric size of each atomic model of fcc crystals is kept about 86 × 80 × 5 lattices in X, Y and Z directions. The crack plane lies on the $(\bar{1}1\bar{1})_M$ plane, the crack propagation direction runs along $[1\bar{1}\bar{2}]_M/[1\bar{1}\bar{2}]_T$ (X direction), and the crack front direction along $[110]_M/[\bar{1}\bar{1}0]_T$ orientation (Z direction). The geometric size of each twinned fcc crystal was kept to about 86 × 80 × 5 lattices in the X, Y, and Z directions for all fcc metals, and varied TBs were introduced into the fcc single crystals along $[\bar{1}1\bar{1}]_M/[1\bar{1}1]_T$ direction (Y direction). The method used to control the thermostat and barostat with NPT or other dynamic settings for MD simulation can be seen in Chapter 3.

5.3 Results and discussion

5.3.1 Stacking fault energy

The fcc structure was stacked in a sequence of three types of (111) planes-ABCABCABC. As the atoms in (111) plane were subjected to local shear stress, the arrangement of atomic structure ABCABC...was changed from the original position

layer A to layer B, or B to C, or C to A, or in the opposite direction B to A…; this process must overcome the minimum energy barrier, namely the unstable fault energy (r_{usf}) or unstable twin fault energy (r_{utf}) to reach a new local minimum energy for crystalline structures, and then the intrinsic dislocation, extrinsic dislocation and twin are formed in turn.

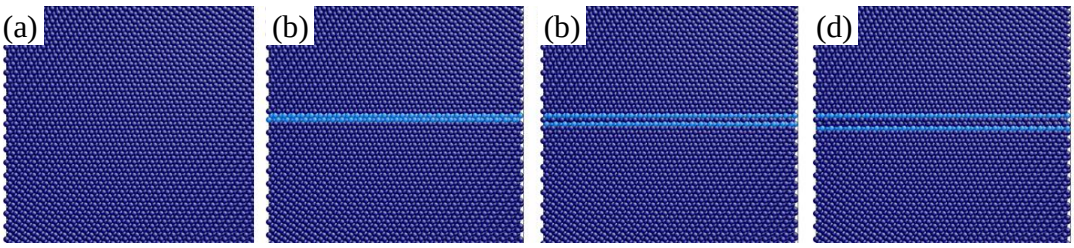

Figure 5.1 Atomic model for calculating the stacking fault energy by moving the distance of group atoms with times of $(1/6)^{1/2}$ along [1-1-2] in (-11-1) plane. (a) Perfect fcc crystal; (b) Intrinsic stacking fault; (c) Extrinsic stacking fault; (d) Twinning boundaries separated by two (-11-1) planes. Dark and light blue colour was assigned to the perfect fcc and hcp atoms, respectively.

According to the definition of stacking fault energy, the stable or unstable stacking fault energy can be calculated through the minimum energy pathway along a (111) plane, also known as the generalised stacking-fault (GSF) energy curve, and the generalised twinning-fault (GTF) curve or γ surfaces.

(i) Perfect fcc-intrinsic stacking fault (ISF): energy path of a crystal transformed from a perfect fcc structure into an ISF of energy r_{sf}. The saddle point of the transition defines the unstable stacking fault energy, r_{usf} (see Figure 5.2 for Cu).

(ii) Intrinsic stacking fault (ISF)-extrinsic stacking fault (ESF): the energy path of a crystal when its transition forms from an ISF into an ESF of energy (r_{esf}). The saddle point of the transition defines the unstable energy (r_{utf}) (see Figure 5.2 for Cu).

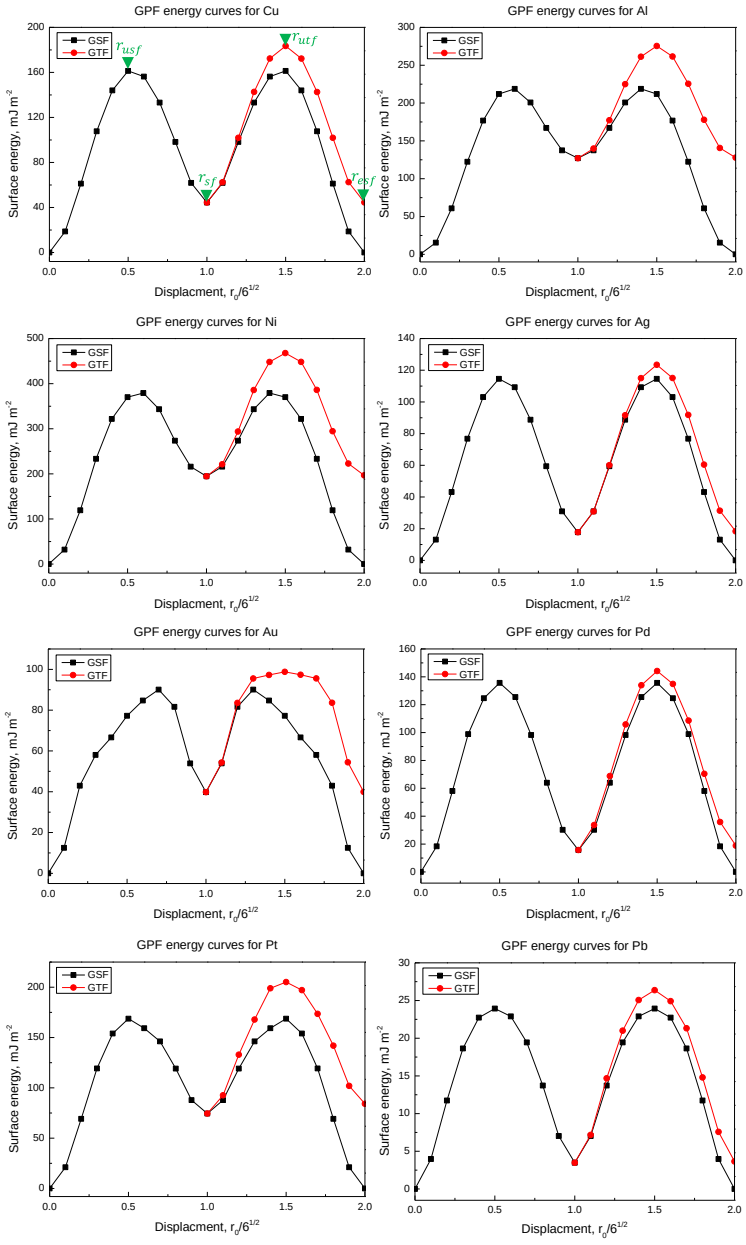

Figure 5.2 GPF energy curves for different fcc metals. r_0 is the lattice parameter.

The atomic model for calculating the stacking fault energy is shown in Figure 5.1. The stacking fault energy can be determined by comparing the energy in the system before and after displacing the group atoms in a specific region within the times of the slip vectors distance in $[1\bar{1}\bar{2}]$ direction in $(\bar{1}1\bar{1})$ slip plane. All the calculated results of stacking fault energy for various fcc metals are shown in Figure 5.2.

5.3.2 Free surface energy

Free surface energy is defined as the change in free energy when a solid is separated into two parts a large distance along the normal direction of a crystallographic plane (seen in Figure 5.3). Its value can be calculated as (shown in Table 5.1):

$$r_{sur(ijk)} = \frac{(E_{end} - E_{init})}{2A} \tag{5.1}$$

Where $r_{sur(ijk)}$ is the free surface energy of (ijk) plane, A is the section area perpendicular to the $r_{sur(ijk)}$ plane. E_{init} is the initial total energy and E_{end} is the amount of energy after displacement along normal direction of the (ijk) plane.

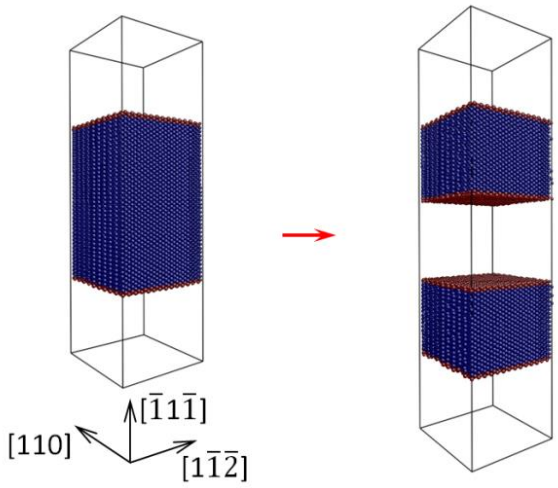

Figure 5.3 Atomic model for calculating the free surface energy. The dark blue and red atoms represent the perfect fcc and free surface atom, respectively.

Table 5.1 Free surface energy at various orientations in fcc metals.

Unit (mJ/m^2)	Cu	Al	Ni	Ag	Au	Pd	Pt	Pb
$r_{sur(\bar{1}1\bar{1})}$	1239	428	1284	862	1202	1515	2083	348
$r_{sur(100)}$	1345	496	1405	940	1301	1628	2178	385
$r_{sur(1\bar{1}\bar{2})}$	1434	536	1510	991	1426	1741	2354	404
$r_{sur(110)}$	1475	581	1586	1017	1538	1793	2396	423

5.3.3 Ideal tensile strength

The method to calculate the ideal tensile strength is similar to calculating the free surface energy; it assumes that a bulk crystal is being cut across a crystallographic plane into two parts and the two half parts are then pulled along the normal direction of crystallographic plane (as shown in Figure 5.4), and then the total energy of the system will increase with the value *d*, which is the distance between the two separated surfaces. The excess energy per unit area of the surface - r is plotted as a function of *d* in Figure 5.4. As the value *d* increased enough the value of r gradually converged to the free surface energy r_{sur}.

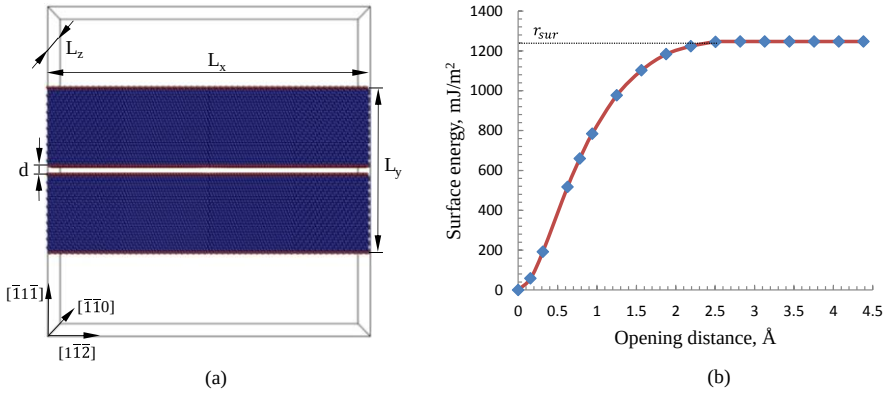

Figure 5.4 (a) Atomic model for separating a bulk crystal across a (-11-1) plane by the distance *d*. (b) The excess energy per unit area r with opening distance d for Cu single crystal.

Figure 5.4(b) shows that the maximum slope of the r curve has a unit of stress, while we defined the ideal tensile strength of the crystal along the normal direction, $\sigma_c = \max[\frac{\partial r}{\partial d}]$. If the ideal tensile strength is too strong for the materials, the material could fail in shear, leading to ductile fracture behaviour.

5.3.4 Ideal shear strength

The ideal tensile strength is not the only indicator used to determine brittle versus ductile behaviour, despite being reported in the reference [238], but also by the result

of its competition with the ideal shear strength. The method for computing the ideal shear strength is shown in Figure 5.5. The atomic model includes two parts (across the $(\bar{1}1\bar{1})$ plane), the low part is fixed and the upper part is displaced by a value d along the $[1\bar{1}\bar{2}]$ direction, followed by minimisation with short time steps for the system. The excess energy divided by the cross sectional area by Lx × Ly, is called the relaxed generalised stacking fault energy or r surface, here it is called $\tilde{r}(d)$. The ideal shear strength is defined by the maximum slope of $\tilde{r}(d)$ curve, $\tau_c = \max[\frac{\partial \tilde{r}}{\partial d}]$.

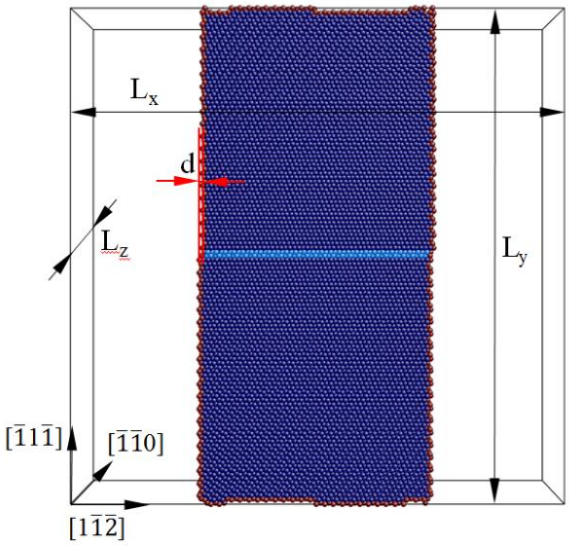

Figure 5.5 Atomic model for shearing a bulk crystal across a (-11-1) plane by distance *d*.

5.3.5 Results

MD simulations using EAM potential were carried out to calculate the stacking fault energy and surface energy in bulk models of fcc metals, with each case being conducted at full minimisation to ensure the accuracy of those parameters. Table 5.2 shows the results, which agree with Li et al. [94, 125, 239, 240]. It can be seen from this table that for different fcc metals, the energy had large differences that would result in an obvious distinction in the mechanical property of different metals. In order to speculate on the competition between crack cleavage and dislocation emission at

the crack tip, the ratio of surface energy ($2r_{sur} - r_{usf}$) to unstable stacking fault energy (r_{usf}) was calculated. Because of the low twinning energy, the equation can be approximately simplified to $2\,r_{sur}/r_{usf}$. In the prediction of brittle versus ductile fracture, the small ratio represents the preferential brittle fracture, so the twinned Al, Ni, Ag, Cu may be more brittle than the Au, Pb, Pd, Pt metals.

Table 5.2 Calculated energetic parameters by MD method. Stacking fault energy (r_{sf}), unstable stacking fault energy (r_{usf}), unstable twin fault energy (r_{utf}), surface energy (r_{sur}) and twinned boundary energy (r_{tb}) for various fcc metals.

Metal	r_{sf} (mJ/m^2)	r_{usf} (mJ/m^2)	r_{utf} (mJ/m^2)	r_{sur} (mJ/m^2)	r_{tb} (mJ/m^2)	r_{sf}/r_{usf}	r_{utf}/r_{usf}	$\frac{(2r_{sur}-r_{tb})}{r_{usf}}$	Crack mode
Al[a]	127.06	218.77	275.46	428	64.91	0.53	1.26	3.25	Brittle
Ni[b]	194.64	379.21	467.84	1284	98.28	0.51	1.23	6.77	Brittle
Ag[c]	17.76	114.59	123.45	862	9.16	0.15	1.08	14.97	Brittle
Cu[d]	44.39	161.31	183.47	1239	22.24	0.28	1.14	15.22	Brittle
Pd[e]	15.72	135.68	144.17	1515	8.50	0.12	1.06	22.27	Ductile
Pt[f]	74.49	168.71	205.11	2083	38.44	0.44	1.22	24.47	Ductile
Au[g]	39.78	90.07	98.8	1193	19.88	0.44	1.10	26.47	Ductile
Pb[h]	3.48	23.94	26.37	348	1.79	0.15	1.10	29.00	Ductile

EAM potential: a [239]; b [215]; c [240]; d [190]; e, f, h [241]; g [242].

Figure 5.6 shows the engineering stress-strain curves of the MD simulation for various twinned fcc metals (with twinning spacing of 20 atomic layers). By combining the ratio of surface energy to unstable stacking fault listed in Table 5.2, we can see a striking brittle and ductile fracture as the stress dropped sharply or the strain rate hardened when the ratio increased to some levels; also, a small value ($2\,r_{sur}/r_{usf}$) exhibited brittle fracture, while the large value preferred ductile fracture; this was the as the prediction in continuum theory [19, 227], although with a small difference in magnitude. For a small value such as Al, Ni, Cu, Ag, the relatively low surface energy (corresponding to a low barrier that generated a new surface) and the relatively high unstable stacking fault (the larger energy barrier to atomic shear on the slip plane)

suggested brittle fracture where the crack can cleave without any dislocation emissions around the crack tip. For a higher ratio of $2\,r_{sur}/r_{usf}$ such as Au and Pb, the dislocation activities became easier prior to crack cleavage because by then, plastic deformation dominated the fracture behaviour by dislocation nucleation/mobility, and by its interaction with inserted twinning, the fracture showed a completely ductile manner; this showed that Au and Pb were the most ductile metals with the largest ductile parameters of the fcc metals presented in my study.

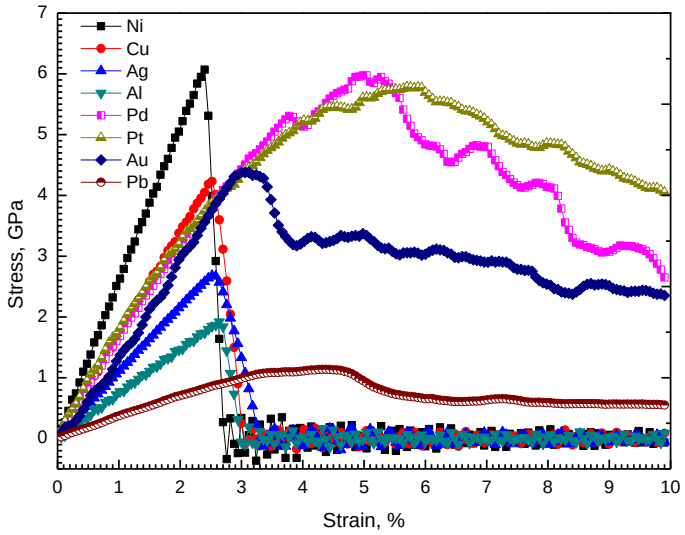

Figure 5.6 Tensile stress vs strain rate for varied fcc metals with twinning spacing of 20 atomic layers. A transition from brittle to ductile fracture is shown as the ratio between free surface energy and changes in the unstable stacking fault energy.

Moreover, in the ductile fracture cases, the obvious strain hardening effect due to dislocations was blocked by the twinning boundaries [11, 125], and in the ductile twinning fcc metals, the maximum flow stress was almost proportional to the unstable stacking fault energy, similar to the Ref. [125]. Based on the MD simulation of twinned fcc metals (twinning spacing was 20 atomic layers), the ratio $2\,r_{sur}/r_{usf}$ was a good indicator for forecasting the brittle versus ductile fracture of a given potential atomic model, as done by Rice [19].

The detailed crack propagation mechanism at the crack tip can be explained from the atomic scale. Figure 5.7 shows the two distinct fracture behavior for Cu (brittle) and Au (ductile). The cooper with relatively low ductile indicator ($2\,r_{sur}/r_{usf}$) suggests the much strong tensile characteristic competing over the shear effect. Atomic bonding is easy breaking rather than dislocation nucleation. The crack moves forward with flat surfaces. In comparison of Cu, Au (high $2\,r_{sur}/r_{usf}$) owns low dislocation energy barrier, dislocation/twinning activities occupy a significant role in the whole crack propagation process, leading to the final material failure by surface necking.

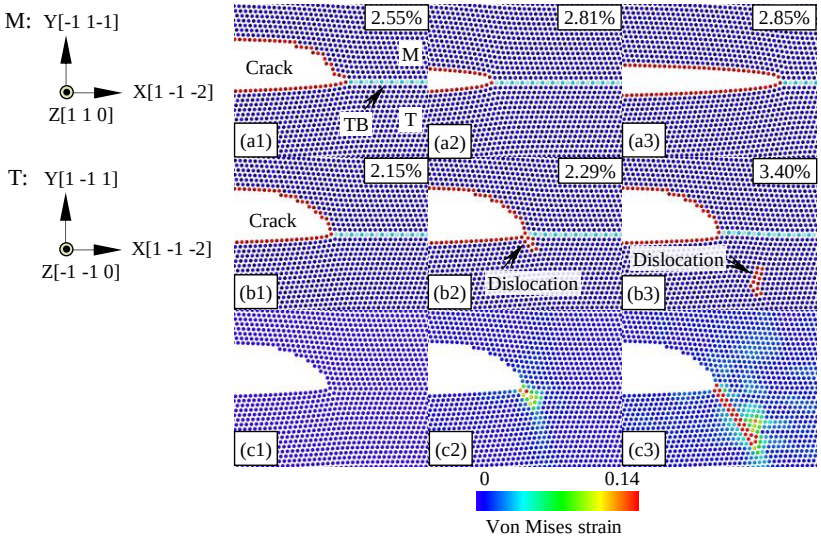

Figure 5.7 Atomistic views of crack propagation with twinning spacing of 20 atom layers. (a) Cu, (b1) Au. The atoms are coloured according to the CNA, red represents the surface atoms or disorder atoms, blue and cyan is the perfect fcc atom and hcp atom, respectively. The same colours in light and dark shades means two different atomic layers in [110] direction. (a) Brittle cleavage fracture was seen without any dislocation nucleation (with a relatively low value of $2r_{sur}/r_{usf}$). (b1)-(b2) Dislocation was emitted prior to the crack cleavage (high value of $2r_{sur}/r_{usf}$), the deformation mechanism was mainly dominated by the dislocation/twinning activities, and crack propagation shows a noticeable ductile behaviour.

Besides that, an alternative criterion was also made to determine the brittle and ductile response by the ideal tensile strength (σ_c) and ideal shear strength (τ_c), while the

method used to calculate the ideal strength can be referred to in literature [238], where each parameter was calculated by MD simulation at a temperature of almost 0 K after enough energy relaxation, as shown in Table 5.3. We compared the indicator value of $A = (\sigma_c.S)/\tau_c$, where S was the Schmid factor. When A<1 the metals tended towards brittle fracture due to the strong shear effect to atom shear on the slip plane, but conversely, A>1 meant ductile behaviour.

Table 5.3 Calculated ideal tensile strength and ideal shear strength parameters by MD simulation.

Metal	σ_c(GPa)	τ_c(GPa)	$\sigma_c.S/\tau_c$	Prediction of Crack mode
Al	8.79	2.76	0.516	Brittle
Ni	24.35	11.20	0.683	Brittle
Ag	10.46	3.66	0.897	Brittle
Cu	16.84	4.88	1.085	Brittle
Pd	17.12	4.15	1.296	Ductile
Pt	21.63	4.97	1.368	Ductile
Au	11.62	2.58	1.416	Ductile
Pb	3.24	0.62	1.653	Ductile

In Table 5.3, when Au, Pb, Pd, Pt were all within the values of A and much larger than 1, they showed obvious ductile fracture, but for other fcc metals, brittle fracture was predicted for Cu when the indicator A was very close to 1 and was helped by the inserted twinning effect, then Cu could still be cleaved in a brittle fracture. The predicted approach is consistent with my MD observations.

However, as the thickness of the twinning spacing changed, continuum theory cannot be used to predict brittle versus ductile behaviour, because as Figure 5.8 shows, in metals such as Cu and Ag at extreme low temperatures, fractures no longer propagate in a brittle fashion because the thickness of twinned spacing has decreased to a critical value, which in turn triggers the brittle-to-ductile transition (seen in Chapter 3, also

referred to Ref. [94] for Cu). This action occurs because the high stress concentration at the crack tip can induce twinning dislocation nucleation on neighbouring twin boundaries, which then activates more dislocation motions upon crack propagation, leading to the final ductile fracture manner. The influence of temperature on this brittle versus ductile fracture transition contributes to the prediction of its failure, as discussed in Chapters 3 and 4.

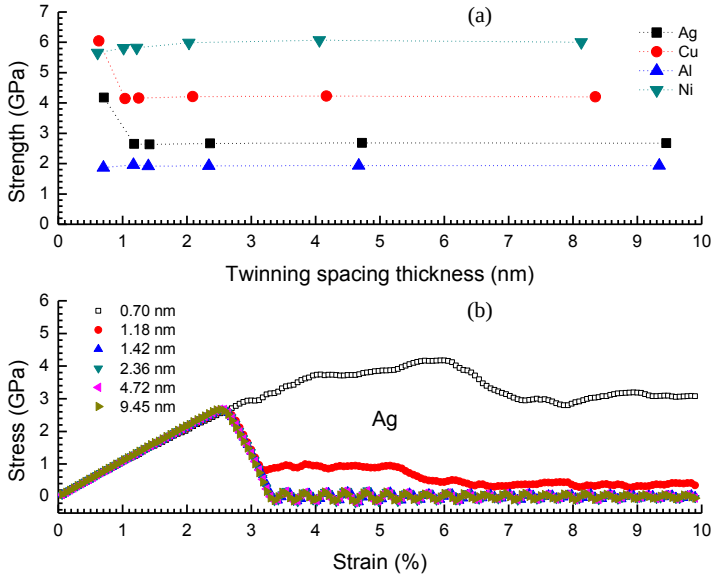

Figure 5.8 (a) Max stress vs twinning spacing thickness in fcc metals. (b) Stress vs strain rate curves with varied twinning spacing in Ag. The low peak stress for the same material suggests the more brittleness, where the high max stress represents the ductile failure.

5.4 Summary

In summary, the results provide an atomic scale view of changes of the crack-tip event from crack cleavage to dislocation activities in fcc twinned crystals under extremely low temperatures. Classic theories of the ratio of surface energy and unstable stacking fault energy, as well as the ideal tensile strength and ideal shear strength in determining the brittle versus ductile fracture of nano-twinned crystal models can help in a specific range of twinning spacing thickness (such as a twinning

spacing with 20 atomic layers), but they are unable to predict brittle and ductile response when the thickness of the twinning spacing is outside the limited range (seen in Figure 5.3), or the temperature (seen in Chapters 3 and 4) is outside the critical value. Moreover, other factors should also be considered: the size effect, surface features, the applied strain rate, and the used inter-atomic potentials and crystal orientation, all of which may alter the applicability of the continuum theories.

Chapters 3, 4, and 5 are all focused on the brittle versus ductile fracture in nanotwinned fcc metals. In Chapter 6 the brittle versus ductile fracture in single Ni crystal without the pre-existing twin will be investigated.

CHAPTER 6 BRITTLE VERSUS DUCTILE FRACTURE IN SINGLE CRYSTAL NICKEL

6.1 Introduction

Previous chapters explained that the transition from brittle-to-ductile fracture in nanotwinned fcc structures using MD simulation was triggered by localised phase transformation as the temperature increased. However, the pre-existing twin boundary (TB) has an intrinsic kind of brittle structure that may change the brittle versus ductile fracture behaviour, so it is natural to ask: (i) whether the brittle versus ductile fracture transition could occur in a single crystal without TB, (ii) whether the mechanism for brittle cleavage in twinned crystal is suitable for the fracture mechanism in single crystal, (iii) whether the mechanism of brittle-to-ductile fracture transition by phase transformation in twinned single crystal is applicable to the case in a single crystal?

Previous brittle versus ductile fracture behaviour using MD simulations mostly focused on the diamond structure and body-centred structure of the materials. Those studies found that the crystallographic orientation (including the cleavage plane and crack front direction) would influence the final fracture behaviour [40, 212, 243-246], and elastic anisotropy should also induce some directional anisotropy of lattice trapping. The preferred cleavage plane and direction for the fracture propagation were explained via experiments. Researchers [69] studied the intrinsic brittleness and ductility of inter-granular fracture along the coherent and incoherent symmetrical tilt GBs in cooper and found that brittle cleavage induced crack propagation in one direction and dislocation emission in another direction. Such directional anisotropy also existed in the intrinsic ductility of incoherent GBs, as seen by the way dislocation emission was favoured in both crack propagation directions. Furthermore, fracture toughness not only depended on the direction of propagation, it also depended on the

position of the crack tip in tungsten bricrystal, as observed by Möller and Bitzek [179], who called it the bond trapping effect of GB cracks.

Very few studies exist regarding the brittle versus ductile fracture transition in single fcc crystals. The mechanism for its transition is still vague. Apart from the effect of crystallographic structure with a specific cleavage plane, and crack propagation and crack front direction, the properties of materials (e.g. stable and unstable stacking fault energy, and free surface energy) also play an important role in plastic deformation. In this chapter, a single crystal of Ni was used to study brittle versus ductile fracture by considering the crystallographic structure for the initial pre-existing central crack.

6.2 Model set-up

Atomic models with 9 kinds of practically relevant crystallographic orientations for single Ni crystal were established (see Table 6.1). The atomic model is shown in Figure 6.1 with domain sizes in X (517.33~524.33 Å), Y (517.33~524.33 Å) and Z (24.39~25.87 Å) directions. The atom number ranged from 604800~650000. Due to the characteristic ductility for single Ni crystal, a through-thickness pre-existing central crack was introduced into the single crystal rather than a left hand edge crack in nanotwinned fcc single crystal. The idea was to reduce the effect of outmost boundary on crack propagation. The length and height of crack was about 50 Å (major axis -- X axis) and 16 Å (minor axis -- Y axis) and it was in the shape of an ellipse. The crack cleavage plane was parallel to the normal direction of XZ plane and the crack front direction was oriented along the Z axis.

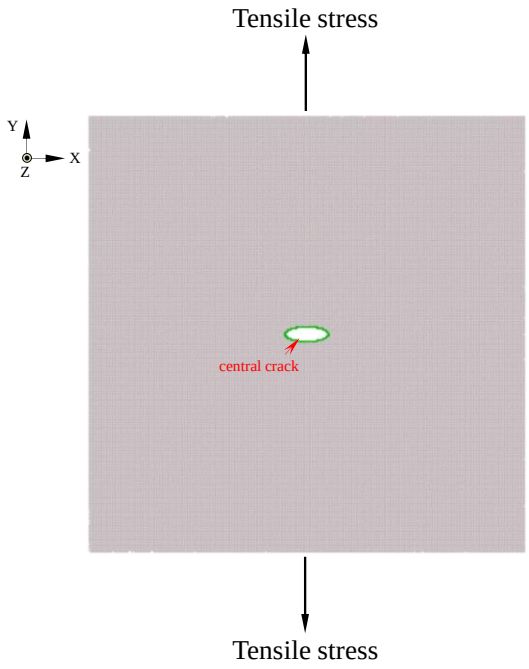

Figure 6.1 Simulation cell of single Ni crystal with a centred-notched crack.

The EAM interatomic potential developed by Mishin et al. [247] was used in all the simulations, which were carried out in a constant NPT ensemble. Periodic boundary conditions were applied in all directions. In this study, as with Chapters 3-5, the energy of each simulation was minimised by the conjugate gradient method (cg method). Random velocities were initially assigned to atoms, followed by relaxation by increasing the temperature to the desired value (here it was 1 K) and controlling the external pressure at 0 Bar in three directions for 250 ps with a time step of 0.005 ps. After relaxation, the simulation cell was then subjected to 24% deformation at a constant strain rate of 2×10^{8} s^{-1} along the Y direction while the normal stresses along the other two directions were fixed at zero in order to simulate uniaxial loading using the Parinello-Rahman barostat. The temperature was maintained at the desired value in the X and Z directions using the thermostat. The simulation time was 1200 ps with a time step of 0.005 ps, and Ovito software [198] was used to visualise the atomic configuration. The CA tool [192] and DXA code [193] developed by Stukowski and his co-workers were used to identify dislocations and stacking faults respectively, and

the results were viewed using ParaView software.

Table 6.1 Cases with 9 different crystallographic orientations and their corresponding deformation failure modes. Crack cleavage plane is perpendicular to the Y axis and crack front direction is oriented along the Z direction. BDT means brittle-to-ductile fracture transition during tension deformation.

Crack orientation	Labelled	Model size (lattices)	r_{sf} (mJ/m^2)	r_{usf} (mJ/m^2)	r_{utf} (mJ/m^2)	r_{sur} (mJ/m^2)	$\frac{2r_{sur}}{r_{usf}}$	Crack mode
X [100] Y [010] Z [001]	1-{100} <100>	X 148 Y 148 Z 7	125.28	365.67	427.46	1879	8.79	BDT
X [0$\bar{1}\bar{1}$] Y [100] Z [0$\bar{1}$1]	2-{100} <110>	X 105 Y 148 Z 5	125.28	365.67	427.46	1879	8.79	Ductile
X [1$\bar{1}\bar{2}$] Y [110] Z [1$\bar{1}$1]	3-{110} <111>	X 90 Y 105 Z 4	125.28	365.67	427.46	2049	9.59	Ductile
X [100] Y [011] Z [0$\bar{1}$1]	4-{110} <110>	X 148 Y 105 Z 5	125.28	365.67	427.46	2049	9.59	Ductile
X [01$\bar{1}$] Y [011] Z [100]	5-{110} <100>	X 105 Y 105 Z 7	125.28	365.67	427.46	2049	9.59	Ductile
X [1$\bar{1}\bar{2}$] Y [$\bar{1}$1$\bar{1}$] Z [110]	6-{111} <110>	X 90 Y 86 Z 5	125.28	365.67	427.46	1630	7.63	Semi_brittle
X [$\bar{1}\bar{1}$0] Y [$\bar{1}$1$\bar{1}$] Z [1$\bar{1}\bar{2}$]	7-{111} <112>	X 105 Y 86 Z 4.5	125.28	365.67	427.46	1630	7.63	Ductile
X [$\bar{1}$1$\bar{1}$] Y [$\bar{1}$12] Z [110]	8-{112} <110>	X 86 Y 90 Z 5	125.28	365.67	427.46	1958	9.16	BDT
X [$\bar{1}\bar{1}$0] Y [$\bar{1}$12] Z [$\bar{1}$1$\bar{1}$]	9-{112} <111>	X 105 Y 90 Z 4	125.28	365.67	427.46	1958	9.16	Ductile

6.3 Results and discussion

6.3.1 Macroscopic stress-strain behaviour

MD results for atomic configurations with different crack planes and crack front orientations were presented, where all simulations were carried out under the same working conditions. Figure 6.2 shows the tension stress (or $\bar{\sigma}_y$) versus strain under different crack configuration orientations, and indicate that the tension stress varied sharply with the varying crack plane and crack front directions. The stress in cases with crack systems of $\{100\}\langle 100\rangle$, $\{111\}\langle 110\rangle$ and $\{112\}\langle 110\rangle$ soon dropped to almost 0 GPa, whereas the stress in cases with other crack systems did not decrease to 0 GPa, it had a series of serrations. The strength and slope of stress-strain differed due to the pronounced anisotropic features. Figure 6.3 shows the evolution of crack geometries with the tensile strain for different crack tip configurations; these big differences suggest that the fracture mechanisms varied with the given cleavage plane, direction of crack propagation, and orientation of the crack front.

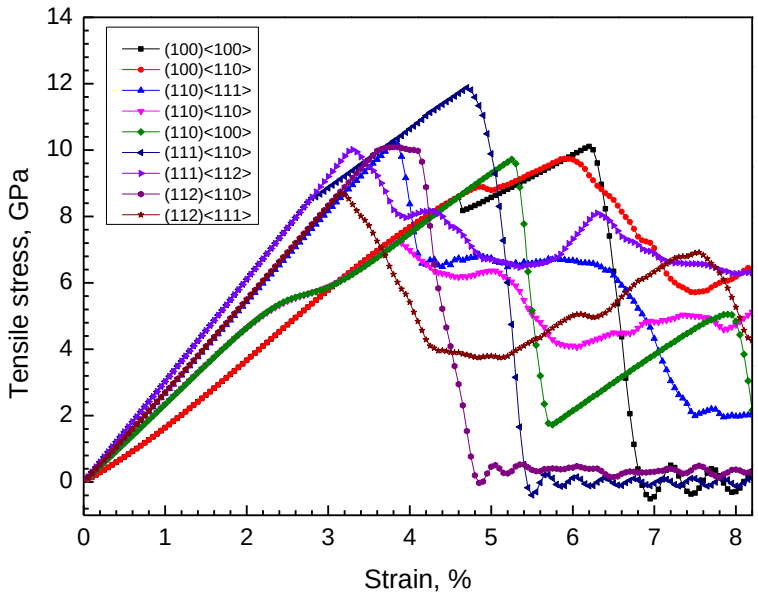

Figure 6.2 Tension stress-strain curves for the different crack plane and crack front orientations.

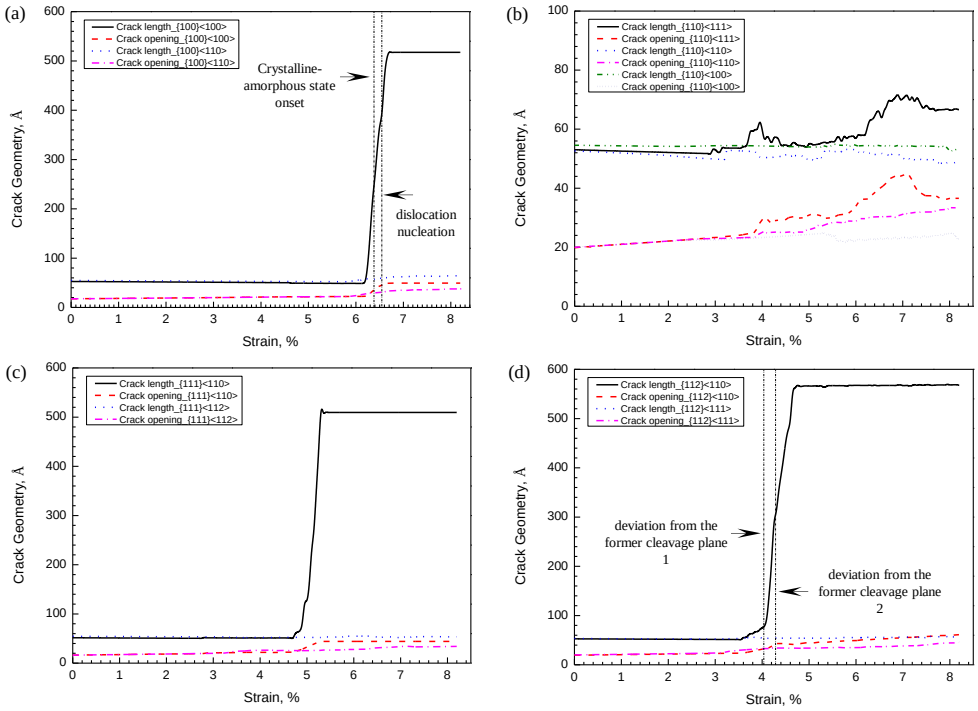

Figure 6.3 Evolution of variables for crack configuration orientations with crack planes located in (a) {100}, (b) {110}, (c) {111} and (d) {112} plane.

The following parts were forwarded to reveal the detailed brittle versus ductile fracture under different crack configuration orientations. Although it was very difficult to quantitatively compare the plastic deformation of two crack propagation systems due to crack orientations, they were also sensitive to the pre-existing sizes of the central cracks and the microscopic shapes at the crack tip, size of the simulation cell, or even the specific position of the crack tip [179].

6.3.2 {100}<100> and {100}<110> orientations

The sequence of snapshots of crack propagation with crack system {100}⟨100⟩ are shown in Figure 6.4, and indicate the brittle-to-ductile fracture transition through three stages of crack propagation; atomic cleavage, void nucleation, an dislocation nucleation. The onset of crack propagation began at about 6.2% deformation (see Figure 6.1). Atoms ahead of the crack tip exhibited a perfect de-bonding process

along the (010) crack plane and left a mirror surface, as seen in Figure 6.4(b). As the tensile deformation continued the atomic configuration ahead the crack tip showed a crystalline-amorphous state (local structure transformation). The voids were allowed to nucleate and join the main crack. The surface of the crack was corrugated (see Figure 6.4(c2)), and inhomogeneous dislocations were further nucleated and emitted from the void (see Figure 6.4(d)).

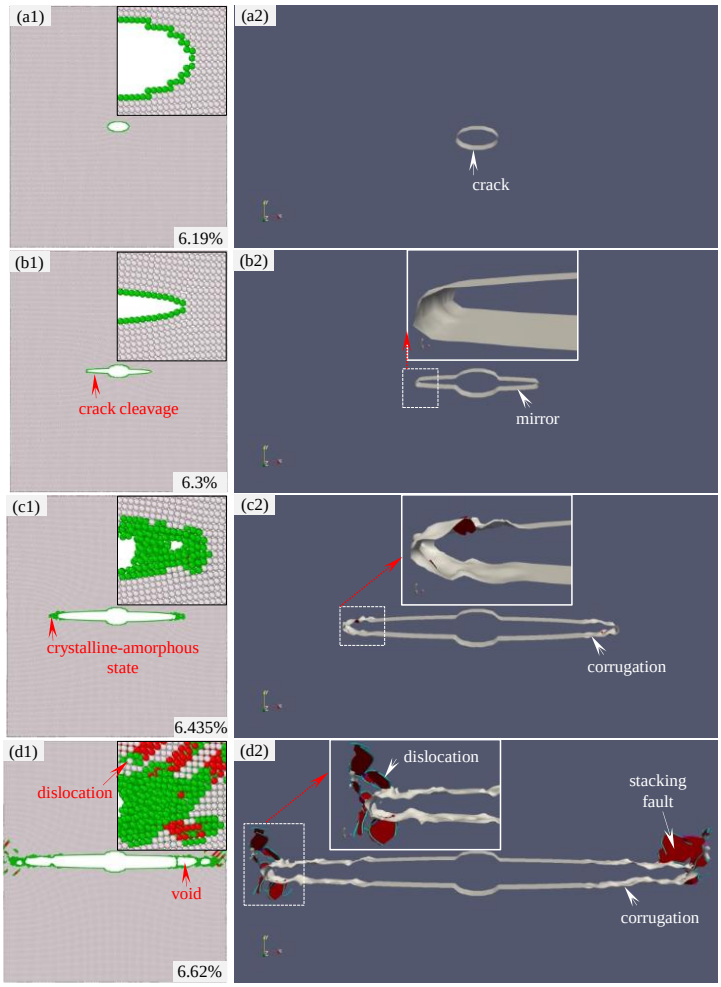

Figure 6.4 Snapshots of the simulation cell with crack system of {100}<100> subjected to different strains at (a) ε = 6.15%; (b) ε = 6.3%; (c) ε = 6.435%; (d) ε = 6.62%. (a1)-(d1) Atoms are colored based on the CNA method. The blue, green, and red atoms represented fcc, hcp, and the disorder structure atom, respectively. (a2-d2) Silver and red colours mean free surface and stacking fault, and colourful vector lines represent dislocations.

Figure 6.5 shows a sequence of atomic configurations of stress distributions with a crack system of {100}⟨100⟩, and the zoom-in images focused on the local region at the right-hand crack. In Figure 6.5(a), there were highly concentrated tensile stress and stress triaxiality factors around the crack tip just before the atomic bonds began to break. These atomic bonds cleaved further along the X direction (see Figure 6.5(b)). This criterion of crack cleavage was shown in Chapters 3-4. The formation of a new free surface was associated with the release of energy, as seen in the enlarged images of Figure 6.5(b). The elastic wave is shown as being symmetrical about the central crack plane. The atomic bonds usually broke between the atoms in (001) plane along $[\bar{1}\bar{1}0]$ and $[1\bar{1}0]$ directions and in (100) plane along $[0\bar{1}\bar{1}]$ direction.

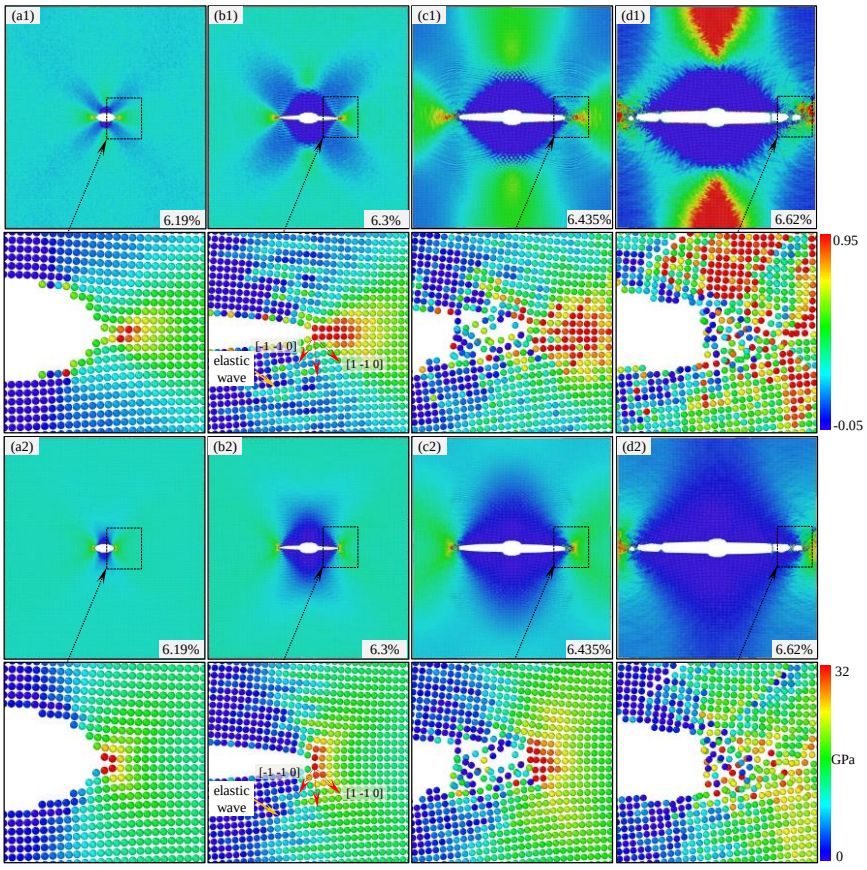

Figure 6.5 Snapshots of the stress distributions with crack system of {100}<100> subjected to different strains at (a) ε = 6.15%; (b) ε = 6.3%; (c) ε = 6.435%; (d) ε = 6.62%. (a1)-(d1) σ_{tri}, and (a2-d2) σ_y.

Figure 6.5(c) shows that voids were generated ahead the crack tip, with large tensile stress and stress triaxiality distributions at its local region. The difference being that the concentrated stress was not constrained at a small region in front of the crack tip as occurred at the completed atomic cleavage stage. This means that the voids can still grow under the large local stresses. There was no obvious elastic wave direction due to the disordered atomic debonding around the voids. Figure 6.5(d) shows there were no highly concentrated stress regions ahead the void because the dislocation was being nucleated from the voids.

To understand the mechanism of brittle-to-ductile fracture transition in $\{100\}\langle100\rangle$ crack system, the brittle cleavage stage must be examined first so the atomic configurations around the crack tip were examined during atomic cleavage in a range of 4.17 Å $\leqslant$ Z $\leqslant$ 8.17 Å, as shown in Figure 6.6; as the crack propagated two adjacent (010) planes that were identical to the atomic bonds breaking in the brittle fracture cases of nanotwinned Cu and Ni crystals were set apart. The tensile stress was used to analyse the crack propagation because it is one of the most important driving forces in atomic debonding, and eight atoms distributed around the crack tip are selected for analysis. Figure 6.6 shows there was a high stress distribution near the crack tip and the highest value of σ_y was associated with the atom in front of the crack tip. In Figure 6.6(a), Atom A1 has the highest σ_y at 6.331% deformation, followed by Atom B1. Due to Group-A and Group-B atoms being symmetrical to the central plane, the tensile stresses of Group-A and Group-B atoms were almost always equal to each other, but when the deformation strain increased to 6.332%, the bonds began to break between Atom A1 and Atom B1 as Atom A1 moved up and Atom B1 moved down, as shown in Figure 6.6(c). The distance between A1 and B1 and between B1 and A2 increased significantly, and the position of maximum σ_y transferred to Atom A2. At the same time, the tensile stresses of Atom A1 and Atom

B1 decreased to a low level (see Figure 6.6(d)). Figure 6.6(a2-d2) shows that all the atoms moved only at the initial (001) plane.

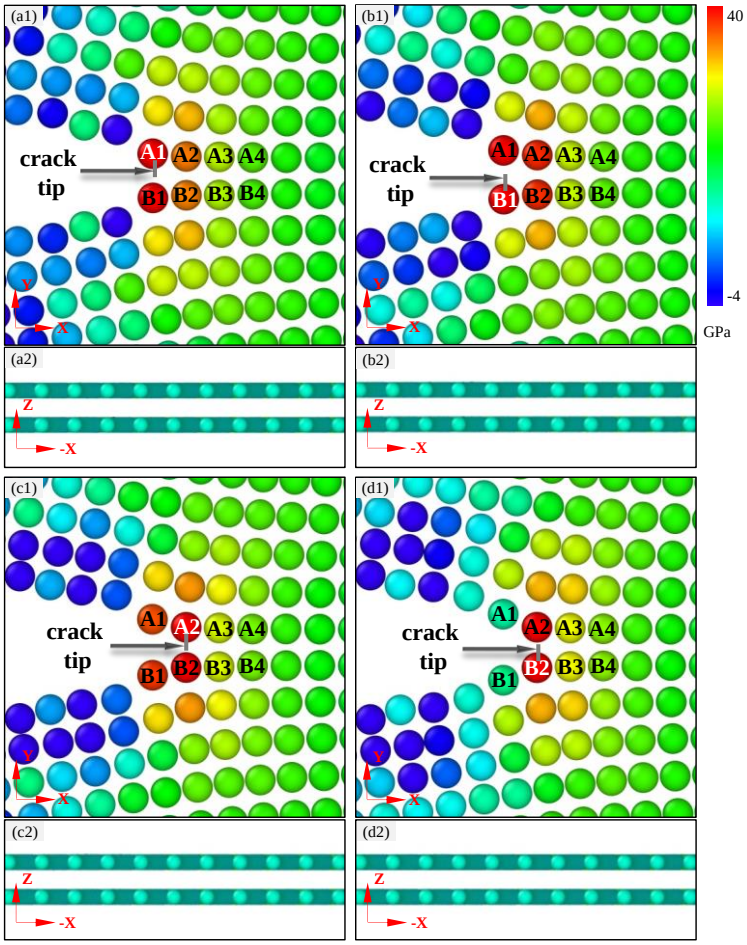

Figure 6.6 A sequence of atomic configurations around the crack tip with crack system of {100}<100>: (a) ε = 6.331%; (b) ε = 6.3315%; (c) ε = 6.332%; (d) ε = 6.3325%. (a-d) 4.17 Å ≤ Z ≤ 8.17 Å.

Figure 6.7(a) shows the tensile stress as a function of the imposed deformation strain for the A1-A4 and B1-B4 atoms. All the curves had a similar pattern, such that σ_y increased initially with increasing strain and then decreased after it reached a peak value. The stress for Atom A1 and Atom B1, or Atom A2 and Atom B2, or Atom A3 and Atom B3, or Atom A4 and Atom B4 was almost equal because of the symmetrical geometric structure. The curves for the two neighbouring atoms intersected at a certain point, for example, σ_y for Atom A1/B1 and Atom A2/B2 had

an intersecting point (Point I_2) at ε = 6.332%. It was clear too that between Point I_1 and Point I_2, the stress for Atom A1 and Atom B1 was higher than the stress for other atoms A2-A4 and B2-B4, which overlapped with the maximum tensile stress curve assigned by the black dashed line. This means that the maximum crack tip position was located at Atom A1 or Atom B1, as seen in Figure 6.7(b).

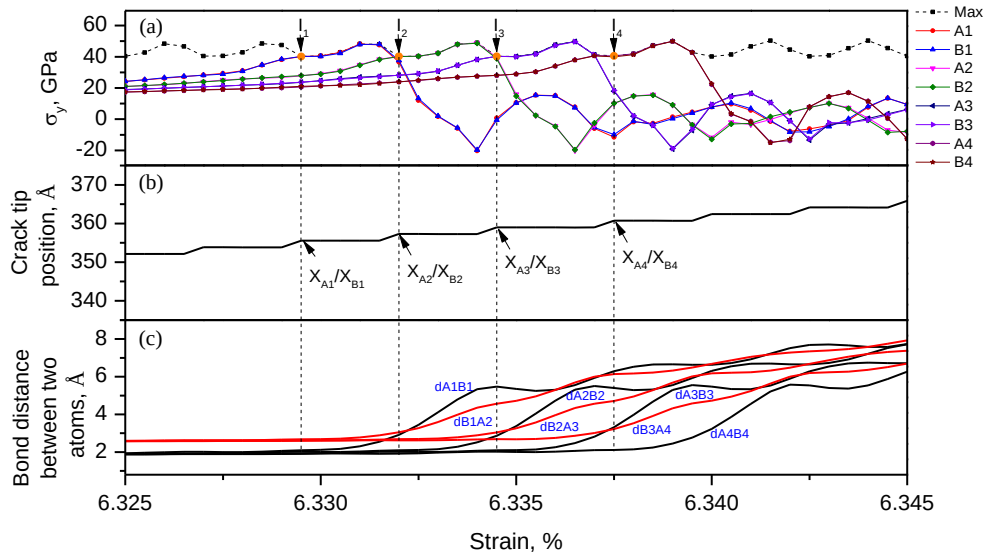

Figure 6.7 Simulation results of selected atoms at {100}<100> crack system: (a) σ_y; (b) crack tip position; (c) bond distance between a Group-A atom and a Group-B atom.

As the atomic debonding between Atom A1 and Atom B1 continued, the σ_y of them was gradually relieved, which corresponds to the gradually decreasing curve after the peak value (see Figure 6.7(a)). Elastic deformation piled up to the forward region and covered Atom A2 or Atom B2, and therefore their stresses increased. To the right of I_2, the stress for Atom A2/B2 exceeded that for Atom A1/B1, but by then the crack tip had moved to the position of Atom A2/B2. At the interaction of Point I_3 (ε = 6.3345%) and I_4 (ε = 6.3375%), the atomic bonds between Atom A3 and Atom B3, and between Atom A4 and Atom B4 began to break. In Figure 6.7(c), the distances between Group-A and Group-B atoms were tracked, and as Figure 6.5 and Figure 6.6 shows, the highest tensile stress at the crack tip triggered the atom bonds breaking,

which led to an increasing distance between the two marked atoms. This coincided with the distance of d_{A1B1}(/d_{B1A2}), d_{A2B2}(/d_{B2A3}), d_{A3B3}(/d_{B3A4}) and d_{A4B4} starts to increase sharply at Point I_1, I_2, I_3, and I_4, respectively.

The perfect atomic cleavage along the central crack plane shifted to the void movement ahead the crack tip as the imposed strain increase to a critical value. The following part will reveal the transition mechanism from the atomic viewpoint. Figure 6.8 shows a sequence of atomic configurations around the crack tip for two successive (001) planes that were initially located at Z = 5.268 Å and Z = 7.036 Å, and which are defined as the first (001) plane and the second (001) plane respectively. The atoms on the first (001) plane and the second (001) plane were coloured near-blue and near-yellow, according to their Z coordinates, respectively, as shown in Figure 6.8(a1-d1). Figure 6.8(a2-d2) shows the same atomic configurations as in Figure 6.8(a1-d1), using the CNA method to assign colour to each atom. The grey and green atoms represented the perfect fcc structure and disordered structures, respectively.

The atoms A1~A5, B1~B5, C1~C5, D1~D5, E1~E5 and F1~F5 ahead of the crack tip were marked as shown in Figure 6.8(a). This snapshot depicts the instant of onset of Z direction movement for atom at 6.3735% deformation. All the atoms were still located on their original (001) planes, and the atoms for Group A and B, Group C and E, Group D and F were relatively symmetric to the central crack plane. At small time intervals, Atom A1 and Atom B1 moved towards the Z and -Z directions, respectively in Figure 6.8(b), and Atom B2 showed a slight displacement along the -Z direction, which suggested that atoms tend to move out of the original (001) plane. At ε = 6.3375%, Atom A1, Atom B1, and Atom B2 moved continually along the Z and -Z direction with a large displacement, while Atoms A4 and Atom B4 moved out of the (001) plane in the opposite Z direction. The symmetric geometrical relationship shown in Figure 6.8(a) was ruined, and the atomic configuration inclined to become a

disordered arrangement ahead the crack tip, being called a local structure transformation. With the same theory, more atoms were involved in moving in the Z direction (e.g. Atom A5, Atom B5, and Atom E5) when the strain reached 6.3835%.

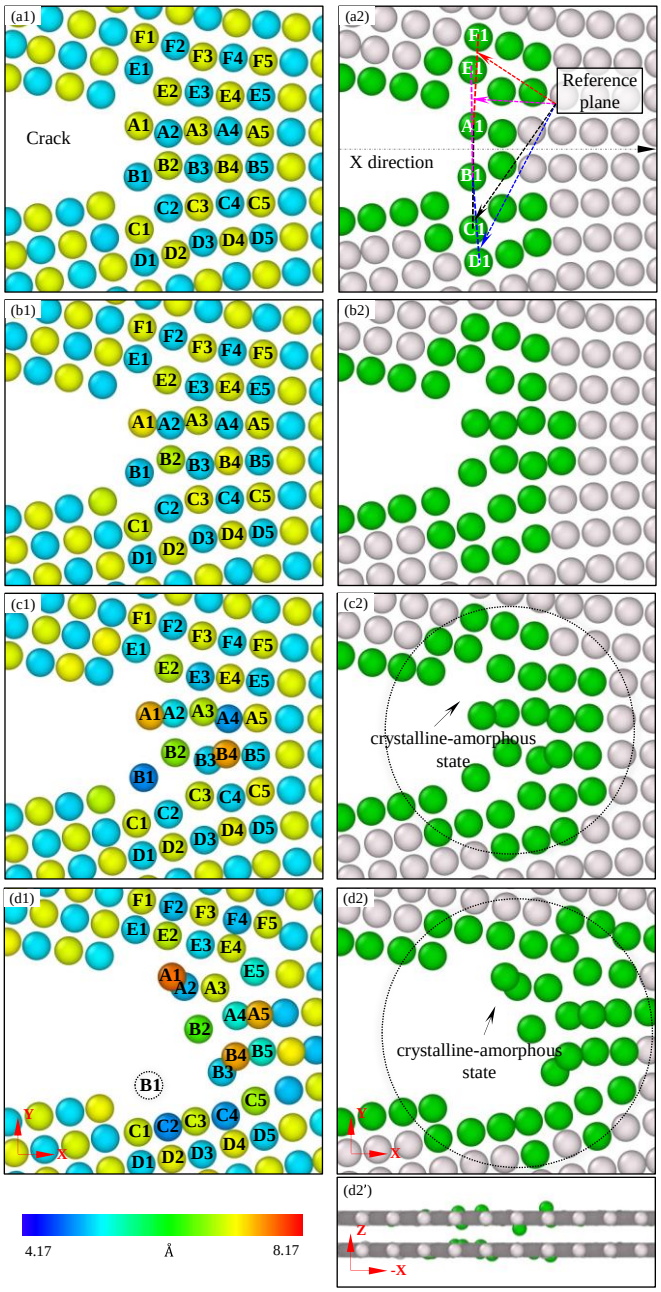

Figure 6.8 Atomic configuration (a1-a5) and local crystal structure (b1-b5) around the crack tip for two successive (001) planes at different strains: (a1-b1) ε = 6.3735%; (a2-b2) ε = 6.3750%; (a3-b3) ε = 6.3775%; (a4-b4) ε = 6.3835%.

It is worth noting that Atom B1 had moved into the adjacent (001) plane along the -Z direction, leaving a vacancy in the original position in (001) plane, as shown in Figure 6.8(d). Displacement in the Z can be identified very well in Figure 6.8(d2) because such a movement results in a crystalline-amorphous structure, and the newly formed disordered non-crystalline structure shields the atom at the crack tip and impedes the increase of its stresses at this small concentrated region. Figure 6.5 shows that the region of stress concentration had extended to a remotely large region which arrested the bond breaking process just ahead of the crack tip. Atomic cleavage between the two (010) planes was not a regular occurrence along the original crack plane, although its cleavage speed had decreased, as the slope indicates in Figure 6.3(a).

Since the Z direction displacement, crack propagation changed from brittle to ductile fracture, where the void nucleated in front of the crack tip, and then joined the main crack. This process was same as the previous study [200] regarding single Ni. To understand the underlying reason for local structure transformation, I tracked the distance between each two atoms by Group-A and Group-C, Group-A and Group-F, Group-B and Group-D, Group-B and Group-E, where the two atoms were located in the same (001) plane. These maximum distances between two Groups always occurred near the crack tip. In Figure 6.9, the bond distances of d_{A1C1}, d_{A1F1}, d_{B1D1}, d_{B1E1} as a function of the imposed strain were plotted, and indicated that they slowly increased with the strain. The bond distance of d_{A1C1} and d_{B1E1} was much larger than d_{A1F1} and d_{B1D1}, but after 6.36% of deformation, the bond distances for all the groups had a large increase. As the bond distances of d_{A1C1} and d_{B1E1} reached a critical value of almost 5.667 Å at $\varepsilon = 6.373\%$, structure transformation occurred because when the bond distance between two atoms are in the same (001) plane, the space between those two atoms is enlarged, which in turn creates a large attractive force between the atoms around the enlarged region. When the space between Group-A atoms and

Group-C atoms (such as Atom B1 in Figure 6.8(b1)) becomes large enough, the force will assist those atoms (e.g. B1) to overcome the energy barrier and take up the space in the closest neighbouring (001) plane. These few early movement of atoms in the Z direction induces more atoms to move along the Z direction due to the increasing space between them. This transforms the structure from an fcc structure to a random network with a disordered structure.

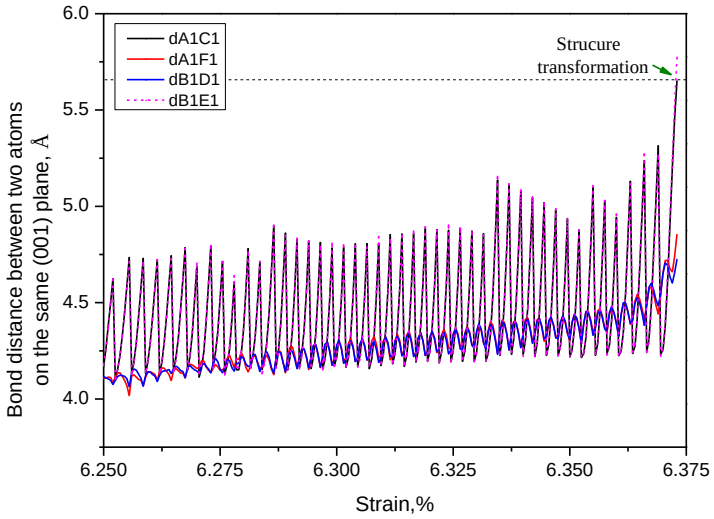

Figure 6.9 The distance between the atomic bonds of two Groups as a function of the imposed strain.

The increasing distance in the bonds between the two Group's atoms can be explained by the change of angle between the reference plane and the X direction. The reference planes across two atoms of Group-A and Group-C, Group-A and Group-F, Group-B and Group-D, Group-B and Group-E, that are parallel to the Z axis, are defined in Figure 6.8(a2). The angle between the reference planes and the X axis was labelled as a_{A1C1} (or θ_{AC}), a_{A1F1} (or θ_{AF}), a_{B1D1} (or θ_{BD}), a_{B1E1} (or θ_{BE}), respectively. Its relationship with the applied strain was plotted in Figure 6.10. These angles generally increased with the imposed strain, and the reference planes are rotated and inclined to the Y axis as the crack propagates, which leads to higher angles, as seen in Figure

6.10. This increased angle helps atoms such as Atom E1 and Atom C1 to move towards the crack opening direction, and increases the distance between two atoms of Group-A and Group-C, Group-A and Group-F, Group-B and Group-D, Group-B and Group-E; this agrees with the increased bond distances of d_{A1C1}, d_{A1F1}, d_{B1D1}, d_{B1E1} in Figure 6.9.

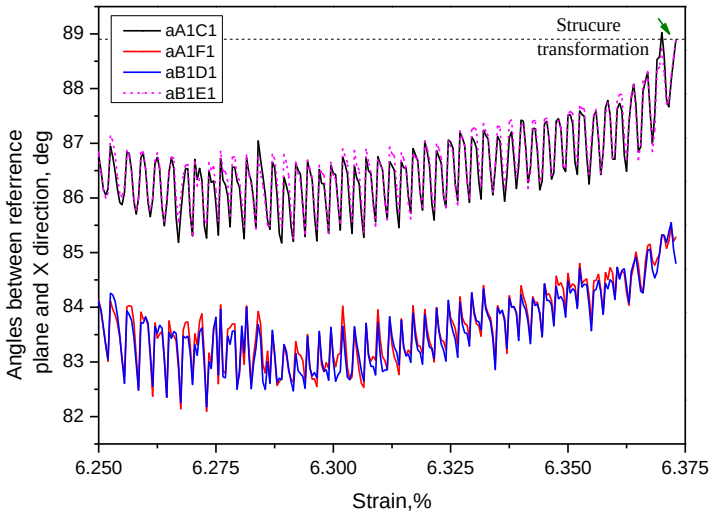

Figure 6.10 Angle θ between reference plane and the X direction as a function of the imposed strain.

As with the study in nanotwinned Cu and Ni discussed in Chapters 3 and 4, the dynamic atomic movement induces the transformation of local structure that leads to a final brittle-to-ductile fracture transition, but due to the different and specific atomic orientations, the consequent atomic configurations are different. In nanotwinned Cu and Ni, the structure was able to transfer to a local base-centred orthorhombic structure and form a local twin ahead of the crack tip. However, in {100}⟨100⟩ orientation system, the Z direction atomic movement cannot induce the structure to transform into a stable structure due to the non-planar arrangement, although a very few bcc and hcp atoms were seen ahead of the crack tip. The atomic structure had a disordered arrangement known as a crystalline-amorphous state rather than a

dislocation/twin formation. The beginnings of similar crystalline-amorphous states have found in most thermodynamically and kinetically favourable modes, and will compete against crack cleavage and dislocation [248] in silicon, although high stresses were concentrated around the crystalline-amorphous region, and void was expected to dominate the crack-tip response. When the atom bonds rotated slightly the stress concentration in front of the crystalline-amorphous region decreased to a lower level, dislocation nucleation and emission was another underlying mechanism for plastic deformation (see Figure 6.4(d)).

While the {100}⟨110⟩ crack system depended on the front of the crack, it was difficult for the atomic bonds to break during tensile deformation. I checked the stress states at the crack tip region in Figure 6.11 and noted that the local stress distributions could not meet the conditions required for crack propagation. Moreover, the distribution of tensile stress and stress triaxiality was not highly concentrated, especially with stress triaxiality which had already proven to be one of the most important criteria for fracture cleavage, which means that breaking the atom bonds cannot be triggered by local stresses. The relatively high stresses near the crack tip prefer to be released by dislocation activities.

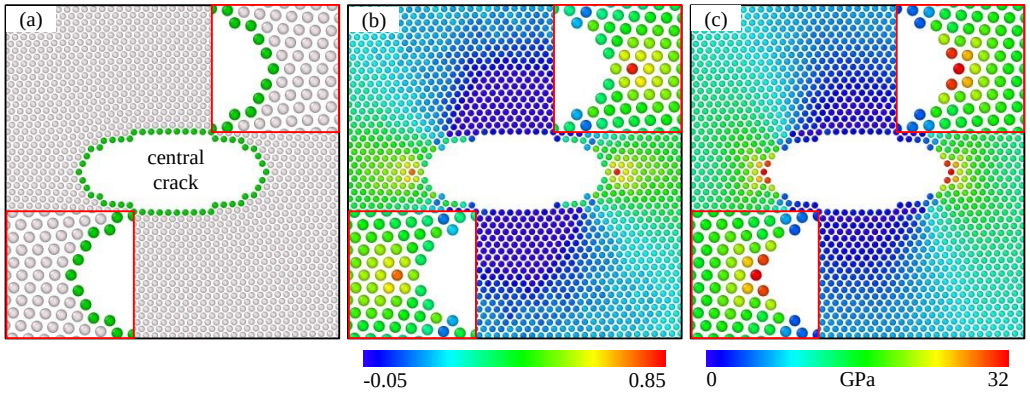

Figure 6.11 Field contours of stress indicators distribution just before the onset of dislocation nucleation near the crack tip with a crack system of {100}<110>: (a) CNA; (b) σ_{tri}; (c) σ_y.

In Figure 6.12, the leading partial dislocation $\boldsymbol{A\delta}$ was nucleated in (111) slip plane (see Figure 6.12(b)), followed by the trailing partial dislocation $\boldsymbol{\delta B}$ in the same slip plane, and then a perfect dislocation $\boldsymbol{AB}$ was formed in Figure 6.12(c). On the right hand side of the crack tip, another partial dislocation $\boldsymbol{A\beta}$ was nucleated in $(1\bar{1}\bar{1})$ slip plane at the left-hand side of crack tip in Figure 6.12(d). The perfect $\boldsymbol{AB}$ dislocation along the (111) plane was unstable, and dissociated into the two partial dislocations $\boldsymbol{A\delta + \delta B}$ that were again in the same (111) plane. Because the partial dislocation $\boldsymbol{A\delta}$ can be equivalent to the dissociated dislocation $\boldsymbol{\delta C + \delta B}$, the perfect dislocation $\boldsymbol{AB}$ finally changed into dislocations by $\boldsymbol{\delta C + 2\delta B}$ (see Figure 6.12(e)). Similarly, the trailing partial dislocation $\boldsymbol{\beta D}$ combined with the leading partial dislocation $\boldsymbol{A\beta}$ to form a perfect dislocation $\boldsymbol{AD}$, which further dissociated into one partial dislocation $\boldsymbol{\beta C}$ and a complicated dislocation structure within $2\boldsymbol{\beta D}$ in Figure 6.12(f). A new perfect dislocation $\boldsymbol{CB}$ formed by two partial dislocations $\boldsymbol{C\delta}$ and $\boldsymbol{\delta B}$ moved down toward the left-bottom side in Figure 6.12(f), and encountered the partial dislocation $\boldsymbol{C\delta}$. Its reaction resulted in a residual partial dislocation $\boldsymbol{\delta B}$ with the same vector with another leading partial dislocation $\boldsymbol{\delta B}$. These same two partial dislocations destabilised the local atomic structure due to their high energy. This caused atoms in the same (111) plane to energetically favour slipping in the opposite direction ($\boldsymbol{B\delta}$), and left trails of vacancy behind the jog (it is referred to in Figure 6.12(h-i)). Note that that the vacancy was pinned at the inner of the atomic model. Figure 6.12(h-i) shows that $\boldsymbol{C\delta}$ and $\boldsymbol{\delta B}$ partial dislocations were emitted from the upper-right hand side of the crack tip, and the $\boldsymbol{C\delta}$ partial dislocation was translated into two partial dislocation $\boldsymbol{\delta A}$ and $\boldsymbol{\delta B}$ on the nearest neighbouring (111) plane. Therefore, an extrinsic stacking fault by two $\boldsymbol{\delta B}$ partial dislocation on an adjacent (111) plane was observed. Further successive dislocation activities were involved with the increased tensile deformation to reduce the stress concentration and impede crack cleavage ahead of the crack tip. This means the crack system of $\{100\}\langle 110\rangle$ exhibited fully ductile behaviour by dislocation-mediated deformation mechanism.

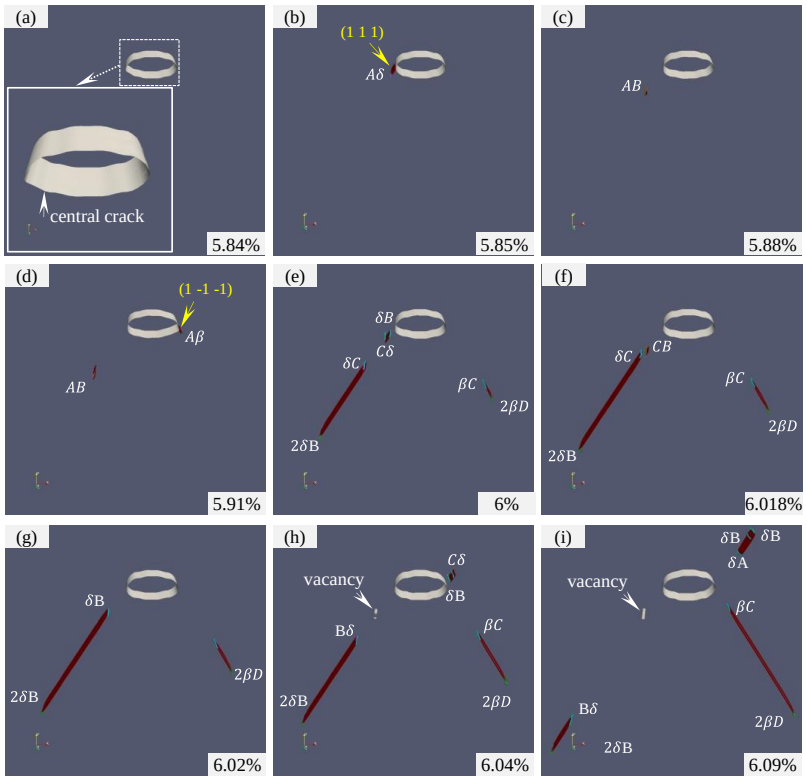

Figure 6.12 Snapshots of the simulation cell with crack system of {100}<110> subjected to different strains.

6.3.3 {110}<111>, {110}<110> and {110}<100> orientations

Cracks on the {110} plane and with ⟨111⟩ crack front direction showed ductile behaviour caused by dislocation movement. Figure 6.13 depicts the evolution of deformation mechanisms near the crack surface at an early stage of deformation, while dislocation was nucleated and emitted from the crack tip. Note the difference in the crack system of {100}⟨110⟩, where dislocation was nucleated from the ledge ahead of the crack in the crack system of {110}⟨111⟩. The atomic bond was able to cleave for a very short distance when the stress reached a critical value, but because the stress concentration was not distributed uniformly along the crack front due to its crystallographic structure, the atomic bonds between two atomic layers along the Y axial direction broke while others still remained intact. It led to a non-synchronous crack propagation at the crack front that left a group of ledges forming on it (see inset

in Figure 6.13(a)). As discussed in Chapters 3-4 and in other previous literatures, the ledge acted like a facilitated source for dislocation nucleating. In Figure 6.13(b), and (c), the Shockley partial dislocations were nucleated from the ledges and glide in slip planes. In Figure 6.13(d), the stair-rod dislocation connected the stacking faults in two slip planes: $\frac{1}{6}\langle 2\bar{1}1\rangle + \frac{1}{6}\langle \bar{1}1\bar{2}\rangle \rightarrow \frac{1}{6}\langle 10\bar{1}\rangle$, where the magenta coloured lines corresponded to the stair-rod dislocation. The stair-rod dislocations did not locate into the slip system in either glide plane because they generally resist the motion of other dislocations that give the model a hardening effect. Slip caused by dislocation gliding in these slip planes blunts the crack tip and reduces stress concentration at the crack tip. No obvious brittle crack propagation by atomic bonds breaking occurred during the whole deformation process for this crack system.

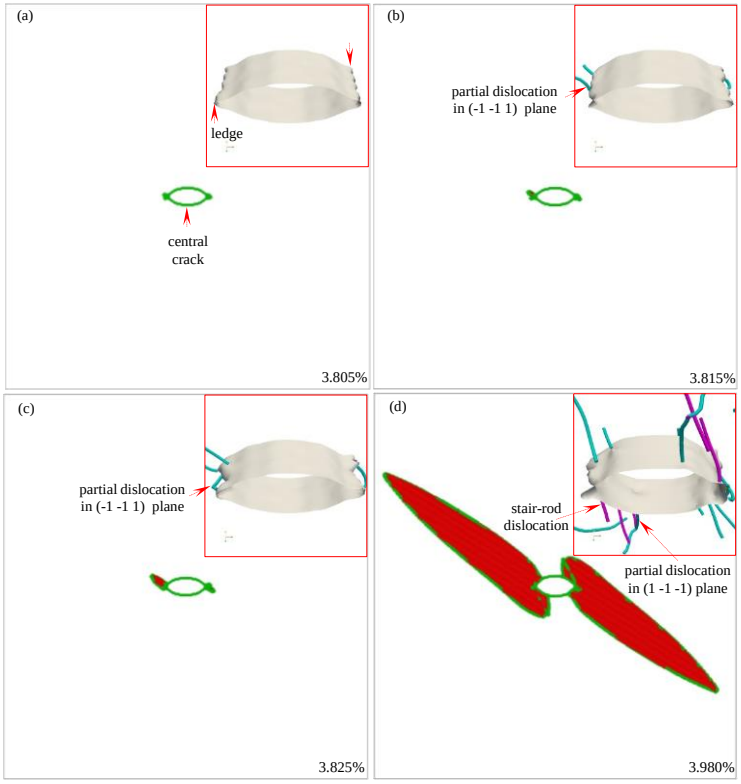

Figure 6.13 Snapshots of the simulation cell with crack system of {110}<111> subjected to different strains. Enlarged images show the near-tip structure as well as the crack face. Atoms or dislocation vectors were coloured according to the CNA, DXA, and CA. Perfect fcc atoms are filtered in CNA visualised images.

The formation mechanism of a non-synchronous crack can be understood in Figure 6.14 where two slices of atomic configurations along the Z direction were used to analyse the underlying reason for the non-synchronous crack (see Figure 6.14(a), and the stress states ahead of the crack tip exhibited non-uniformed features along the Z axis. The stress triaxiality shows a high concentration at the left-hand region of the crack tip and a relatively low concentration at the right-hand region of the crack tip in Slice 1, while the distribution in Slice 2 was the opposite (see Figure 6.14(b)). As with the stress triaxiality, tensile stress had a large value on the left-hand side of crack tip and small value at the right-hand side of the crack tip in Slice 1. In Slice 2 the scenario of tensile stress distribution was the opposite of Slice 1. The atomic cleavage of the crack was its response to the local stress states because the atomic bonds at this region, where stress triaxiality and tensile stress is high, are subjected to a sufficient local strain deformation and will therefore cleave. Crack cleavage can take place at the left-hand crack tip, but it cannot take place at the right-hand crack tip in Slice 1. However, in Slice 2, the atomic bonds break at the right-hand side of crack tip, not at the left hand side, which means that crack cleavage at both sides of crack tip cannot occur in the Z direction; this explains the non-synchronous crack propagation at the crack front that led to the formation of a series of ledges at the crack front (see Figure 6.13). Figure 6.14 shows there was a sharp difference in the stress distribution at the crack tip for the adjacent two atomic planes in Slice 1 or in Slice 2, all of which may contribute to the non-synchronous crack propagation. Dislocations nucleated from the ledges gradually govern the deformation. This deformation mechanism was identical to the mechanism in nanotwinned Cu and Ni single structures at high temperatures.

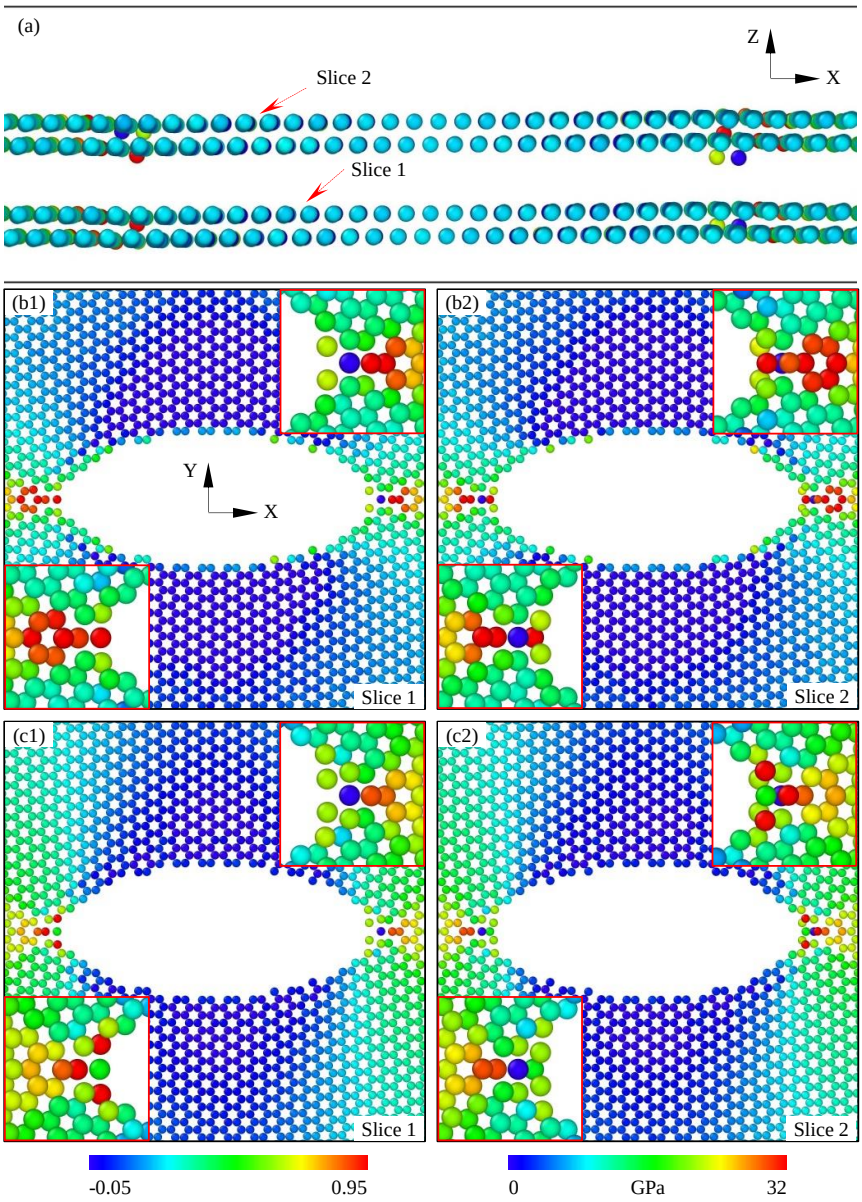

Figure 6.14 Field contours of stress indicators distribution nearby the crack tip just before the onset of atom bonds breaking for {110}<111> crack system. (a) Slice 1--2.9 Å ≤ Z ≤ 6.9 Å, Slice 2--10.9 Å ≤ Z ≤ 14.9 Å; (b) σ_{tri}; (c) σ_y.

As in the {110}⟨110⟩ and {110}⟨100⟩ crack systems, dislocation in the slip planes were mainly activated because deformation exhibited a very obvious ductile behaviour, which was similar to the {110}⟨111⟩ crack system. However, the evolution of the deformation mechanism with mechanical behaviour for the {111} crack planes was not the same because of the various lattice orientations. This was

identified by the tensile stress-strain curves shown in Figure 6.3. At the elastic stage, orientations of {110}⟨110⟩ and {110}⟨100⟩ showed the same elastic deformation, while the orientation of {110}⟨111⟩ had the bigger tensile stress and the effective young's modulus. When the stress reached a maximum value at about 3.8% deformation in {110}⟨111⟩ crack system, the stress dropped sharply as atomic cleavage occurred ahead of the crack tip, followed by a ledge forming at the crack front. The crack cleavage was prior to the dislocation nucleation. In contrast, for the {110}⟨110⟩ and {110}⟨100⟩ crack systems, the Shockley partial dislocation was nucleated at about 3.8% and 5.25% deformation from the crack tip without atomic cleavage, respectively. The stress then decreased because the dislocation motion released the elastic strain in the system which in turn, suppressed the propagation of crack cleavage at the crack front. The deformation mechanism in those two orientation systems was associated with the dislocation and can be divided two categories: (i) twin partials contributing to the deformation, and (ii) only dislocation motion contributed to deformation. As Figure 6.15(a) shows for {110}⟨110⟩ orientation, the Shockley partial dislocation was nucleated at the crack front, leaving the stacking fault behind, and then more dislocations began to nucleate and emit from the crack tip in different slip planes, leading to a significant decrease in the tensile stress. Partial dislocations were continually nucleated from the crack tip in the adjacent slip planes, which led to the formation of twin (see Figure 6.15(c)), which implied that the trailing of partial dislocations were suppressed in this specifically atomic crack configuration. Twin acts like an obstacle to the dislocation move [125], so when it approached the TBs, a high shear stress was needed for the dislocations to penetrate the TBs; this led to dislocations being blocked between the TBs (see the white dashed circles in Figure 6.15(c)). This blocking dislocation-twin interaction performed a less plastic deformation than the free movement of dislocation on the slip planes with the result being that the atomic model was hardened and the systemic tensile stress increased as the strain deformation increased. Once the local shear stress

reached the condition of dislocation interaction with the TBs, the dislocation can directly or indirectly penetrate the TBs, the detailed mechanism is referred to [122, 155], leaving the stair-rod dislocation on it or a step in the twin plane. The dislocation and twin activities caused crack tip blunting and prevented the crack from propagating. The length of the crack and the crack tip opening displacement versus strain relationship is shown in Figure 6.3(b).

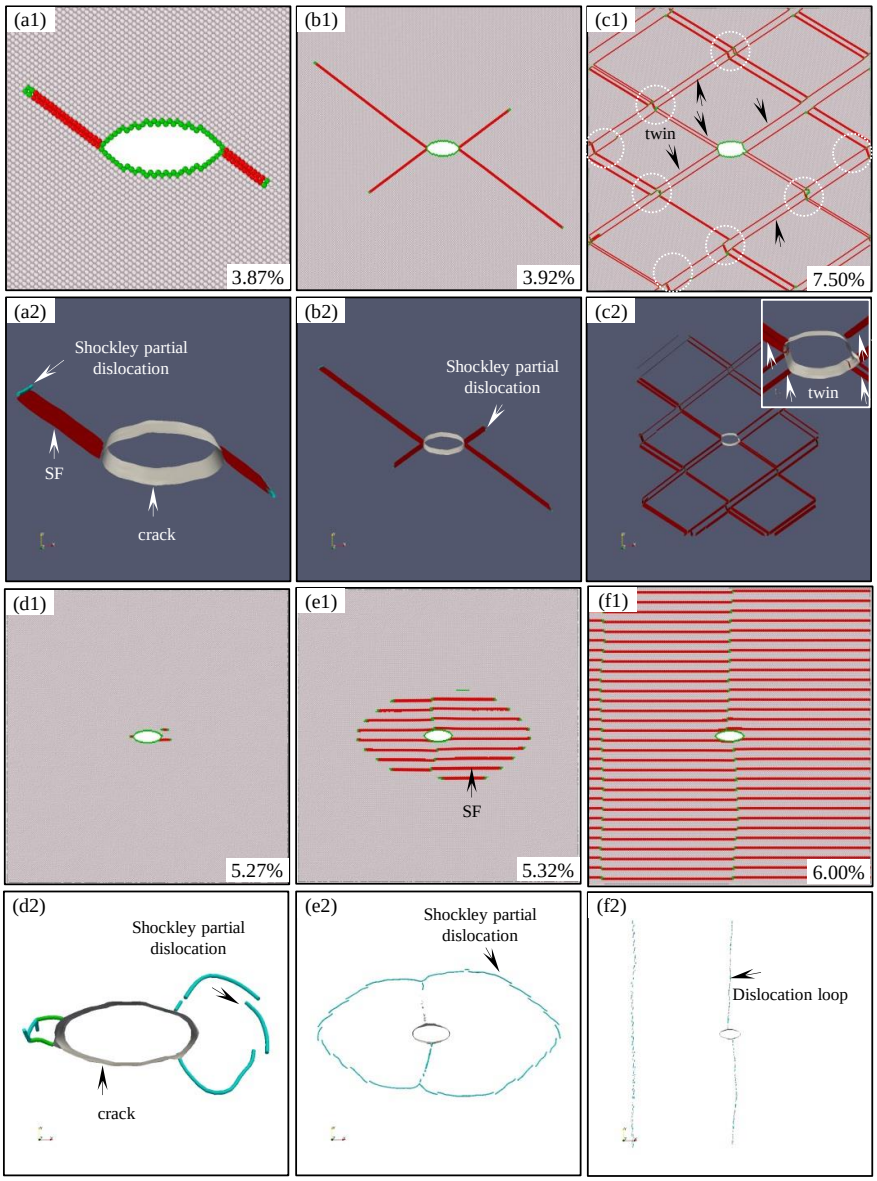

Figure 6.15 Snapshots of the simulation cell with crack system of (a-c) {110}<110> and (d-f) {110}<100> orientations.

Unlike the {110}⟨110⟩ orientation, only a few deformation twins were nucleated in {110}⟨100⟩ orientation because the partial dislocations interacted with each other to construct many dislocation loops (see Figure 6.15(f)). How the dislocation loops contributed to the hardening effect that caused an increase in the tensile stress is still not clear. The breaking of atomic bonds at the crack tip was suppressed, as expected, due to the dislocation activity, while the crack propagation and opening distance under an incremental loading is as shown in Figure 6.3(b). These intriguing results showed that not only crack cleavage, but also the crack opening were suppressed.

To summarise the {110} crack plane, regardless of the crack front configuration, dislocation motion favoured deformation mechanism, which indicated that the crack orientation ({110} plane) is an intrinsic ductility orientation and is single Ni. The results are good in accordance with highest amount of energy needed to create new free surfaces and biggest value of $2r_{sur}/r_{usf}$ compared to the other three orientations (see Table 6.1).

6.3.4 {111}<110> and {111}<112> orientations

The fracture of {111} plane showed a pronounced crack propagation dependence on the specific crack front orientations. With the ⟨110⟩ crack front direction, the crack underwent a semi-brittle propagation fashion, and with the ⟨112⟩ crack front direction, deformation was dominated by the complicated dislocation activities. Figure 6.16 shows snapshots of crack propagation on the {111} plane with ⟨110⟩ crack front direction. At ε = 2.8% deformation, as seen in Figure 6.16(a), Shockley partial dislocation was activated from the crack tip because atoms glide easily along the {111} plane due to the small geometric confinement at the crack tip. Partial dislocation was involved into the twins by successive multiple-atomic glides on the adjacent {111} planes in Figure 6.16(b). Due to the implications of periodic boundary condition, the fact that dislocations travels across the whole model could not be ignored, and it may give rise to the sort of softening effect of the atomic system.

Stress subsequently accumulated with the increasing imposed strain ahead of the crack to trigger the atomic bonds breaking, because the local stresses increased enough. In Figure 6.16(c-d), this crack system shows semi-brittle fracture where at each side of central crack, the crack propagated with full atomic cleavage and half atomic cleavage which coexist with the dislocations on the top and bottom of the central crack plane. At each interaction terminals of dislocation and free surface, series of steps were left behind after the atoms glided away from the free surface, as seen the enlarged images in Figure 6.16(c-d). This distinctive crack cleavage process at two sides of central crack plane suggested that the brittle or ductile response of this crack orientation depended on the directional anisotropy feature.

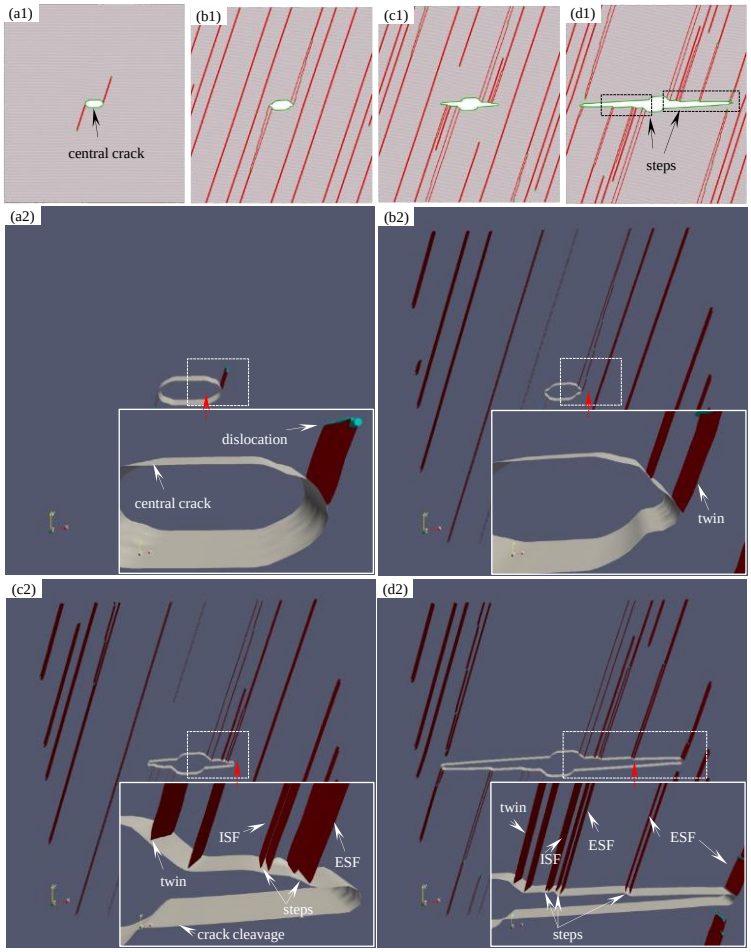

Figure 6.16 Snapshots of the simulation cell with crack system of {111}<110> subjected to different strains at (a) ε = 2.8%; (b) ε = 4.85%; (c) ε = 5.05%; (d) ε = 5.25%.

To reveal the crack cleavage's dependence on the specific lattice orientation for crack orientation of $\{111\}\langle 110\rangle$, several representative snapshots of crack dynamics from the complete crack cleavage stage to the dislocation nucleation stage for the half atomic model to the right are shown in Figure 6.17. Those snapshots are limited to the two (110) layers with the regime of $9.1\ \text{Å} \leq Z \leq 12.1\ \text{Å}$ where the crack propagation process was driven forward by two adjacent planes across the central crack plane being separated along the Y direction. Figure 6.17(b-c) shows that the atomic cleavage was related to the high tensile stress and stress triaxiality ahead of the crack tip, along with the local elastic strain, which constructed the basic conditions for atomic de-bonding. This criterion was discussed in Chapters 3 and 4. Because the atoms located in front of the crack tip always had the highest tensile stress for full crack cleavage I used this feature to define the crack tip position. Due to the special geometry, the atoms with the biggest tensile stress and stress triaxiality were always located in $(\bar{1}1\bar{1})$ planes, below the central crack cleavage plane, which meant that the deformation ability of the upper and lower lattices orientated to the central plane was different.

Six atoms near the crack tip were selected analyse the atomic cleavage process labelled A, B, C, D, E, and F. Atom D always had the largest tensile stress and was assigned at the crack tip (see Figure 6.17(b)). At ε = 5.0515% in Figure 6.17, the front shape of the crack was composed of highlighted yellow lines connected by the vertices of Atoms A, B, E and D. The crack was effectively moved forwards by the bonds breaking between Atom A and Atom E, and Atom A and Atom D. Atom A moved upwards and Atom D and Atom E moved downwards. In the next instant deformation, the three upper atoms A, B, C would be diverted to the positions of A', B', C'. The shape of the crack front was then constructed by the dashed black lines with the vertices of atoms A', B', E and D. I averaged the distances between Atoms B and E, while Atoms A and D were regarded as the crack tip opening

distance: $d_{CTOD} = (\Delta_{BE} + \Delta_{AD})/2$ (or $d_{CTOD} = ((\Delta_{B'E} + \Delta_{A'D}))\ /\ 2$). Because the atomic structure and its corresponding stress field were not uniform for two parts up and down to the central crack plane, their response to the local deformation of these two parts around the crack tip were different.

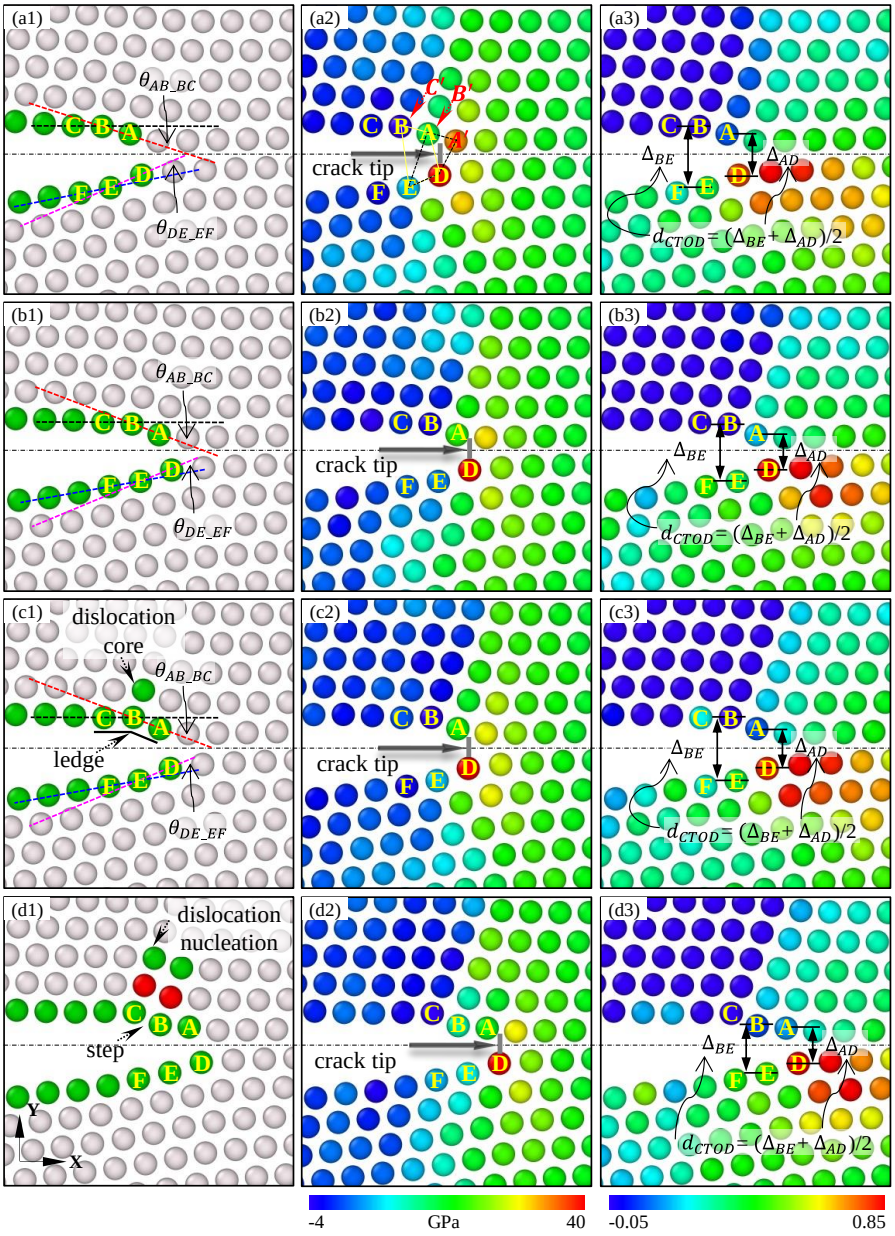

Figure 6.17 Field contours of stress indicators distribution just before the onset of dislocation nucleation nearby the crack tip with crack system of {111}<110> at (a) ε = 5.0515%; (b) ε = 5.0540%; (c) ε = 5.0555%; (c) ε = 5.0575%. (a1-d1) CNA; (a2-d2) σ_y; (a3-d3) σ_{tri}.

As Figure 6.17 shows, the atoms sharing the same $(\bar{1}11)$ planes with Atom D were the main driving force for the atomic bonds breaking due to the high tensile stress and stress triaxiality. This can be clearly identified by the moving distance of the upper and lower atoms on free surfaces away from the central crack plane. As the strain increased the specific local atomic configurations for Group A, B, and C, and Group D, E, and F showed essentially differential characteristics, but when the strain increased to 5.0555%, as shown in Figure 6.17(c), one ledge was formed by Atoms A, B, and C and the ledge served as the source of dislocation core nucleation. Finally, partial dislocation was nucleated at this ledge region at 5.0575% as shown in Figure 6.17(d). To better understand the dynamic mechanism for dislocation nucleation, reference planes were defined that cut through Atom A and Atom B, Atom B and Atom C, Atom D and Atom E, and Atom E and Atom F and parallel to the Z axis, being marked as Plane AB, BC, DE and EF, respectively. The angle ($a_{AB\_BC} = \theta_{AB\_BC}$) between Plane AB and Plane BC, and the angle ($a_{DE\_EF} = \theta_{DE\_EF}$) between Plane DE and Plane EF are shown schematically in Figure 6.17.

Figure 6.18(a) shows the θ_{AB_BC} and θ_{DE_EF} as the function of imposed strain, where the time instant t_1, t_2, t_3, corresponds to Figure 6.17(a), (b) and (c) snapshots respectively. Both angles showed a roughly increasing trend with increasing strains, and each angle exhibited up and down curves as the strains varied. The up and down trend of curves was caused by the varied moving distance for Atoms C and F compared to Atoms B and E from the central crack plane. If Atoms C and F moved away from the central crack plane, while Atoms B and E were still close to the central plane, it means that θ_{AB_BC} has a large value or θ_{DE_EF}. However, when the atomic bond occurred mainly between Atoms B and E, Atom B and Atom E moved away from the central crack plane towards Atom C and Atom F, which led to a small value of θ_{AB_BC} or θ_{DE_EF}. It was observed that in Figure 6.17, the stress distribution was mainly concentrated in front of the crack region which was below the central crack

plane and the local plastic response by Group A, B, C atoms and Group D, E and F atoms did not coincide. It can be seen that before ε = 5.0485%, the peaks and valleys for θ_{AB_BC} or θ_{DE_EF} roughly corresponded, which means that bond breaking was dominated by atoms F, E and D moving in turn with, atoms C, B, and A. θ_{DE_EF} was closer to the constant value, while θ_{AB_BC} showed a large fluctuation. As the imposed strain proceeded to Point t_2 and Point t_3, the atomic cleavage ability at the crack tip became weaker because θ_{AB_BC} or θ_{DE_EF} had high values. For Point t_3 (ε = 5.0555%) in particular, θ_{DE_EF} approached its maximum value, which promoted the formation of a ledge at the upper free surface ahead of the crack tip.

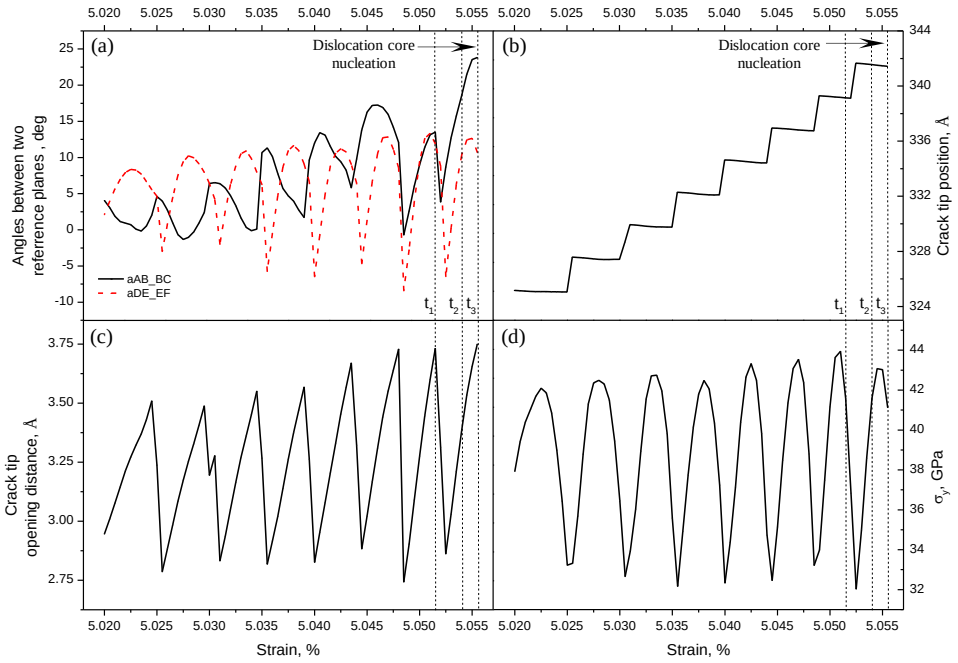

Figure 6.18 Simulation results of selected atoms at {111}<110> crack system: (a) Angle ($a_{AB-BC} = \theta_{AB-BC}$) between plane AB and BC, and angle ($a_{DE-EF} = \theta_{DE-EF}$) between plane DE and EF; (b) Crack tip position; (c) Crack tip opening distance; (d) Maximum tensile stress at the crack tip.

The crack tip opening distance shown in Figure 6.18(c) has serrated shapes because of the dynamic crack tip shape shown in Figure 6.17(a2). The peak value of the crack tip opening distance generally increased with increasing strain, and at ε = 5.0555% strain,

reached its highest value. As a consequence, the stress required for atomic cleavage increased because of this lowering of the crack opening stress intensity at the blunt tip, as shown in Figure 6.18(d). Crack blunting dominated the local plasticity, and it induced a change in the shape of the crack tip leading to the formation of a small ledge at the crack tip. This coincided with the increasing θ_{AB_BC} value in Figure 6.18(a). The occurrence of a ledge has already proved to be sensitive to the nucleation of dislocation [104]. Leading partial dislocation was nucleated at the ledge region, as seen in the Figure 6.17(d1), leaving one step behind on the free surface. The stress intensity piled up again at the crack tip to induce more atomic cleavage at the crack tip, but after the crack tip passed the dislocation region, parameters θ_{AB_BC}, θ_{DE_EF}, the crack tip opening distance was smoothed to a low level. Those values were dynamical and increased repeatedly with the increasing strain until next partial dislocation was nucleated and emitted from the free surface. This intrinsic differential for the upper and lower parts of the central crack enabled us to explain that the "clean" brittle fracture through the generation of perfectly flat atomic surfaces in one free surface, and semi-brittle fracture with a serials of steps on another opposite free surface through dislocation emission, as seen in Figure 6.16(d). These characteristics can be also used to understand the twin effects on the crack cleavage in nanotwinned single Cu and Ni crystals, and the directional orientation dependence feature for crack cleavage [69]. It was not difficult speculate that if another side within dislocation emission had the same atomic configuration within the side of complete atomic cleavage, i.e., the two sides of crystals with respect to the central crack plane shared the same crystal lattice points in a symmetrical manner. The crack would have exhibited a fully brittle fracture fashion without steps caused by the dislocation activity on the surface facets, just as the pre-existing twin affected the brittle behaviour in single twinned Cu and Ni crystals. The results of a fully atomistic approach offer insights into the mechanism where a pure single Ni crystal exhibited intrinsic ductility.

The detailed results with ⟨112⟩ crack front direction are shown in Figure 6.19. Unlike the other ductile crack systems, full dislocation with a burger vector of $1/6\,[101]$ slipping on (010) plane at about 3.25% deformation was the first to be nucleated from the crack front (see Figure 6.19(a)). This type of dislocation was rarely observed in previous literatures because most of them were shown the Shockley partial dislocation being nucleated on the major $\{111\}$ plane. This dislocation was also observed in the former chapter in the single twinned Cu crystal with identical crystal orientation. Those results proved that the type of dislocation was determined by its atomic crack configuration and the high local stress intensities. This dislocation finally reflected to the Shockley partial dislocations in the stable $\{111\}$ slip planes.

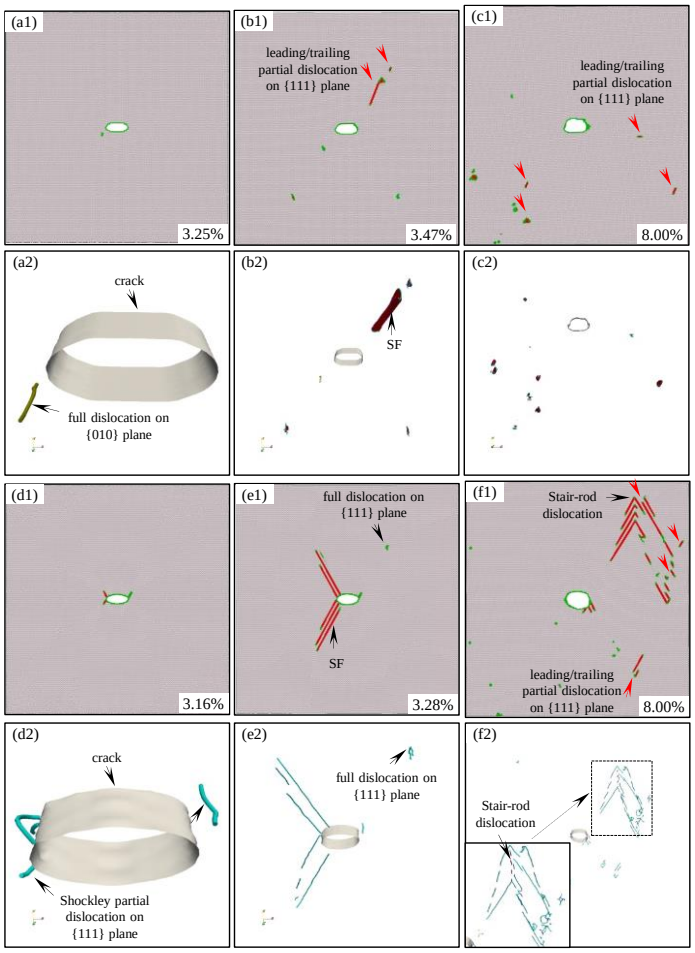

Figure 6.19 Snapshots of the simulation cell with crack system of (a-c) {111}<112> and (d-f) {112}<111> orientations.

As Figure 6.19(b-c) shows, more leading Shockley partial dislocations were nucleated at the crack front, followed by trailing partial dislocations. The successive structures by leading and trailing partial dislocations connected by the stacking faults were formed together with the full dislocations and stair-rod dislocations after their reactions by two partial dislocations to take over the major accommodation for plastic deformation. The pre-existing central crack almost always remained stagnant except for the opening distance along the Y axis direction. Their relationship between crack length, crack opening distance, and strain are shown in Figure 6.3(c).

6.3.5 {112}<110> and {112}<111> orientations

Similar to the $\{111\}\langle 112\rangle$ crack system, for the case of $\{112\}\langle 111\rangle$ system, the leading and trailing partial dislocation structures connected by the stacking faults were the main contributors to plastic deformation. The difference being that rather than full dislocation on (010) plane, the Shockley partial dislocation on $\{111\}$ plane was nucleated and emanated in front of the crack tip (see Figure 6.19). The trailing partial dislocations would be to slip on the same slip plane with the leading partial dislocation, reacting with the formed leading partial dislocation. One of the results of this reaction was to generate stair-rod dislocations which resulted in an enhanced hardening effect of the atomic model. This effect is shown in the stress-strain curve of Figure 6.2 by the increasing tensile stress as the tensile deformation enlarged. The crack tip kept opening and showed no appreciable sign of brittle cleavage (see Figure 6.3(d)).

As in the $\{112\}\langle 110\rangle$ crack system, the crack first propagated on the $(1\bar{1}\bar{1})$ plane, then diverted to another mixed plane accompanied by the dislocation activity. Figure 6.20 shows the competing crack-tip processes for $\{112\}\langle 110\rangle$ crack system. In Figure 6.20(a), the $(\bar{1}1\bar{1})$ plane was perpendicular to the crack cleavage plane and parallel to the tensile direction, which means that the Shockley partial dislocations were prone to nucleate and emit on the $(\bar{1}1\bar{1})$ planes from both sides of the crack tip owing to small

geometric constraints. The subsequent growth of the twin from the crack tip happened when the leading partial dislocation was followed by twinning partial dislocations on the adjacent slip planes, with the same formation mechanism seen in studies [56, 59]. After the twinned region widened and extended outwards as the partial dislocations propagated away from the crack tip, the model gradually reached a relatively stable configuration. Local elastic strain with a combination of large stress accumulated ahead the crack tip.

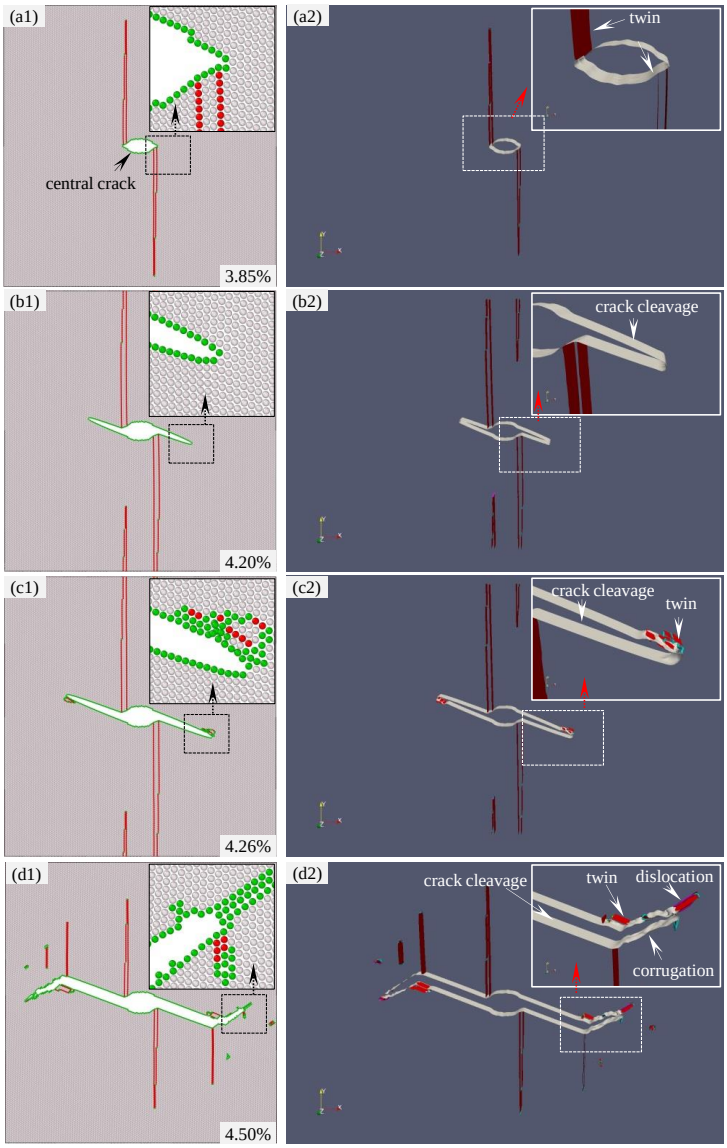

Figure 6.20 Snapshots of the simulation cell with crack system of {112}<110> subjected to different strains at (a) ε = 3.85%; (b) ε = 4.20%; (c) ε = 4.26%; (d) ε = 4.50%.

For increased imposed strain, the concentrated stresses ahead of the crack induced the atomic bond breakage seen in Figure 6.20(b). Remarkably, such crack cleavage was deflected from the original given crack plane to the $(1\bar{1}\bar{1})$ plane, unlike $\{100\}\langle100\rangle$ and $\{111\}\langle110\rangle$ crack orientations where crack cleavage occurred at the given cleavage plane. No dislocations were involved in this process, and the crack had a clean mirror smooth surface. As crack cleavage continued, the twin process starting with the phase transformation event induced by the out-of-plane movement was formed ahead of the crack tip, as shown in Figure 6.20(c). The twin formation effectively impeded the atomic bonds from breaking, leading to the dislocation to nucleate from the crack tip. The dislocations glided along the mismatched multi-planes ahead of the twin region proceeding forward. This process was associated with the bonds breaking along the gliding plane with increasing strain in the direction of the Y axis. The crack was still able to advance slowly upwards along the mixed planes, but it deviated from the former cleavage plane. The whole process yielded observable corrugated surface features, as seen in Figure 6.20(d).

Figure 6.21 shows the sequence of two-layer (110) stacking atomic configurations around the crack tip during crack cleavage for $\{112\}\langle110\rangle$ crack system where there was a region of high stress concentration in front of the crack tip. As discussed previously, those highly concentrated stresses ahead of the crack tip induced crack cleavage. Group-A atoms, labelled A1, A2, A3, A4, and Group-B atoms, labelled B1, B2, B3, B4 were aligned with the upper and lower $(1\bar{1}\bar{1})$ planes that were almost parallel to the crack cleavage plane. Two Group's disordered atoms labelled C, D and E, F nearest to the crack tip were located on the upper and lower free surfaces. I used them to represent the crack shape, and only referred to the profiles constituted by the blue solid lines. The crack shape should be shifted to another shape constituted by Atom C, Atom D and Atom E′ and Atom F′ with increasing applied strain (hence, the crack tip opening distance defines as: $d_{CTOD} = (\Delta_{CE} + \Delta_{DF})/2$ or $d_{CTOD} = ((\Delta_{CE'} +$

$\Delta_{DF'}$)) / 2). Figure 6.21 shows that all high stress indicators concentrated at the side of Group-A atoms, which was the same with the scenarios in {111}⟨110⟩ crack system. These features suggested that up and below the crack cleavage plane, the atomic dynamic plastic deformation at two sides was not exactly the same. Because the largest tensile stress was always located on Group-A atoms ahead of crack tip, this characteristic was used to define the crack tip position. At ε = 4.1495% deformation, Atom A1 had the largest tensile stress so the crack tip position was located at Atom A1, as seen in Figure 6.21(a). The crack remained forward as the crack tip moved from the Atom A1 position to the position of Atom A2 in Figure 6.21(b). The Group-A atoms and Group-B atoms moved upwards and downwards in the direction of the tension during crack cleavage. At ε = 4.1570% in Figure 6.21(c), the crack tip has moved to the Atom A3 position.

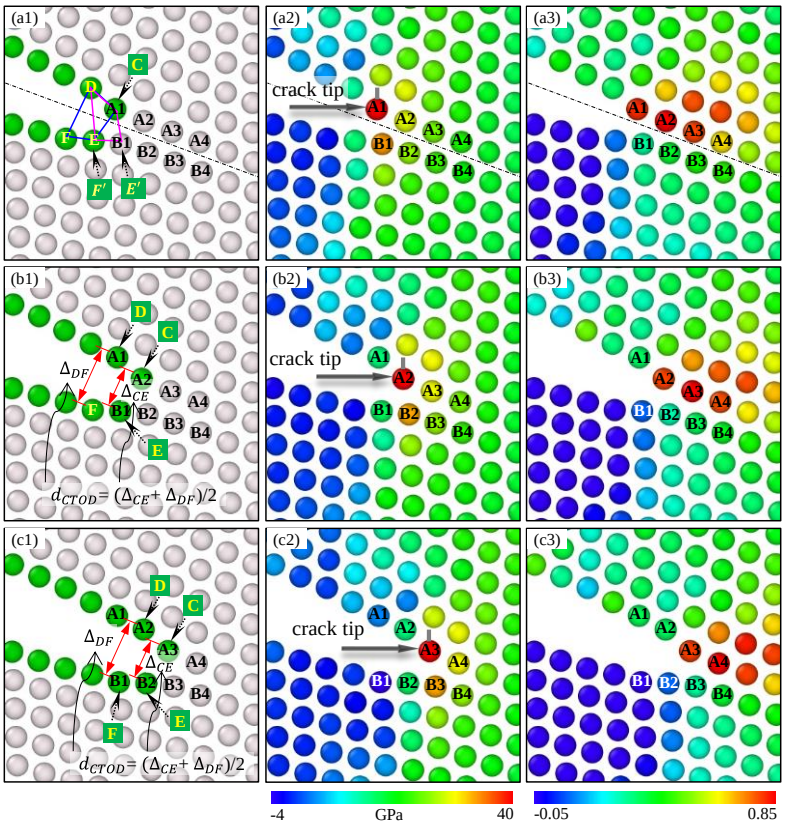

Figure 6.21 A sequence of snapshots about the crack cleavage process with the crack system of {112}<110> at (a) ε = 4.1495%; (b) ε = 4.1535%; (c) ε = 4.1570%. (a1-c1) CNA; (a2-c2) σ_y; (a3-c3) σ_{tri}.

This above event was plotted in Figure 6.22(a), and shows that all the curves around the tensile stress versus strain of the selected atoms exhibited a very similar pattern, where σ_y initially increased to a peak value with increasing strain and then decreased to almost 0 GPa. It was noted that the tensile stress of the Group-A atoms intersected with the maximum tensile stress of systemic model, marked I_1, I_2, I_3, I_4. Of these intersections, the tensile stresses of the Group-A atoms equalled the value of the maximum tensile stress, and were all larger than the Group-B atoms. This implied that the Group-A atoms were the main atoms driven over the Group-B atoms. For example, between Point I_1 and Point I_2, the tensile stress of Atom A1 gradually increased to a peak value and then Atom A1 was dragged further away from its original position along the +Y direction while Atom B1 was moving along the -Y direction. The current crack tip position was located at the position of Atom A1. The tensile stress for Atom B1 was always lower than Atom A1, but after Atoms A1 and B1 moved further away their tensile stresses began to return to approximately 0 GPa. To the right of Point I_2, a larger stress was diverted towards Atom A2, and the crack tip moved to this position. The curve of the crack tip position against strain was plotted in Figure 6.22(b). Once the tensile stress of Group-A atom reached the maximum value of the system, its atomic bonds with the corresponding Group-B atom broke and the crack tip was then located at the Group-A atom. Thus the crack tip can be seen at the position of X_{A1} (A1) to the right Point of I_1 at $\varepsilon = 4.1455\%$. When the stress of Atom A2 exceeded the stress of Atom A1, the crack tip moved to X_{A2} (A2) from X_{A1} (A1), while the crack tip changed to the X_{A3} (A3) and X_{A4} (A4) positions at 4.155% and 4.157% deformation, respectively.

Figure 6.22(c) plots the crack tip opening distance as a function of applied strain. Because the shape of the crack had changed dynamically, the tip exhibited an array of serrations as the crack opened and their peak values generally remained constant during the perfect crack cleavage process. The bond distance of the two atoms at the

crack tip is shown in Figure 6.22(d), and indicated that this distance increased sharply after the bond broke, as seen by the d_{A1B1}, d_{A1B2} after Point I_1. This response corresponded completely with the crack tip position in Figure 6.22(b) and the crack tip opening distance in Figure 6.22(c).

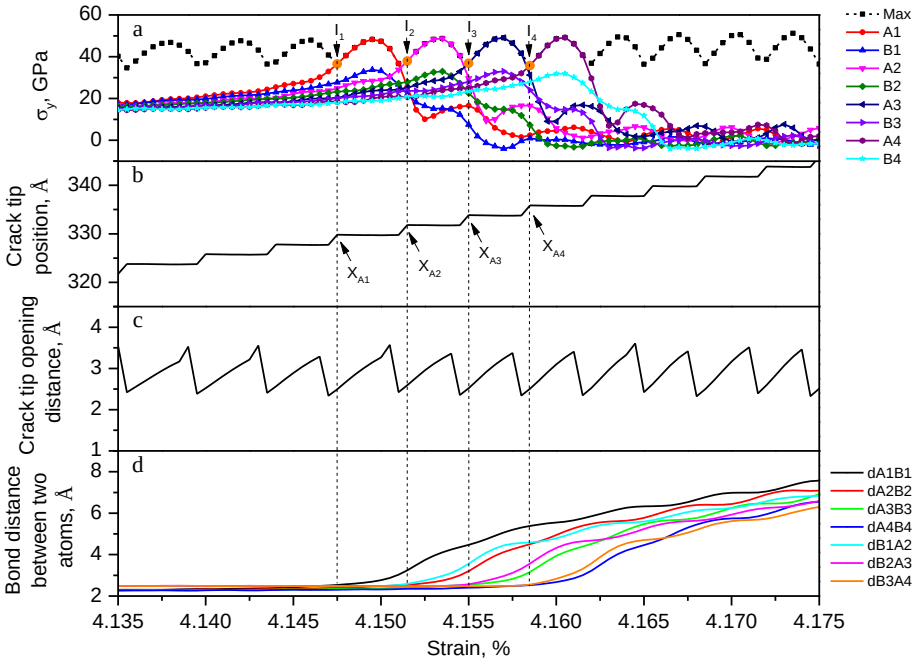

Figure 6.22 Simulation results of selected atoms at {112}<110> crack system: (a) σ_y; (b) crack tip position; (c) crack tip opening distance (CTOD); (d) bond distance between a Group-A atom and a Group-B atom.

A perfect crack cleavage movement was prevented by out-of-plane movement along the Z direction (phase transformation) for {112}⟨110⟩ orientation, accompanied by the formation of another twin. A detailed analysis of atomic configuration around the crack tip for two successive (110) planes was used to reveal the transformation mechanism, as seen in Figure 6.23(a1-e1). The first (110) configuration was marked by red atoms and the second (110) was marked by blue atoms. Five Groups of atoms, labelled A1-A6, B1-B6, C1-C6, D1-D6, and E1-E6, were located in front of the crack

tip (see Figure 6.23(a1)), while Figure 6.23(a2-e2) showed the same atomic sections being assigned according to the CNA method.

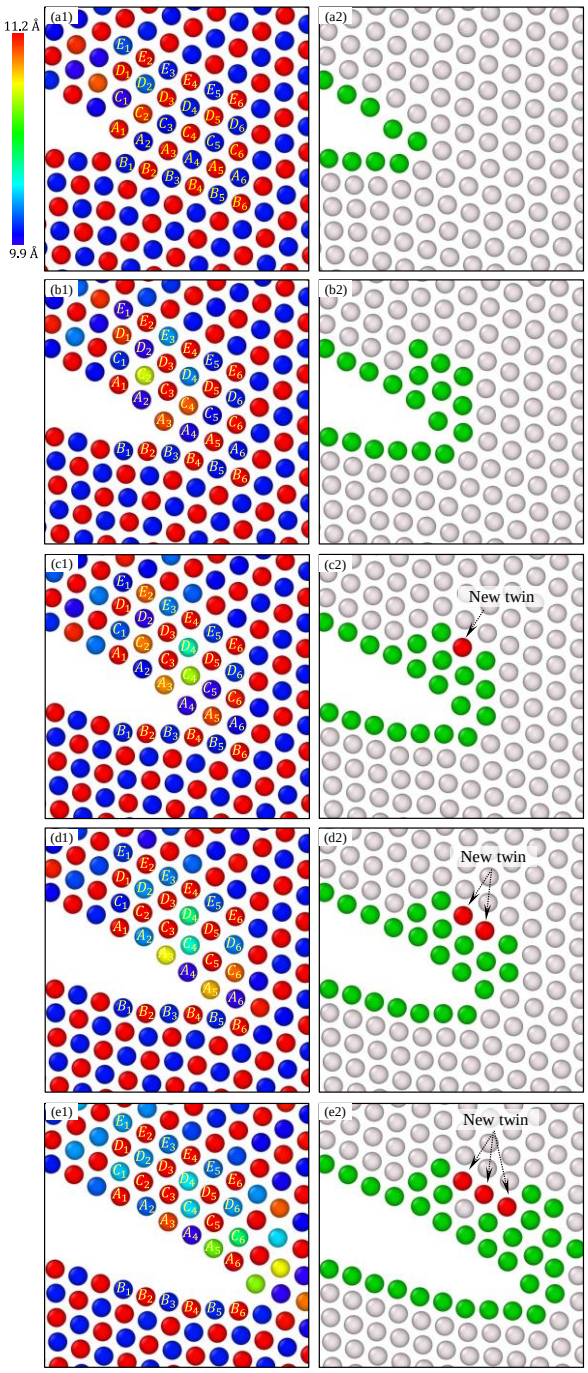

Figure 6.23 Atomic configuration (a1-e1) and local crystal structure (a2-e2) around the crack tip with crack system of {112}<110> at (a) ε = 4.2250%; (b) ε = 4.2280%; (c) ε = 4.2325%; (d) ε = 4.2345%; (e) ε = 4.2410%.

An inspection of Figure 6.22(a1) revealed that all the atoms remained in these two (110) facets. It was worth noting that the Atom C_2 changed from near blue to near lime at ε = 4.2280% deformation in Figure 6.23(b1), which indicated that initially, the atom in the first (110) facet shuffled towards the second (110) facet. Atom C_3 changed from blue to red, which denoted that Atom C_3 had squeezed into the second (110) plane from the first (110) plane. This showed that phase transformation had occurred by identifying five atoms C_2, D_3, C_3, A_3, C_4 that were roughly located at the same first (110) plane; this was identical with the phase transformation by the fcc structure to the transition of the base-centred orthorhombic structure in nanotwinned single Cu and Ni crystal. This newly formed phase structure was unstable because A_3 sprung back towards D_3 after the atomic bonds between A_3 and B_3 broke and one of its constitutive atoms C_4 began to shuffle from the first (110) configuration towards the second (110) configuration, as seen in Figure 6.23(c1) (detailed information was given in Chapters 3 and 4). Atom C_2 sprang back to the original first (110) configuration.

Figure 6.23(c2) shows that a new twin had been formed due to the phase transformation. Figure 6.23(d1-d2) showed that a twin had been extended because Atom C_4 continued to move towards the second the (110) configuration and Atom C_5 shuffled from the second (110) configuration to the first (110) configuration. Atom C_6 and Atom A_5 followed a similar trend as they moved from the first (110) configuration to the second (110) configuration, as seen in Figure 6.23(e). Since a new twin was formed, it shielded the atom at the crack tip and stopped its stresses from increasing, which also arrested the bond breaking process. The atomic configuration ahead of the crack tip was subsequently changed.

The phase transformation was obviously related to the changes in the bond distances ahead of the crack tip, but to reveal the basic reason for this phase transformation, the

maximum bond distance between the two labelled groups' atoms in Figure 6.23 was marked; for example d_{AD} represents the maximum atomic bond distance between Group-A atoms and Group-D atoms, but as Figure 6.24 shows, the bond distance was a function of the applied strain. As the strain increased, both d_{AD} and d_{CE} showed a generally increasing trend, but when the distance between the two atoms approached a critical value, phase transformation began. This can be explained by the fact that if the bond distance between the two atoms is large enough it will attract the atom located to the closest neighbouring (110) plane to fill in the larger space and help overcome the energy barrier. Such out-of-plane movement along (110) plane leads to a final phase transformation. The increasing bond distance is correlated with the angle of reference plane at the crack tip with respect to the $(\bar{1}12)$ plane (X direction).

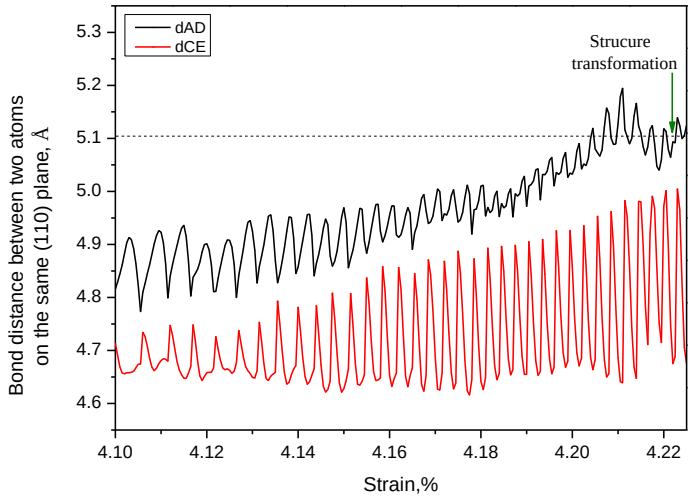

Figure 6.24 Bond distance between Group-A atoms and Group-D atoms, and Group-C atoms and Group-E atoms as a function of the imposed strain.

The angles between the reference plane and X direction versus strain are plotted in Figure 6.25. The angles a_{AD} (θ_{AD}) and a_{CE} (θ_{CE}) referred to the references cutting through Atoms A and D, and Atoms C and E, and being parallel to the Z direction. The increasing trend for a_{AD} (θ_{AD}) and a_{CE} (θ_{CE}) agreed with the trend for d_{AD} and d_{CE} increasing with various imposed strains. It was expected that as the crack propagated,

the stress released in the left-hand side of the crack tip region would cause the lattice to expand along the X direction, while the lattice on the right-hand side of the crack was still subjected to shrinking along the X direction due to the imposed strain along the Y direction. This led to a higher a_{AD} (θ_{AD}) and a_{CE} (θ_{CE}) because the increased crack length provided more stretching space between Group-A and Group-D, Group-C and Group-E (similar information can be seen in Chapters 3 and 4). This increase in the distance between the atomic bonds helped the phase transformation as the atoms moved towards the neighbouring (110) planes.

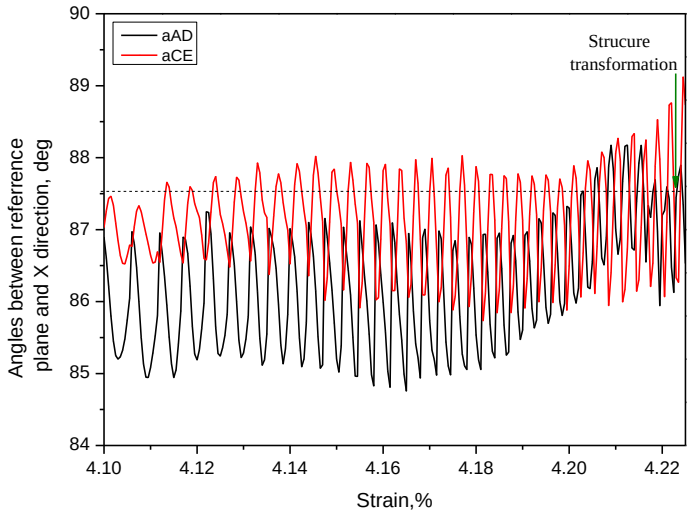

Figure 6.25 Angle (θ_{AD}/θ_{CE}) between Plane AD/CE and the X direction as a function of the imposed strain.

Unlike the phase transformation inducing dislocation from the mismatched region ahead of the twin in nanotwinned single Cu and Ni crystal, in a single crystal with the $\{112\}\langle 110\rangle$ crack orientation, the dislocation did not nucleate immediately after the first twin formed around the crack tip; probably due to the different crack orientations and specific atomic configurations around the crack tip just before the out-of-plane movement along the Z direction. For the twinned crystal, the full dislocation $1/2[1\bar{1}0]$ in (001) was nucleated from the mismatched boundary ahead of the twin. The Schmid Factor for the slip plane in the slip direction for an applied tensile load in $[\bar{1}1\bar{1}]$

direction was calculated as 0.471405, which means that the dislocation could easily be nucleated along the mismatched boundary. However, the $\{112\}\langle 110\rangle$ crack system in a single crystal did not own this feature, while the Schmid Factor for the Shockley partial dislocation and the full $\langle 110\rangle$ dislocation with the tensile force was 0.39284 and 0.35355, respectively. The dislocation facilitation in this crack system was not as strong as in the twinned crystal. Figure 6.26 shows snapshots of this atomic configuration after the twin was being formed. The emergence of twin triggered more atoms at its forward region to take out-of-plane movements along Z direction (see Figure 6.26(a)). This resulted in a newly extended twin being formed around one side of the crack tip, as seen in Figure 6.26(b). The elastic wave release was further hindered by the twin formation. Crack-tip blunting dominated the deformation process and induced a change in the shapes of the crack tips. The stress required for brittle fracture increased to make it more difficult for the atomic bonds to break, and the crack almost stopped propagating at that moment. Partial dislocation was sensitively activated from the lower part of crack tip along the $(\bar{1}1\bar{1})$ plane, as seen in Figure 6.26(c). A ledge formed intrinsically by the crack tip blunting after dislocation emission from the crack tip; this agreed with the observation that a ledge occurred in the experiment after the dislocation was generated. The ledge coincided roughly with the $\langle 101\rangle$ direction and was located at the forward region of the twin. At this region the loading then exhibited a mode II shear component that induced the nucleation of dislocations [104, 212]. In Figure 6.26(d), mixed dislocations were emitted from this region (the detailed dislocation activity was referred to Figure 6.27), and then the full dislocations migrated away from the twin region after the trailing partial dislocations were nucleated, as seen in Figure 6.26(c). A void began to generate in the front of the twin region after the mixed full dislocation moved further away in Figure 6.26(f), and slowly grew to join the main crack (Figure 6.26(h)). This result was a different phenomenon from the twinned crystal where the crack almost stopped to propagate because the dislocation was nucleated and emitted. Note that the crack was diverted to

other slip planes consisting of the {111} planes and {001} planes. The leading partial dislocations were nucleated ahead of the crack tip and emitted away, followed by the trailing partial dislocation (see Figure 6.26(g-h)). These mixed dislocations constituted by the Shockley partial dislocations and stair-rod dislocations were continuously nucleated from the crack tip and dominated the consequent plastic deformation as the strain increased. This process was accompanied by the atomic bonds breaking, while the crack moved slowly forwards and left corrugations on the surface of the crack surface (see Figure 6.26(h-i)). This result suggested that once the twin was formed ahead of the crack tip, as induced by local structure transformation, the crack propagated in a ductile fashion with the concurrent movements by atomic bonds breaking and dislocation emission.

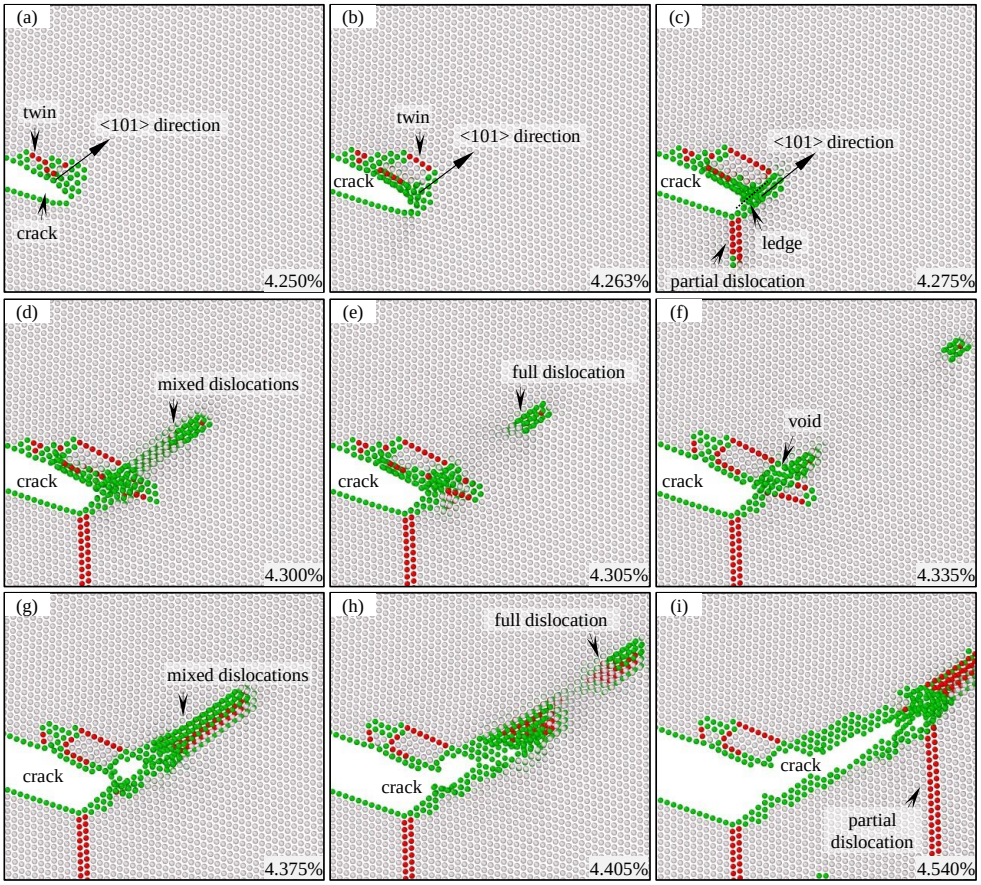

Figure 6.26 A sequence of snapshots of atomic configuration around the crack tip about the birittle-to-ductile fracture transtion with {112}<110> crack orientation.

The same snapshots in Figure 6.26 of detailed dislocation activities are shown in Figure 6.27. It is known that brittle fracture stems from competition between full crack cleavage and the beginning of dislocation nucleation. The emission of dislocations shielded crack cleavage and triggered plastic deformation. As seen in Figure 6.27(c), after the twin was being formed ahead of the crack tip, the blunting crack opening activated the $1/6\,[1\bar{1}\bar{2}]$ partial dislocation that parallels the tensile direction to nucleate and emit in the $(\bar{1}1\bar{1})$ plane. At ε = 4.3% in Figure 6.27(d), a complicated defect structure was emitted from the ledge. This structure was constructed by a series of interactions between dislocations that glide in $\{111\}$ and $\{100\}$ planes; these dislocation reactions can be described by:

$$1/6\,[\bar{2}11] + 1/6\,[1\bar{2}\bar{1}] \rightarrow\ 1/6\,[\bar{1}\bar{1}0] \tag{6.1}$$

Shockley partial + Shockley partial→ Stair-rod dislocation

$$1/6\,[1\bar{2}1] + 1/6\,[\bar{2}1\bar{1}] \rightarrow\ 1/6\,[\bar{1}\bar{1}0] \tag{6.2}$$

$$1/6\,[2\bar{1}1] + 1/6\,[1\bar{2}\bar{1}] \rightarrow\ 1/2\,[1\bar{1}0] \tag{6.3}$$

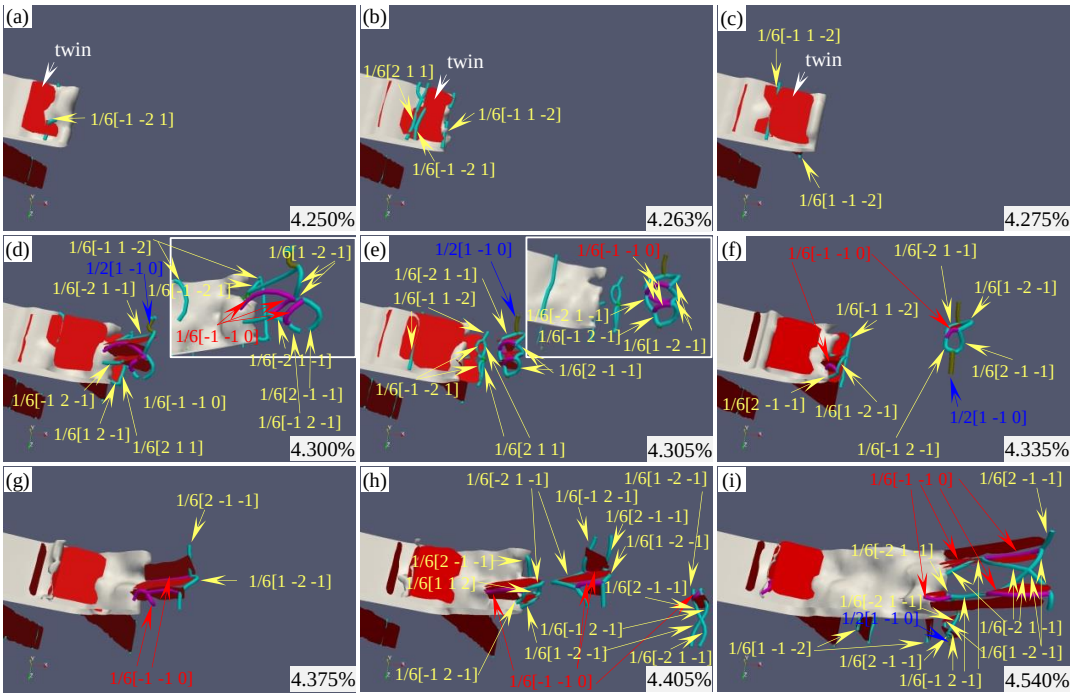

Figure 6.27 A sequence of snapshots of dislocation actvities around the crack tip about the birittle-to-ductile fracture transtion with {112}<110> crack orientation.

The types of dislocation can be seen by the vector lines assigned with different colours in Figure 6.27(d). This defect structure collectively moved forward by combining it with the nucleation of trail partial dislocations as the strain deformation increased (see Figure 6.27(d)). A new dislocation loop was formed in front of the crack tip by partial dislocations of $1/6\,[\bar{1}\bar{2}1]$, $1/6\,[211]$ and $1/6\,[\bar{1}1\bar{2}]$. When the strain increased to ε = 4.335%, a void was nucleated and taken as the source for more dislocations nucleation. A V-shaped defect structure bounded by leading $1/6\,[\bar{2}11]$ and $1/6\,[1\bar{2}\bar{1}]$ Shockley partial dislocations that intersected at a $1/6\,[\bar{1}\bar{1}0]$ stair-rod dislocation was formed at the crack tip, as seen in Figure 6.27(f-g). The previously formed defect structure shown in Figure 6.27(e) kept on migrating along the <101> direction. Note there was no full dislocation when the burger vector $1/2\,[1\bar{1}0]$ was nucleated on {100} plane after ε = 4.305% from the crack tip, it gave way to the Shockley partial dislocations and their associated stair-rod dislocations. In Figure 6.27(h), the $1/6\,[\bar{1}\bar{1}0]$ stair-rod dislocations connected by $1/6\,[\bar{2}11]$ and $1/6\,[1\bar{2}\bar{1}]$, $1/6\,[1\bar{2}1]$ and $1/6\,[\bar{2}1\bar{1}]$ Shockley partial dislocations glided away from the crack tip where a new and similar defect structure consisting of partial dislocations and stair-rod dislocations was formed. Another defect structure that originally generated from the crack tip travelled across the periodic boundary to enter the other side of the lattice matrix, as seen in the defect structure at the bottom right of the image in Figure 6.27(h). As the enlarging strain increased, a significant amount of stair-rod dislocation structures combined with the Shockley partial dislocations were successively nucleated from the crack tip; this was accompanied by the formation of the occasional $1/6\,[1\bar{1}\bar{2}]$ partial dislocation which was parallel to the tensile direction, just as the deformation at ε = 4.54% in Figure 6.27(i). This phenomenon of complicated dislocation activities and relatively slow crack propagation obviously showed that a fracture creates a transition from brittle fashion with a clean flat crack facet to ductile fashion with a rough corrugated crack facet.

6.4 Summary

The results showed deviations from the theoretical fracture criteria [19] that were very hard to explain using the classic Griffith and Rice criterion because it omitted effects such as the creation of surface steps at the crack tip by dislocations [231], directional anisotropy [69, 249], tensile strains [228, 229], and lattice/bonding trapping [179, 235, 250, 251]. My results revealed that the deformation mechanism of nine crack orientations in single crystals with the pre-existing central crack depended mainly on the specific crack system and the atomic configuration around the crack tip. The major observations can be summarised as follows:

(1) For {110} crack plane system, the crack front with <100> orientation showed brittle-to-ductile fracture transition. At the early stage of deformation the crack propagated in a brittle manner by perfect crack cleavage without any dislocation nucleation, but at the latter stage when the strain increased to a critical value, the crack became ductile through the void and dislocation propagation because as the imposed strain increased, the spacing between the atoms ahead of the crack tip increased to a critical value to induce local phase transformation by out-of-plane movement along the Z direction. This led to an atomic crystalline-amorphous state around the crack tip due to the non-planar arrangement. Dislocation could not be immediately nucleated ahead of crack tip because as the atomic bonds break, a series of voids begin to form and join the main crack. Dislocations were activated as the atoms ahead of the voids rotated to a critical value, and the surface of the crack became corrugated. However, with the ⟨110⟩ crack front direction, the crack was obviously ductile and the leading and trailing partial dislocations dominated the whole plastic deformation process, and the crack had almost no propagation.

(2) The cases with {110} crack plane system revealed an intrinsically ductile behaviour by the participation of dislocations and twins. The dislocations were

nucleated directly or indirectly in the vicinity of the crack tip to stop the atomic bonds from breaking so as a consequence, the crack obviously could not propagate.

(3) For cracks on the {111} plane, the simulated results showed a different deformation mechanism. Here, leading partial dislocations preferred to nucleate from the crack tip for ⟨112⟩ crack front direction, followed by a trailing partial dislocation, and the crack tended towards blunt without any obvious propagation. As for the ⟨110⟩ crack front direction, it was astonishing to see that the crack system showed brittle and ductile fracture behaviour for each part of the upper and lower central crack, respectively. This characteristic could be used to explain the effect of the twin as an intrinsic brittle boundary for the atomic model. Because of the distinct deformation characteristics for two parts of the crack cleavage plane, as increasing with the increasing imposed strain, a ledge would gradually form at the ductile side and trigger the dislocation to nucleate at this region. This had profound aspects for the free surface facets in that half of one side was very flat, and another half side an array of steps on the surface.

(4) The {112} crack plane with the $\langle \bar{1}1\bar{1} \rangle$ crack front direction showed a pronounced ductile behaviour through the defect structures by the partial dislocation and the stair-rod dislocation, while the ⟨110⟩ crack front orientation showed brittle-to-ductile fracture transition. The brittle fracture was preceded by a full crack cleavage in the $(1\bar{1}\bar{1})$ slip plane without any dislocation activity. The twin formation caused by the local phase transformation through out-of-plane movement along the Z axis induced the crack propagation to divert to other planes. This twin/phase transformation-induced brittle-to-ductile fracture transition was identical to the case with twinned Cu and Ni. These results validated the new mechanism for twinning nucleation by phase transform rather than successive partial dislocations slipping in the neighbouring slip planes [56]. The deformation mechanism for ductility after local phase transformation

was different for the single crystal and twinned single crystal; it depended mainly on the specific crack orientation and atomic configuration at the crack tip.

This chapter has increased our understanding of the brittle versus ductile fracture mechanism with varying crack orientations in single Ni crystal. In the next chapter, I focused on studying the brittle versus ductile fracture transition in Ni polycrystal by considering the effect of hydrostatic pressure; this work has rarely been carried out in previous literatures.

CHAPTER 7 BRITTLE VERSUS DUCTILE FRACTURE IN POLYCRYSTALLINE NICKEL UNDER TENSILE HYDROSTATIC STRESS

7.1 Introduction

Materials have structural defects that are unavoidably introduced during production processes [252], which means that complex deformation arises from the interplay between dislocation, GB, pre-existing TB, defects, and free surfaces, etc [11, 64, 106, 249]. GBs that make contact with the free surface slide easier than those within the inner GB structures due to smaller geometric constraints. GB/surface triple junctions or voids, or the sites where the coherence of pre-existing TB are being lost, serve as effective sources for dislocation nucleation. In addition, the detwinning of a pre-existing TB and its role in blocking dislocation migration also influences plastic deformation, all of which may change the mechanical properties such as strength, yield stress, ductility, hardness and toughness, etc. Further, the pre-existing voids/cracks may grow, coalesce, and form into intragranular or intergranular fracture as the imposed strain increases, which mean that deformation is controlled by the crossover processes of dislocation/twin, GB, and the propagation of voids and cracks.

The effect of pressure on plastic deformation is still not clear, although investigations revealed that nanocrystalline copper exhibited an unexpected ultrahigh strength behind the shock front [165] because as the shock loading increased, the softening mechanism was limited and the flow stresses were doubled compared to those at low pressure due to the GB sliding movement being suppressed. Similar results regarding an ultra-high strength behind the shock front due to increased dislocation activities were proved by Yuan et al. [166]. Luo et al. [164, 167, 168, 253] studied the spall damage and void growth/collapse induced by a shock wave loading in Cu where the shock waves also induced local and bulk melting associated with anisotropy, premelting, superheating, supercooling and re-crystallisation [169]. Other researches focused on the effect of hydrostatic pressure on deformation. Uniaxial compression

experiments under a high hydrostatic pressure were carried out [161, 163] and revealed that dislocation activity still occurred in a few nm-length scale at high hydrostatic pressure in polycrystalline Ni [161]. An MD simulation of the effects of hydrostatic pressure on deformation mechanisms in Al [170] and Cu [171, 172] was also carried out and revealed that hydrostatic pressure contributed to a different behaviour of dynamic GB de-cohesion in bicrystal [170]; above and below the critical hydrostatic pressure, dislocation increased or decreased as the hydrostatic pressure increase, but this feature was related to the grain sizes. GB thickening increased as the hydrostatic pressure increased for all gain sizes [171], whereas GB sliding was suppressed by the increasing hydrostatic pressure because of the increasing barriers for GB sliding [172]. However, no work has ever been carried out to study the influence of hydrostatic pressure (tensile or compressive) on the transition from ductile-to-brittle fracture in polycrystalline fcc structures. While previous studies have already shown that void nucleation is associated with the localised hydrostatic pressure [68, 200, 211], a consideration of the effect of hydrostatic stress on the transition of ductile-to-brittle fracture in polycrystal is very important, so in this paper I used an MD simulation to explore the transition from ductile to brittle fracture in polycrystalline Ni with a central pre-existing crack under tensile hydrostatic stress, and to reveal the mechanism of the onset of void and crack propagation.

7.2 Model set-up

MD simulations were performed with the open-source code LAMMPS [196] to investigate the influence of hydrostatic stress on the fracture behaviour of nano grained nickel. The EAM interatomic potential [190] was employed in all the simulations. This potential was calibrated using experimental and ab initio data for Ni. It has been shown to precisely predict the lattice properties, point and extended defects, various structural energies and transformation paths. The geometric size of the simulation domain was 355.52 Å × 337.92 Å × 123.2 Å in the X, Y and Z directions, respectively, with 1302485 atoms in total as shown in Figure 7.1. Grains

were generated by virtue of the Voronoi polyhedral construction. Randomly selected crystallographic orientations were assigned to all the grains and most GBs were high-angle GBs. A through-Z crack with an elliptical shape was placed in the centre of the sample and its size was 50 Å × 20 Å × 123.2 Å in the X, Y, Z directions, respectively.

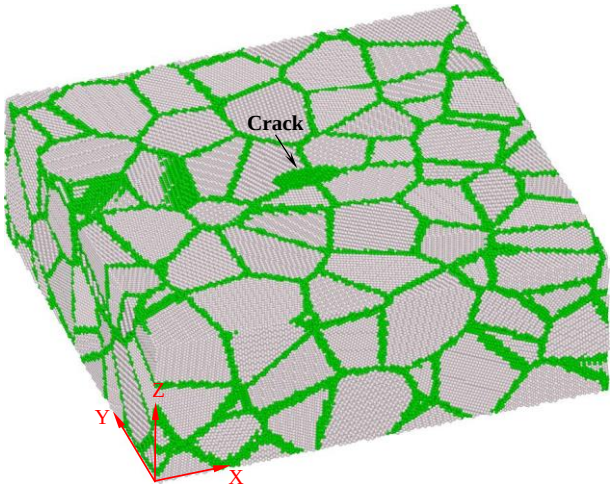

Figure 7.1 Schematic simulation of polycrystalline Nickle under tensile hydrostatic stress. Atoms were assigned based on CNA method. Grey, red, and green spheres represent fcc, hcp, and grain boundary atoms, respectively.

In the simulation the atoms were first subjected to energy minimisation by the conjugate gradient method, and relaxed at 1 K and zero pressure along three directions for 200 ps using the Nose-Hoover isobaric-isothermal ensemble (NPT) with a time step of 3 femtoseconds. Once the system reached the thermal and pressure equilibrium, a constant strain rate of 2×10^{8} s^{-1} was applied along the Y axis with a time step of 5 femtoseconds until it stretched to a strain (ε) of 30% and the temperature was maintained at 1 K. During the deformation the tensile hydrostatic stress was applied to all the atoms. MD simulations with various tensile hydrostatic stresses (σ_m) ranging from 0 GPa to 5 GPa were carried out in X, Z directions using NPT. The periodical boundary condition was imposed in all three directions. Ovito [198] software was used to visualise the deformation plasticity, while the can method

was used to identify the perfect fcc lattices (grey atoms), stacking faults (red atoms), and GBs, dislocation cores and free surface structures (green atoms). The stress components were calculated using the expression taken from the Virial theorem, and the average atom volume was used in the stress calculations [199]. The derivative stress along the y direction ($\sigma_y^{'} = \bar{\sigma}_y - \sigma_m$) was then determined and discussed in the following context, where $\bar{\sigma}_y$ was the normal stress along the y direction.

7.3 Results and discussion

7.3.1 Influence of hydrostatic stress on brittle versus ductile fracture

Figure 7.2(a) shows the derivative stress along the y direction (σ_y') as a function of the applied strain (ε) for various hydrostatic stresses (σ_m). σ_y' exhibits a nearly-linear relationship in the early stage of the deformation. The slopes of the curves gradually decrease after the strain exceeds about 4% until the maximum stress, followed by the decrease of the stress with increasing the strain. It can be seen that both the maximum σ_y' and its corresponding strain decreases with the hydrostatic stress. The toughness was calculated by the integration of each of the stress-strain curves and plotted in Figure 7.2(b) as a function of the hydrostatic stress. When the hydrostatic stress is low ($\sigma_m \leq 1$ GPa), the toughness is high and it is independent of the hydrostatic stress. As the hydrostatic stress increases the toughness decreases. When the hydrostatic stress is equal to and great than 4.5 GPa, the toughness remains at a very low value. These results clearly imply that the fracture behaviour of the studied nano grained Ni strongly depends on the applied hydrostatic stress. Three failure modes can be identified: ductile failure for 0 GPa $\leq \sigma_m \leq$ 1 GPa, ductile-to-brittle transition for 1.5 GPa $\leq \sigma_m \leq$ 4 GPa and brittle failure for $\sigma_m \geq$ 4.5 GPa. Under the uniaxial tension condition, the increase of tensile hydrostatic stress could transfer the fracture from the ductile mode to the brittle mode.

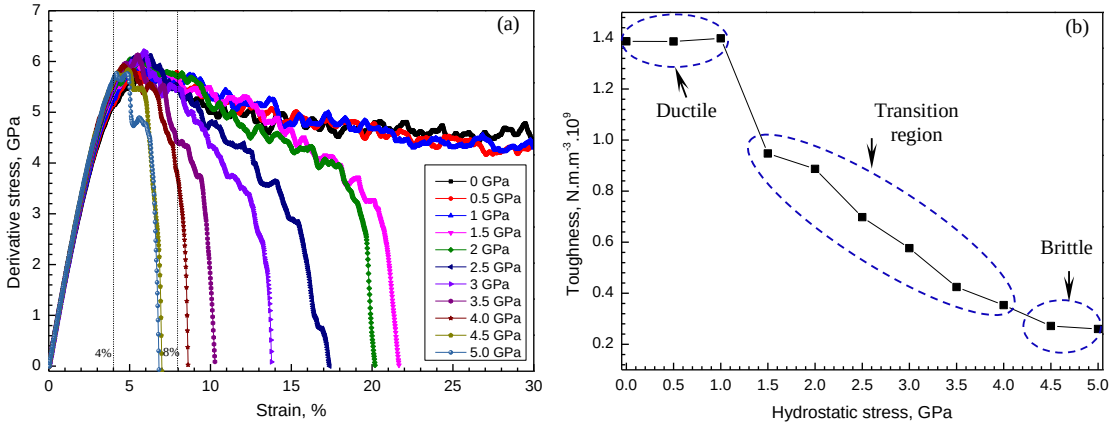

Figure 7.2 (a) σ'_y -ε curves for various hydrostatic stresses. (b) Toughness versus the hydrostatic stress.

Figure 7.3 shows snapshots of simulation cell at four strains (4%, 6%, 8% and 12%) after fcc and hcp atoms are removed. Figure 7.3(a), (b), and (c) correspond to three hydrostatic stresses of 0, 3 and 4.5 GPa, respectively. It can be seen from Figure 7.3(a1)~(a4) that without the hydrostatic stress a series of voids nucleate at the GBs as the deformation proceeds. However, they did not evolve into a large crack. For the case of 3 GPa (Figure 7.3(b)), more voids nucleated at the same strain compared to the previous case. These voids then coalesced with the main crack, generating an intergranular fracture. Intergranular fracture was much more apparent for the case of 4.5 GPa (Figure 7.3(c)) and it moved faster than the cases with lower hydrostatic stresses.

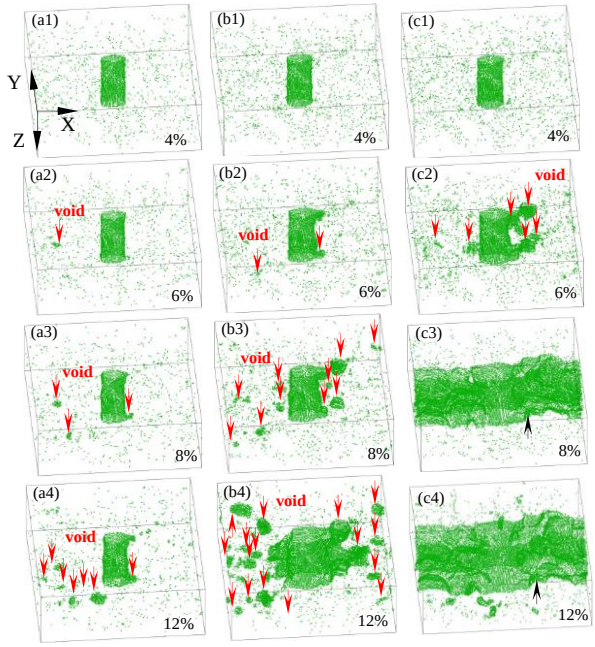

Figure 7.3 Snapshots of simulation cell at four strains (4%, 6%, 8% and 12%) for three hydrostatic stresses: (a) 0 GPa, (b) 3 GPa and (c) 4.5 GPa. fcc and hcp atoms are removed.

In order to understand these distinct failures under tensile hydrostatic stress I focussed on the scenarios of deformation at an early stage for cases with 0, 3, and 4.5 GPa tensile hydrostatic stresses (see Figure 7.4) because early deformation contributed to the origin of these differences in the final failure of this sample. At an elastic stage, only a few partial dislocations nucleated at the GBs or the central crack where the deformation was almost free of dislocation plasticity, but the linear trend switched when the first trailing partial dislocation was formed. With our interatomic potential of Ni, r_{sf} and r_{usf} were calculated as r_{sf} = 125.29 mJ/m^2 and r_{usf} = 365.67 mJ/m^2 and the value of r_{sf}/r_{usf} was 0.34. According to the Ref. [107], the extent to which the trailing partial dislocation formed can be understood in terms of the ratio of r_{sf}/r_{usf} because when the ratio approached unity the energy barrier for creating a trailing partial dislocation was very low, and a trailing partial dislocation was quite difficult to generate in Ni.

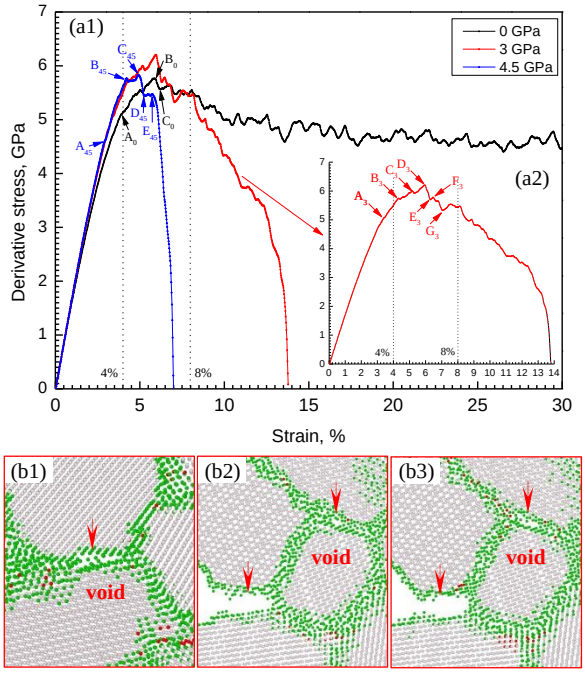

Figure 7.4 (a) Equivalent stress versus strain curves of selected analysing cases. (b) Atomistic configuration at the time point of tension strength.

Figure 7.5 shows that the extrinsic stacking fault (Figure 7.5(a), corresponding to point A_0 on the stress-strain curve in Figure 7.4(a1)) and full dislocations (Figure 7.5(b-c), corresponded to the points of A_3 and A_{45} on their stress-strain curves, respectively in Figure 7.4(a2), and Figure 7.4(a1)) was formed by combining the first trailing partial dislocation with the leading partial dislocation in either the neighbouring or the same slip planes, and this deformation entered the non-linear plastic stage. Before the equivalent stress reached its maximum value, the stress for all cases underwent a strain hardening effect [125]. This process went along with the complex motions of dislocation, GB, or void. I examined the tensile strength of samples (B0-0 GPa, D3-3 GPa, and C45-4.5 GPa in Figure 7.4(a)) and found that the tension strength occurred at the point where the void formed (Figure 7.4(b)), and where continuous movements of void nucleation, growth, and coalescence directly determine the manner in which the sample would fail.

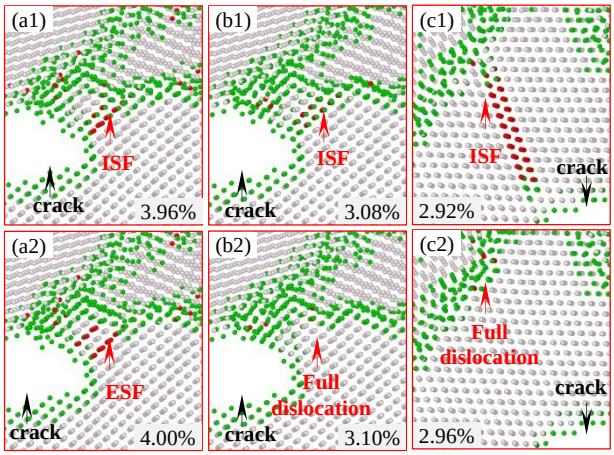

Figure 7.5 Atomistic illustration of the first trailing partial dislocation. (a) 0 GPa. (b) 3 GPa. (c) 4.5 GPa. ISF is the intrinsic stacking fault, and ESF is the extrinsic stacking fault.

To explore the mechanism of void onset, it is necessary to understand the brittle versus ductile fracture transition under tensile hydrostatic stress. Figure 7.6(a) shows the cross sections at a time step just before the initial void nucleation for the case with 3 GPa of hydrostatic stress (B_3 in Figure 7.4(a2)). The stress triaxiality at an atom was defined as the ratio of the mean stress and von Mises stress at atom. The regions of large stress concentrations-stress triaxiality (σ_{tri}) and tensile stress (σ_y) are distributed at the GBs (see black arrows in Figure 7.6(a2) and Figure 7.6(a3)). As the tensile deformation extended, the void was nucleated (Figure 7.6(b1)) in the region where the stress triaxiality and tensile stress concentrated ahead of the crack tip. After the void was nucleated the localised stress triaxiality and tensile stress were relieved (see Figure 7.6(b2-b3)), and it was then seen that the void nucleation mechanism was associated with local stress triaxiality, tensile stress, and localised deformation. The equivalent stress versus strain curve did not drop sharply, there was a slight decrease and then the nucleated void was stopped by the front of the GB triple junction composed by G1, G2, and G3. Plastic deformation caused by the main crack blunting and limited void growth exhibited an increasing rather than decreasing equivalent stress (see stage of B_3-C_3 in Figure 7.4(a2)). In Figure 7.6(c), the void joined the main

crack (corresponding to the C_3 in Figure 7.4(a2)), and the σ_{tri} and σ_y between G1 and G2 were almost reduced to 0, while those at regions between G3 and G4, σ_{tri} and σ_y maintained similar values.

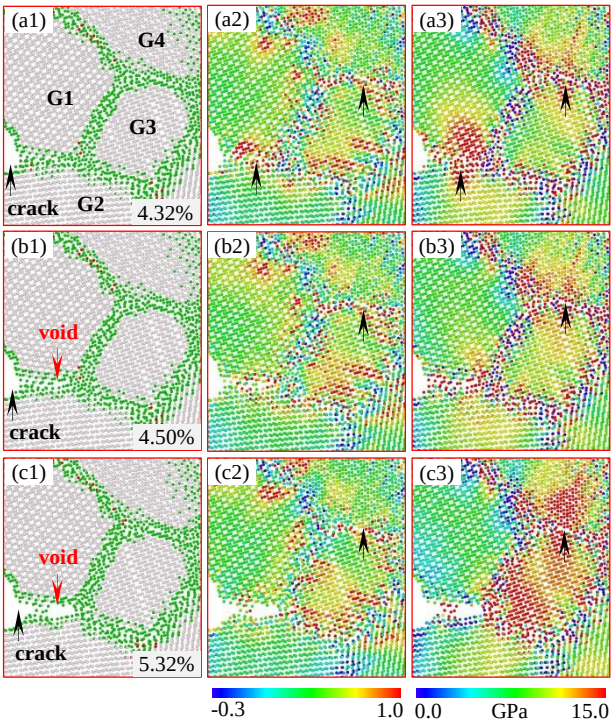

Figure 7.6 Atomistic illustration of the onset of void under the case of 3 GPa: (a1-b1) CNA; (a2-c2) σ_{tri}; (a3-c3) σ_y.

After the void joined the main crack, the equivalent stress decreased and then increased continually due to the triple junction barrier of GB between the G1, G2, and G3 (see the strain point of C_3 on the stress-strain curve in Figure 7.4(a2)) for crack growth. The G1 movement became much easier because the geometric constraints were limited. G1 slid along G3 while the atoms on GB between G1 and G3 shuffled. This was identified by comparing with the magenta vectors with the original and current positions of the atoms, as shown in Figure 7.7(a1). The movement of G1's created a localised tensile region around the G1, G3 and G4, (see the black arrows in Figure 7.7(a1)), and that caused additional stress triaxiality and a build up of tensile

stress at GB between G3 and G4 (Figure 7.7(a2-a3)), unlike those shown in Figure 7.6(c2-c3). At a deformation strain of 6%, the tensile stress reached its maximum value (tensile strength, see D_3 in Figure 7.4(a2)), but as deformation continued the plastic deformation between G3 and G4 became incompatible and voids nucleated from this region within a high σ_{tri} and σ_y (see Figure 7.7(b)). The stress indicators, including σ_{tri} and σ_y, soon recovered to almost 0 (see Figure 7.7(b2-b3)); this process corresponds to point E_3 on the stress-strain curve in Figure 7.4(a2) where the systemic tensile stress largely dropped.

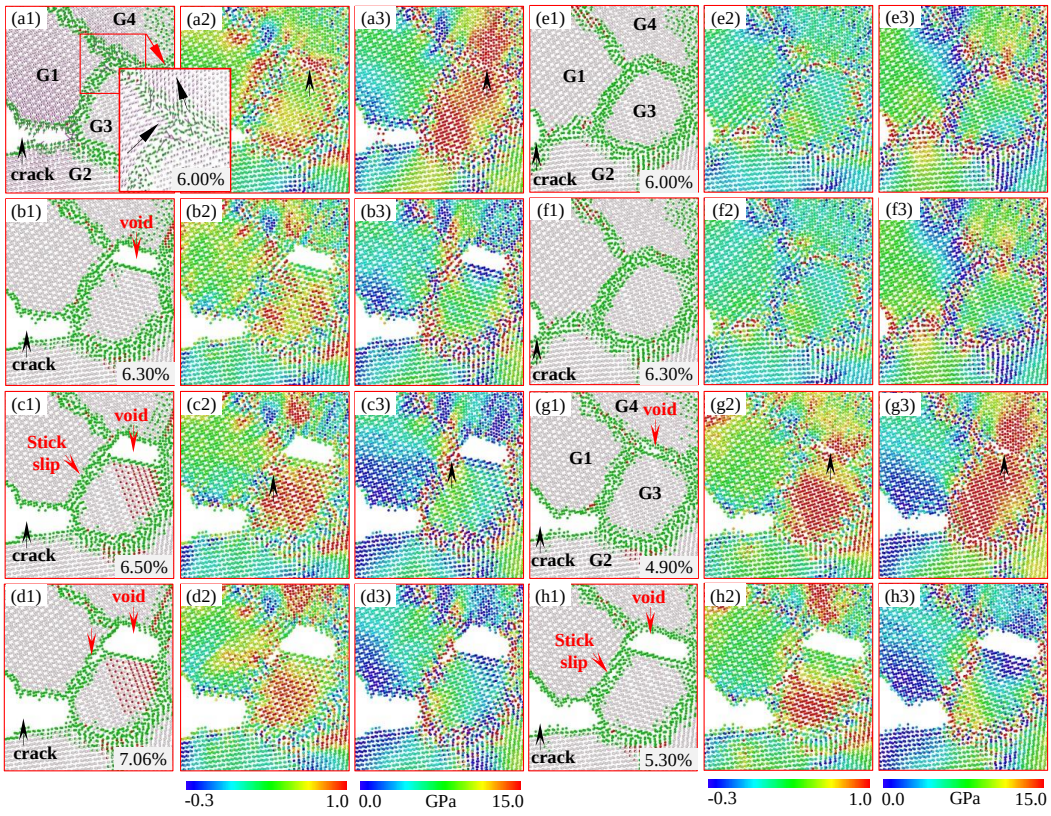

Figure 7.7 Atomistic illustration of cross-sections of tensile deformation at early strain stages. Cases with tensile hydrostatic stress of (a-d) 3 GPa; (e-f) 0 GPa; (g-h) 4.5 GPa. (a1-d1, e1-h1) CNA; (a2-d2, e2-h2) σ_{tri}; (a3-d3, e3-h3) σ_{y}.

Figure 7.7(c) shows that the stick slip between G1 and G3 occurred because the special geometric structure contributed to a slight increase in stress (corresponding to

the F_3 in Figure 7.4(a2)); σ_{tri} and σ_y then accumulated to a high level which induced a new void to nucleate on the GB between G1 and G2 (see Figure 7.7(d)). Stress fell again, as shown in Figure 7.7(a2) (corresponding to the G_3), after which a further series of voids nucleated, grew, coalesced, or joined with other voids or the main crack, with the result that intergranular fracture occurred where the tensile hydrostatic stress was 3 GPa. Furthermore, the consequence of serrations for the stress-strain curve resulted from successive movements of void nucleation, growth, and coalescence with other voids or cracks.

For cases with 0 and 4.5 GPa tensile hydrostatic stress in Figure 7.7(e-f) and Figure 7.7(g-h), there was a big difference in σ_{tri} and σ_y. It was noted that at deformation strains of 6% and 6.3% for 0 GPa tensile hydrostatic stress in Figure 7.7(e-f), there were no obvious regions of concentration for σ_{tri} and σ_y, unlike with 3 GPa tensile hydrostatic stress in Figure 7.7(a-b), and especially for σ_{tri}. Voids did not nucleate at the same region in the case with 3 GPa of tensile hydrostatic stress, but the stress reached its tensile strength when a void is nucleated on the other GB region (see Figure 7.4(a1) and Figure 7.4(b1)), and then decreased (see the B_0 and C_0 stage in Figure 7.4(a1)). With 4.5 GPa of tensile hydrostatic stress, the deformation mechanism was similar to the case with 3 GPa tensile hydrostatic stress because it was involved with, (i) the void nucleating ahead of the crack and then joining the main crack, (ii) the second void nucleating at the GB between G3 and G4, (iii) stick slip along the GB between G1 and G2 and the void nucleating on GB, and (iv) then combining with main crack (corresponding to points B_{45}, C_{45}, D_{45}, E_{45} in Figure 7.4(a1)). It was examined the mechanism of void nucleation and found they were all related to three parameters, including a large σ_{tri} and σ_y and enough localised regional deformation. Therefore the conditions for void nucleation or crack growth in polycrystal must satisfy three requisites: (1) $\sigma_{tri} \geq \sigma_{tri\_crit}$; (2) $\sigma_y \geq \sigma_{y\_crit}$ and (3) $\varepsilon_p \geq \varepsilon_{p\_crit}$. That is in accordance with the continuum plasticity theory in Ref. [211].

It was noted that the strain that occurred in the first void nucleation did not always refer to the strain that reached the stress strength. That was a slightly different result from the defect-free polycrystalline structure because high stress concentrated ahead of the crack tip due to a central crack in the atomic model, while void nucleation and growth in the main crack should have occurred, with a blocking effect from the surrounding GB triple junctions. The stress did not drop sharply when the first void nucleated, as was expected in the defect-free sample.

I examined the different failures in those cases with 0, 3, and 4.5 GPa tensile hydrostatic stress. The deformation features at 4% strain were focused, which shows an almost elastic deformation for each case, albeit with few dislocation activates (see Figure 7.4(a)). The distinct stress distribution was the driving force for the difference in fracture behaviour [68]. Figure 7.8(a2-c2), (a3-c3), and (a4-c4) showed that in those cases with tensile hydrostatic stress, the magnitudes of σ_{tri}, σ_y and σ_m increased and the regions of concentrated stress also increased (see the red arrows in Figure 7.8), compared to the case that was free of tensile hydrostatic stress. Basically, the greater the tensile hydrostatic stress applied the larger the σ_{tri}, σ_y and σ_m values and the more concentration regions were shown. This indicated that increasing magnitudes of σ_{tri}, σ_y, or the increasing of its corresponding concentration regions provided more sources for the subsequent void nucleation or crack propagation, which means void nucleation and crack propagation are more likely in cases with a higher tensile hydrostatic stress. The Z direction displacement that was normal to the tensile direction can be used to represent GB movements such as sliding, migration, and diffusion by seeing its discontinuities displaced in this direction. As Figure 7.8(a5-c5) shows, the application of tensile hydrostatic stress largely suppressed the GB motions. It is well known that dynamic fracture depends on the interplay of dislocation, GB, and void nucleation/crack propagation, and a smaller dislocation or GB movement is also supposed to facilitate the brittleness of fracture, so the result of suppressing GB

due to the tensile hydrostatic stress applied indicates further trends for brittle fracture. Figure 7.8(a6-c6) shows the von Mises shear strain at 4 % deformation strain under three different tensile hydrostatic stresses. It was easy to visualise the GB and dislocation activity by the von Mises shear strain because the larger GB and dislocation movement is shown in red.

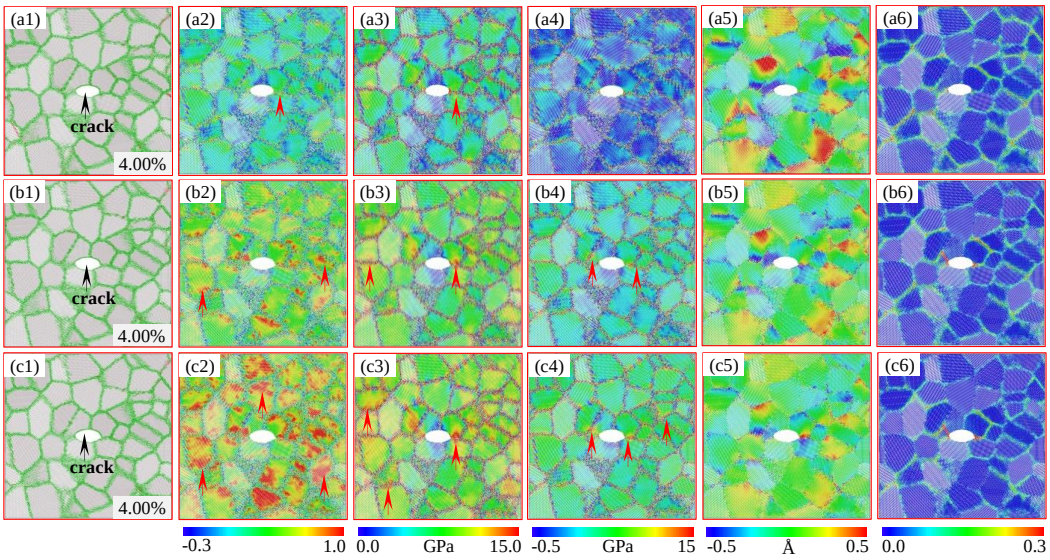

Figure 7.8 Cross-sections of tensile deformation at 4%. Cases with tensile hydrostatic stress of (a) 0 GPa; (b) 3 GPa; (c) 4.5 GPa. (a1-c1) CNA; (a2-c2) σ_{tri}; (a3-c3) σ_y; (a4-c4) σ_m; (a5-c5) Displacement along Z direction; (a6-c6) Von Mises shear strain. Red arrows represent the regions of high concentration of stress indicator.

Figure 7.9 shows sectional views of plastic deformation at 8% strain after the stress reached its maximum strength. The strengthen effect of tensile hydrostatic stress on σ_{tri}, σ_y, and σ_m was the same as reported in Figure 7.8 (see Figure 7.9(a2-c2), (a3-c3), (a4-c4)). Voids were nucleated at those regions where σ_{tri}, σ_y concentrated. After the void/crack propagation the σ_{tri}, σ_y, and σ_m were relieved to lower stress states, and as a consequence, other regions with a high σ_{tri}, σ_y concentration must share more load, which resulted in successive processes of void nucleation or crack growth.

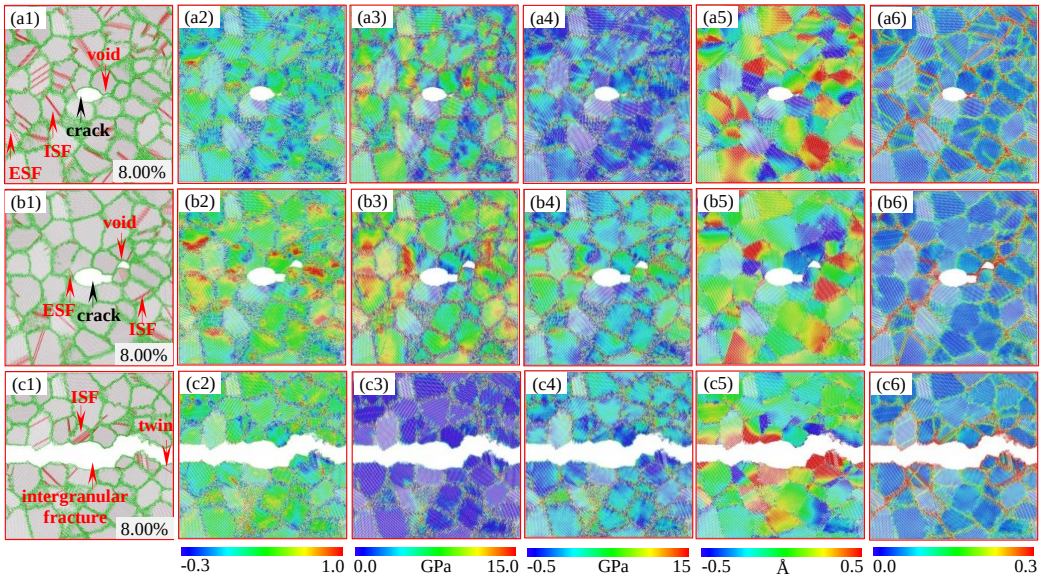

Figure 7.9 Cross-sections of tensile deformation at 8%. Cases with tensile hydrostatic stress of (a) 0 GPa; (b) 3 GPa; (c) 4.5 GPa. (a1-c1) CNA; (a2-c2) σ_{tri}; (a3-c3) σ_y; (a4-c4) σ_m; (a5-c5) Displacement along Z direction; (a6-c6) Von Mises shear strain. Red arrows represent the regions of high concentration of stress indicator.

Those cases with greater tensile hydrostatic stress exhibited more active movements of void nucleation, coalescence, and crack growth. It was seen that the brittle fracture manner with obvious intergranular fracture through rapid growth and coalescence of voids/crack occurred in this case with 4.5 GPa tensile hydrostatic stress. Moreover, the nucleation of dislocation cores was also suppressed by the tensile hydrostatic stress, while cases with less tensile hydrostatic stress had higher density dislocations. Dislocation activities such as partial/full dislocation or intrinsic stack fault (ISF), extrinsic stacking fault (ESF) and twin can be visualised by CNA and the von Mises shear strain (see Figure 7.9(a1-c1) and Figure 7.9(a6-c6)). These weak dislocation activities in cases with high external tensile hydrostatic stresses suggested that it might also help to improve brittle failure behaviour.

Interaction between the dislocation and the GB is very complicated. It has been observed in the simulations that dislocations can be emitted, trapped, absorbed, reflected or transmitted from the GBs, as seen in Figure 7.10. This interplay between dislocation and GB can be inspected by a high local value (tensile or compressive hydrostatic stress/mean stress) (seen insets in Figure 7.10).

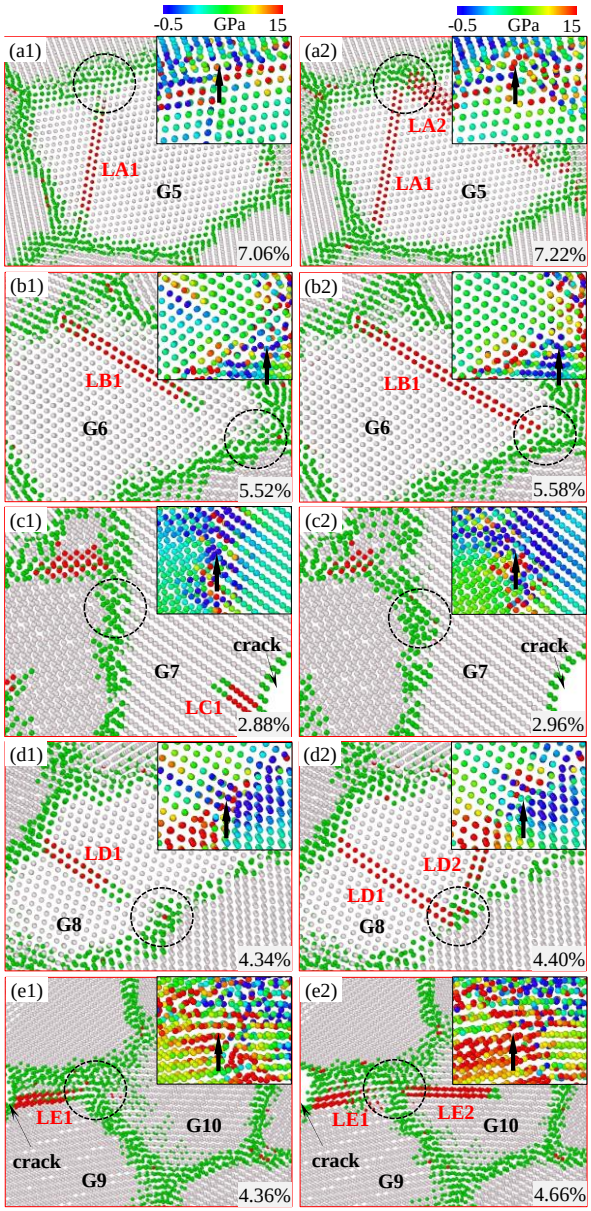

Figure 7.10 Interactions of dislocation with grain boundary: (a) emission, (b) trapping, (c) absorption, (d) reflection, (e) transmission. Insets are represented by Mean stress.

Figure 7.10(a) shows a dislocation being emitted from the GB. In Figure 7.10(a1) a partial dislocation LA1 travelled across Grain G5 to reach a GB where it was under compressive stress. The arrival of the LA1 led to a temporary increase of local compressive stress, as shown in the inset of Figure 7.10(a1). A new partial dislocation labelled LA2 is then emitted from the interaction point of the LA1 and the GB (see Figure 7.10(a2)). This process of dislocation emission from GB is accompanied by discrete atomic activity (including atomic shuffling and free-volume migration) that is similar to the simulation under indentation in Ref. [186]. Figure 7.10(b) displays a dislocation trapped on the GB. A leading partial dislocation LB1 nucleated at the left top GB of Grain G6 (Figure 7.10(b1)) and travelled towards another GB as shown in Figure 7.10(b2) without being followed by a trailing partial dislocation. The interaction region of the LB1 and the GB, marked by a black circle in Figure 7.10(b2), was subject to the tensile stress as shown in the inset of Figure 7.10(b2). The tensile stress caused the LB1 to be trapped by the GB. Likewise, if the leading partial dislocation is followed by a trailing partial dislocation on the same slip plane and approaches the GB region which exhibits a local tensile stress, then the leading partial dislocation can be absorbed by the GB. The dislocation absorption could be observed in Figure 7.10(c). The LC1 dislocation was nucleated from the crack and then absorbed by a GB circled in Figure 7.10(c2).

The fourth type of the dislocation-GB interaction was the dislocation reflection as shown in Figure 7.10(d). Similar to the dislocation emission from GB (Figure 7.10(a)), the partial dislocation LD1 propagated to a GB under compressive hydrostatic stress. When the LD1 reached this GB, it was reflected by the latter. A close examination of the local GB structure showed that the dislocation reflection did not involve the GB atom's shuffling. Apart from the above four dislocation-GB interactions, the dislocation could glide across the GB to the neighbouring grains. The slip transfer parameter $m' = \cos\alpha \cos\beta$ [49, 254] could be defined to evaluate the

two slip systems across a GB, where α and β were the angle between the slip planes and the slip directions of the two slip system, respectively. If the α and β angles were less than 35^o and 15^o respectively, the dislocation could transmit through the GB [186, 255]. In Figure 7.10(e1), the dislocation LE1 in Grain G9 nucleated from the crack tip and reached a GB region under compressive stress. It then travelled through the GB and became the partial dislocation LE2 in Grain G10 (see Figure 7.10(e2)). It has been noted that the angle between the LE1 and LE2 slip planes was 11^o and the angle between the LE1 and LE2 slip directions was 9.55^o, which satisfied the geometric condition for the dislocation transmission through the GB.

The above observations demonstrate that the dislocation-GB interactions were related to the local stress state. The local tensile stress around the GB was favourable for the dislocation trapping and absorption, whereas the local compressive stress facilitated the dislocation emission, reflection and transmission. All the processes of dislocation-GB interaction were associated with atomic shuffling and free volume migration (change of GB atomic number and rearrangement of GB structure) except the type of reflection. This implied that the ductility of the model may be improved to some extent by the interplay of dislocation and GB. I further checked the types of dislocation-GB interaction processes and found that the trapping and absorption types take up almost all the percentage of the five types. As discussed in Figure 7.9, it was known that dislocation nucleation was largely suppressed because the extra tensile hydrostatic stress applied weakened the dislocation-GB interaction for cases with external tensile hydrostatic stress due to less dislocation density. In other words, the applied tensile hydrostatic stress decreased the one possible way of improving ductility by the intricate interplay between dislocation and GB processes. In that sense the cases with tensile hydrostatic stress may be more brittle and have less plasticity due to dislocation-GB interaction, although we cannot exactly quantify that the underlying improvement in ductility of the model would be achieved by the

interaction of dislocation and GB. From the different types of interaction of dislocation-GB related to local pressure, it was known that the detailed interplay between dislocation and GB was influenced by the external tensile hydrostatic stress which resulted in in different local tensile hydrostatic stress distributions (see Figure 7.8(a4-c4)).

The MD simulations showed that the brittle versus ductile fracture was competitive and cooperative plasticity: (1) GB and void/crack was used as a source for dislocation or twin nucleation (Figure 7.8 and Figure 7.9); (2) GB served as a sink for dislocation emission, trapping, absorption, reflection, and transmission (Figure 7.10); (3) void nucleation arose directly from the incompatibility of local plastic deformation of two neighbouring GBs when the three prerequisites were satisfied (Figure 7.6 and Figure 7.7); (4) twin/dislocation induced avoid nucleation by providing additional plastic strain at the region with high σ_{tri}, σ_y (as shown in Figure 7.13), the mechanism was similar to the void nucleation in bcc polycrystalline Mo [50]; (5) stick slip occurred along the GB from the special geometric relations associated with the void/crack (Figure 7.7) and (6) GB slid and migrated (Figure 7.7-Figure 7.10). I used the following energy equation to quantify this plasticity, $\Delta E_{el} = E_{sur} + \Delta E_{GB} + E_{pl} + E_{heat}$ [170], where ΔE_{el} is a decrease in the elastic energy stored as the void/crack propagates; E_{sur} represents the energy used to generate a new free surface (e.g. void and crack); ΔE_{GB} represents the energy used to destroy the GB interface; E_{pl} is the energy needed for all plastic processes; and E_{heat} is the heat released during tensile deformation. Each item of energy (E_{sur}, ΔE_{GB}, E_{pl} and E_{heat}) that corresponds to the atomic movement in MD can be calculated by the energy needed to form a free surface, the energy for all atoms where CNA=5, excluding the free surface atoms, the energy for all atoms of CNA=2, and the energy for atoms with decreasing or increasing kinetic energy (a detailed description can be seen in the Ref. [170]).

Figure 7.11 shows the evolution of atomic numbers for the interplay between dislocation, GB, and void/crack growth during tensile deformation in the absence and presence of external tensile hydrostatic stress. Here the perfect fcc atoms' number almost exhibited an increasing tendency with increasing tensile hydrostatic stress (seen Figure 7.11(a)). The void motion increased with increasing tensile hydrostatic stress (Figure 7.11(b)), but it should be noted that the final number of void atom did not obey the fully increasing trend; it depended on the speed of void nucleation, growth of the void/cracks, the number of voids before intergranular fracture, and the path for intergranular fracture. For example, in the cases with 0 tensile hydrostatic stress (e.g. 0-1 hydrostatic), due to the very small numbers of void core nucleation and very limited void/crack growth motion, the final void atoms were very low level and did not experience intergranular fracture. For cases with tensile hydrostatic stresses of 2 and 3 GPa, and 4 and 5 GPa, unlike with just 2 GPa, more voids were nucleated with 3 GPa of tensile hydrostatic stress before they coalesced with the crack to form intergranular fracture, while the number of final void atoms with 3 GPa tensile hydrostatic stress was more than with 2 GPa. With 5 GPa of tensile hydrostatic stress there were less final void atoms than those with 3 GPa tensile hydrostatic stress; this coincided with the intergranular fracture proceeding on a straighter path along the middle of the model (see Figure 7.3(b) and (c)), where there was less surficial area of free surfaces for the case with 5 GPa tensile hydrostatic stress. The dislocation and GB-associated movements were suppressed because of tensile hydrostatic stress, (Figure 7.11(c) and Figure 7.11(d)). As deformation increased, the elastic energy combined with the energy of the destroyed GB gradually changed into energy for the void/crack, plasticity, and heat release.

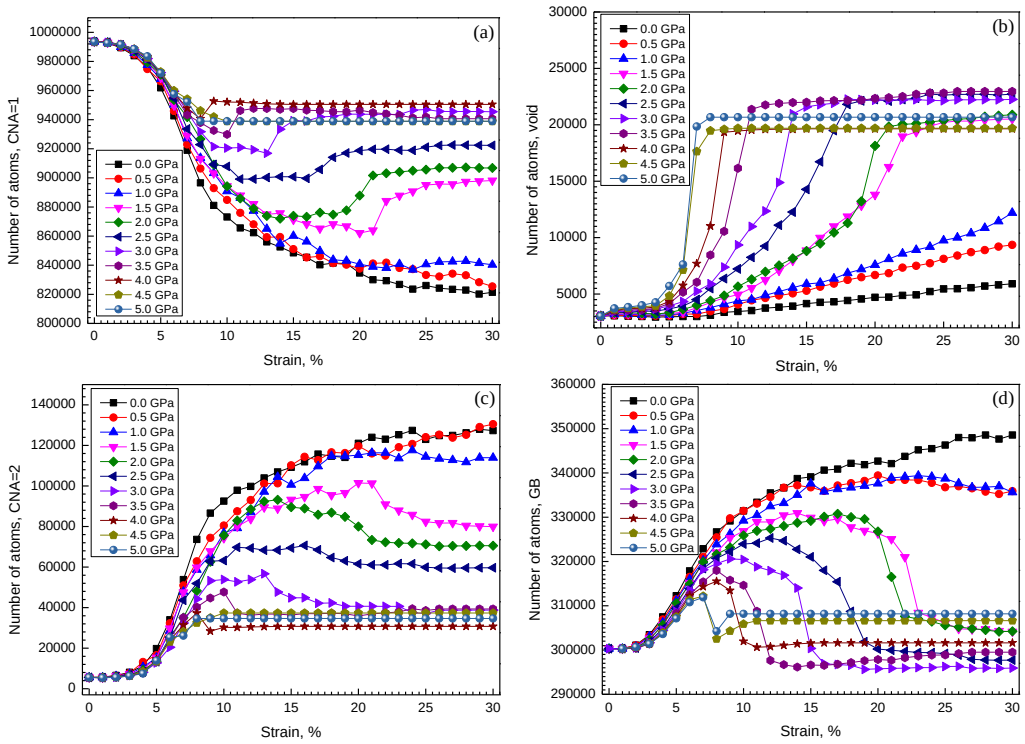

Figure 7.11 Evolution of atom numbers of (a) fcc, (b) hcp, (c) grain boundary, (d) free surface.

Figure 7.12 plots the evolution of each of type of energy. The largest component of energy released in tensile deformation with and without tensile hydrostatic stress was not for creating a free surface (void/crack), it was the energy for plastic deformation. The gaps between the energy needed for plastic deformation and free surface shrunk as the tensile hydrostatic stress increased. Another great release of energy was for destroying the GBs because below a critical tensile hydrostatic stress, the potential energy for destroying GBs was greater than the potential energy for propagating voids and cracks. Because the simulation work was carried out at an extremely low temperature (1 K), the contribution made by the heat released was almost ignored. I was also tested the effect of temperature on the heat release by using the same tensile hydrostatic stress and found that the contribution made by the released heat obviously increased as the temperature increased (this was shown in following parts).

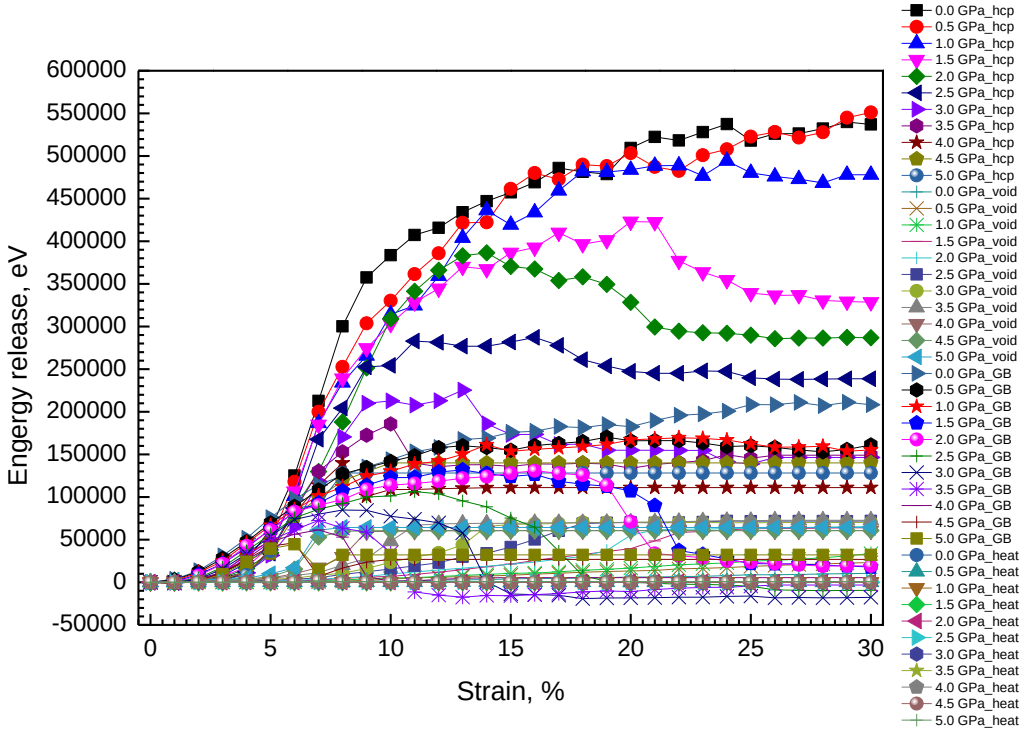

Figure 7.12 The energy released through energy for free surface formation, dislocation/twin activity, heat dissipation, and the energy to destroy the GB surface.

As proposed above, void nucleation proceeded on the GB which exhibited a high concentration of σ_{tri}, σ_y when the local plastic deformation increased to a critical value. The void nucleation stemmed from a direct and incompatible plastic deformation between two neighbouring grains. Alternatively, the mismatching of two neighbouring grains was assisted by the dislocation/twin movements which led to a final GB crack that was called the dislocation/twin-induced void nucleation. The sequence of snapshots shown in Figure 7.13 captures the dislocation/twin-induced void nucleation in detail, and the schematic mechanism of void nucleation induced by dislocation/twin is shown in Figure 7.13(a), to mediate lattice dragging caused by the dislocation/twin, where the G11 was subjected to a displacement Δ along the dislocation/twin interfaces by $\Delta = d(\vec{b} \cdot \vec{n})$, where $\vec{b}$ is the burger vector of dislocation/twin; $\vec{n}$ is the normal direction of GB; and d is the width of the dislocation/twin. The displacement Δ was not allowed if no other compatible plastic

deformation occurred in G11. The situation would intensify as the dislocation/twin activities continued, until the G11 and G12 separated to form a local GB crack. A similar mechanism of dislocation/twin induced void nucleation in bcc metal is referred to in the Ref. [50]. To understand the process, I checked how the atomic movement contributed to the void nucleation shown in Figure 7.13(b). The extrinsic stacking faults L3 and L4 are nucleated in G11 in Figure 7.13(b1), while L3 and L4 were extended further by local shear stress along the slip planes in G11. Here, the driving force came mainly from the favourable shear effect of G11 rather than G12 and G13 because there were less geometric constraints when a crack is present. L4 extended into the twin structure by way of the "partial dislocation-overlapping" [109] shown in Figure 7.13(b2), so the GB between G11 and G12 was subjected to a pulling force along the direction of the L4 burger vector, which increased the concentration of stress surrounding it (see Figure 7.14(c2)). As the more complex twin and detwinning movements of L3 and L4 proceeded further, the localised σ_{tri}, σ_y and plastic strain on the local GB region reached threshold values. Voids were nucleated on the GB between G11 and G12 when those two grains were unable to accommodate local plastic deformation (see the red arrows in Figure 7.13). The voids then coalesced and were transferred into a pronounced intergranular fracture along GB between G11 and G12, followed by stress relieving. Figure 7.13 shows that the dislocation/twin movement facilitated nucleation of the void by providing further local plastic strain or stress assistance for the local region of GB. Alternatively, the void can be a source site for dislocation and twin nucleation. In Figure 7.13(b5), the void took a dislocation source. Full dislocation nucleated and moved towards the twin in G12 and interacted with it. A stair rod was left on TB and a partial dislocation moved along the TB. Figure 7.15 shows the dislocation/twin emitted from the site of the void/crack on the GB.

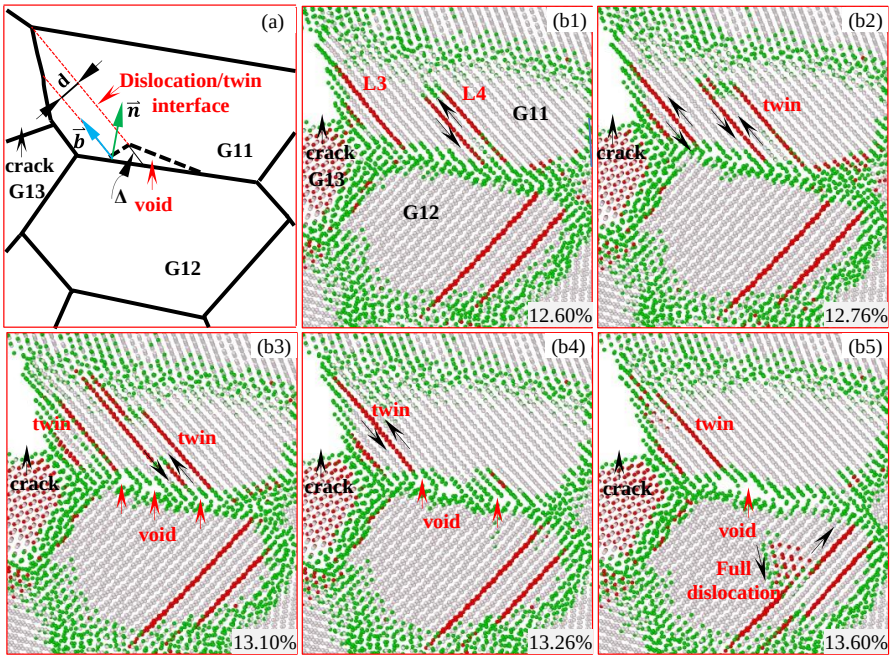

Figure 7.13 Dislocation/twin movement induced the nucleation of void. (a) Schematic mechanism of dislocation/twin-induced void nucleation. (b) A series of snapshots for void nucleation, assigned by CNA.

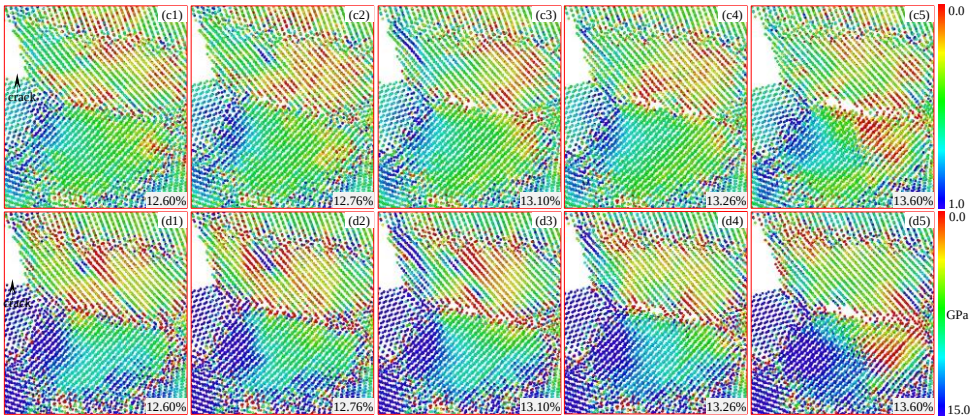

Figure 7.14 (Figure 7.13 continued) Stress distributions. (c) σ_{tri}; (d) σ_y.

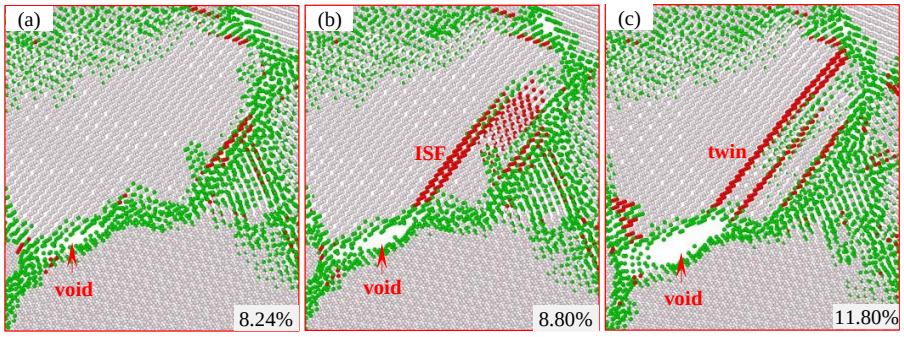

Figure 7.15 Void as a source for dislocation/twin nucleation.

In the MD simulations, the atomic model was prepared using random grain orientations, a procedure that resulted in generally high angle GBs but also some low angle GBs and GBs that were close to a perfect twin structure. Previous experiments revealed that grain misorientation may help to change the ductility of materials [256-258]. Grains with a large fraction of high-angle GBs exhibited higher ductility by GB sliding. The simulation showed that the ductility of material with high angle GB can be improved by grain coalescence (as shown in Figure 7.16). This was attributed that the coalescence of two neighbouring grains associated with many dislocation or twin activities, which largely contributed to the high plastic deformation. As Figure 7.16(a) shows, the misorientation between G14 and G15 was calculated to be 27^0, but at 4% strain deformation, the GB between G14 and G15 was gradually annihilated through dislocation (labelled L5) and twin (labelled T1) movement (see Figure 7.16(b)). T1 jogged along the path of original GB and then combined with other twin partial dislocations which slid perpendicular to the normal direction of T1. The results were that the intrinsic stacking fault L6 was left behind by the twin partial dislocation and the twin band thickness increased layer by layer along the T1 normal direction by T1 jogging (see Figure 7.16(c)). L5 moved across G15 to the GB triple junction consisting of G15, G16, and G17 (Figure 7.16(c-d)). At a strain of 14% deformation occurred, as shown as in Figure 7.16(e1), where L5 was absorbed at the GB, and the T1 boundary migrated to the position of T4. G14 coalesced with G15 by involving

dislocation emissions and twin migration. This disappearance of GB accompanied by dislocation/twin activity apparently contributes to the improvement of ductility of material. It was clear that the process of two grain coalescence was accomplished by atomic shuffling and lattice rotation, and was identified by the displacement vectors of the original and current atom positions shown in Figure 7.16(e2).

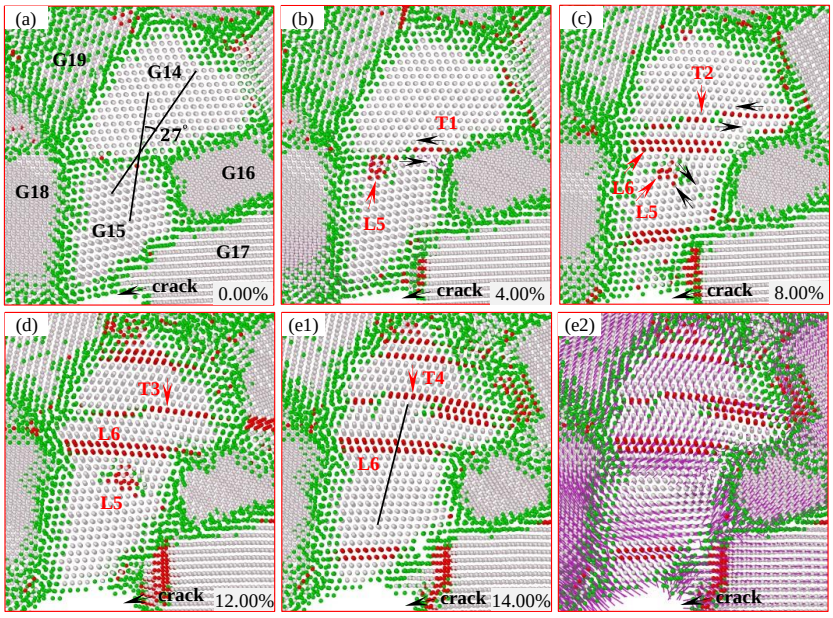

Figure 7.16 Successive snapshots of the vicinity of grain 14-19 with tensile hydrostatic stress of 0 GPa, showing the mechanism by which GB was disappeared. Magenta line is the track of displacement vector.

The low-angle GB (or TB) was validated to resist plastic deformation by collectively moving (shown in Figure 7.17 also see Ref. [259]). The misorientation of G20 and G21 is 8.5^{o}. With increasing strain deformation, the GB between G20 and G21 evolved into a local twin structure where the two grains formed a central structure around which several grains moved cooperatively within the structure. This formed entity structure inside the simulation cell offered resistance to plastic deformation. There was no dislocation in the two grains even at very high strain deformation. The

collective movement of grains 20 and 21 is shown in Figure 7.17(c) by the local von Mises shear strain. A question was proposed from the MD results that the ductility of materials can be improved by designing special crystalline structures without incorporating low angle GBs and TBs, which were expected to resist GB sliding or migration. Future work can proceed to study ductility by comparing two different kinds of atomic models using the random and self-defined methods to generate grain distributions.

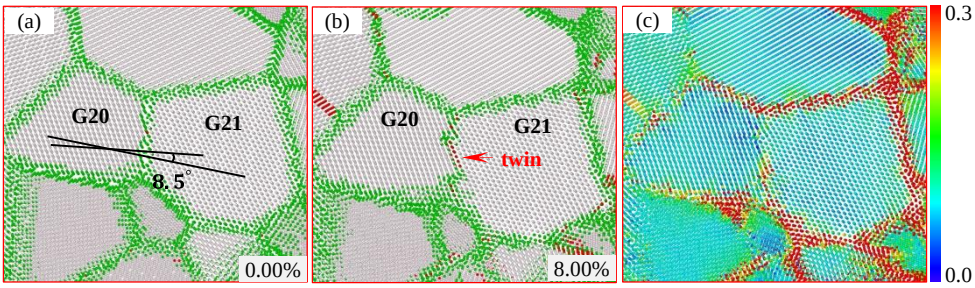

Figure 7.17 Void as a source for dislocation/twin nucleation with tensile hydrostatic stress of 3 GPa.

7.3.2 Influence of temperature on brittle versus ductile fracture

Temperate influences brittle versus ductile fracture, as many studies have shown using in situ experiments and MD simulations [81, 85, 104, 260]. Due to the intrinsic ductile features for Ni, I investigated the influence of temperature on brittle versus ductile fracture in polycrystalline Ni based on the existing external tensile hydrostatic stress. Here, the value of tensile hydrostatic stress with 1.8 GPa remained constant for all cases by varying the temperature. The mechanical properties of polycrystalline under the 1.8 GPa tensile hydrostatic stress with varying temperature are shown in Figure 7.18, and as Figure 7.18(a1) shows, the derivative stresses first increased linearly with extended strain at the elastic stage, and continued to increase nonlinearly to a maximum stress at about 5.7% at the initial plastic stage, and then gradually decreased, but at the latter plastic stage the cases with low temperature were more

brittle. Their corresponding derivative stresses dropped earlier and faster than those at high temperatures. Figure 7.18(a1) shows that the derivative stress was almost at a stable flow stress state with 30% deformation when the temperature was higher than 400 K.

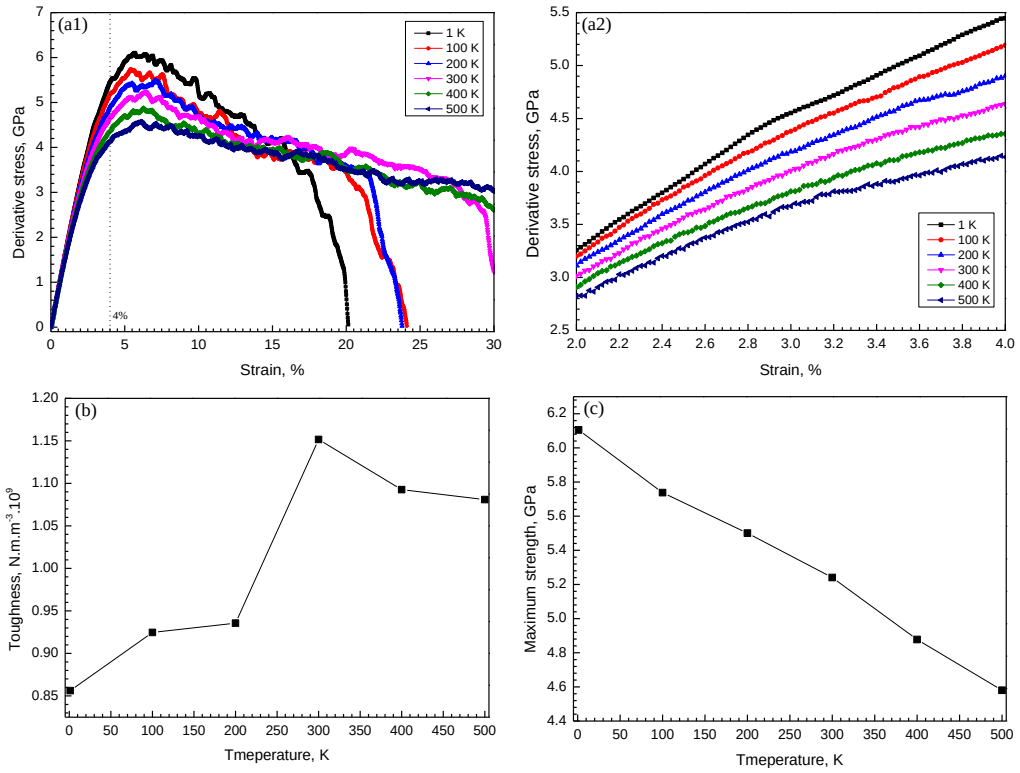

Figure 7.18 (a) Derivative stress-strain curves for tensile deformation with varying temperature at constant 1.8 GPa tensile hydrostatic stress. (b) Toughness versus tensile hydrostatic stress. (c) Maximum strength versus tensile hydrostatic stress.

Figure 7.18(a2) shows the monotonic and increasingly effective elastic modulus, while Figure 7.18(b) calculated the toughness of polycrystalline Ni with 30% deformation strain by measuring the area between the stress and strain. The toughness roughly increased with an increasing temperature, and at 300 K the toughness reached its highest value, which was slightly more than at 400 and 500 K. The strength of polycrystalline Ni decreased as the temperature increased.

As discussed before, void nucleation must satisfy three conditions to occur, and a lower temperature leads to more brittle fracture behaviour. This phenomenon is shown in Figure 7.19, where the atomic configuration at 4% deformation strain was used to explore brittleness at a low temperature, while deformation still belongs to the elastic stage (see Figure 7.18). Here the magnitude of σ_{tri}, σ_y and the number of concentration regions were suppressed savagely by the increasing temperature. Due to a larger thermal fluctuation at higher temperatures, the stresses were more likely to be released by the atoms vibrating, which causes smaller and fewer regions of concentrated stress. The results also indicate that the atomic activity involving atomic shuffling and free volume migration was more active when the atomic model was bathed in a higher temperature. This activity can be identified by its displacement in the Z direction and the von Mises shear strain shown in Figure 7.19, and by comparing it with the initial states of atomic configurations without deformation.

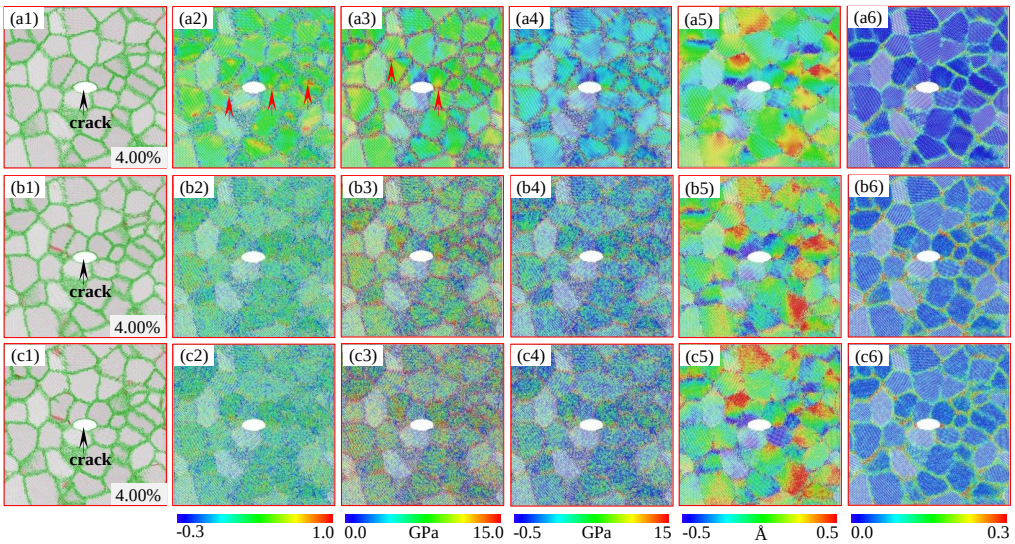

Figure 7.19 Cross sections of tensile deformation at 4%. Cases with temperatures of (a) 1 K; (b) 300 K; (c) 500 K. (a1-c1) CNA; (a2-c2) σ_{tri}; (a3-c3) σ_y; (a4-c4) σ_m; (a5-c5) displacement along Z direction; (a6-c6) von Mises shear strain. Red arrows represent the regions of high concentration of stress indicators.

From Chapter 3 and Chapter 4 indicated that high temperatures triggered localised phase transformation and twin formation near the crack tip, which caused further dislocation activities. When the temperature exceeded a critical value, the thermal fluctuation directly induced the formation of a ledge at the crack tip, followed by the emission of dislocations around the ledges. The dislocation activities shielded crack propagation, from which it can be deduced that at a low temperature the fractures were more brittle due to the volume of sources for void nucleation and propagation, and less dislocation/twin activity by comparison, with higher temperatures.

Figure 7.20 captured the evolution of void nucleation and propagation at temperatures of 1 K, 300 K, and 500 K, while perfect fcc and hcp atoms were being removed. At an elastic stage (4% deformation), a through-thickness central crack along the Z direction was located in the middle of the model without any void nucleation and crack propagation. As the imposed strain increased to 8% deformation the void nucleated at the GBs where the large values of σ_{tri} and σ_y were subjected to a large local plastic deformation (see the red arrows in Figure 7.20(a2-c2)). This process corresponded to the series of drops of derivative stress-strain curves in Figure 7.18. The nucleated voids gradually coalesced with other voids or the main crack, as the strain extended. The ability and speed of coalescence was dependent on the temperature, thus with 20% deformation at 1 K, the voids joined with other voids and a mother crack to form the obvious intergranular fracture. In contrast, with a temperature of 500 K, only a few voids nucleated at 30% deformation and the main crack did not appear to propagate ahead, indeed this deformation exhibited an almost ductile mode. At 300 K the sample was deformed within the intergranular facture failure manner which proceeded inside the atomic model at 30% strain.

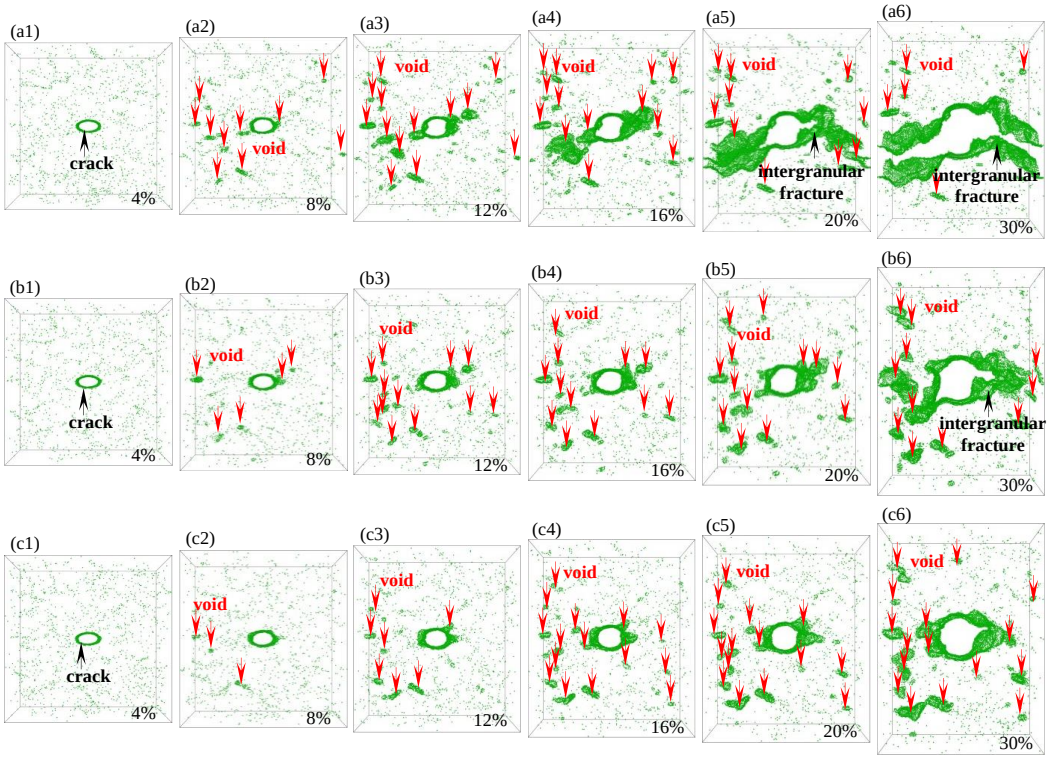

Figure 7.20 A sequence of snapshots of tensile deformation with temperatures of (a) 1 K, (b) 300 K and (c) 500 K. fcc and hcp atoms are filtered.

Figure 7.21 shows a sequence of cross sectional snapshots during tensile deformation at temperatures of 1 K, 300 K, and 500 K. After the plastic deformation, dislocation and twin activities were accompanied by the evolution of void and crack propagation where dislocation and twin preferred to nucleate at the triple junction of GB or the void/crack. This detailed information is shown by the black, blue, and red arrows which correspond to the ISF, ESF, and twin respectively in Figure 7.21(a). The dislocation/twin activity was generally enhanced by the increasing strain deformation. From Figure 7.21, it can be seen that dislocation/twin densities at high temperature are higher than at low temperature.

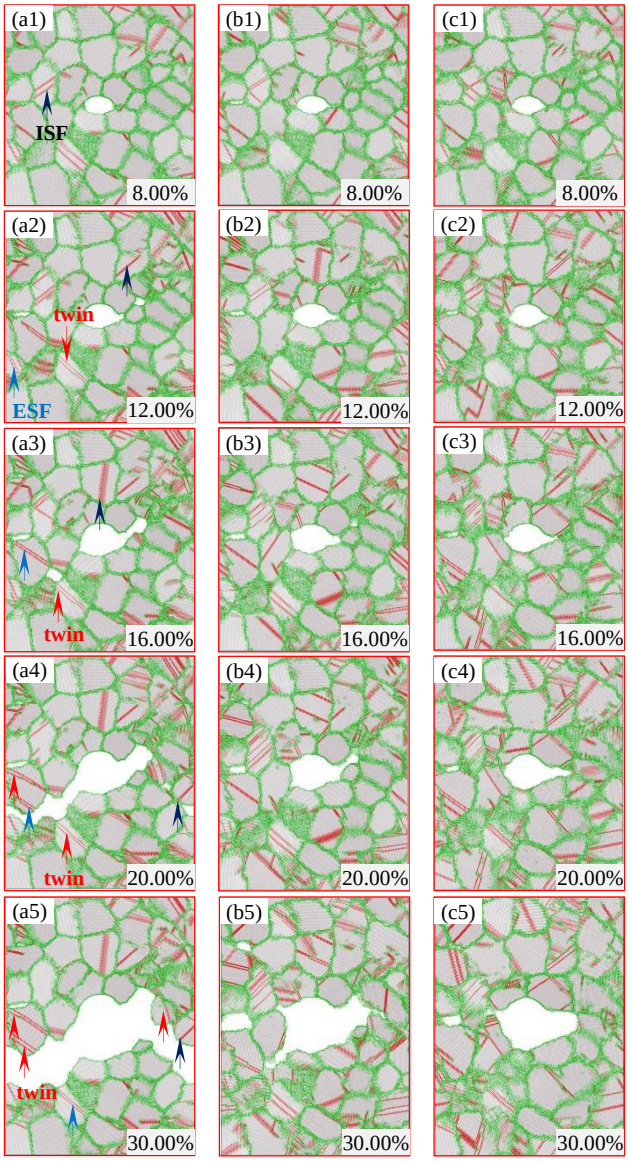

Figure 7.21 A sequence of cross-sectional snapshots of atomic configuration with temperatures of (a) 1 K, (b) 300 K and (c) 500 K.

I quantified the competitive mechanisms between void, dislocation/twin and perfect, and GB atoms by recording the number of each type of atomic configuration under different temperatures in Figure 7.22. The number of perfect fcc structured atoms increases as the temperature decreased before 7.8% deformation. For the single case event, the number of fcc atoms decreased as the deformation strain extended; this was attributed to the fact that parts of the fcc structure atoms were transferred to the hcp

structured atoms by dislocation/twin and void atoms. This decreasing trend was more noticeable with low temperatures (e.g. 1 K). At the latter stage of deformation, at low temperatures, the sample was almost completely fractured and the number of fcc atoms rebounded to a relatively high level. This can be partially understood by some percentages of hcp atoms being annihilated back to a perfect fcc structure through the stick slip movement ahead of the crack tip, or the errors caused by the external and existing tensile hydrostatic stress. At high temperatures such as 300 K, 400 K, 500 K, the value of the fcc atom number fluctuated slightly. Figure 7.22(b) shows the evolution of free surface atoms, including voids and the mother crack, during deformation, so as the strain increased, the voids/crack atoms increased monotonically. There was a similar trend when the voids/crack atoms increased with a decreasing temperature, indicating that a low temperature exhibited a more brittle fracture failure.

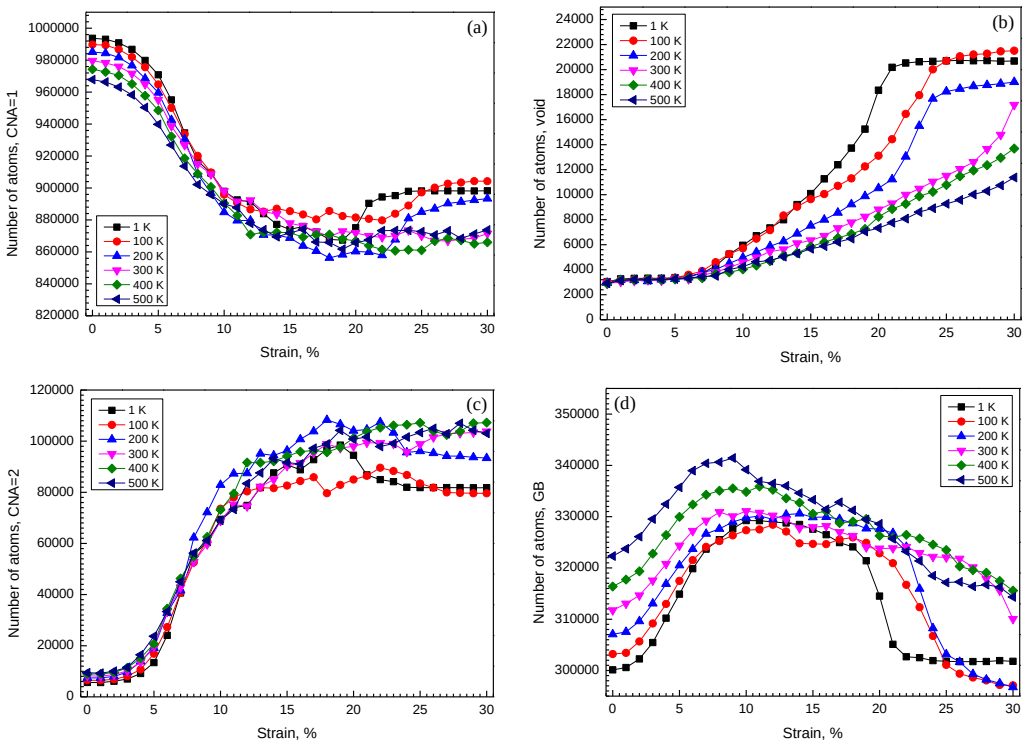

Figure 7.22 Evolution of atom numbers of (a) fcc, (b) hcp, (c) grain boundary, (d) free surface at temperatures of 1 K, 100 K, 200 K, 300 K, 400 K, 500 K.

Figure 7.22(c) shows the dislocation/twin activity during tensile deformation, and indicates that large thermal fluctuations roughly promote more dislocation/twin nucleation and emissions. Such dislocation/twin activity was demonstrated to impede the propagation of void/cracks. Atoms for GB increased with the imposed strain (see Figure 7.22(d)) at the early deformation stage, but when a succession of voids nucleated or coalesced on the GB, the GB atoms quickly decreased. It was observed that a decreasing temperature plays an active role in constrain GB movements. The above analysis suggests that macroscopic failure is a function of varying temperatures.

It is possible to determine the contribution that each structural state makes to the potential energy of the system (including free surface energy, GB energy, plastic energy, heat), as shown in Figure 7.23. The energy released for plastic deformation takes up the greatest percentage ratio of all energy contributed towards plastic deformation. This can be known by calculating the sum of the excess potential energy of all the hcp atoms in the system. A high temperature tends to show a larger energy release, which agrees with the discussion shown in Figure 7.22. The next part of the energy was released in the form of GB and heat. This release process depended largely on the temperature and strain applied. The energy needed to destroy the GB interface increased to a peak value and then gradually decreased to a low level; this was mainly attributed to the propagation of voids and cracks. Figure 7.23 shows that the higher the temperature, the less GB movement was suppressed. At a low temperature, the energy for heat dissipation can be ignored, but this scenario shifted rapidly due to the increasing temperature. The energy needed to create a new free surface contributed to a small ratio compared to other forms of energy release; with the exception of the case with a very low temperature. Thus it can be seen that this contribution of energy increased with the increasing strain deformation after the nucleation and coalescence of voids or the propagation of cracks. By analysing each

contribution of energy released, that polycrystalline Ni exhibits an intrinsic ductile characteristic can be known.

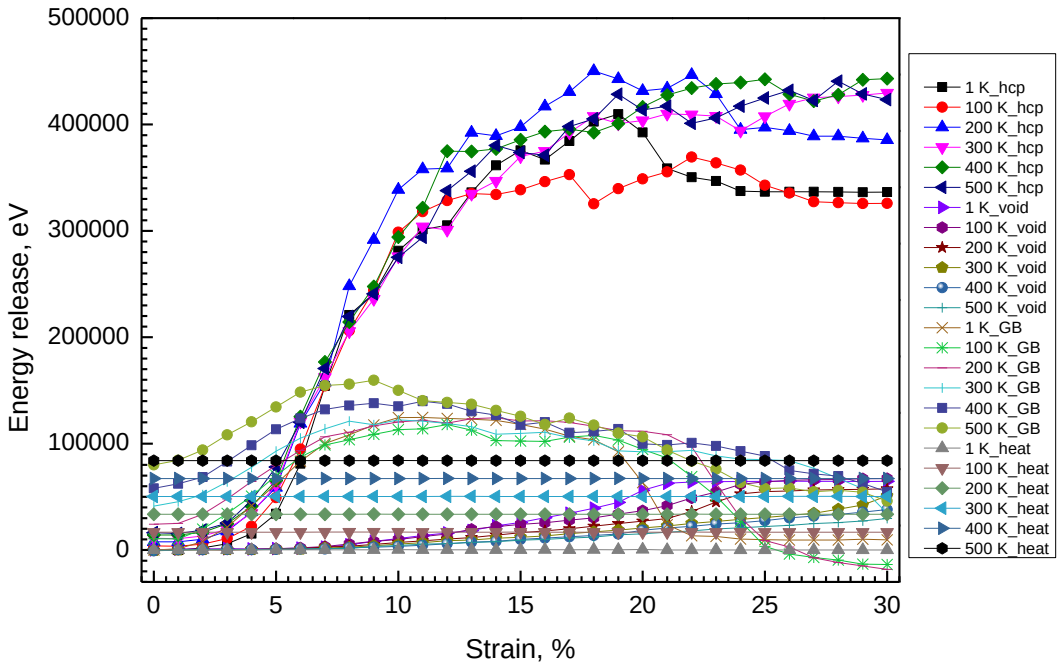

Figure 7.23 The energy released through energy for free surface formation, dislocation/twin activity, heat dissipation, and the energy to destroy the GB surface at temperatures of 1 K, 100 K, 200 K, 300 K, 400 K, 500 K.

7.4 Summary

In summary, I studied the effects of external tensile hydrostatic stress on the deformation and failure of nano-polycrystalline nickel using an MD simulation. It was validated the mechanism of void nucleation and growth from atomic views and observed a ductile-to-brittle fracture transition with an apparent intergranular fracture by controlling the tensile hydrostatic stress applied onto polycrystalline Ni. This can be understood from the following factors. (1) Void nucleation and growth must meet three requirements: (i) $\sigma_{tri} \geq \sigma_{tri\_crit}$, (ii) $\sigma_y \geq \sigma_{y\_crit}$ and (iii) $\varepsilon_p \geq \varepsilon_{p\_crit}$. Due to an increase in the tensile hydrostatic stress, the magnitude of σ_{tri}, σ_y, and σ_m and their concentration regions increased and thus provided more sites for void nucleation

and growth. (2) The effect of suppressing the dislocation cores nucleation and GB movements (e.g. sliding, migration, diffusion) strengthened as the increasing tensile hydrostatic stress increased, but it reduced the ductility of the sample. (3) Hydrostatic stress reduced the interplays between dislocation and GB (including emission, trapping, absorption, reflection and transmission) due to less dislocation density under tensile hydrostatic stress, which was presumably expected to improve the ductility of the samples. The kind of interaction of dislocations with GBs was decided by the local tensile and compressive stress state and local geometric structure. It was found that the interplay between dislocation and GB were often associated with the atomic activity via atomic shuffling and free volume migration. My simulation also showed that the temperature also influenced the brittle versus ductile fracture, such that a low temperature leads to a more brittle fracture because of more σ_{tri} and σ_y concentration regions, big values for void/crack propagation, and less dislocation/twin and GB activity. Such findings help us understand the plastic deformation/failure of defective nano-polycrystalline materials under multiple directions of force (e.g. hydrostatic stress) or different temperatures.

CHAPTER 8 CONCLUSIONS AND FUTURE WORK

In this thesis, MD simulations of brittle versus ductile fracture under uniaxial tensile deformation that considered the different factors of influence were carried out in nanocrystalline fcc structures. These atomic models covered nanotwinned single, single, polycrystalline crystals, and factors of influence included temperature, twin spacing distance, model size, applied strain rate, crystallographic orientations of lattice crystal, specific crack configuration orientations, and the tensile hydrostatic stress.

Chapter 3 described the tensile deformation and failure of nanotwinned Cu with a pre-existing edge-notched crack. By controlling the temperature, my simulations revealed a clear temperature-dependent brittle-to-ductile fracture transition of nanaotwinned Cu, and accounted for the complicities induced by the mechanics of the crack at an atomic scale. At an extremely low temperature (e.g. 1.1 K), the crack propagated in a brittle mode because the perfect atomic bonds broke along the twin boundary. As the temperature increased (e.g. 10 K), the occurrence of local phase transformation accompanied by formation of a twin around the crack tip induced a dislocation nucleation that resulted in a final fracture transition from brittle mode to ductile mode when the dynamic atomic bond distance around the crack exceeded a critical value as the brittle crack propagated. The increasing thermal fluctuation under higher temperatures (e.g. 40 K) activated a dislocation nucleation because a ledge was generated ahead of the crack tip that led to a ductile fracture mode. Moreover, other factors such as the twinning spacing distance, model size, and the imposed strain rate helped to influence brittle versus ductile fracture.

The brittle versus ductile fracture of metal is determined by a competition between the crack cleavage and dislocation activity associated with the material's intrinsic

property such as the free surface energy, and unstable/stable stacking fault energy. This means that brittle/ductile fracture depends mainly on material itself, so in Chapter 4 a brittle versus ductile fracture in nanotwinned Ni was studied with the same model and working conditions of nanotwinned Cu. The simulations showed similar results to the cases in nanotwinned Cu, but for Ni it exhibited a higher brittle-to-ductile fracture temperature and a more distinct crack propagation speed at various temperatures. Moreover, a predication of brittle or ductile fracture in other fcc nanotwinned crystals in Chapter 5 was carried out under the constraint of twin spacing distances at low temperatures. The results indicated that classic theories regarding the ratio of free surface energy and unstable stacking fault energy, as well as the ideal tensile strength and ideal shear strength in determining the brittle versus ductile fracture of nanotwinned fcc crystals, could be applicable under the confined twin spacing distances. A small value for brittle fracture is better, whereas a large value supports ductile fracture, which is in good agreement with the prediction of continuum theories. However, as the twinning spacing varied to some specific values, the continuum theory is no longer suitable.

Twin boundary is but one kind of intrinsic brittle boundaries in fcc crystal [69], but it can enhance brittleness during crack propagation. In Chapter 6, the brittle versus ductile fracture in single Ni crystal with a centred-notched crack rather than a pre-inserting twin, while being subjected to uniaxial tensile deformation, was discussed. It demonstrated that specific fracture behaviour depended not only on the specific lattice crystal orientations (e.g. crack cleavage plane), but also on the the specific crack crystallographic directions (including details of the crack propagation direction and crack front direction). Dislocation activities were responsible for all the ductile fractures, but there was also a brittle-to-ductile fracture transition at the brittle stage of fracture for some crack orientations that was caused by the formation of a ledge or local phase transformation (followed by the formation of crystalline-amorphous state

or twin) around the crack tip at the latter stage. This result agreed with the observations of nanotwinned Cu and Ni, but it was pointed out that a crystalline-amorphous state would form around the crack tip if the atoms shuffled to a non-planar arrangement for twin formation once phase transformation occurs.

Furthermore, the sample of real material usually had a complex structure with GBs subjected to multi-axial imposed stresses, so to mimic real working conditions more accurately, brittle versus ductile fracture in polycrystalline Ni under tensile hydrostatic stress was studied in Chapter 7 by applying a uniaxial tensile deformation. A ductile-to-brittle fracture transition occurred after changing the bathed external tensile hydrostatic stress because the increasing tensile hydrostatic stress leads to a more sites with a high concentration of σ_{tri}, σ_y compared to non-hydrostatic stress, for void nucleation and crack growth. Moreover the interplay between dislocation and GB can occur by dislocation emission, trapping, absorption, reflection, and transmission, but it depends mainly on the local stress states and local geometric structures. A higher temperature contributed to a more ductile fracture in polycrystalline Ni at a given tensile hydrostatic stress.

Although such findings help us understand the plastic deformation/failure of defective nano-polycrystalline fcc materials (e.g. tensile/compressive hydrostatic stress). It should be worth noting that the structure without a pre-existing crack (defects) in fcc metals may experience a different mechanical deformation from structure with an initial crack. The same atomic structures without pre-existing cracks will exhibit more ductile fracture behaviour. In addition, due to the intrinsically limitations of MD simulation in time and length scale, it requires unrealistically high deformation rates to be applied in a MD simulation, which is many orders of magnitude higher than the commonly used values in experiments. Therefore, it is still quite challenging to relate the simulation reliably to the actual deformation in experiments.

There are still many directions that could still be explored:

(1) The notched crack in this thesis was set up in the middle of the atomic model along the Y direction, but the effects of crack size and details of its position were not included. Previous studies already showed that those factors influenced the plastic deformation or failure of the atomic model [134, 261, 262]. Base on the current models, a deeper study of brittle versus ductile fracture can be extended by considering the effects of crack size, the specific position of the crack tip.

(2) In the models of nanotwinned crystal and single crystal for fcc metals (e.g. Cu, Ni), the formation of a ledge and local phase transformation around the crack tip induced the transition of brittle-to-ductile fracture, but could the same mechanism take place in bcc metals (e.g. Fe, Tungsten) or even diamond cubic structures (e.g. Si), and if not, what is the new mechanism for the brittle-to-ductile transition in these materials? Experiments have already showed that brittle-to-ductile fracture could happen in single-crystal Iron and Tungsten [81, 85], and the similar atomic models in this thesis for bcc structures such as Fe could be used for future investigations into the mechanism of brittle versus ductile fracture.

(3) The atomic models in this thesis were limited to pure crystals, but there are many impurities in real crystals. A model with an accumulation of hydrogen (H) around a crack tip at atomic scale in α-iron has been proposed by Song and Curtin [263]. Their MD results revealed that ductile-to-brittle fracture transition was caused by a dramatic suppression of dislocation emission at the crack tip due to the aggregation of H. Whether the atomic impurities at the crack tip can influence crack propagation in fcc metals (e.g. single crystal, or nanotwinned single crystal, or polycrystal of Cu/Ni) is still not clear, so further research could be carried out using MD simulation in fcc metals to study how impurities influence brittle versus ductile fracture transition.

(4) The misorientation distribution of grain in polycrystalline fcc metals could influence the ductility of the material [259]. In the current work, randomly selected seeds of grain and random crystallographic orientation were used to generate the polycrystalline model. Further work can be carried out using the model within particularly defined grain seeds and grain misorientations to study the behaviour of fracture at a given external tensile hydrostatic stress and temperature in polycrystalline Ni/Cu. In addition, more accurate and quantitative (or general) conclusions can be drawn by considering the influential factors such as repeatability of polycrystalline models, models with or without pre-existing TBs, crystalline orientations, geometric size of atomic model, etc.

REFERENCES

[1] M. J. Buehler, *Atomistic modeling of materials failure,* 2008.

[2] L. Lu, Y. Shen, X. Chen, L. Qian, and K. Lu, "Ultrahigh Strength and High Electrical Conductivity in Copper," *Science,* vol. 304, pp. 422-426, 2004.

[3] L. Lu, X. Chen, X. Huang, and K. Lu, "Revealing the maximum strength in nanotwinned copper," *Science,* vol. 323, pp. 607-610, 2009.

[4] E. O. Hall, "The deformation and ageing of mild steel: III Discussion of results," *Proceedings of the Physical Society. Section B,* vol. 64, pp. 747-753, 1951.

[5] J. Schiøtz, F. D. Di Tolla, and K. W. Jacobsen, "Softening of nanocrystalline metals at very small grain sizes," *Nature,* vol. 391, pp. 561-563, 1998.

[6] J. Schiøtz, T. Vegge, F. D. Di Tolla, and K. W. Jacobsen, "Atomic-scale simulations of the mechanical deformation of nanocrystalline metals," *Physical Review B - Condensed Matter and Materials Physics,* vol. 60, pp. 11971-11983, 1999.

[7] H. Van Swygenhoven, A. Caro, and D. Farkas, "A molecular dynamics study of polycrystalline fcc metals at the nanoscale: Grain boundary structure and its influence on plastic deformation," *Materials Science and Engineering A,* vol. 309-310, pp. 440-444, 2001.

[8] V. Yamakov, D. Wolf, S. R. Phillpot, A. K. Mukherjee, and H. Gleiter, "Dislocation processes in the deformation of nanocrystalline aluminium by molecular-dynamics simulation," *Nat Mater,* vol. 1, pp. 45-8, Sep 2002.

[9] X. Li, Y. Wei, L. Lu, K. Lu, and H. Gao, "Dislocation nucleation governed softening and maximum strength in nano-twinned metals," *Nature,* vol. 464, pp. 877-80, Apr 8 2010.

[10] Z. Wu, Y. W. Zhang, M. H. Jhon, H. Gao, and D. J. Srolovitz, "Nanowire failure: Long = brittle and short = ductile," *Nano Letters*, vol. 12, pp. 910-914, 2012.

[11] Z. X. Wu, Y. W. Zhang, M. H. Jhon, J. R. Greer, and D. J. Srolovitz, "Nanostructure and surface effects on yield in Cu nanowires," *Acta Materialia*, vol. 61, pp. 1831-1842, 2013.

[12] H. Zhou, X. Li, S. Qu, W. Yang, and H. Gao, "A Jogged Dislocation Governed Strengthening Mechanism in Nanotwinned Metals," *Nano Letters*, vol. 14, pp. 5075-5080, 2014/09/10 2014.

[13] A. A. Griffith, "The phenomena of rupture and flow in solids," *Philosophical Transactions of the Royal Society of London*, vol. 221, pp. 163-198, 1921.

[14] G. R. Irwin, "Analysis of stresses and strains near the end of crack traversing a plate," *Journal of Applied Mechanics, Transactions ASME*, vol. 24, pp. 361-364, 1957.

[15] D. S. Dugdale, "Yielding of steel sheets containing slits," *Journal of the Mechanics and Physics of Solids*, vol. 8, pp. 100-104, 1960.

[16] G. I. Barenblatt, "The formation of equilibrium cracks during brittle fracture. General ideas and hypotheses. Axially-symmetric cracks," *Journal of Applied Mathematics and Mechanics*, vol. 23, pp. 622-636, 1959.

[17] J. R. Rice and R. Thomson, "DUCTILE VERSUS BRITTLE BEHAVIOUR OF CRYSTALS," *Phil Mag*, vol. 29, pp. 73-97, 1974.

[18] J. R. Rice and G. E. Beltz, "The activation energy for dislocation nucleation at a crack," *Journal of the Mechanics and Physics of Solids*, vol. 42, pp. 333-360, 1994.

[19] J. R. Rice, "Dislocation nucleation from a crack tip: An analysis based on the Peierls concept," *Journal of the Mechanics and Physics of Solids*, vol. 40, pp. 239-271, 1992.

[20] S. J. Zhou and R. Thomson, "Dislocation emission at ledges on cracks," *Journal of Materials Research,* vol. 6, pp. 639-653, 1991.

[21] L. B. Freund and J. W. Hutchinson, "High strain-rate crack growth in rate-dependent plastic solids," *Journal of the Mechanics and Physics of Solids,* vol. 33, pp. 169-191, 1985.

[22] A. S. Argon, "Brittle to ductile transition in cleavage fracture," *Acta Metallurgica,* vol. 35, pp. 185-196, 1987.

[23] W. T. Ashurst and W. G. Hoover, "Microscopic fracture studies in the two-dimensional triangular lattice," *Physical Review B,* vol. 14, pp. 1465-1473, 1976.

[24] F. F. Abraham, D. Brodbeck, W. E. Rudge, and X. Xu, "A molecular dynamics investigation of rapid fracture mechanics," *Journal of the Mechanics and Physics of Solids,* vol. 45, pp. 1595-1619, 1997.

[25] F. F. Abraham, D. Brodbeck, R. A. Rafey, and W. E. Rudge, "Instability dynamics of fracture: A computer simulation investigation," *Physical Review Letters,* vol. 73, pp. 272-275, 1994.

[26] J. Fineberg, S. Gross, M. Marder, and H. Swinney, "Instability in dynamic fracture," *Physical Review Letters,* vol. 67, pp. 457-460, 1991.

[27] K. B. Broberg, "Cracks and Fracture," *Academic Press, San Diego, CA, USA,* 1999.

[28] D. J. Andrews, "RUPTURE VELOCITY OF PLANE STRAIN SHEAR CRACKS," *J Geophys Res,* vol. 81, pp. 5679-5687, 1976.

[29] Y. Huang and H. Gao, "Intersonic crack propagation - Part I: The fundamental solution," *Journal of Applied Mechanics, Transactions ASME,* vol. 68, pp. 169-175, 2001.

[30] P. H. Geubelle and D. V. Kubair, "Intersonic crack propagation in homogeneous media under shear-dominated loading: Numerical analysis," *Journal of the Mechanics and Physics of Solids,* vol. 49, pp. 571-587, 2001.

[31] A. J. Rosakis, "Intersonic shear cracks and fault ruptures," *Advances in Physics*, vol. 51, pp. 1189-1257, 2002.

[32] M. J. Buehler, H. Gao, and Y. Huang, "Atomistic and continuum studies of a suddenly stopping supersonic crack," *Computational Materials Science*, vol. 28, pp. 385-408, 2003.

[33] F. F. Abraham, "From the Cover: Simulating materials failure by using up to one billion atoms and the world's fastest computer: Brittle fracture," *Proceedings of the National Academy of Sciences*, vol. 99, pp. 5777-5782, 2002.

[34] J. Swadener, M. Baskes, and M. Nastasi, "Molecular Dynamics Simulation of Brittle Fracture in Silicon," *Physical Review Letters*, vol. 89, 2002.

[35] M. J. Buehler, F. F. Abraham, and H. Gao, "Hyperelasticity governs dynamic fracture at a critical length scale," *Nature*, vol. 426, pp. 141-146, 2003.

[36] M. J. Buehler and H. Gao, "Dynamical fracture instabilities due to local hyperelasticity at crack tips," *Nature*, vol. 439, pp. 307-10, Jan 19 2006.

[37] B. deCelis, A. S. Argon, and S. Yip, "Molecular dynamics simulation of crack tip processes in alpha-iron and copper," *Journal of Applied Physics*, vol. 54, p. 4864, 1983.

[38] S. Kohlhoff, P. Gumbsch, and H. F. Fischmeister, "Crack propagation in b.c.c. crystals studied with a combined finite-element and atomistic model," *Philosophical Magazine A: Physics of Condensed Matter, Structure, Defects and Mechanical Properties*, vol. 64, pp. 851-878, 1991.

[39] V. Shastry and D. Farkas, "Molecular statics simulation of fracture in α-iron," *Modelling and Simulation in Materials Science and Engineering*, vol. 4, pp. 473-492, 1996.

[40] V. A. Borodin and P. V. Vladimirov, "Molecular dynamics simulations of quasi-brittle crack development in iron," *Journal of Nuclear Materials*, vol. 415, pp. 320-328, 2011.

[41] K. Nishimura and N. Miyazaki, "Molecular dynamics simulation of crack propagation in polycrystalline material," *CMES - Computer Modeling in Engineering and Sciences,* vol. 2, pp. 143-154, 2001.

[42] Y. Takahashi, M. Tanaka, K. Higashida, K. Yamaguchi, and H. Noguchi, "An intrinsic effect of hydrogen on cyclic slip deformation around a {110} fatigue crack in Fe–3.2wt.% Si alloy," *Acta Materialia,* vol. 58, pp. 1972-1981, 2010.

[43] A. Latapie and D. Farkas, "Molecular dynamics simulations of stress-induced phase transformations and grain nucleation at crack tips in Fe," *Modelling and Simulation in Materials Science and Engineering,* vol. 11, pp. 745-753, 2003.

[44] K. S. Cheung, R. J. Harrison, and S. Yip, "Stress induced martensitic transition in a molecular dynamics model of α-iron," *Journal of Applied Physics,* vol. 71, p. 4009, 1992.

[45] Y.-F. Guo and D.-L. Zhao, "Atomistic simulation of structure evolution at a crack tip in bcc-iron," *Materials Science and Engineering: A,* vol. 448, pp. 281-286, 2007.

[46] Y.-F. Guo, Y.-S. Wang, D.-L. Zhao, and W.-P. Wu, "Mechanisms of martensitic phase transformations in body-centered cubic structural metals and alloys: Molecular dynamics simulations," *Acta Materialia,* vol. 55, pp. 6634-6641, 2007.

[47] S. L. Frederiksen, K. W. Jacobsen, and J. Schiøtz, "Simulations of intergranular fracture in nanocrystalline molybdenum," *Acta Materialia,* vol. 52, pp. 5019-5029, 2004.

[48] A. Latapie and D. Farkas, "Molecular dynamics investigation of the fracture behavior of nanocrystalline α-Fe," *Physical Review B,* vol. 69, 2004.

[49] Y. Zhang, P. C. Millett, M. Tonks, and S. B. Biner, "Deformation twins in nanocrystalline body-centered cubic Mo as predicted by molecular dynamics simulations," *Acta Materialia,* vol. 60, pp. 6421-6428, 2012.

[50] Y. Zhang, P. C. Millett, M. Tonks, and B. Biner, "Deformation-twin-induced grain boundary failure," *Scripta Materialia,* vol. 66, pp. 117-120, 2012.

[51] A. Latapie and D. Farkas, "Effect of grain size on the elastic properties of nanocrystalline α-iron," *Scripta Materialia,* vol. 48, pp. 611-615, 2003.

[52] D. Farkas and B. Hyde, "Improving the ductility of nanocrystalline bcc metals," *Nano Letters,* vol. 5, pp. 2403-2407, 2005.

[53] P. B. Hirsch and S. G. Roberts, "Comment on the brittle-to-ductile transition: A cooperative dislocation generation instability; dislocation dynamics and the strain-rate dependence of the transition temperature," *Acta Materialia,* vol. 44, pp. 2361-2371, 1996.

[54] M. D. W. A. C. D. Farkas, "Multiple-dislocation emission from the crack tip in the ductile fracture of Al," *Philosophical Magazine A,* vol. 81, pp. 1241-1255, 2001.

[55] E. B. Tadmor and S. Hai, "A Peierls criterion for the onset of deformation twinning at a crack tip," *Journal of the Mechanics and Physics of Solids,* vol. 51, pp. 765-793, 2003.

[56] S. Hai and E. B. Tadmor, "Deformation twinning at aluminum crack tips," *Acta Materialia,* vol. 51, pp. 117-131, 2003.

[57] S. J. Noronha and D. Farkas, "Effect of dislocation blocking on fracture behavior of Al and α-Fe: a multiscale study," *Materials Science and Engineering: A,* vol. 365, pp. 156-165, 2004.

[58] Y. T. Zhu, X. Z. Liao, S. G. Srinivasan, Y. H. Zhao, M. I. Baskes, F. Zhou, *et al.*, "Nucleation and growth of deformation twins in nanocrystalline aluminum," *Applied Physics Letters,* vol. 85, p. 5049, 2004.

[59] D. H. Warner, W. A. Curtin, and S. Qu, "Rate dependence of crack-tip processes predicts twinning trends in f.c.c. metals," *Nat Mater,* vol. 6, pp. 876-881, 2007.

[60] V. I. Yamakov and E. H. Glaessgen, "Nanoscale fracture: To twin or not to twin," *Nat Mater,* vol. 6, pp. 795-796, 2007.

[61] D. H. Warner and W. A. Curtin, "Origins and implications of temperature-dependent activation energy barriers for dislocation nucleation in face-centered cubic metals," *Acta Materialia,* vol. 57, pp. 4267-4277, 2009.

[62] D. Farkas, H. Van Swygenhoven, and P. Derlet, "Intergranular fracture in nanocrystalline metals," *Physical Review B,* vol. 66, 2002.

[63] K. Kadau, T. C. Germann, P. S. Lomdahl, B. L. Holian, D. Kadau, P. Entel, *et al.*, "Molecular-dynamics study of mechanical deformation in nano-crystalline aluminum," *Metallurgical and Materials Transactions A: Physical Metallurgy and Materials Science,* vol. 35 A, pp. 2719-2723, 2004.

[64] D. Farkas, S. Van Petegem, P. M. Derlet, and H. Van Swygenhoven, "Dislocation activity and nano-void formation near crack tips in nanocrystalline Ni," *Acta Materialia,* vol. 53, pp. 3115-3123, 2005.

[65] D. Farkas, "Fracture Resistance of Nanocrystalline Ni," *Metallurgical and Materials Transactions A,* vol. 38, pp. 2168-2173, 2007.

[66] I. A. Ovid'ko and A. G. Sheinerman, "Grain size effect on crack blunting in nanocrystalline materials," *Scripta Materialia,* vol. 60, pp. 627-630, 2009.

[67] A. Cao and Y. Wei, "Atomistic simulations of crack nucleation and intergranular fracture in bulk nanocrystalline nickel," *Physical Review B,* vol. 76, 2007.

[68] Z. X. Wu, Y. W. Zhang, M. H. Jhon, and D. J. Srolovitz, "Anatomy of nanomaterial deformation: Grain boundary sliding, plasticity and cavitation in nanocrystalline Ni," *Acta Materialia,* 2013.

[69] Y. Cheng, Z. H. Jin, Y. W. Zhang, and H. Gao, "On intrinsic brittleness and ductility of intergranular fracture along symmetrical tilt grain boundaries in copper," *Acta Materialia,* vol. 58, pp. 2293-2299, 2010.

[70] S. W. Kim, X. Li, H. Gao, and S. Kumar, "In situ observations of crack arrest and bridging by nanoscale twins in copper thin films," *Acta Materialia,* vol. 60, pp. 2959-2972, 2012.

[71] J. Zhang and S. Ghosh, "Molecular dynamics based study and characterization of deformation mechanisms near a crack in a crystalline material," *Journal of the Mechanics and Physics of Solids,* vol. 61, pp. 1670-1690, 2013.

[72] F. Yuan and X. Wu, "Atomistic scale fracture behaviours in hierarchically nanotwinned metals," *Philosophical Magazine,* vol. 93, pp. 3248-3259, 2013.

[73] E. Bitzek and P. Gumbsch, "Mechanisms of dislocation multiplication at crack tips," *Acta Materialia,* vol. 61, pp. 1394-1403, 2013.

[74] G. Q. Xu and M. J. Demkowicz, "Healing of nanocracks by disclinations," *Physical Review Letters,* vol. 111, 2013.

[75] B. Li, M. Sui, E. Ma, and S. Mao, "Reversible Twinning in Pure Aluminum," *Physical Review Letters,* vol. 102, 2009.

[76] M. Brede, "The brittle-to-ductile transition in silicon," *Acta Metallurgica Et Materialia,* vol. 41, pp. 211-228, 1993.

[77] S. G. Roberts, M. Ellis, and P. B. Hirsch, "Dislocation dynamics and brittle-to-ductile transitions," *Materials Science and Engineering A,* vol. 164, pp. 135-140, 1993.

[78] M. Khantha, D. P. Pope, and V. Vitek, "The brittle-to-ductile transition - I: A cooperative dislocation generation instability," *Scripta Metallurgica et Materiala,* vol. 31, pp. 1349-1354, 1994.

[79] S. G. Roberts, A. S. Booth, and P. B. Hirsch, "Dislocation activity and brittle-ductile transitions in single crystals," *Materials Science and Engineering A,* vol. 176, pp. 91-98, 1994.

[80] S. G. Roberts, "Modelling crack tip plastic zones and brittle-ductile transitions," *Materials Science and Engineering: A,* vol. 234–236, pp. 52-58, 1997.

[81] P. Gumbsch, J. Riedle, A. Hartmaier, and H. F. Fischmeister, "Controlling factors for the brittle-to-ductile transition in tungsten single crystals," *Science,* vol. 282, pp. 1293-1295, 1998.

[82] F. C. Serbena and S. G. Roberts, "The brittle-to-ductile transition in germanium," *Acta Metallurgica Et Materialia,* vol. 42, pp. 2505-2510, 1994.

[83] A. Giannattasio and S. G. Roberts, "Strain-rate dependence of the brittle-to-ductile transition temperature in tungsten," *Philosophical Magazine,* vol. 87, pp. 2589-2598, 2007.

[84] T. D. Joseph, M. Tanaka, A. J. Wilkinson, and S. G. Roberts, "Brittle-ductile transitions in vanadium and iron-chromium," *Journal of Nuclear Materials,* vol. 367-370 A, pp. 637-643, 2007.

[85] M. Tanaka, E. Tarleton, and S. G. Roberts, "The brittle-ductile transition in single-crystal iron," *Acta Materialia,* vol. 56, pp. 5123-5129, 2008.

[86] M. Tanaka, A. J. Wilkinson, and S. G. Roberts, "Ductile-brittle transition of polycrystalline iron and iron-chromium alloys," *Journal of Nuclear Materials,* vol. 378, pp. 305-311, 2008.

[87] Y. J. Hong, M. Tanaka, and K. Higashida, "The effect of arsenic on the brittle-to-ductile transition in Si single crystals," *Materials Transactions,* vol. 50, pp. 2177-2181, 2009.

[88] M. Tanaka, K. Maeno, and K. Higashida, "The effect of boron/antimony on the brittle-to-ductile transition in silicon single crystals," *Materials Transactions,* vol. 51, pp. 1206-1209, 2010.

[89] H. Li and F. Ebrahimi, "Ductile-to-brittle transition in nanocrystalline metals," *Advanced Materials,* vol. 17, pp. 1969-1972, 2005.

[90] H. Li and F. Ebrahimi, "Transition of deformation and fracture behaviors in nanostructured face-centered-cubic metals," *Applied Physics Letters,* vol. 84, pp. 4307-4309, 2004.

[91] C. Peng, Y. Zhan, and J. Lou, "Size-Dependent Fracture Mode Transition in Copper Nanowires," *Small,* vol. 8, pp. 1889-1894, 2012.

[92] G. Richter, K. Hillerich, D. S. Gianola, R. Mönig, O. Kraft, and C. A. Volkert, "Ultrahigh Strength Single Crystalline Nanowhiskers Grown by Physical Vapor Deposition," *Nano Letters,* vol. 9, pp. 3048-3052, 2009/08/12 2009.

[93] C. Peng, Y. Ganesan, Y. Lu, and J. Lou, "Size dependent mechanical properties of single crystalline nickel nanowires," *Journal of Applied Physics,* vol. 111, 2012.

[94] D. Jang, X. Li, H. Gao, and J. R. Greer, "Deformation mechanisms in nanotwinned metal nanopillars," *Nat Nano,* vol. advance online publication, 2012.

[95] J. Wang, F. Sansoz, J. Huang, Y. Liu, S. Sun, Z. Zhang, *et al.*, "Near-ideal theoretical strength in gold nanowires containing angstrom scale twins," *Nat Commun,* vol. 4, p. 1742, 2013.

[96] K. S. Cheung and S. Yip, "A molecular-dynamics simulation of crack-tip extension: The brittle-to-ductile transition," *Modelling and Simulation in Materials Science and Engineering,* vol. 2, pp. 865-892, 1994.

[97] A. Machová, G. E. Beltz, and M. Change, "Atomistic simulation of stacking fault formation in bcc iron," *Modelling and Simulation in Materials Science and Engineering,* vol. 7, pp. 949-974, 1999.

[98] Y.-F. Guo, C.-Y. Wang, and D.-L. Zhao, "Atomistic simulation of crack cleavage and blunting in bcc-Fe," *Materials Science and Engineering: A,* vol. 349, pp. 29-35, 2003.

[99] P. Hora, V. Pelikan, A. Machova, A. Spielmannova, J. Prahl, M. Landa, *et al.*, "Crack induced slip processes in 3D," *Engineering Fracture Mechanics,* vol. 75, pp. 3612-3623, 2008.

[100] A. Uhnáková, A. Machová, and P. Hora, "Ductile-brittle behavior along crack front and T-stress," vol. 465, ed, 2011, pp. 69-72.

[101] A. Machová and G. E. Beltz, "Ductile-brittle behavior of (0 0 1)[1 1 0] nano-cracks in bcc iron," *Materials Science and Engineering A,* vol. 387-389, pp. 414-418, 2004.

[102] G. E. Beltz and A. Machová, "Effect of T-stress on dislocation emission in iron," *Scripta Materialia,* vol. 50, pp. 483-487, 2004.

[103] J. Song and W. A. Curtin, "Atomic mechanism and prediction of hydrogen embrittlement in iron," *Nat Mater,* vol. advance online publication, 2012.

[104] D. Sen, C. Thaulow, S. V. Schieffer, A. Cohen, and M. J. Buehler, "Atomistic Study of Crack-Tip Cleavage to Dislocation Emission Transition in Silicon Single Crystals," *Physical Review Letters,* vol. 104, 2010.

[105] J. Han, L. Fang, J. Sun, Y. Han, and K. Sun, "Length-dependent mechanical properties of gold nanowires," *Journal of Applied Physics,* vol. 112, 2012.

[106] H. Zhou and S. Qu, "The effect of nanoscale twin boundaries on fracture toughness in nanocrystalline Ni," *Nanotechnology,* vol. 21, 2010.

[107] H. Van Swygenhoven, P. M. Derlet, and A. G. Froseth, "Stacking fault energies and slip in nanocrystalline metals," *Nat Mater,* vol. 3, pp. 399-403, Jun 2004.

[108] A. Frøseth, H. Van Swygenhoven, and P. M. Derlet, "The influence of twins on the mechanical properties of nc-Al," *Acta Materialia,* vol. 52, pp. 2259-2268, 2004.

[109] V. Yamakov, D. Wolf, S. R. Phillpot, and H. Gleiter, "Deformation twinning in nanocrystalline Al by molecular-dynamics simulation," *Acta Materialia,* vol. 50, pp. 5005-5020, 2002.

[110] X. Z. Liao, F. Zhou, E. J. Lavernia, D. W. He, and Y. T. Zhu, "Deformation twins in nanocrystalline Al," *Applied Physics Letters,* vol. 83, p. 5062, 2003.

[111] A. G. Frøseth, P. M. Derlet, and H. Van Swygenhoven, "Grown-in twin boundaries affecting deformation mechanisms in nc-metals," *Applied Physics Letters,* vol. 85, p. 5863, 2004.

[112] A. G. Frøseth, P. M. Derlet, and H. Van Swygenhoven, "Twinning in nanocrystalline fee metals," *Advanced Engineering Materials,* vol. 7, pp. 16-20, 2005.

[113] Y. T. Zhu, X. Z. Liao, and X. L. Wu, "Deformation twinning in nanocrystalline materials," *Progress in Materials Science,* vol. 57, pp. 1-62, 2012.

[114] K. S. Kumar, H. Van Swygenhoven, and S. Suresh, "Mechanical behavior of nanocrystalline metals and alloys11The Golden Jubilee Issue—Selected topics in Materials Science and Engineering: Past, Present and Future, edited by S. Suresh," *Acta Materialia,* vol. 51, pp. 5743-5774, 2003.

[115] F. C. Frank and W. T. Read Jr, "Multiplication processes for slow moving dislocations [7]," *Physical Review,* vol. 79, pp. 722-723, 1950.

[116] V. Yamakov, D. Wolf, S. R. Phillpot, A. K. Mukherjee, and H. Gleiter, "Deformation-mechanism map for nanocrystalline metals by molecular-dynamics simulation," *Nat Mater,* vol. 3, pp. 43-7, Jan 2004.

[117] V. Yamakov, D. Wolf, M. Salazar, S. R. Phillpot, and H. Gleiter, "Length-scale effects in the nucleation of extended dislocations in nanocrystalline Al by molecular-dynamics simulation," *Acta Materialia,* vol. 49, pp. 2713-2722, 2001.

[118] A. Lasalmonie and J. L. Strudel, "Influence of grain size on the mechanical behaviour of some high strength materials," *Journal of Materials Science,* vol. 21, pp. 1837-1852, 1986.

[119] T. Shimokawa, A. Nakatani, and H. Kitagawa, "Grain-size dependence of the relationship between intergranular and intragranular deformation of nanocrystalline Al by molecular dynamics simulations," *Physical Review B,* vol. 71, p. 224110, 2005.

[120] K. Lu, L. Lu, and S. Suresh, "Strengthening materials by engineering coherent internal boundaries at the nanoscale," *Science,* vol. 324, pp. 349-352, 2009.

[121] L. Zhu, H. Ruan, X. Li, M. Dao, H. Gao, and J. Lu, "Modeling grain size dependent optimal twin spacing for achieving ultimate high strength and related high ductility in nanotwinned metals," *Acta Materialia,* vol. 59, pp. 5544-5557, 2011.

[122] T. Zhu, J. Li, A. Samanta, H. G. Kim, and S. Suresh, "Interfacial plasticity governs strain rate sensitivity and ductility in nanostructured metals," *Proc Natl Acad Sci U S A,* vol. 104, pp. 3031-3036, 2007.

[123] Z. You, X. Li, L. Gui, Q. Lu, T. Zhu, H. Gao, *et al.*, "Plastic anisotropy and associated deformation mechanisms in nanotwinned metals," *Acta Materialia,* vol. 61, pp. 217-227, 2013.

[124] C. Deng and F. Sansoz, "Size-dependent yield stress in twinned gold nanowires mediated by site-specific surface dislocation emission," *Applied Physics Letters,* vol. 95, 2009.

[125] C. Deng and F. Sansoz, "Fundamental differences in the plasticity of periodically twinned nanowires in Au, Ag, Al, Cu, Pb and Ni," *Acta Materialia,* vol. 57, pp. 6090-6101, 2009.

[126] A. Stukowski, K. Albe, and D. Farkas, "Nanotwinned fcc metals: Strengthening versus softening mechanisms," *Physical Review B - Condensed Matter and Materials Physics,* vol. 82, 2010.

[127] Z. X. Wu, Y. W. Zhang, and D. J. Srolovitz, "Deformation mechanisms, length scales and optimizing the mechanical properties of nanotwinned metals," *Acta Materialia,* vol. 59, pp. 6890-6900, 2011.

[128] Z. X. Wu, Y. W. Zhang, and D. J. Srolovitz, "Dislocation-twin interaction mechanisms for ultrahigh strength and ductility in nanotwinned metals," *Acta Materialia,* vol. 57, pp. 4508-4518, 2009.

[129] Y. Zhang and H. Huang, "Do twin boundaries always strengthen metal nanowires?," *Nanoscale Research Letters,* vol. 4, pp. 34-38, 2009.

[130] A. J. Cao and Y. G. Wei, "Molecular dynamics simulation of plastic deformation of nanotwinned copper," *Journal of Applied Physics,* vol. 102, 2007.

[131] A. J. Cao, Y. G. Wei, and S. X. Mao, "Deformation mechanisms of face-centered-cubic metal nanowires with twin boundaries," *Applied Physics Letters,* vol. 90, 2007.

[132] M. Sun, R. Cao, F. Xiao, and C. Deng, "Surface and interface controlled yielding and plasticity in fivefold twinned Ag nanowires," *Computational Materials Science,* vol. 79, pp. 289-295, 2013.

[133] A. Cao and Y. Wei, "Atomistic simulations of the mechanical behavior of fivefold twinned nanowires," *Physical Review B,* vol. 74, p. 214108, 2006.

[134] Y. Wei, "Anisotropic size effect in strength in coherent nanowires with tilted twins," *Physical Review B - Condensed Matter and Materials Physics,* vol. 84, 2011.

[135] J. J. Zhang, A. Hartmaier, Y. J. Wei, Y. D. Yan, and T. Sun, "Mechanisms of anisotropic friction in nanotwinned Cu revealed by atomistic simulations," *Modelling and Simulation in Materials Science and Engineering,* vol. 21, 2013.

[136] S. Qu, G. Wang, H. Zhou, and Z. Huang, "Can nanoscale twin boundaries serve as dislocation sources in single crystals?," *Computational Materials Science,* vol. 50, pp. 1567-1570, 2011.

[137] F. Yuan and X. Wu, "Size effects of primary/secondary twins on the atomistic deformation mechanisms in hierarchically nanotwinned metals," *Journal of Applied Physics,* vol. 113, 2013.

[138] Y. M. Wang, F. Sansoz, T. LaGrange, R. T. Ott, J. Marian, T. W. Barbee Jr, *et al.*, "Defective twin boundaries in nanotwinned metals," *Nat Mater,* vol. 12, pp. 697-702, 2013.

[139] J. H. Yoo, S. I. Oh, and M. S. Jeong, "The enhanced elastic modulus of nanowires associated with multitwins," *Journal of Applied Physics,* vol. 107, 2010.

[140] L. Yue, H. Zhang, and D. Y. Li, "Defect generation in nano-twinned, nano-grained and single crystal Cu systems caused by wear: A molecular dynamics study," *Scripta Materialia,* vol. 63, pp. 1116-1119, 2010.

[141] Y. Zhang and H. Huang, "Controllable introduction of twin boundaries into nanowires," *Journal of Applied Physics,* vol. 108, 2010.

[142] A. J. Cao and Y. G. Wei, "Formation of fivefold deformation twins in nanocrystalline face-centered-cubic copper based on molecular dynamics simulations," *Applied Physics Letters,* vol. 89, p. 041919, 2006.

[143] T. Sinha and Y. Kulkarni, "Anomalous deformation twinning in fcc metals at high temperatures," *Journal of Applied Physics,* vol. 109, 2011.

[144] E. L. Wood and F. Sansoz, "Growth and properties of coherent twinning superlattice nanowires," *Nanoscale,* vol. 4, pp. 5268-5276, 2012.

[145] C. Deng and F. Sansoz, "Repulsive force of twin boundary on curved dislocations and its role on the yielding of twinned nanowires," *Scripta Materialia,* vol. 63, pp. 50-53, 2010.

[146] K. Chen, S. Q. Shi, and J. Lu, "Tensile deformation properties of single crystal copper with nanotwins," *Computational Materials Science,* vol. 83, pp. 269-276, 2014.

[147] Y. Lu, J. Song, J. Y. Huang, and J. Lou, "Fracture of Sub-20nm Ultrathin Gold Nanowires," *Advanced Functional Materials,* vol. 21, pp. 3982-3989, 2011.

[148] Y.-F. Guo *, C.-Y. Wang, and Y.-S. Wang, "The effect of stacking faults or twin formation on crack propagation in bcc iron," *Philosophical Magazine Letters,* vol. 84, pp. 763-770, 2004.

[149] X. X. Chen and A. H. W. Ngan, "Specimen size and grain size effects on tensile strength of Ag microwires," *Scripta Materialia,* vol. 64, pp. 717-720, 2011.

[150] C. P. Frick, B. G. Clark, S. Orso, A. S. Schneider, and E. Arzt, "Size effect on strength and strain hardening of small-scale [1 1 1] nickel compression pillars," *Materials Science and Engineering: A,* vol. 489, pp. 319-329, 2008.

[151] A. Kunz, S. Pathak, and J. R. Greer, "Size effects in Al nanopillars: Single crystalline vs. bicrystalline," *Acta Materialia,* vol. 59, pp. 4416-4424, 2011.

[152] J. Biener, A. M. Hodge, J. R. Hayes, C. A. Volkert, L. A. Zepeda-Ruiz, A. V. Hamza, *et al.*, "Size effects on the mechanical behavior of nanoporous Au," *Nano Letters,* vol. 6, pp. 2379-2382, 2006.

[153] J. R. Greer and J. T. De Hosson, "Plasticity in small-sized metallic systems: intrinsic versus extrinsic size effect," *Prog. Mater. Sci.,* vol. 56, pp. 654-724, 2011.

[154] P. Gu and M. Dao, "Size-dependent deformation in nanograins and nanotwins," *Applied Physics Letters,* vol. 102, 2013.

[155] C. Deng and F. Sansoz, "Enabling ultrahigh plastic flow and work hardening in twinned gold nanowires," *Nano Lett.,* vol. 9, pp. 1517-1522, 2009.

[156] X. W. Gu, C. N. Loynachan, Z. Wu, Y. W. Zhang, D. J. Srolovitz, and J. R. Greer, "Size-dependent deformation of nanocrystalline Pt nanopillars," *Nano Letters,* vol. 12, pp. 6385-6392, 2012.

[157] Y. Zhu, Z. Li, and M. Huang, "Coupled effect of sample size and grain size in polycrystalline Al nanowires," *Scripta Materialia,* vol. 68, pp. 663-666, 2013.

[158] C. Deng and F. Sansoz, "Near-Ideal Strength in Gold Nanowires Achieved through Microstructural Design," *ACS Nano,* vol. 3, pp. 3001-3008, 2009/10/27 2009.

[159] C. Deng and F. Sansoz, "Effects of twin and surface facet on strain-rate sensitivity of gold nanowires at different temperatures," *Physical Review B - Condensed Matter and Materials Physics,* vol. 81, 2010.

[160] H. S. Park, K. Gall, and J. A. Zimmerman, "Deformation of FCC nanowires by twinning and slip," *Journal of the Mechanics and Physics of Solids,* vol. 54, pp. 1862-1881, 2006.

[161] B. Chen, K. Lutker, S. V. Raju, J. Yan, W. Kanitpanyacharoen, J. Lei, *et al.*, "Texture of nanocrystalline nickel: Probing the lower size limit of dislocation activity," *Science,* vol. 338, pp. 1448-1451, 2012.

[162] L. Miyagi, W. Kanitpanyacharoen, P. Kaercher, K. K. M. Lee, and H. R. Wenk, "Slip systems in MgSiO3 post-perovskite: Implications for D″ anisotropy," *Science,* vol. 329, pp. 1639-1641, 2010.

[163] L. Pizzagalli, J. L. Demenet, and J. Rabier, "Theoretical study of pressure effect on the dislocation core properties in semiconductors," *Physical Review B - Condensed Matter and Materials Physics,* vol. 79, 2009.

[164] L. P. Dávila, P. Erhart, E. M. Bringa, M. A. Meyers, V. A. Lubarda, M. S. Schneider, *et al.*, "Atomistic modeling of shock-induced void collapse in copper," *Applied Physics Letters,* vol. 86, pp. 1-3, 2005.

[165] E. M. Bringa, A. Caro, Y. Wang, M. Victoria, J. M. McNaney, B. A. Remington, *et al.*, "Materials science: Ultrahigh strength in nanocrystalline materials under shock loading," *Science,* vol. 309, pp. 1838-1841, 2005.

[166] F. Yuan and X. Wu, "Shock response of nanotwinned copper from large-scale molecular dynamics simulations," *Physical Review B - Condensed Matter and Materials Physics,* vol. 86, 2012.

[167] W. Z. Han, Q. An, S. N. Luo, T. C. Germann, D. L. Tonks, and W. A. Goddard, "Deformation and spallation of shocked Cu bicrystals with Σ3 coherent and symmetric incoherent twin boundaries," *Physical Review B - Condensed Matter and Materials Physics,* vol. 85, 2012.

[168] S.-N. Luo, T. C. Germann, T. G. Desai, D. L. Tonks, and Q. An, "Anisotropic shock response of columnar nanocrystalline Cu," *Journal of Applied Physics,* vol. 107, pp. -, 2010.

[169] A. M. He, S. Q. Duan, J. L. Shao, P. Wang, and S. N. Luo, "Local and bulk melting of shocked columnar nanocrystalline Cu: Dynamics, anisotropy, premelting, superheating, supercooling, and re-crystallization," *Journal of Chemical Physics,* vol. 139, 2013.

[170] V. Yamakov, E. Saether, D. R. Phillips, and E. H. Glaessgen, "Dynamics of nanoscale grain-boundary decohesion in aluminum by molecular-dynamics simulation," *Journal of Materials Science,* vol. 42, pp. 1466-1476, 2007.

[171] F. Yuan and X. Wu, "Hydrostatic pressure effects on deformation mechanisms of nanocrystalline fcc metals," *Computational Materials Science,* vol. 85, pp. 8-15, 2014.

[172] E. M. Bringa, A. Caro, and E. Leveugle, "Pressure effects on grain boundary plasticity in nanophase metals," *Applied Physics Letters,* vol. 89, 2006.

[173] T. Zhu, J. Li, A. Samanta, A. Leach, and K. Gall, "Temperature and strain-rate dependence of surface dislocation nucleation," *Physical Review Letters,* vol. 100, 2008.

[174] A. M. Iskandarov, S. V. Dmitriev, and Y. Umeno, "Temperature effect on ideal shear strength of Al and Cu," *Physical Review B,* vol. 84, p. 224118, 2011.

[175] M. A. Tschopp and D. L. McDowell, "Influence of single crystal orientation on homogeneous dislocation nucleation under uniaxial loading," *Journal of the Mechanics and Physics of Solids,* vol. 56, pp. 1806-1830, 2008.

[176] F. Wang, T. Chen, T. Zhu, Y. Gao, and J. Zhao, "Uniaxial tension-induced breaking in the gold nanowire with the influence of defects and temperatures," *Journal of Applied Physics,* vol. 110, 2011.

[177] A. T. Jennings, J. Li, and J. R. Greer, "Emergence of strain-rate sensitivity in Cu nanopillars: transition from dislocation multiplication to dislocation nucleation," *Acta Materialia,* vol. 59, pp. 5627-5637, 2011.

[178] M. A. Tschopp and D. L. McDowell, "Grain boundary dislocation sources in nanocrystalline copper," *Scripta Materialia,* vol. 58, pp. 299-302, 2008.

[179] J. J. Möller and E. Bitzek, "Fracture toughness and bond trapping of grain boundary cracks," *Acta Materialia,* vol. 73, pp. 1-11, 7// 2014.

[180] V. Yamakov, D. Wolf, S. R. Phillpot, and H. Gleiter, "Dislocation–dislocation and dislocation–twin reactions in nanocrystalline Al by molecular dynamics simulation," *Acta Materialia,* vol. 51, pp. 4135-4147, 2003.

[181] Z. H. Jin, P. Gumbsch, K. Albe, E. Ma, K. Lu, H. Gleiter, *et al.*, "Interactions between non-screw lattice dislocations and coherent twin boundaries in face-centered cubic metals," *Acta Materialia,* vol. 56, pp. 1126-1135, 2008.

[182] Z. H. Jin, P. Gumbsch, E. Ma, K. Albe, K. Lu, H. Hahn, *et al.*, "The interaction mechanism of screw dislocations with coherent twin boundaries in different face-centred cubic metals," *Scripta Materialia,* vol. 54, pp. 1163-1168, 2006.

[183] E. Bitzek, C. Brandl, P. Derlet, and H. Van Swygenhoven, "Dislocation Cross-Slip in Nanocrystalline fcc Metals," *Physical Review Letters,* vol. 100, 2008.

[184] I. Shabib and R. E. Miller, "Deformation characteristics and stress–strain response of nanotwinned copper via molecular dynamics simulation," *Acta Materialia,* vol. 57, pp. 4364-4373, 2009.

[185] Y. T. Zhu, X. L. Wu, X. Z. Liao, J. Narayan, L. J. Kecskés, and S. N. Mathaudhu, "Dislocation–twin interactions in nanocrystalline fcc metals," *Acta Materialia,* vol. 59, pp. 812-821, 2011.

[186] A. Hasnaoui, P. M. Derlet, and H. Van Swygenhoven, "Interaction between dislocations and grain boundaries under an indenter - A molecular dynamics simulation," *Acta Materialia,* vol. 52, pp. 2251-2258, 2004.

[187] H. Vanswygenhoven and P. Derlet, "Chapter 81 Atomistic Simulations of Dislocations in FCC Metallic Nanocrystalline Materials," vol. 14, pp. 1-42, 2008.

[188] H. Van Swygenhoven, P. M. Derlet, and A. G. Frøseth, "Nucleation and propagation of dislocations in nanocrystalline fcc metals," *Acta Materialia,* vol. 54, pp. 1975-1983, 2006.

[189] Z. Pan, Y. Li, and Q. Wei, "Tensile properties of nanocrystalline tantalum from molecular dynamics simulations," *Acta Materialia,* vol. 56, pp. 3470-3480, 2008.

[190] Y. Mishin, M. Mehl, D. Papaconstantopoulos, A. Voter, and J. Kress, "Structural stability and lattice defects in copper: ab initio, tight-binding, and embedded-atom calculations," *Phys. Rev. B,* vol. 63, p. 224106, 2001.

[191] A. Cao, Y. Wei, and E. Ma, "Grain boundary effects on plastic deformation and fracture mechanisms in Cu nanowires: Molecular dynamics simulations," *Physical Review B,* vol. 77, 2008.

[192] A. Stukowski, V. V. Bulatov, and A. Arsenlis, "Automated identification and indexing of dislocations in crystal interfaces," *Modelling and Simulation in Materials Science and Engineering,* vol. 20, p. 085007, 2012.

[193] A. Stukowski and K. Albe, "Extracting dislocations and non-dislocation crystal defects from atomistic simulation data," *Modelling and Simulation in Materials Science and Engineering,* vol. 18, 2010.

[194] "https://en.wikipedia.org/wiki/Supercomputer."

[195] X. Li, "Large-scale Atomistic Simulations of Deformation and Fracture Mechanisms of Nanotwinned Metals," *PhD thesis*, 2012.

[196] S. Plimpton, "Fast parallel algorithms for short-range molecular dynamics," *Journal of Computational Physics,* vol. 117, pp. 1-19, 1995.

[197] M. Parrinello and A. Rahman, "Polymorphic transitions in single crystals: A new molecular dynamics method," *Journal of Applied Physics,* vol. 52, pp. 7182-7190, 1981.

[198] A. Stukowski, "Visualization and analysis of atomistic simulation data with OVITO-the Open Visualization Tool," *Modelling and Simulation in Materials Science and Engineering,* vol. 18, 2010.

[199] J. Diao, K. Gall, and M. L. Dunn, "Atomistic simulation of the structure and elastic properties of gold nanowires," *Journal of the Mechanics and Physics of Solids,* vol. 52, pp. 1935-1962, 2004.

[200] S. Xu and X. Deng, "Nanoscale void nucleation and growth and crack tip stress evolution ahead of a growing crack in a single crystal," *Nanotechnology,* vol. 19, p. 115705, Mar 19 2008.

[201] M. A. Meyers and K. K. Chawla, *Mechanical Behavior of Materials*: Cambridge University Press, 2009.

[202] L. B. Freund, *Dynamic Fracture Mechanics*. New York: Cambridge University Press, 1990.

[203] H. Gao, Y. Huang, and F. F. Abraham, "Continuum and atomistic studies of intersonic crack propagation," *Journal of the Mechanics and Physics of Solids,* vol. 49, pp. 2113-2132, 2001.

[204] H. M. Ledbetter and E. R. Naimon, "Elastic Properties of Metals and Alloys. II. Copper," *Journal of Physical and Chemical Reference Data,* vol. 3, pp. 897-935, 1974.

[205] A. Hartmaier and P. Gumbsch, "Brittle-to-ductile transition and dislocation activity at crack tips," *Journal of Computer-Aided Materials Design,* vol. 6, pp. 145-155, 1999.

[206] S. J. Zhou, P. S. Lomdahl, R. Thomson, and B. L. Holian, "Dynamic crack processes via molecular dynamics," *Physical Review Letters,* vol. 76, pp. 2318-2321, 1996.

[207] F. F. Abraham and J. Q. Broughton, "Large-scale simulations of brittle and ductile failure in fee crystals," *Computational Materials Science,* vol. 10, pp. 1-9, 1998.

[208] S. Glasstone, K. Laidler, and H. Eyring, *The Theory of Rate Processes*. New York: McGraw Hill, 1941.

[209] H. Kimizuka, H. Kaburaki, F. Shimizu, and J. Li, "Crack-tip dislocation nanostructures in dynamical fracture of fee metals: A molecular dynamics study," *Journal of Computer-Aided Materials Design,* vol. 10, pp. 143-154, 2003.

[210] C. B. Cui and H. G. Beom, "Molecular dynamics simulations of edge cracks in copper and aluminum single crystals," *Materials Science and Engineering A,* vol. 609, pp. 102-109, 2014.

[211] J. H. Chen, Q. Wang, G. Z. Wang, and Z. Li, "Fracture behavior at crack tip - A new framework for cleavage mechanism of steel," *Acta Materialia,* vol. 51, pp. 1841-1855, 2003.

[212] C. Thaulow, D. Sen, and M. J. Buehler, "Atomistic study of the effect of crack tip ledges on the nucleation of dislocations in silicon single crystals at elevated temperature," *Materials Science and Engineering A,* vol. 528, pp. 4357-4364, 2011.

[213] M. Khantha, D. P. Pope, and V. Vitek, "Dislocation screening and the brittle-to-ductile transition: A Kosterlitz-Thouless type instability," *Physical Review Letters,* vol. 73, pp. 684-687, 1994.

[214] A. S. Argon and S. R. Maloof, "Fracture of tungsten single crystals at low temperatures," *Acta Metallurgica,* vol. 14, pp. 1463-1468, 1966.

[215] M. I. Mendelev, M. J. Kramer, S. G. Hao, K. M. Ho, and C. Z. Wang, "Development of interatomic potentials appropriate for simulation of liquid and glass properties of NiZr2 alloy," *Philosophical Magazine,* vol. 92, pp. 4454-4469, 2012/12/11 2012.

[216] M. A. Meyers and K. K. Chawla, "Mechanical Behavior of Materials," *Cambridge University Press*, 2009 2009.

[217] W. D. Wang, C. L. Yi, and K. Q. Fan, "Molecular dynamics study on temperature and strain rate dependences of mechanical tensile properties of ultrathin nickel nanowires," *Transactions of Nonferrous Metals Society of China (English Edition)*, vol. 23, pp. 3353-3361, 2013.

[218] T. Aihara, R. Kaneko, M. H. F. Sluiter, and Y. Kawazoe, "Molecular dynamics simulation of temperature dependence of dislocation behavior in fcc Ni single crystal under tensile condition," *Materials Transactions*, vol. 42, pp. 425-428, 2001.

[219] C. Thaulow, S. V. Schieffer, I. R. Vatne, D. Sen, and E. Østby, "Crack Tip Opening Displacement in atomistic modeling of fracture of silicon," *Computational Materials Science*, vol. 50, pp. 2621-2627, 2011.

[220] H. Zhou, S. Qu, and W. Yang, "Toughening by nano-scaled twin boundaries in nanocrystals," *Modelling and Simulation in Materials Science and Engineering*, vol. 18, 2010.

[221] P. Gumbsch, S. J. Zhou, and B. L. Holian, "Molecular dynamics investigation of dynamic crack stability," *Physical Review B - Condensed Matter and Materials Physics*, vol. 55, pp. 3445-3455, 1997.

[222] E. Bouchaud, J. P. Bouchaud, D. S. Fisher, S. Ramanathan, and J. R. Rice, "Can crack front waves explain the roughness of cracks?," *Journal of the Mechanics and Physics of Solids*, vol. 50, pp. 1703-1725, 2002.

[223] T. Cramer, A. Wanner, and P. Gumbsch, "Energy dissipation and path instabilities in dynamic fracture of silicon single crystals," *Physical Review Letters*, vol. 85, pp. 788-791, 2000.

[224] R. W. Armstrong, "Cleavage crack propagation within crystals by the Griffith mechanism versus a dislocation mechanism," *Materials Science and Engineering*, vol. 1, pp. 251-254, 1966.

[225] A. Kelly, W. R. Tyson, and A. H. Cottrell, "Ductile and brittle crystals," *Philosophical Magazine*, vol. 15, pp. 567-586, 1967/03/01 1967.

[226] S. J. Zhou, A. E. Carlsson, and R. Thomson, "Crack blunting effects on dislocation emission from cracks," *Physical Review Letters*, vol. 72, pp. 852-855, 1994.

[227] G. Xu, A. S. Argon, and M. Ortiz, "Nucleation of dislocations from crack tips under mixed modes of loading: Implications for brittle against ductile behaviour of crystals," *Phil. Mag. A*, vol. 72, pp. 415-451, 1995.

[228] Y. Cheng, M. X. Shi, and Y. W. Zhang, "Atomistic simulation study on key factors dominating dislocation nucleation from a crack tip in two FCC materials: Cu and Al," *International Journal of Solids and Structures*, vol. 49, pp. 3345-3354, 2012.

[229] Y. Sun, G. E. Beltz, and J. R. Rice, "Estimates from atomic models of tension-shear coupling in dislocation nucleation from a crack tip," *Materials Science and Engineering A*, vol. 170, pp. 67-85, 1993.

[230] F. Cleri, S. Yip, D. Wolf, and S. R. Phillpot, "Atomic-scale mechanism of crack-tip plasticity: Dislocation nucleation and crack-tip shielding," *Physical Review Letters*, vol. 79, pp. 1309-1312, 1997.

[231] J. Knap and K. Sieradzki, "Crack Tip Dislocation Nucleation in FCC Solids," *Physical Review Letters*, vol. 82, pp. 1700-1703, 1999.

[232] Y. W. Zhang, T. C. Wang, and Q. H. Tang, "Brittle and ductile fracture at the atomistic crack tip in copper crystals," *Scripta Metallurgica et Materiala*, vol. 33, pp. 267-274, 1995.

[233] T. Zhu, J. Li, and S. Yip, "Atomistic characterization of three-dimensional lattice trapping barriers to brittle fracture," *Proceedings of the Royal Society A: Mathematical, Physical and Engineering Sciences*, vol. 462, pp. 1741-1761, 2006.

[234] Y. F. Guo and C. Y. Wang, "Atomistic study of lattice trapping behavior for brittle fracture in bcc-iron," *Computational Materials Science,* vol. 40, pp. 376-381, 2007.

[235] N. Bernstein and D. W. Hess, "Lattice trapping barriers to brittle fracture," *Physical Review Letters,* vol. 91, pp. 025501/1-025501/4, 2003.

[236] R. Thomson, C. Hsieh, and V. Rana, "Lattice trapping of fracture cracks," *Journal of Applied Physics,* vol. 42, pp. 3154-3160, 1971.

[237] P. Gumbsch, "Atomistic study of brittle fracture: toward explicit failure criteria from atomistic modeling," *Journal of Materials Research,* vol. 10, pp. 2897-2907, 1995.

[238] K. Kang and W. Cai, "Brittle and ductile fracture of semiconductor nanowires - molecular dynamics simulations," *Philosophical Magazine,* vol. 87, pp. 2169-2189, 2007.

[239] M. I. Mendelev, M. J. Kramer, C. A. Becker, and M. Asta, "Analysis of semi-empirical interatomic potentials appropriate for simulation of crystalline and liquid Al and Cu," *Philosophical Magazine,* vol. 88, pp. 1723-1750, 2008.

[240] P. L. Williams, Y. Mishin, and J. C. Hamilton, "An embedded-atom potential for the Cu-Ag system," *Modelling and Simulation in Materials Science and Engineering,* vol. 14, pp. 817-833, 2006.

[241] X. W. Zhou, R. A. Johnson, and H. N. G. Wadley, "Misfit-energy-increasing dislocations in vapor-deposited CoFe/NiFe multilayers," *Physical Review B - Condensed Matter and Materials Physics,* vol. 69, pp. 144113-1-144113-10, 2004.

[242] G. Grochola, S. P. Russo, and I. K. Snook, "On fitting a gold embedded atom method potential using the force matching method," *Journal of Chemical Physics,* vol. 123, 2005.

[243] P. Gumbsch and R. M. Cannon, "Atomistic Aspects of Brittle Fracture," *MRS Bulletin,* vol. 25, pp. 15-20, 2000.

[244] M. Marder and S. Gross, "Origin of crack tip instabilities," *Journal of the Mechanics and Physics of Solids,* vol. 43, pp. 1-48, 1995.

[245] R. Pérez and P. Gumbsch, "Directional Anisotropy in the Cleavage Fracture of Silicon," *Physical Review Letters,* vol. 84, pp. 5347-5350, 2000.

[246] J. Riedle, P. Gumbsch, and H. F. Fischmeister, "Cleavage Anisotropy in Tungsten Single Crystals," *Physical Review Letters,* vol. 76, pp. 3594-3597, 1996.

[247] Y. Mishin, D. Farkas, M. J. Mehl, and D. A. Papaconstantopoulos, "Interatomic potentials for monoatomic metals from experimental data and ab initio calculations," *Physical Review B - Condensed Matter and Materials Physics,* vol. 59, pp. 3393-3407, 1999.

[248] S. Huang, S. Zhang, T. Belytschko, S. S. Terdalkar, and T. Zhu, "Mechanics of nanocrack: Fracture, dislocation emission, and amorphization," *Journal of the Mechanics and Physics of Solids,* vol. 57, pp. 840-850, 2009.

[249] D. Jang, X. Li, H. Gao, and J. R. Greer, "Deformation mechanisms in nanotwinned metal nanopillars," *Nature Nanotechnology,* vol. 7, pp. 594-601, 2012.

[250] S. Yip, J. Li, and T. Zhu, "Atomistic characterization of three-dimensional lattice trapping barriers to brittle fracture," *Proceedings of the Royal Society A: Mathematical, Physical and Engineering Sciences,* vol. 462, pp. 1741-1761, 2006.

[251] J. J. Möller and E. Bitzek, "Comparative study of embedded atom potentials for atomistic simulations of fracture inα-iron," *Modelling and Simulation in Materials Science and Engineering,* vol. 22, p. 045002, 2014.

[252] C. Wang, Q. Han, and D. Xin, "Fracture analysis of single-layer graphene sheets with edge crack under tension," *Molecular Simulation,* pp. 1-8, 2014.

[253] S. N. Luo, T. C. Germann, and D. L. Tonks, "The effect of vacancies on dynamic response of single crystal Cu to shock waves," *Journal of Applied Physics,* vol. 107, 2010.

[254] J. Luster and M. A. Morris, "Compatibility of deformation in two-phase Ti-Al alloys: Dependence on microstructure and orientation relationships," *Metallurgical and Materials Transactions A,* vol. 26, pp. 1745-1756, 1995.

[255] W. M. Ashmawi and M. A. Zikry, "Grain boundary effects and void porosity evolution," *Mechanics of Materials,* vol. 35, pp. 537-552, 2003.

[256] N. Q. Chinh, P. Szommer, Z. Horita, and T. G. Langdon, "Experimental evidence for grain-boundary sliding in ultrafine-grained aluminum processed by severe plastic deformation," *Advanced Materials,* vol. 18, pp. 34-39, 2006.

[257] P. Xue, B. L. Xiao, and Z. Y. Ma, "High tensile ductility via enhanced strain hardening in ultrafine-grained Cu," *Materials Science and Engineering A,* vol. 532, pp. 106-110, 2012.

[258] Y. Zhao, Y. Zhu, and E. J. Lavernia, "Strategies for improving tensile ductility of bulk nanostructured materials," *Advanced Engineering Materials,* vol. 12, pp. 769-778, 2010.

[259] A. Hasnaoui, H. Van Swygenhoven, and P. M. Derlet, "Dimples on nanocrystalline fracture surfaces as evidence for shear plane formation," *Science,* vol. 300, pp. 1550-2, Jun 6 2003.

[260] K. Cheung and S. Yip, "Brittle-ductile transition in intrinsic fracture behavior of crystals," *Physical Review Letters,* vol. 65, pp. 2804-2807, 1990.

[261] C. B. Cui and H. G. Beom, "Molecular dynamics simulations of edge cracks in copper and aluminum single crystals," *Materials Science and Engineering: A,* vol. 609, pp. 102-109, 2014.

[262] A. Adnan and C. T. Sun, "Evolution of nanoscale defects to planar cracks in a brittle solid," *Journal of the Mechanics and Physics of Solids,* vol. 58, pp. 983-1000, 2010.

[263] J. Song and W. A. Curtin, "Atomic mechanism and prediction of hydrogen embrittlement in iron," *Nature Materials*, vol. 12, pp. 145-151, 2013.